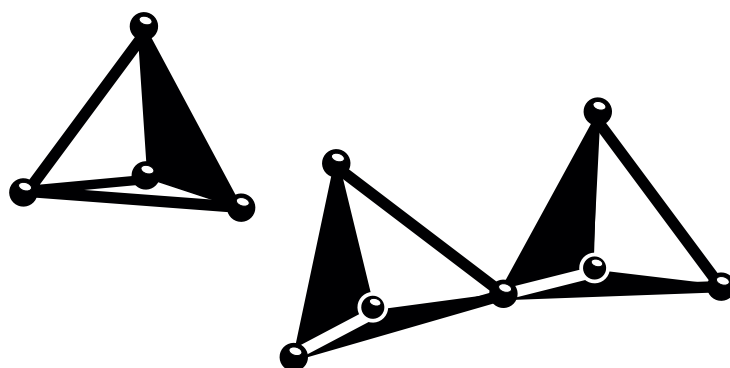


DISSERTATION

**Structure Activity Correlations of
Vanadium and Molybdenum
Oxide Catalysts
Supported on
Nanostructured Materials**



von

JULIANE SCHOLZ

TECHNISCHE UNIVERSITÄT BERLIN



Structure Activity Correlations of Vanadium and Molybdenum Oxide Catalysts Supported on Nanostructured Materials

vorgelegt von Diplom-Chemikerin

Juliane Scholz

Potsdam

von der Fakultät II – Mathematik und Naturwissenschaften
der Technischen Universität Berlin
zur Erlangung des akademischen Grades

Doktor der Naturwissenschaften

– Dr. rer. nat. –

genehmigte Dissertation

Promotionsausschuss:

Vorsitzender: Prof. Dr. rer. nat. Thomas Friedrich

Berichter/Gutachter: Prof. Dr. rer. nat. Thorsten Ressler

Berichter/Gutachter: Prof. Dr. rer. nat. Christian Hess

Tag der wissenschaftlichen Aussprache: 04. Februar 2014

Berlin 2014

D 83

*" [...] it is prudent to remind ourselves that,
in catalysis, almost everything we investigate is interesting.
But not everything is important."*

Sir John Meurig Thomas
in "Turning Points in Catalysis".[1]

Zusammenfassung

Vanadium- und Molybdänoxide, aufgebracht auf einem basischen *MgO/SBA-15*-Träger mit hoher spezifischer Oberfläche, erwiesen sich als geeignete Modellkatalysatorsysteme für die Untersuchung von Struktur-Aktivitäts-Korrelationen in der katalytischen Partialoxidation von Alkenen und Alkanen. Die *V/MgO/SBA-15*- und *Mo/MgO/SBA-15*-Katalysatoren wurden mit Beladungen im Bereich von 1–10 wt.% V bzw. Mo (0.2–5.9 Metallatome pro nm²) hergestellt. Die kombinierte Anwendung verschiedener Methoden (Röntgenabsorptions- und DR-UV-Vis-Spektroskopie, N₂-Adsorption, Röntgenbeugung, Ramanspektroskopie und Gaschromatographie) ermöglichte die strukturelle und funktionelle Charakterisierung der Metalloxidkatalysatoren. Die Untersuchungen ergaben, dass die Vanadium- und Molybdänoxidspezies aus tetraedrischen [MO₄]-Metalloxeinheiten bestanden. Der Verknüpfungsgrad der Vanadiumoxideinheiten war stark beladungsabhängig und nahm mit steigender Oberflächenbedeckung von monomeren hinzu verknüpften [VO₄]-Tetraedern zu. Im Gegensatz zu der Vanadiumoxidstruktur, war die Struktur der Molybdänoxide unabhängig von der Katalysatorbeladung. Die Molybdänoxidspezies lag als eine Mischung aus [MoO₄]- und [Mo₂O₇]-Einheiten im Verhältnis ~ 3:2 von monomeren zu dimeren Einheiten vor. Weiterhin fand ein Vergleich der auf *MgO/SBA-15* aufgetragenen Vanadium- und Molybdänoxide mit Oxiden statt, die auf anderen Materialien aufgebracht waren. Im Vergleich zu den oligomerisierten Metalloxeinheiten auf SBA-15 und CMK-3, konnten auf *MgO/SBA-15* gering verknüpfte Metalloxeinheiten bei vergleichsweise hohen Beladungen stabilisiert werden. Dies lässt sich auf die basische Oberfläche des *MgO/SBA-15*-Trägers zurückführen.

Aufbauend auf der strukturellen Grundcharakterisierung der Katalysatorsysteme wurden die katalytischen Eigenschaften in der Selektivoxidation von Propen und der oxidativen Dehydrogenierung von Propan in einem Labor-Festbettreaktor getestet. Die Untersuchung der Katalysatoren mittels *In-Situ*-Spektroskopie ermöglichte die Herleitung von Struktur-Eigenschafts-Beziehungen. Daraus ergab sich, dass sowohl die Trägereigenschaften als auch das Redoxverhalten der Vanadium- und Molybdänoxide einen entscheidenden Einfluss auf die Katalyse ausübten. Die partielle Reduktion der aktiven Spezies während der Reaktion korrelierte direkt mit der katalytischen Aktivität. Es wurde angenommen, dass die Reduzierbarkeit der Metalloxidspezies mit steigender Stärke der Oxid-Träger-Wechselwirkung zunahm. Die Turnover-Rate von *V/MgO/SBA-15* als eine Funktion der Oberflächenbedeckung wies einen "Vulkan-ähnlichen" Verlauf auf. Bei optimaler Bedeckung bestand die Katalysatorstruktur vornehmlich aus [V₂O₇]-Einheiten. Diese Struktur-Aktivitäts-Korrelation konnte genutzt werden, um im Sinne eines "rationalen Katalysatordesigns" die optimale Bedeckung zu generieren.

Schlagwörter:

Vanadium- und Molybdänoxide, Nanostrukturierte Trägermaterialien, MgO, Selektivoxidations-Katalysatoren, XAS, EXAFS, DR-UV-Vis Spektroskopie, Struktur-Aktivitäts-Korrelationen

Abstract

Vanadium and molybdenum oxides supported on an alkaline, high surface area *MgO/SBA-15* support were introduced as catalyst model system for investigating structure activity correlations in selective oxidation of alkenes and alkanes. *V/MgO/SBA-15* and *Mo/MgO/SBA-15* catalysts were prepared in a loading range between 1–10 wt.% V or Mo (0.2–5.9 metal atoms per nm²). Structural and functional characterization of the supported metal oxide catalysts was performed by using a combination of various techniques (X-ray absorption and diffuse reflectance UV-Vis spectroscopy, N₂ physisorption, X-ray diffraction, Raman spectroscopy, and gas chromatography). It was found that the vanadium and molybdenum oxide species consisted of tetrahedral metal oxide [MO₄] units. The degree of oligomerization of the vanadium oxide units depended on catalyst loading. With increasing surface coverage the degree of oligomerization increased from monomeric to oligomeric [VO₄] tetrahedra. In contrast to the vanadium oxide structure, the structure of the supported molybdenum oxides was independent of catalyst loading and surface coverage. The molybdenum oxide species consisted of a mixture of [MoO₄] and [Mo₂O₇] units. The ratio between monomeric and dimeric units was estimated to 3:2. The vanadium and molybdenum oxides supported on *MgO/SBA-15* were compared to oxide species supported on other support materials, such as SBA-15 and CMK-3. Compared to the oligomerized metal oxide species on SBA-15 and CMK-3, low oligomerized metal oxide units could be stabilized on *MgO/SBA-15* at comparably high catalyst loadings. This was attributed to the alkaline surface of the *MgO/SBA-15* support.

Catalytic performance of the oxide catalysts in selective propene oxidation and oxidative dehydrogenation of propane was tested in a laboratory fixed-bed reactor. To deduce structure activity correlations the catalysts were investigated by *in situ* spectroscopy. The nature of the support and the redox properties of the supported vanadium and molybdenum oxides were shown to have a tremendous impact on catalytic properties. Partial reduction of the active metal oxide species during reaction was directly correlated to catalytic activity. It was assumed that reducibility of the supported catalysts increased with decreasing strength of the oxide-support interaction. For *V/MgO/SBA-15* acrolein turnover frequency as a function of surface coverage exhibited a "vulcano type" behavior. At optimal vanadium oxide surface coverage the catalyst structure consisted of mainly [V₂O₇] units. This structure activity correlation allowed preparing the optimal surface coverage in terms of a "rational catalyst design".

Keywords:

Vanadium and Molybdenum Oxides, Nanostructured Support, MgO, Selective Oxidation Catalysts, XAS, EXAFS, DR-UV-Vis Spectroscopy, Structure Activity Correlations, Propene Oxidation

Contents

| | |
|---|-------------|
| Zusammenfassung | V |
| Abstract | VII |
| Contents | IX |
| Abbreviations | XIII |
| 1 Introduction | 1 |
| 1.1 Motivation | 1 |
| 1.2 Scope and Outline of this Work | 2 |
| 2 Scientific Background | 4 |
| 2.1 Supported Metal Oxides | 4 |
| 2.1.1 Support Material | 4 |
| 2.1.2 Vanadium Oxides | 6 |
| 2.1.3 Molybdenum Oxides | 8 |
| 2.2 Partial Oxidation Reactions | 10 |
| 2.3 Vanadium and Molybdenum Oxide Systems in Partial Oxidation Reactions..... | 11 |
| 3 Characterization Methods | 14 |
| 3.1 X-Ray Absorption Spectroscopy | 15 |
| 3.2 Diffuse Reflectance UV-Vis Spectroscopy | 17 |
| 3.3 Nitrogen Physisorption | 19 |
| 3.4 X-Ray Diffraction..... | 21 |
| 3.5 Thermal Analysis..... | 23 |
| 3.6 Raman Spectroscopy | 23 |
| 3.7 Elemental Analysis | 25 |
| 3.8 Catalytic Characterization | 26 |
| 4 Synthesis and Optimization of Support Material | 28 |
| 4.1 Experimental..... | 28 |
| 4.1.1 Sample Preparation | 28 |
| 4.1.2 Sample Characterization | 29 |
| 4.2 Results and Discussion | 32 |
| 4.2.1 Textural Properties – Surface Area and Pore Structure..... | 32 |
| 4.2.2 Chemical Properties – Applicability in Catalytic Reaction | 36 |
| 4.2.3 Physical Properties – Thermal Stability | 37 |
| 4.3 Conclusions | 42 |

| | | |
|----------|---|-----------|
| 5 | Structural Characterization of Supported Oxide Catalysts | 43 |
| 5.1 | Experimental..... | 43 |
| 5.1.1 | Sample Preparation..... | 43 |
| 5.1.2 | Sample Characterization..... | 45 |
| 5.2 | Supported Vanadium Oxides..... | 48 |
| 5.2.1 | Vanadium Oxide Catalyst Dispersion and Surface Properties | 48 |
| 5.2.2 | Diffuse Reflectance UV-Vis and Raman Spectroscopy | 51 |
| 5.2.3 | X-Ray Absorption Near Edge Structure | 56 |
| 5.2.4 | X-Ray Absorption Fine Structure | 57 |
| 5.3 | Supported Molybdenum Oxides..... | 60 |
| 5.3.1 | Molybdenum Oxide Catalyst Dispersion and Surface Properties | 60 |
| 5.3.2 | Diffuse Reflectance UV-Vis and Raman Spectroscopy | 62 |
| 5.3.3 | X-Ray Absorption Near Edge Structure | 64 |
| 5.3.4 | X-Ray Absorption Fine Structure | 65 |
| 5.4 | Influence of Support Material | 69 |
| 5.4.1 | MgO-coated SBA-15 (<i>MgO/SBA-15</i>)..... | 69 |
| 5.4.2 | Influence on Supported Vanadium Oxides..... | 70 |
| 5.4.3 | Influence on Supported Molybdenum Oxides..... | 72 |
| 5.4.4 | Dehydration/Dehydroxylation of Support Material | 75 |
| 5.5 | Conclusions | 77 |
| 6 | Catalytic Properties / <i>In Situ</i> Characterization of Supported Oxide Catalysts..... | 81 |
| 6.1 | Experimental..... | 81 |
| 6.1.1 | Sample Characterization..... | 81 |
| 6.2 | Influence of Heat and Mass Transport Limitations..... | 86 |
| 6.3 | Supported Vanadium Oxides..... | 87 |
| 6.3.1 | Catalytic Performance in Selective Propene Oxidation | 87 |
| 6.3.2 | Behavior under Propene Oxidizing Conditions..... | 92 |
| 6.3.3 | Catalyst Reducibility | 94 |
| 6.3.4 | Redox Properties of the Catalyst | 97 |
| 6.3.5 | Catalytic Performance in Oxidative Dehydrogenation of Propane | 100 |
| 6.4 | Supported Molybdenum Oxides..... | 104 |
| 6.4.1 | Catalytic Performance in Selective Propene Oxidation | 104 |
| 6.4.2 | Structural Evolution under Catalytic Conditions..... | 106 |
| 6.4.3 | Hydrocarbon Chemisorption and Coke Formation | 108 |
| 6.4.4 | Catalyst Reducibility | 111 |
| 6.4.5 | Redox Properties of the Catalyst | 113 |

| | | |
|----------|---|--------------|
| 6.5 | Influence of Support Material | 114 |
| 6.5.1 | Silica SBA-15 as Support Material | 114 |
| 6.5.2 | Carbon CMK-3 as Support Material | 119 |
| 6.5.3 | Influence of Support on Catalytic Behavior | 123 |
| 6.5.4 | Water-Gas Shift Reaction Proceeding as Side-Reaction | 125 |
| 6.6 | Catalytic Activity – A Comparison between Vanadium and Molybdenum Oxide Catalysts | 126 |
| 6.7 | Conclusions | 129 |
| 7 | Summary and Outlook..... | 133 |
| 7.1.1 | Support Material | 133 |
| 7.1.2 | Structure of Supported Vanadium and Molybdenum Oxides | 134 |
| 7.1.3 | Catalytic Properties and Structure Activity Correlations | 136 |
| 7.1.4 | Outlook | 139 |
| | Bibliography | 141 |
| | Appendix | 159 |
| | Epilogue..... | XVII |
| | Publications | XVII |
| | Talks | XVIII |
| | Posters..... | XVIII |
| | Danksagung..... | XXI |
| | Eidesstattliche Versicherung..... | XXIII |

Abbreviations

| | |
|---------------|--|
| AA | acetic aldehyde |
| Abs. | absorption |
| Acro | acrolein |
| AHM | ammonium heptamolybdate |
| atan | arctangent |
| BET | Brunauer-Emmet-Teller |
| BJH | Barrett-Joyner-Halenda |
| Chap. | Chapter |
| CMK-3 | mesoporous carbon (carbon mesostructures at KAIST " <i>Korea Advanced Institute of Science and Technology</i> " No. 3) |
| CNF | carbon nanofibers |
| CT | charge transfer |
| DFT | density functional theory |
| DR | diffuse reflectance |
| DR-UV-Vis | diffuse reflectance-ultraviolet-visible |
| DTA | differential thermoanalysis |
| DTG | derivative thermogravimetric |
| ECD | electron capture detector |
| <i>e.g.</i> | for example (Latin " <i>exempli gratia</i> ") |
| eq. | equation |
| <i>et al.</i> | and others (Latin " <i>et alii</i> ") |
| <i>etc.</i> | and so on (Latin " <i>et cetera</i> ") |
| EXAFS | extended X-ray absorption fine structure |
| F-127 | Pluronic [®] F-127, triblock copolymer |
| FID | flame ionization detector |
| FT | Fourier transformed |
| Func. | function |
| FWHM | full width at half maximum |

| | |
|----------------------|---|
| HASYLAB | Hamburg Synchrotron Radiation Laboratory |
| hex-MoO ₃ | molybdenum trioxide in hexagonal modification |
| <i>i.e.</i> | that is (Latin " <i>id est</i> ") |
| Inc. | Incorporated |
| IR | infrared |
| Iso | isopropyl alcohol |
| IUPAC | International Union of Pure and Applied Chemistry |
| KM | Kubelka-Munk |
| LMCT | ligand-to-metal charge transfer |
| m/e | mass-charge ratio |
| <i>MgO/SBA-15</i> | support material; MgO-coated SBA-15 |
| Mix. | mixture |
| MLCT | metal-to-ligand charge transfer |
| Mo/CMK-3 | molybdenum oxides supported on CMK-3 |
| Mo/CNF | molybdenum oxides supported on hollow carbon nanofibers |
| <i>Mo/MgO/SBA-15</i> | molybdenum oxides supported on <i>MgO/SBA-15</i> |
| Mo/SBA-15 | molybdenum oxides supported on SBA-15 |
| <i>nano-MgO</i> | nanoporous magnesium oxide |
| Nd:YAG | neodymium-doped yttrium aluminum garnet |
| NLDFT | non-local density functional theory |
| No. | number |
| Norm. | normalized |
| ODH | oxidative dehydrogenation |
| P-123 | Pluronic [®] 123, triblock copolymer |
| PA | propionic aldehyde |
| p.a. | Latin " <i>pro analysi</i> " |
| PE | polyethylene |
| Phys. | physical |
| PZC | point of zero charge |
| QEXAFS | "quick EXAFS" |

| | |
|---------------------|--|
| RT | room temperature |
| SBA-15 | mesoporous silica (Santa Barbara amorphous type material No. 15) |
| SDAs | structure-directing agents |
| SOP | selective oxidation of propene |
| TA | thermal analysis |
| TCD | thermal conductivity detector |
| Temp. | temperature |
| TG | thermogravimetry |
| TOF | turnover frequency |
| unc. | uncalcined |
| UV | ultraviolet |
| VCI | Verband der Chemischen Industrie |
| V/CMK-3 | vanadium oxides supported on CMK-3 |
| <i>V/MgO/SBA-15</i> | vanadium oxides supported on <i>MgO/SBA-15</i> |
| V/SBA-15 | vanadium oxides supported on SBA-15 |
| Vis | visible |
| WGS | water-gas shift |
| wt.% | weight percent |
| XAFS | X-ray absorption fine structure |
| XANES | X-ray absorption near edge structure |
| XAS | X-ray absorption spectroscopy |
| XRD | X-ray diffraction |
| XRF | X-ray fluorescence |

1 Introduction

1.1 Motivation

With an annual business volume over 184 billion Euros the chemical industry is one of the biggest German economic sectors. About roughly one quarter of the overall production of principle organic chemicals and intermediates is based on selective oxidation reactions (VCI 2012 [2]). Through catalytic reaction valuable products become available which were otherwise unobtainable or very expensive in production. Today, selective oxidation processes in chemical industry are considered to be well-developed. However, major limitations in catalytic oxidation processes are the formation of undesired by-products which prevent the reaction to run at maximum selectivity and that only few reactions attain total or close-to-total conversion. Even an improvement of catalytic performance resulting in a selectivity increase of one percentage point or less may lead to a considerable increase in profit margin.

Fundamental academic studies in heterogeneous catalysis deal with the crucial problem on how selectivity and reactivity of a catalyst are related to its structure and properties. Generally, a catalyst provides a more facile path to the desired product and lowers the activation energy for the selective process in a chemical reaction. Concerning the variety of possible reaction products it is an intriguing question which properties of the catalyst determine the reaction pathway towards a particular product. Since formation of carbon oxides is thermodynamically favored, another important issue is the elucidation of the factors that prevent the hydrocarbon molecule to undergo total oxidation.

Many partial oxidation catalysts in industrial applications are based on vanadium and molybdenum oxides. Development and optimization of highly active catalysts was mostly done empirically by high-throughput methods. The structure of these catalysts often consists of several cooperating phases. Furthermore, the surface structure, where the catalytic reaction occurs, is rich in structural defects and differs from the structure of the bulk. Therefore, identification of the active catalyst site is very difficult due to a huge variety of possible active surface components. One attempt to gain deeper insight into structure activity relationships is the simplification of the highly complex industrial catalysts to model catalyst systems. Such

model systems exhibit a low complexity allowing the investigation of the influence of individual structural or chemical motifs on catalytic behavior. A promising approach towards model systems is the generation of highly dispersed metal oxide catalysts on well-defined support materials. Compared to bulk materials supported metal oxides feature several advantages such as better thermal stability of particular metal oxide structures, which were otherwise not available under catalytic conditions, and a high surface area. Furthermore, investigation of supported metal oxides allows the correlation of local structural motifs with their catalytic behavior without considering bulk oxide properties.

For deeper elucidating the catalytic properties it is not only important to exhaustively study the as-prepared state of the catalyst system but also its evolution under *in situ* conditions. *In situ* characterization denotes the investigation of a working catalyst with different physico-chemical characterization methods during catalytic reaction. Therefore, the catalyst is studied directly by various spectroscopic techniques. Additionally, catalytic reaction products can be analyzed to deduce information on catalytic performance. Through studies of catalyst model systems valuable information about the nature of the active site under reaction conditions become accessible. This information can be used to optimize the system in terms of "rational catalyst design" leading to the preparation of new and more efficient catalysts.

1.2 Scope and Outline of this Work

The objective of this work was the structural and functional characterization of a catalyst system consisting of vanadium or molybdenum oxides. To reduce structural complexity the vanadium or molybdenum oxides were supported on a nanostructured high surface area support material with alkaline properties. Investigations focused on identifying the metal oxide structure and correlating the structure to their catalytic activity. The scope of this work is schematically represented in Fig. 1.1. Briefly, the work is divided into three major chapters: Synthesis and optimization of the support material (Chap. 4), structural characterization of the dispersed metal oxides (Chap. 5), and investigation of their catalytic properties together with *in situ* characterization (Chap. 6).

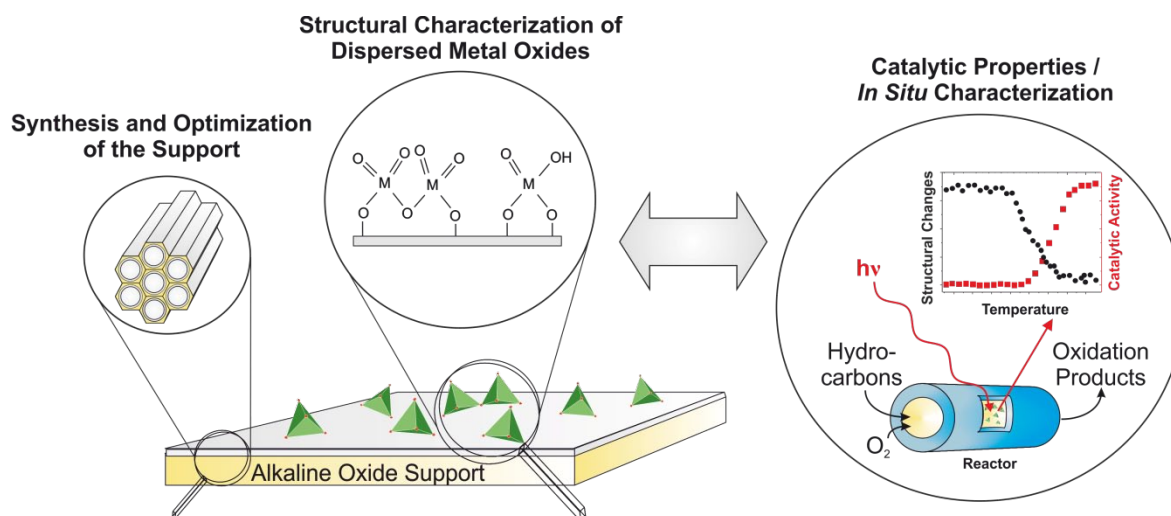


Fig. 1.1 The scope of this work comprises three major chapters: Synthesis and optimization of the support material (Chap. 4), structural characterization of the dispersed metal oxides (Chap. 5), and investigation of their catalytic properties together with *in situ* characterization (Chap. 6).

Within the present work several approaches were used to prepare an alkaline, high surface area oxide support material based on magnesium oxide. The focus lay on the improvement of support properties in terms of thermal stability and applicability in catalysis. After identification of a suitable support, vanadium and molybdenum oxides were supported on the material at various metal oxide loadings. The structure of the supported metal oxide species was thoroughly investigated by a variety of characterization methods. Furthermore, the structure of the oxides was compared to that of vanadium and molybdenum oxides supported on other support materials, such as SBA-15 and CMK-3. Subsequently, the well-studied catalyst model system was analyzed under catalytic reaction conditions. Structural changes and redox characteristics of the working catalysts were investigated and correlated to their catalytic performance. For testing the catalytic behavior in catalytic oxidation reactions, selective oxidation of propene and oxidative dehydrogenation (ODH) of propane were chosen as model reactions. To gain deeper understanding of the influence of the support on catalytic performance, the behavior of the supported metal oxides under reaction conditions was compared to that of vanadium or molybdenum oxides supported on other materials (*e.g.*, SBA-15, CMK-3).

2 Scientific Background

2.1 Supported Metal Oxides

Supported metal oxides consist of active metal oxide species deposited on a high surface area support material. Commonly, the catalytically active metal oxide for selective oxidation catalysis consists of group five or six elements, such as vanadium, molybdenum, niobium, or tungsten. The support material is considered to be inert under catalytic reaction conditions. Therefore, the use of a support allows separation and high dispersion of the catalytically active sites. The dispersed metal oxide phase is typically present as a two-dimensional layer on the support. Depending on the nature of the support, chemical and electronic properties of the supported metal oxide may considerably differ from those of the unsupported bulk oxides. However, the supported metal oxides can generally be assigned to two different species. First, the hydrated oxide species formed under ambient conditions in the presence of water, and second, the dehydrated species, where the water was removed from the surface of the support. The local structure of the hydrated surface metal oxides resembles the oxide structure present in aqueous solution at similar net pH values. The net pH of the hydrated surface is thereby defined as the equilibrated pH at point of zero charge (PZC).[3] For high pH values the metal oxides tend to be present as isolated tetrahedral metal(M)-oxide(O) $[MO_4]$ units while at low pH the structure changes to oligomerized chains or clusters of the oxide units.[4-6]

2.1.1 Support Material

The development of highly ordered mesoporous materials, which possess large specific surface areas, has significantly expanded the possibilities of dispersing metal oxides for catalytic purpose. Mesoporous materials are defined as porous solids with pore sizes in the range of 2 nm to 50 nm, commonly possessing specific surface areas between 500–1200 nm²/g. A well-established method to generate mesopore systems is the utilization of supramolecular aggregates as structure-directing agents (SDAs).[7-10] The self-organization of the SDAs promotes the formation of an inorganic network around the organic aggregates. Removal of the organic template leads to a highly ordered mesoscopic architecture of inorganic molecules. Fig. 2.1 illustrates the formation process. The surfactants which are used as SDAs con-

sist of a hydrophobic tail with a hydrophilic head and arrange in spherical micelles when dissolved in a polar solvent. At concentrations higher than the critical micelle concentration the surfactants self-assemble into micellar liquid crystals which then serve as a template for the formation of organic-inorganic composites by addition of a silica precursor. Subsequent calcination of the composite results in mesoporous materials with highly ordered pore structures.

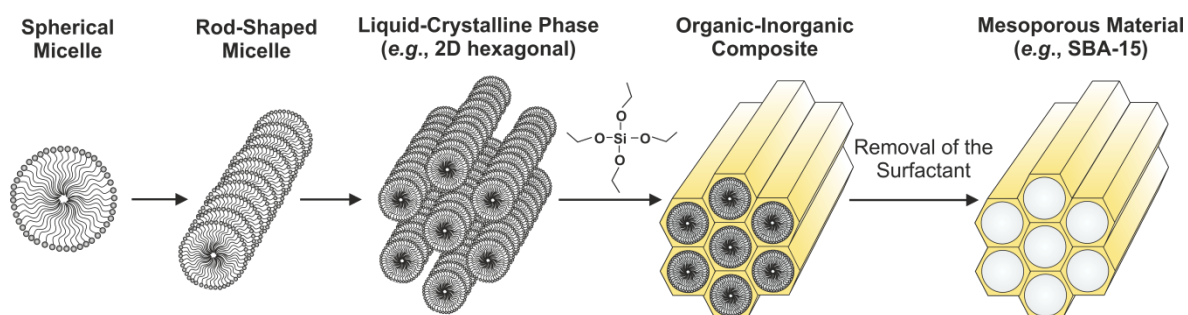


Fig. 2.1 Schematic representation of the preparation of mesoporous materials via the use of structure-directing agents (adapted from [11]).

The introduction of non-ionic block copolymers as SDAs allowed the synthesis of a new family of mesoporous materials with a highly ordered arrangement of mesopores exhibiting a narrow pore size distribution. Advantages of these block copolymers were the tunability of their ordering properties by adjusting solvent composition, molecular weight, or copolymer architecture, and the possibility of generating larger structural features than it was possible with low-molecular-weight surfactants.[9] A very prominent representative of the resulting mesoporous materials is the silica SBA-15, which consists of a two-dimensional hexagonally ordered pore system where the mesopores are connected by a network of micropores.[10]

The use of SDAs for the synthesis of mesoporous materials is suitable for materials which readily form amorphous phases, like silica or aluminosilicates. However, for most metal oxides aggregation in micellar solutions is inhibited by the tendency of these systems to form dense, crystalline phases. This problem can be overcome by the so-called nanocasting, where silica or carbon phases are used as rigid structure template.[12,13] In this procedure the porous nanostructure template is impregnated with a precursor solution. After a complete filling of the pores the precursor is transformed to the desired metal oxide by thermal treatment. Removal of the template then results in the metal oxide as its negative replica. Using

mesoporous silica as template yielded in the generation of several new mesoporous metal oxides, such as WO_3 [14], Fe_2O_3 [15], Cr_2O_3 [16], NiO [17], and Mn_xO_y [18]. Removal of the silica matrix, however, requires rather harsh conditions, like etching with hydrofluoric (HF) acid or concentrated sodium hydroxide (NaOH) solution. Therefore, silica matrices are only suitable for metal oxide, which are stable under these extreme pH conditions. Magnesium oxide, for example, is soluble at very low and very high pH. Thus, mesoporous MgO cannot be synthesized this way. The use of carbon instead of silica as structure template offers an alternative since it can be removed by controlled thermal combustion. The carbon matrix itself can be prepared by structure replication of a silica template.[19,20] Thus, the entire process resembles a double replication procedure. The mesoporous metal oxide is the negative replica of the parent carbon template and a positive replica of the original silica matrix. The successful synthesis of a variety of mesoporous oxides, like MgO[21,22], ZnO[23], CeO_2 [24] and TiO_2 [25], has been reported. Nevertheless, the procedure is rather complicated and the yield of mesoporous metal oxides is low.

Another approach of generating mesoporous material is a surfactant-assisted sol-gel route. Xiong *et al.* have successfully demonstrated the synthesis of mesoporous ZnO in a hydrothermal approach by using the triblock copolymer F-127 as template reagent and the metal acetate as ZnO precursor.[26] Porous MgO nanoplates were generated by a hydrothermal dissolution-recrystallization process.[27] However, the specific surface area of the porous MgO was rather low compared to mesoporous oxides prepared by nanocasting. A completely different approach is the introduction of the desired metal oxide into mesoporous silica. Thereby, the material benefits from thermal stability and large surface area of the parent silica but exhibits different surface properties. Wei *et al.* reported the transformation of the acidic silica surface of SBA-15 to an alkaline surface by *in situ* coating with MgO.[28] Post-synthesis coating of the SBA-15 surface to alter its surface properties was successfully realized for Al_2O_3 [29], MgO[30], and TiO_2 [31].

2.1.2 Vanadium Oxides

Vanadium(V) oxides, being present as four-, five- or six-coordinated $[\text{VO}_x]$ species, exhibit a great structural variability. The four-coordinated vanadate species consist of isolated (orthovanadate), dimeric (pyrovanadate), or polymeric chainlike (metavanadate) $[\text{VO}_4]$ units.

Therefore, they can be distinguished by their number of bridging V–O–V bonds. Octahedral $[\text{VO}_6]$ vanadates are very common structures in higher oligomerized vanadium oxide species, *e.g.*, in the clusters of ammonium decavanadate $(\text{NH}_4)_6\text{V}_{10}\text{O}_{28}$. The octahedral units are often highly distorted as in the structure of bulk vanadium pentoxide V_2O_5 which possesses a very long sixth V–O bond. Hence, the vanadium species in V_2O_5 are effectively considered to exhibit a square-pyramidal $[\text{VO}_5]$ coordination. The variety of possible coordinations is demonstrated by the structure of vanadium oxides in aqueous solutions at varying vanadate concentrations and pH. Fig. 2.2 depicts a selection of common vanadium oxide structures present at different pH values. A summary of the existing vanadium oxide species in dependency on concentration and pH is given in the Pourbaix diagram.[3]

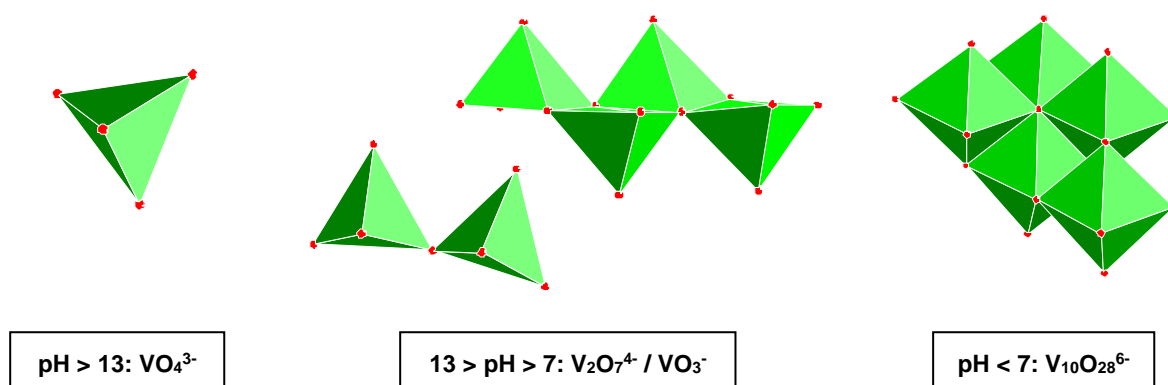


Fig. 2.2 Schematic representation of selected vanadium oxide structures present in aqueous solution at varying pH values.

According to Deo *et al.* the structure of supported hydrated vanadium oxides strongly depends on the net surface pH at PZC of the supporting oxide.[4] The structure of vanadium oxides supported on acidic silica type materials, for instance, is supposed to consist of two-dimensional layers of adjacent polyvanadates with a highly distorted octahedral coordination of the oxygen atoms around the vanadium center.[32-34] On alkaline support oxides like magnesium oxide a predominantly monomeric species of tetrahedrally coordinated vanadium centers is expected. However, the affinity of vanadium to form magnesium vanadates as bulk compounds upon calcination of the material was reported to inhibit a high vanadium oxide dispersion on the MgO surface.[4,35]

Dehydrated structures of supported vanadium oxides are observed at elevated temperatures regardless of the presence of water in the gas phase and are commonly independent of the support material. The vanadium centers in the dehydrated state may be present as isolated monovanadates $[\text{VO}_4]$, oligomerized $[\text{V}_2\text{O}_7]$ units, with bridging V–O–V bonds, and V_2O_5 nanocrystallites. The surface coverage has a crucial influence on the dominating vanadium oxide species. Hence, monovanadates predominately form at low coverages ($2\text{--}3$ V atoms/ nm^2) and condensate to accumulated polyvanadates at higher coverages ($6\text{--}8$ V atoms/ nm^2).^[33] On silica, however, the maximum surface coverage before formation of V_2O_5 nanocrystallites is much lower than that on other support materials, like Al_2O_3 , TiO_2 , and ZrO_2 .^[36]

2.1.3 Molybdenum Oxides

Unlike bulk vanadium oxides, which are often composed of tetrahedral $[\text{VO}_4]$ units, molybdenum(VI) oxides are usually present as higher coordinated species. These polymolybdates consist of octahedral $[\text{MoO}_6]$ groups.^[3] The structure of bulk alpha molybdenum trioxide ($\alpha\text{-MoO}_3$), for instance, resembles a three-dimensional structure of highly distorted $[\text{MoO}_6]$ units. The high distortion leads to an effective five-fold coordination around the molybdenum atom with a very long sixth Mo–O distance. However, exceptions from the polymolybdate structure are orthomolybdates, such as Na_2MoO_4 , MgMoO_4 , CuMoO_4 , *etc.*, which consist of isolated tetrahedral $[\text{MoO}_4]$ units. The observable structures of bulk molybdenum oxides resemble those of molybdates present in aqueous solution at varying pH as depicted in Fig. 2.3. Isolated tetrahedral MoO_4^{2-} ions are present at high pH values, whereas at low pH oligomerized molybdenum oxide species, such as the heptamolybdate $\text{Mo}_7\text{O}_{24}^{6-}$ or octamolybdate $\text{Mo}_8\text{O}_{26}^{4-}$ anions, are formed.^[5,6]

To investigate molybdenum oxides other than $\alpha\text{-MoO}_3$ supported molybdenum oxides are frequently used. The nature of the support material is known to strongly influence the metal oxide-support interaction. Al_2O_3 and silica type support materials like SBA-15 are well-established and the interactions with the supported oxides are reasonably understood.^[37-41] The hydrated state consisted of highly oligomerized molybdenum oxide species with an octahedral coordination sphere around the molybdenum center.^[42] The dehydrated structure of supported molybdenum oxides consists of a mixture of tetrahedrally and octahedrally coordi-

nated species. The degree of oligomerization of the oxide units was shown to be dependent on surface coverage.[42,43] Only few studies report on molybdenum oxides supported on alkaline support materials, such as magnesium oxide.[44-47]

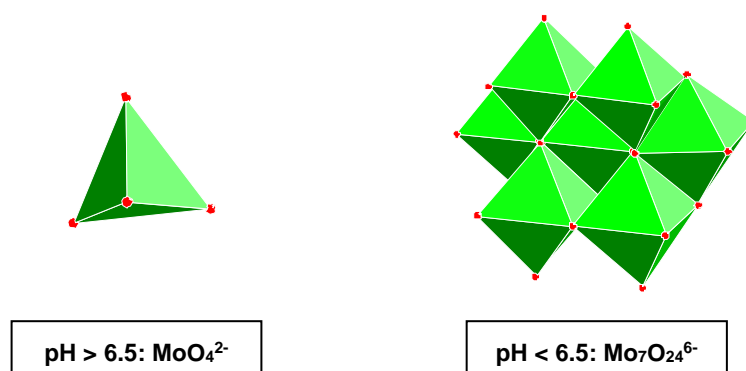


Fig. 2.3 Schematic representation of selected molybdenum oxide structures present in aqueous solution at varying pH values.

According to Wachs *et al.* the structure of supported metal oxides is correlated to the net pH at the point of zero charge (PZC) of the oxide support. They investigated the structural dependency of vanadium oxides supported on several oxide materials on the net pH and predicted a tetrahedral molybdenum oxide species on the surface of an alkaline support.[48] This has later been confirmed by Aritani *et al.* for MgO-supported molybdenum oxides.[47] Furthermore, Bare *et al.* reported isolated tetrahedral molybdenum oxide species for uncalcined samples between weight loadings of 5–20 wt.%. Accordingly, calcination led to a transformation of the tetrahedral molybdenum oxides to an octahedral species. They correlated the structural change to the loss of surface hydroxyl groups during calcination.[45,46] Stampf *et al.* detected the formation of [MoO₄] tetrahedra by simply mixing MoO₃ with MgO mechanically, which indicated that molybdenum ions very easily diffuse from the MgO surface into the bulk material.[49] Llorente *et al.* considered the bulk diffusion of the molybdenum ions to be temperature dependent, thus leading to the formation of MgMoO₄ at temperatures above 820 °C and highly dispersed MoO₃ at moderate calcinations temperatures.[44]

2.2 Partial Oxidation Reactions

Major processes in the field of selective oxidation reactions include allylic and aromatic oxidation, epoxidation of olefins, and methanol oxidation.[50] In allylic oxidation an olefin, *e.g.*, propene, is oxidized at the allylic position. The molecule is activated by abstraction of a hydrogen in α -position to the double bond resulting in an allylic intermediate. In case of propene oxidation insertion of lattice oxygen from the catalyst gives acrolein or acrylic acid as reaction product. Fig. 2.4 schematically depicts the allylic oxidation reaction for the selective oxidation of propene to acrolein.

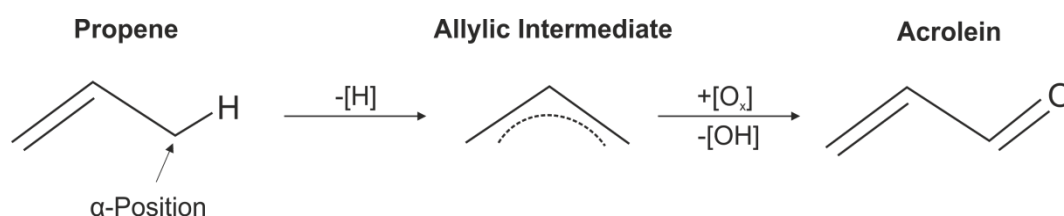


Fig. 2.4 Reaction scheme of selective propene oxidation to acrolein. An allylic intermediate is generated by hydrogen abstraction in α -position to the double bond. Oxygen insertion then leads to the formation of acrolein.

Suitable catalyst systems commonly contain transition metal oxides, such as vanadates and molybdates. The metal centers in such compounds are able to easily change their oxidation state and reversibly store oxygen. Furthermore, these metal oxides feature an intermediate M–O bond strength which was postulated to be required for selective oxidation reactions.[51] A detailed determination of the surface reaction mechanism in heterogeneously catalyzed selective oxidation reactions is still a challenge for recent fundamental researches. Grasselli proposed at least seven conceptual principles to be important for selective oxidation by metal oxide catalysts. These principles encompass the role of lattice oxygen, metal-oxygen bond strength, host structure, redox properties, multi-functionality of active sites, site isolation, and phase cooperation.[51] Generally, oxidation of hydrocarbons with lattice oxygen proceeds via an active surface site of the catalyst which is then reoxidized by gas-phase oxygen in a separate step. This process is commonly associated with the Mars-van-Krevelen[52] or "redox-type" mechanism (Fig. 2.5).

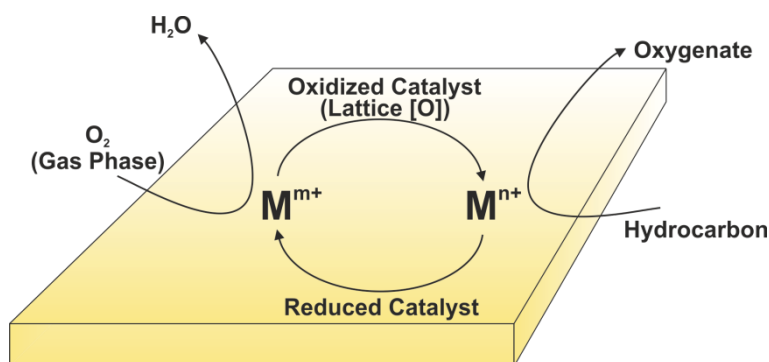


Fig. 2.5 Schematic representation of the Mars-van-Krevelen or "redox-type" mechanism for selective oxidation reactions on metal oxide catalysts (adapted from [53]).

A useful selective oxidation catalyst should consist of metal oxides which possess inherent redox properties that enable a cyclic reduction-reoxidation process. Reoxidation of the catalyst requires the activation of molecular gas phase oxygen. If gaseous O_2 is not quickly converted to nucleophilic lattice O^{2-} oxygen, the reoxidation process might produce electrophilic oxygen adspecies, such as radicalic ions (O^\cdot , O_2^\cdot) or $O_2^{2\cdot}$, on the catalyst surface. The attack of electrophilic oxygen at electron-rich regions of the hydrocarbon, *e.g.*, the double bond, leads to over-oxidation and C–C bond cleavage. Usually, catalyst selectivity is ascribed to the reaction of lattice oxygen.[54] Lattice O^{2-} oxygen exhibits nucleophilic properties and a lower oxidation potential than gaseous oxygen and can therefore react more selective.

2.3 Vanadium and Molybdenum Oxide Systems in Partial Oxidation Reactions

Supported metal oxides are frequently used to investigate partial oxidation reactions. Recent efforts concern the manner and extent to which the surface oxide structure is influenced by the support. Activity in various catalytic oxidation reactions may be ascribed to various metal-oxygen bonds.[3,55,56] Generally, three types of bonds can be distinguished: terminal $M=O$ bonds, bridging $M-O-M$ bonds, and $M-O$ -support bonds. The individual role of each bond type is still under debate. In the following a brief overview on the current understanding of the catalytic performance of supported vanadium and molybdenum oxides is given.

Vanadium and molybdenum oxide catalysts are of central importance in selective oxidation of hydrocarbons. As part of commercially employed catalysts in selective oxidation of *o*-xylene, benzene, naphthalene or butene vanadium oxides exhibit good catalytic activity and selectivity.[55] Molybdenum oxide catalysts are active in a variety of catalytic reactions, including selective oxidation reactions[57,58], oxidative dehydrogenation of alkanes[59,60], and olefin metathesis[38,61]. Characterization of essential properties of the working catalysts is subject of numerous studies.[55,62-65] The catalytic performance of supported vanadium and molybdenum oxides depends on various factors, *e.g.*, nature of the support, local geometry of the supported metal oxides, and metal oxide dispersion on the support. The redox character as well as acid-base properties of the catalysts have an important influence on catalytic performance.[63,66-69] Both factors are often investigated separately; the redox properties being related to catalytic activity while the acid-base character is attributed to product selectivity.

Understanding the redox behavior is of particular interest since selective oxidation reactions are believed to proceed via reduction and reoxidation of the metal oxide species as part of the catalytic cycle.[52,63,64] Thus, the degree of reduction is determined by reduction and reoxidation rates under catalytic reaction conditions. It has been shown by Ozkan *et al.* that reduced vanadium species exhibit a better catalytic performance in selective pentene oxidation than fully oxidized vanadium oxides. Accordingly, the reduced catalysts exhibited an oxygen to vanadium ratio significantly lower than 2.5.[70] Zazhigalov *et al.* proposed that the active catalyst for *n*-butane oxidation possesses an optimal ratio of V⁵⁺ and V⁴⁺ between 9:1 and 4:1.[71] In case of molybdenum based oxide catalysts the active reaction center was proposed to contain a mixture of Mo⁶⁺ and Mo⁵⁺ centers where the reduced state is somehow stabilized during reaction. Cadus *et al.* reported a synergetic effect of mechanical mixtures of MgMoO₄ and MoO₃. Accordingly, the magnesium molybdate phase was observed to be much more active and selective for oxidative dehydrogenation of propane when in close contact to MoO₃. [72]

Reducibility of the metal oxide catalysts varies with the nature of the support and catalyst loading, which is associated with the degree of oligomerization of the metal oxide units. For uni-molecular reactions, which require only one surface metal oxide site, the catalytic

activity was supposed to be independent on metal oxide loading.[55] Hence, the catalytic performance in oxidative dehydrogenation was reported to be independent of catalyst loading, but varied strongly with the nature of the oxide support.[62] It was found that oligomerized vanadium oxide units were more easily reduced than isolated species under reducing conditions.[63,67] Gao *et al.* directly correlated the reducibility of the vanadium oxide species to its catalytic activity.[63]

Determination of structure and oxidation state of the active catalysts by *in situ* investigation techniques is of key importance to gain fundamental understanding of structure activity correlations. The contribution of the individual structural motifs to the catalytic performance particularly with regard to isolated and oligomeric metal(M)-oxide(O) [MO_x] units is still not completely resolved in the literature. The lack of knowledge prevents the rational design of highly active and selective metal oxide catalysts. Therefore, detailed investigations of suitable catalyst model systems are needed.

3 Characterization Methods

Characterization of supported vanadium and molybdenum oxide catalysts involves using multiple characterization techniques. No individual method is capable of providing all information needed to characterize the local structure of the supported oxides and the support. In the following, a brief overview of the basic principles of each method that was used for catalyst characterization will be given. The descriptions focus on the issues relevant within this work and do not aim at completeness. Detailed explanations and in-depth discussions are provided in the cited references. Table 3.1 summarizes the characterization methods together with the obtainable information regarding oxidation state, dispersion, coordination, and quantitative determination of the supported oxide catalyst and the bare support. To gain deeper insight into structure activity correlations, these characterization techniques have to be combined with studying catalytic performance. Hence, in addition to the methods listed in Table 3.1, catalytic characterization will be briefly explained at the end of the chapter.

Table 3.1 Characterization methods with the obtainable information on supported vanadium and molybdenum oxides and the bare support. Listed are X-ray absorption spectroscopy (XAS), diffuse reflectance UV-Vis (DR-UV-Vis) spectroscopy, N₂ physisorption, X-ray diffraction (XRD), thermal analysis (TA), Raman spectroscopy, and X-ray fluorescence (XRF) spectroscopy.

| Characterization Method | Supported V and Mo Oxides | | | | Support Material |
|------------------------------|---------------------------|--------------|------------|--------------|------------------|
| | Oxidation State | Coordination | Dispersion | Quantitative | |
| XAS | + | + | +/- | +/- | - |
| DR-UV-Vis | + | + | - | +/- | - |
| N ₂ Physisorption | - | - | +/- | - | + |
| XRD | - | - | +/- | - | + |
| TA | - | - | - | - | + |
| Raman | +/- | + | +/- | - | - |
| XRF | - | - | - | + | + |

3.1 X-Ray Absorption Spectroscopy

X-ray absorption spectroscopy (XAS) is an element specific method, which provides detailed information on local structure and chemical state of the absorber atoms.[73,74] The particular asset is the applicability of the method even in the absence of long-range order, which is especially relevant for supported catalysts. The absorption of X-rays leads to the excitation of an electron from a core level. This results in a steep rise of absorption, so-called absorption edge, at the core-level binding energy of the excited electron. A typical X-ray absorption spectrum is depicted in Fig. 3.1. Generally, two regions can be discerned in the spectrum: the X-ray absorption near edge structure (XANES) and the extended X-ray absorption fine structure (EXAFS).

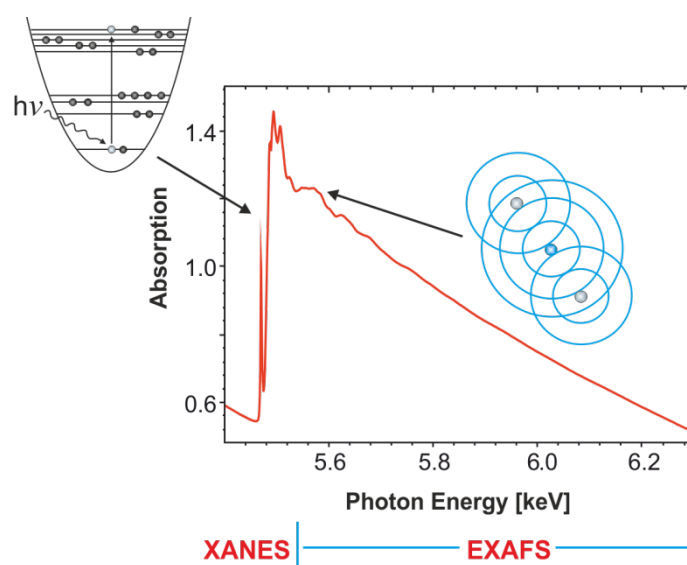


Fig. 3.1 X-ray absorption spectrum. In the XANES region the absorption of an X-ray photon takes place. A schematic representation of the excitation process is given in form of an energetic diagram where an electron (unfilled circle) is excited by a photon of the energy $h\nu$ to a higher unoccupied level. The EXAFS region contains the fine structure of the absorption edge. The scattering process is illustrated by the photoelectron wave (blue circles) emitted from the absorber atom (blue) which is then backscattered at the electron shell of nearby atoms (grey).

The narrow region of the XANES, located in a 50-eV range around the absorption edge, provides detailed information on local electronic and geometric structure.[75] The spectral shape of the near edge region is governed by electron correlation and multiple scattering effects. Interpretation of the data can be done with the help of reference spectra of known compounds.

The XANES pre-edge region is based on the excitation of an electron from a core level to an unoccupied state. Since the transition follows the selection rules, the predominant transitions for the K edge are from s to p orbitals and from p to d orbitals for L_{II} and L_{III} edges. However, due to possible hybridization of the molecule orbitals the pre-edge region may feature significant characteristics, which can be interpreted in terms of coordination geometry and oxidation state.

The EXAFS region is dominated by single scattering events and arises from backscattering of the photoelectron by the electrons of the neighboring atoms. Outgoing and backscattered electron waves interfere. As a result, the cross-section for X-ray absorption is modulated as a function of number and distance of the nearby atoms. The EXAFS function, $\chi(k)$, as a function of the wavenumber, k , of the photoelectron is described as the sum of the scattering contributions of all neighboring atoms[76]:

$$\chi(k) = \sum_i A_i(k) \sin(2kR_i + \phi_i(k)) \quad (3-1)$$

with the amplitude, $A_i(k)$, *i.e.*, scattering intensity due to the i^{th} coordination shell, the distance, R_i , between absorbing atom and atom in the i^{th} shell, and the total phase shift, $\phi_i(k)$.

The amplitude of each scattering contribution, $A_i(k)$, is influenced by the number of neighboring atoms, N , in a coordination shell and is mathematically described as

$$A_i(k) = \frac{N_i S_0^2(k) F_i(k)}{k R_i^2} \cdot \exp(-2k^2 \sigma_i^2) \cdot \exp\left(-\frac{2R_i}{\lambda(k)}\right) \quad (3-2)$$

where $S_0(k)$ is the correction for relaxation effects in the emitting atom, $F_i(k)$ is the backscattering amplitude of the atom in the i^{th} shell, σ^2 is the mean-squared displacement of atoms (Debye-Waller factor), and $\lambda(k)$ is the inelastic mean free path of the electron. The intensity of the emitted electron, which can be assumed as spherical wave, decreases with the distance, R , from the absorbing atom squared. The attenuation of the signal is described by the first term of eq. (3-2). The correction parameter, $S_0(k)$, reduces the amplitude and accounts for the fact, that not all absorbed X-ray photons generate a photoelectron but also electrons with lower kinetic energy. This is due to relaxation processes within the absorber atom. The backscatte-

ring amplitude, $F_i(k)$, represents the scattering performance of the i^{th} neighbor. For a given excitation energy $F_i(k)$ is characteristic for a specific element. The second term of eq. (3-2) accounts for the influence of disorder on the amplitude. The disorder is the sum of a static and a dynamic portion. While the dynamic disorder is strongly temperature depending and can be neglected at low temperatures, the static disorder is proportional to the distance variation of the atoms in the i^{th} coordination shell of the absorber atom. Hence, amorphous solids possess a large static disorder. The last term of eq. (3-2) expresses the exponential attenuation of an electron traveling through a solid, which is dependent on the mean free path of the electron.

Information of the EXAFS function, $\chi(k)$, on chemical coordination environment of the absorbing atom become accessible through Fourier transformation. Thereby, $\chi(k)$ is converted to a pseudo-radial distribution function, $\text{FT}(R)$:

$$\text{FT}(R) = \frac{1}{\sqrt{2\pi}} \int_{k_{\min}}^{k_{\max}} k^n \chi(k) \cdot w(k) \cdot \exp(2ikR) dk \quad (3-3)$$

where n is an integer, usually chosen as 1, 2, or 3 and $w(k)$ is a window function. Function (3-3) represents the density of an atom being at a distance, R , of the absorber. The transform is usually multiplied by k^1 or k^3 to emphasize the role of light, or heavy atoms, respectively.[73]

3.2 Diffuse Reflectance UV-Vis Spectroscopy

Spectroscopy in the ultraviolet (UV; 200–400 nm) and visible (Vis; 400–780 nm) region of the electromagnetic spectrum can be used to characterize various electronic transitions in metal ions such as ligand-to-metal (LMCT) and metal-to-ligand (MLCT) charge transfer or $d-d$ transitions. For metal ions in supported oxide catalysts these electronic transitions depend on various parameters like oxidation state, local and overall symmetry, degree of condensation, polarization effect and size of the counterion, and dispersion on the support.[4,77] Usually, $d-d$ transitions are of moderate or weak intensity because they are forbidden by the Laporte selection rules. However, the selection rules may be partially relaxed by vibronic coupling or mixing of states, *i.e.*, interfering of symmetry properties of neighboring states.[78]

Characterization of heterogeneous catalysts, consisting of nontransparent powders, often requires collecting the diffuse reflected light instead of measuring in transmission mode. This technique has been named diffuse reflectance UV-Vis spectroscopy (DR-UV-Vis). A detailed discussion of the method is given by Kortüm.[79] Secondary to the diffuse reflected light other processes like total reflection or single and multiple scattering occur. DR-UV-Vis spectra usually encompass broad and overlapping bands. A theoretical approach to the description of the scattered light intensity is the Schuster-Kubelka-Munk theory where the incident and scattered light are approximated as two opposite fluxes, which are perpendicular to the surface of the powder sample.[80] The diffuse reflection of the sample, R_∞ , is related to the coefficients for absorption, K , and scattering, S , via the Kubelka-Munk function, $F(R_\infty)$,

$$F(R_\infty) = \frac{(1 - R_\infty)^2}{2R_\infty} = \frac{K}{S} \quad (3-4)$$

The diffuse reflection of the sample, R_∞ , is calculated from the experimentally determined reflection of the sample divided by the reflection of a non-absorbing reflectance standard (e.g., MgO, BaSO₄, Spectralon®). Eq. (3-4) presumes the following idealizing conditions:

- diffuse monochromatic irradiation,
- isotropic light scattering,
- infinite layer thickness,
- low concentration of absorbing centers,
- uniform distribution of the centers, and
- absence of fluorescence.

The diffuse scattered light is usually collected by an integration sphere (also known as Ulbricht sphere), which consists of a hollow sphere coated with a white material (e.g., BaSO₄, Spectralon®). With an integration sphere over 95% of the scattered light is detectable. Unfortunately, it offers little potential for investigations under *in situ* conditions. Alternatively, a so-called Praying Mantis™ diffuse reflectance attachment containing an *in situ* reaction chamber can be used. This attachment consists of two ellipsoidal mirrors, which collect about 20% of the diffusively reflected light. Fig. 3.2 illustrates the two attachment variations for *ex situ* or *in situ* measurements.

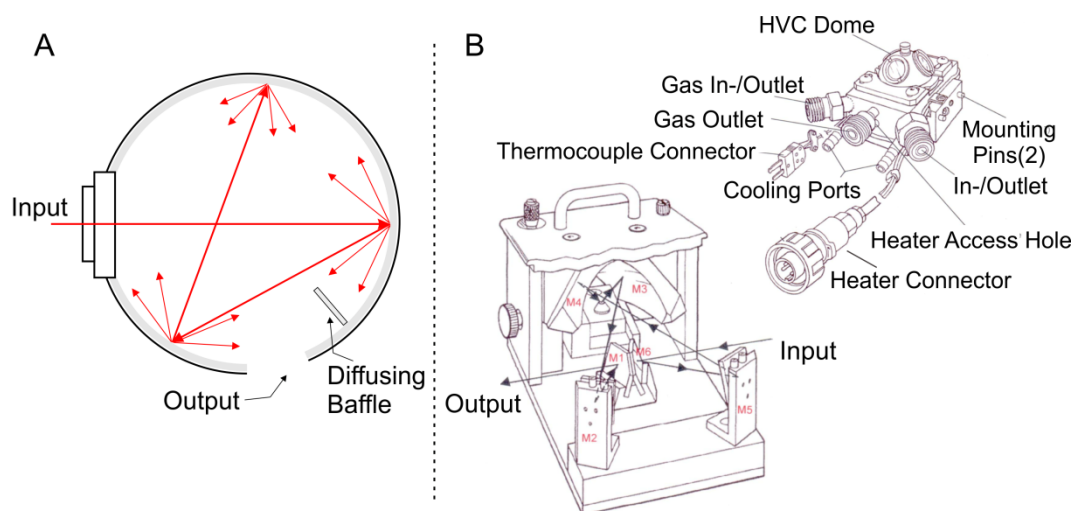


Fig. 3.2 Schematic illustration of an integration sphere (A) for *ex situ* measurements and a Praying Mantis™ attachment (B, left) with reaction chamber (B, right) for *in situ* experiments (B adapted from [81]).

3.3 Nitrogen Physisorption

Evaluation of surface area and pore structure is an important requirement in catalyst characterization, especially in the case of supported catalysts. Physisorption is an interfacial phenomenon, which occurs whenever a gas (adsorptive) is brought into contact with the surface of a solid (adsorbent). At a given temperature, T , the relation between the amount, n , of adsorbed gas by unit mass of the adsorbent and the equilibrium pressure, p , can be expressed by the adsorption isotherm, n ,

$$n = f\left(\frac{p}{p_0}\right)_T \quad (3-5)$$

with the saturation pressure of the adsorptive, p_0 . Generally, the interpretation of a physisorption isotherm starts with the classification into one of the six types proposed by IUPAC.[82] Idealized isotherms of each type are depicted in Fig. 3.3 (left). The reversible type I isotherm corresponds to microporous adsorbents, which exhibit a small external surface area. With increasing pressure the micropores are filled, resulting in a steep increase at low relative pressure, p/p_0 . The measurable volume uptake is mainly governed by the accessible micropores rather than the internal surface area. The reversible type II isotherm constitutes the

typical form for a non-porous or macroporous material. The transition between monolayer and multilayer adsorption is unrestricted. The beginning of the linear middle section, point B, indicates the stage of a complete monolayer. Type IV isotherms exhibit a characteristic hysteresis loop, which is associated with capillary condensation in mesopores. The initial part resembles a type II isotherm, where the completion of monolayer adsorption is indicated by point B. Several industrially used adsorbents give rise to type IV isotherms. The appearances of the hysteresis loop differ significantly but can be classified into four main categories, according to Fig. 3.3 (right). Type III and type V isotherms (Fig. 3.3, left), the latter being the mesoporous analog of type III, are rarely observed. The identification of point B as the transition between mono- and multilayer formation is hardly feasible. Type VI isotherms represent the special case of a stepwise multilayer formation on a uniform non-porous surface.

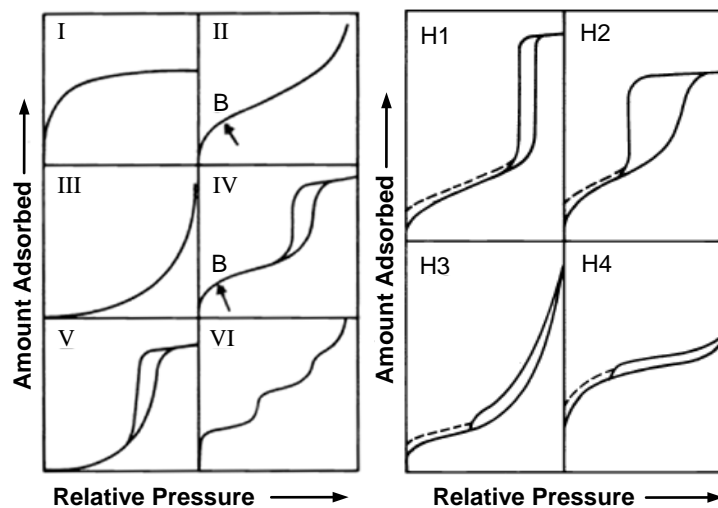


Fig. 3.3 Left: Types of physisorption isotherms according to IUPAC. Right: Classification of hysteresis loops into four categories (adapted from [82]). For details see text.

The phenomenon of capillary condensation can be used to determine the pore size of mesoporous materials. A widespread approach is the Barrett-Joyner-Halenda (BJH) method, which is based on the theoretical evaporation of the pore volume by stepwise reduction of p/p_0 under consideration of a thinning multilayer.[83] Assuming a cylindrical pore shape, the pore radius, r_p , is given as

$$r_p = r_k + t \quad (3-6)$$

where r_k is the Kelvin radius, *i.e.*, the radius of the meniscus, and t the thickness of the multilayer. The Kelvin radius, r_k , is derived from the Kelvin equation which describes the relationship between mesopore size and condensation pressure, p_0 .

Microporosity can be assessed by a t -plot analysis.[84] This method is based on comparison of a reference isotherm of a non-porous solid to the isotherm of a microporous material. The non-porous solid should thereby have a similar surface nature as the studied material. To obtain a t -plot the amount adsorbed is plotted as a function of the corresponding multilayer thickness, t , calculated from the reference isotherm. As long as the multilayer is formed unhindered as in case of a non-porous solid the t -plot gives a straight line passing the origin. Any deviation between reference and studied isotherm is detected as departure of the t -plot from linearity. Slope and intercept of the linearized t -plot can be used to calculate micropore surface area and volume. Recently, computational simulations based on density functional theory (DFT) have been developed for determining pore size distributions. The simulations take into account particular circumstances like varying pore shape or adsorbent properties.[85] These approaches provide reasonable qualitative descriptions, even for pore sizes ranging in between micro- and mesopores, where conventional approaches most often fail to give an adequate theoretical description.

The specific surface area of a catalyst is commonly derived from the physisorption isotherm by the Brunauer-Emmett-Teller (BET) method.[86] Accordingly, the specific surface area, a_{BET} , is obtained from the capacity of the monolayer, n_m , in mol and the area occupied by the adsorbate molecule, σ ,

$$a_{BET} = n_m N_A \sigma \quad (3-7)$$

where N_A is the Avogadro constant.

3.4 X-Ray Diffraction

X-ray diffraction (XRD) is one of most frequently applied techniques for structure determination of catalysts. It is used to identify crystalline phases and to determine microstructural properties. XRD is based on the elastic scattering of monochromatic X-ray photons by the

electrons of atoms arranged in a periodic structure. Depending on the distance between the lattice planes the scattered X-ray photons interfere constructively or destructively. The detectable X-ray photons resulting from constructive interference can be described by the Bragg equation as a relationship between the lattice spacing, d , and the angle, θ , between incident X-rays and the lattice plane

$$n\lambda = 2d \cdot \sin\theta \quad (3-8)$$

where λ is the wavelength of the X-ray photons and n is an integer specifying the order of the reflection. A graphical illustration of the Bragg relationship is given in Fig. 3.4.

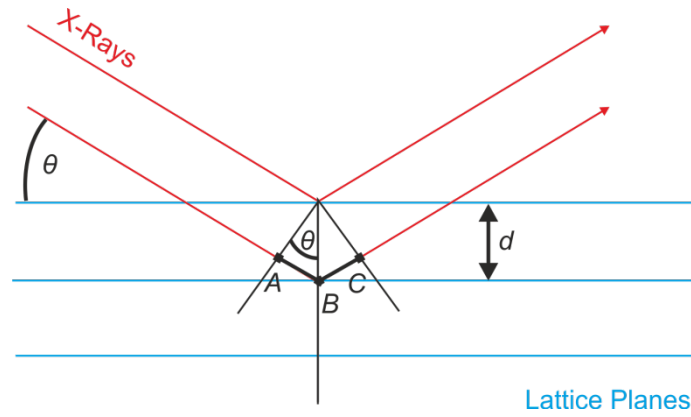


Fig. 3.4 Incident X-rays striking the atoms in an ordered lattice at an angle, θ . The X-rays are scattered and interfere constructively in directions given by the Bragg equation (3-8). Constructive interference takes place only when the path length difference $\overline{AB} + \overline{BC}$ is an integer factor of the wavelength, λ .

Diffraction patterns are measured as a function of the diffraction angle, 2θ . The diffraction peaks can be characterized by the Miller indices, which describe the corresponding lattice planes. Detailed information about data analyzing and structure refinement can be found elsewhere.[87,88] The shape of the diffraction peaks provides additional information on the dimension of the reflecting domains. According to the Scherrer equation the domain size, τ , can be estimated from the integral width, β , of the peak

$$\tau = \frac{\lambda}{\beta \cdot \cos\theta} \quad (3-9)$$

with the X-ray wavelength, λ , and the angle, θ , between incident X-rays and the reflection plane.[88]

3.5 Thermal Analysis

The concept of thermal analysis comprises all techniques, which detect properties of a substance or substance mixture as a function of temperature or time, while the sample undergoes a controlled temperature program.[89] Next to the characterization of a great many of physical and chemical properties, like thermal stability, decomposition, or dehydration, thermal analysis is used to determine mass and caloric changes during endothermic or exothermic reactions.[90] With thermogravimetry (TG) the mass of the sample is monitored with a thermobalance as a function of temperature. Commonly, the thermobalance is coupled to a differential thermoanalysis (DTA) to identify reactions, which proceed without mass change. The DTA is based on the registration of the heat tone, which is caused by chemical reactions or phase transitions. The temperature difference is determined between the sample and a thermally stable reference both undergoing a linear temperature increase. Thus, when a calorimetric change occurs within the sample a deviation from the linear temperature program is detected. Through coupling of the thermal analysis to a mass spectrometer gaseous reactants and products can be identified and monitored.

3.6 Raman Spectroscopy

The Raman effect results from inelastic scattering of electromagnetic radiation by matter, where an energy transfer between photon and molecule takes place. Raman spectroscopy records transitions between different vibrational states. In contrast to infrared (IR) spectroscopy, where the absorption is measured as a function of frequency, Raman spectra display the frequency change with respect to the incident radiation. This frequency difference, the Raman shift, is independent of the wavelength of the incoming beam. The transition process is displayed in Fig. 3.5.

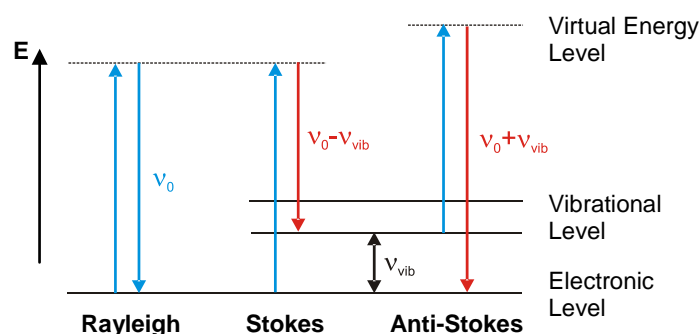


Fig. 3.5 Transitions between vibrational energy levels in Raman spectroscopy. Monochromatic light of the frequency, ν_0 , is scattered by a molecule. The scattering proceeds either without losing energy (Rayleigh scattering), or inelastically. In the process of inelastic scattering the molecule is excited to a higher vibrational level (Stokes scattering) or de-excited from a vibrationally excited mode (anti-Stokes scattering). The energy level diagram illustrates that the scattering process occurs instantaneously via a "virtual level" (dotted line) of higher energy.

The scattered light resulting from the irradiation of the molecule with a monochromatic beam consists of elastically scattered (Rayleigh scattering) and inelastically scattered photons. The latter exhibit an energy difference to the incoming photons which corresponds to the energy interval between the vibrational levels of the molecule. Inelastic scattering mostly results in photons with a lower energy with respect to the incoming beam (Stokes scattering). Occasionally, the light is scattered at molecules which are already in an excited state leading to the transition of the molecule to a lower energetic level. This scattering is called anti-Stokes and results in a shift of the photon energy to higher values with respect to the incoming beam.

Compared to other spectroscopic techniques, Raman scattering exhibits a comparatively small cross-section. Most of the incoming light is scattered elastically resulting in an intense Rayleigh band, which is about three orders of magnitude stronger than the Stokes bands. The use of higher laser intensities to increase Raman signals is limited since it also leads to sample heating or decomposition of surface species. Additionally, sample fluorescence may also hinder the detection of weak Raman bands.[74] Two major improvements can be achieved by using ultraviolet lasers to irradiate the sample. First, the scattering cross-section, which is a function of the fourth power of the frequency, can substantially be increased at lower wavelengths. Second, Raman signals are shifted out of the visible spectral

region where fluorescence occurs. Further details about Raman spectroscopy on metal oxide catalysts can be found in the literature.[73,91]

3.7 Elemental Analysis

For a qualitative and quantitative compositional analysis of metal oxide catalysts X-ray fluorescence (XRF) spectroscopy is most suitable. The method is based on detection of X-ray photons, which are emitted by the sample after irradiation with X-rays. The energy, and accordingly the wavelength, of the emitted fluorescence photons is characteristic for each element and can be used to identify the elemental composition of the sample.[92,93]

Irradiation of the sample with X-ray photons may result in removal of an electron from a core shell. The core hole is filled by an electron from a higher level, which results in the emission of an X-ray photon. The energy of the resulting fluorescence photons not only depends on the energetic state of the core hole but also on the atomic number of the element. The relationship between the energy of the X-ray photon, $h\nu$, and the atomic number, Z , is described by Mosley's law:

$$h\nu = R_H hc(Z - \sigma)^2 \left(\frac{1}{n_1^2} - \frac{1}{n_2^2} \right) \quad (3-10)$$

with the main quantum numbers, n_1 and n_2 , of the final, and the initial energy state of the electron that is filling the core hole, respectively, the Rydberg constant, R_H , the Planck constant, h , the light velocity, c , and a shielding constant, σ . Depending on energy of the excited electron and atomic number of the element the probability of an emitted X-ray fluorescence photon competes with the emission of a so-called Auger electron. For lighter elements the Auger process predominantly occurs. Instead of resulting in the emission of a fluorescence photon the energy released when the atom returns to the ground state can be transferred to another electron from a higher shell. In a consequence the electron is emitted from the atom as Auger electron. Fig. 3.6 schematically represents the excitation process that either results in the emission of an X-ray fluorescence photon or an Auger electron.

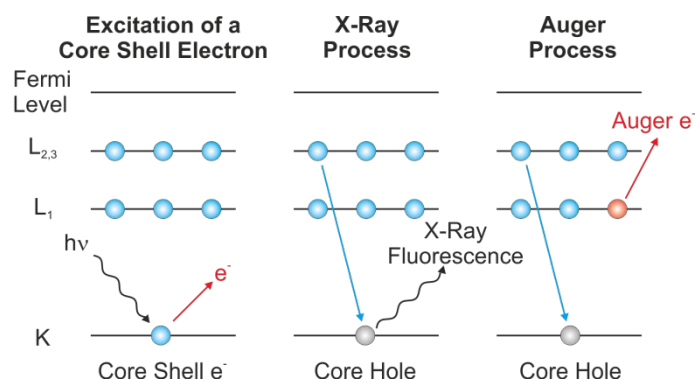


Fig. 3.6 Schematic depiction of electron excitation and relaxation processes. A photoelectron is emitted after excitation by an X-ray photon (left). The core hole is filled by an electron from a higher level resulting in the emission of an X-ray fluorescence photon (middle). Congruently to the fluorescence process the energy can be transferred to another electron, which is emitted as Auger electron (right).

3.8 Catalytic Characterization

The performance of a catalyst is expressed in terms of activity and selectivity in a chemical reaction. Catalytic testing on the laboratory scale can be conducted under steady-state (continuous) or non-steady-state conditions with a reactor operating in integral or differential mode. The integral mode where the reactor is operated at high conversion rates holds the opportunity to test performance and stability of the catalyst under industrially relevant conditions. However, it also features certain disadvantages such as concentration gradients or heat and mass transfer limitations. In the differential mode, *i.e.*, at small conversions, the whole catalyst is exposed to the same reactant concentrations and the influence of products on the reaction mechanism can be neglected. Heat and mass transfer limitations in the differential mode are minimized.

Operation of the reactor gives different types of information depending on the choice of the individual setup. The main issues regarding the use of a laboratory reactor are as follows:

- provision of activity values to enable catalyst comparison,
- study of slow or rapid changes in activity,
- investigation of mass and heat transfer,

- development of kinetic equations to estimate the influence of various factors (composition, pressure, temperature, or contact time) on catalytic performance, and
- retrieval of kinetic data for modeling of industrial reactors.

A detailed description of various reactor types and the individual assets of each setup can be found elsewhere.[94,95] A simple but reliable type is the plug-flow reactor, which may consist of a glass or metal tube with a sintered disc to support the solid catalyst. This reactor operates under steady-state conditions. Nevertheless, it may also provide information about the evolution of catalytic activity while approaching the steady state. In differential mode (small conversion) the whole catalyst is exposed to the reactants under the same conditions.

Reactants are passed through the catalytic bed. At the outlet of the reactor, reaction products can be analyzed by gas chromatography and/or mass spectrometry. In order to identify and quantify reaction products by gas chromatography, the basic principles of this physico-chemical separation process are described in the following. In gas chromatography the sample is injected into the inert gaseous mobile phase (carrier gas) and carried through a heated column that serves as stationary phase. The components of the sample are separated based on their ability to distribute between mobile and stationary phase. The retention time, which is the time each component requires to move from the point of injection to the detector, is strongly dependent on the interaction of the compounds with stationary and mobile phase. Components that strongly interact with the stationary phase exhibit a higher retention time, whereas components, which are not adsorbed, have a lower retention time. If the strength of each component's interaction with the stationary phase is sufficiently different, the sample separates into individual fractions resulting in separately observable bands. These bands are detected as a function of retention time and can be qualitatively and quantitatively analyzed.[96,97] The detector of a chromatography system needs to meet certain criteria, including low detection limits, a linear response over a wide concentration range, and responsiveness to all components or to a specific component class. Thermal conductivity detector (TCD), flame ionization detector (FID), and electron capture detector (ECD) are most widely used.[97]

4 Synthesis and Optimization of Support Material

The aim of this part of the work was the preparation and characterization of a high surface area support material based on magnesium oxide with alkaline properties. Therefore, several synthetic approaches, including nanocasting and surfactant-assisted sol-gel routes, were carried out. The materials were characterized in terms of textural, physical, and chemical properties. For application in catalysis the support material needs to meet the following basic requirements:

- a) textural properties: high surface area, ordered mesopore structure, and narrow pore size distribution,
- b) chemical properties: low activity during catalytic testing,
- c) physical properties: thermal stability in the temperature range used for catalytic testing.

Additionally, a reproducible synthesis of the magnesium oxide based support was sought. In the following the two most promising attempts are introduced and discussed. Briefly, all other synthesis routes resulted in MgO materials which were not suitable for catalytic purposes. In particular, nanocasting via a CMK-3 template yielded only in very small amounts of mesoporous MgO with a varying amount of remaining silica. Thus, it is not discussed in detail but can be read elsewhere.[98] Applicability for catalysis was tested by studying the properties of the supports after metal oxide deposition on their surface.

4.1 Experimental

4.1.1 Sample Preparation

Synthesis of Support Material

Mesoporous magnesium oxides were prepared by two different routes. Nanostructured magnesium oxide, denoted as “*nano-MgO*”, was synthesized using a hydrothermal approach with triblock copolymer P-123 (Aldrich) as template reagent. A similar synthesis proce-

ture has already been reported for mesoporous zinc oxide.[26] Typically, 5.37 g of $\text{Mg}(\text{CH}_3\text{CO}_2)_2 \cdot 4\text{H}_2\text{O}$ (Alfa Aesar, 98%) and 30.03 g of $\text{CO}(\text{NH}_2)_2$ (Roth, 99.6%) were dissolved in 400 ml of deionized water. 154 mg of P-123 were added to the solution and the pH value was adjusted to 4.6 using acetic acid. The solution was stirred for 24 h at room temperature and then kept at 90 °C under hydrothermal conditions for 48 h. The solid product was filtered off, washed with deionized water to neutral pH, and dried for 2 h at 115 °C. The resulting white spherules were calcined under static air at 400 °C for 2 h.

MgO-coated SBA-15, denoted as “*MgO/SBA-15*”, was synthesized using the mesoporous, hexagonally ordered silica SBA-15 as structural template.[21] SBA-15 was prepared according to Zhao *et al.*[10] However, unlike the procedure described by them, calcination was carried out in two steps. Initially, temperature was raised to 180 °C and held for 3 h. In a second step temperature was increased from 180 °C to 550 °C and held at that temperature for 5 h. The heating rate was kept at 1 K/min. The resulting SBA-15 was impregnated with magnesium nitrate. Typically 2.0 g of SBA-15 were stirred for 5 h at room temperature in 20 ml of a 1-M $\text{Mg}(\text{NO}_3)_2$ (hexahydrate, Alfa Aesar, 98%) solution with an $\text{H}_2\text{O}/\text{EtOH}$ ratio of 1:1. The product was filtered off and dried under synthetic air flow at room temperature for 6 h. Calcination of $\text{Mg}(\text{NO}_3)_2$ on SBA-15 was carried out under the same gas flow for 3 h at 450 °C. The heating rate was kept at 2 K/min.

Synthesis of Supported Molybdenum Oxides

For catalytic testing molybdenum oxides were supported on *nano-MgO* and *MgO/SBA-15*. The amount of molybdenum was adjusted to 5 wt.%. Preparation of the samples was done by incipient wetness. Therefore, an aqueous solution of ammonium heptamolybdate $(\text{NH}_4)_6\text{Mo}_7\text{O}_{24} \cdot 4\text{H}_2\text{O}$ (AHM, Fluka, 99.0%) was used. Calcination was carried out under static conditions at 450 °C for 5 h.

4.1.2 Sample Characterization

Nitrogen Physisorption

Nitrogen adsorption/desorption isotherms were measured at -196 °C using a BELSORP-Mini II (BEL Inc. Japan). Prior to measurement samples were degassed under reduced pressure

($\sim 10^{-2}$ kPa) at 110 °C for 30 min. They were kept under the same pressure overnight at 200 °C. Adsorption data were analyzed by using a non-local density functional theory (NLDFT) approach to calculate the size of both micro- and mesopores. A cylindrical pore model for zeolite type materials was used within the ASiQwin™ software (v2.0, Quantachrome). Specific surface areas were obtained by using the Brunauer-Emmett-Teller (BET) method.[86] To calculate the monolayer capacity, n_m , adsorption data were plotted in the linearized form

$$\frac{p}{n_a(p_0 - p)} = \frac{1}{n_m C} + \frac{(C - 1)}{n_m C} \cdot \frac{p}{p_0} \quad (4-1)$$

with the amount adsorbed, n_a , at the relative pressure, p/p_0 , and a constant, C. For reliable results application of the BET theory to the adsorption data plotted according to eq. (4-1) was restricted to the linear range ($p/p_0 \approx 0.05-0.20$). All results matched the validation criteria, which implied a positive C value and a fit residual, R, of at least 0.999. The specific surface area, a_{BET} , was determined according to eq. (3-7) taking the area of a nitrogen molecule, σ , as 0.162 nm^2 .

External surface area (*i.e.*, the surface area not associated with the pores), mesopore area, and micro- and mesopore volume were calculated using a *t*-plot analysis.[84] The thickness of a monomolecular nitrogen layer adsorbed on the surface was taken as 0.354 nm assuming a hexagonally closed-packed arrangement of nitrogen molecules.[99] The Harkins-Jura thickness equation was used as reference isotherm.

Powder X-Ray Diffraction

Powder X-ray diffraction patterns were obtained at a diffractometer (X'Pert PRO MPD, PANalytical) in theta/theta geometry. Cu K alpha radiation (40 kV/40 mA) and a solid state multi-channel (PIXcel®) detector were used. Low-angle diffraction patterns were measured in the transmission mode between 0.4° and $6^\circ 2\theta$ and -0.4° and $-4^\circ 2\theta$ in steps of $0.013^\circ 2\theta$ with a sampling time of 90 s/step. The positive and negative values for the (10 l) diffraction line were averaged. The unit cell constant, a_0 , corresponding to a hexagonal metric, was calculated according to

$$a_0 = 2d_{10l}/\sqrt{3} \quad (4-2)$$

with the lattice spacing, d_{10l} .

Wide-angle diffraction patterns were measured in reflection mode in a range of 5° to $120^\circ 2\theta$ in steps of $0.013^\circ 2\theta$ with a sampling time of 60 s/step. A programmable slit was used to obtain an active irradiation length of 12 mm/step. Analysis of the diffractograms was carried out by using the program X'Pert HighScore Plus (v2.2d, PANalytical).

In situ XRD measurements were conducted on a diffractometer (theta/theta geometry, STOE) using an *in situ* chamber (Anton Paar). Thermal stability tests in a temperature range between 50°C and 450°C were carried out in 20% oxygen (Air Liquide, 4.5) in helium (Air Liquide, 5.0) with a total flow of 100 ml/min. Characteristic diffraction peaks were scanned in a 2θ -range between 33° and $68^\circ 2\theta$ in steps of $0.06^\circ 2\theta$ with a sampling time of 5 s/step.

Thermal Analysis

Thermogravimetry (TG) and differential thermal analysis (DTA) were conducted with a thermobalance (SSC 5200, Seiko Instruments). The oven was purged with a predefined reaction gas mixture consisting of 20% oxygen (Air Liquide, 4.5) and 80% helium (Air Liquide, 5.0). The total flow was kept low to avoid mass transport of the light mesoporous particles. It was adjusted to 50 ml/min. Sample and reference underwent a temperature programmed heat treatment between 30°C and 500°C with a heating rate of 5 K/min.

X-Ray Fluorescence Analysis

Elemental analysis by X-ray fluorescence spectroscopy was performed on an X-ray spectrometer (AXIOS, 2.4 kW model, PANalytical) equipped with a Rh K alpha source, a gas flow detector and a scintillation detector. 75 mg of the sample were diluted with wax (Hoechst wax C micropowder, Merck) at a ratio of 1:1 and pressed into 13 mm pellets. Quantification was performed by standardless analysis with the SuperQ 5 software package (PANalytical).

Catalytic Characterization

Quantitative catalysis measurements were performed in a laboratory fixed-bed reactor connected to an online gas chromatography system (CP-3800, Varian). For catalytic testing 150 mg of the support material were diluted with 250 mg of boron nitride (Alfa Aesar, 99.5%). Hydrocarbons and oxygenated reaction products were analyzed using a Carbowax 52CB capillary column connected to an Al₂O₃/MAPD capillary column, and a fused silica restriction (25 m·0.32 mm), respectively. Each column was connected to a flame ionization detector. Permanent gases (O₂, N₂, CO₂, CO) were separated and analyzed using a “Permanent Gas Analyzer” (CP-3800, Varian) connected to a thermal conductivity detector. Reactant gas flow rates of oxygen, propene, and helium were adjusted through separate mass flow controllers (Bronkhorst) to a total flow of 40 ml/min. A mixture of 5% propene (Linde Gas, 10% propene (3.5) in He (5.0)) and 5% oxygen (Air Liquide, 20% O₂ (4.8) in He (5.0)) in helium (Air Liquide, 6.0) was used for catalytic testing in the range of 20–450 °C. Additionally, reactant and product gas flow was continuously monitored by a mass spectrometer (Omnistar, Pfeiffer) in a multiple ion detection mode.

4.2 Results and Discussion

4.2.1 Textural Properties – Surface Area and Pore Structure

X-Ray Diffraction

The template assisted synthesis of *nano-MgO* with the triblock copolymer P-123 was expected to result in a hexagonal order of the mesoporous structure. However, no diffraction peaks were detected in the low-angle range, indicating the absence of any hexagonal ordering. This might be caused by the low temperature (*i.e.*, 90 °C) during hydrothermal treatment compared to treatment temperatures reported in the literature.[100] Wang *et al.* observed an increasing intensity of the low-angle diffraction peak with increasing treatment temperature from 160 °C to 240 °C. For samples treated at 160 °C no diffraction peaks were detected.[100] Wide-angle X-ray diffraction (XRD) patterns of *nano-MgO*, shown in Fig. 4.1, exhibited peaks that corresponded to crystalline magnesium oxide. Compared to a crystalline MgO reference these peaks were strongly broadened. Hence, crystalline domains were ex-

pected to be comparably small. Domains calculated by the Scherrer formula (eq. (3-9)) amounted to about 5 nm.

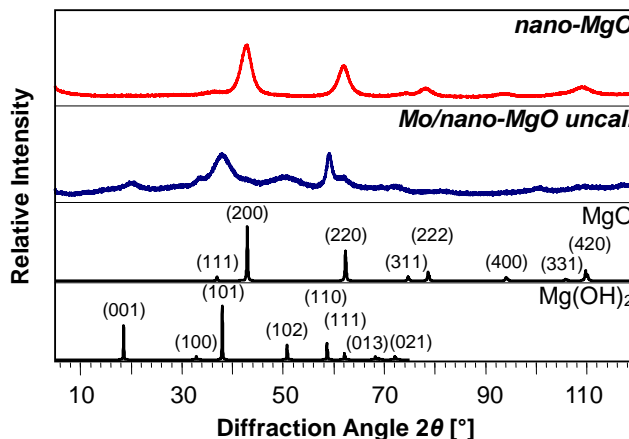


Fig. 4.1 Wide-angle diffraction patterns of *nano-MgO* together with molybdenum oxide supported on *nano-MgO* in the uncalcined stage. Also shown for comparison are diffraction patterns of bulk reference materials MgO (ICSD 009863, [101]) and Mg(OH)₂ (ICSD 079032, [102]).

Fig. 4.2 depicts the low-angle XRD patterns of *MgO/SBA-15* and uncoated SBA-15 with the peaks (10*l*), (11*l*), and (20*l*) corresponding to the two-dimensional hexagonal symmetry. The diffraction peaks were visible for uncoated and MgO-coated SBA-15. Thus, mesoscopic ordering was assumed for both materials. The lattice spacings, d_{10l} , derived from the Bragg equation (eq.(3-8)), and unit cell constants, a_0 , corresponding to the hexagonal pore arrangement, are given in Table 4.1. No crystalline magnesium oxide was detected by wide-angle XRD for the MgO-coated SBA-15 (Fig. 4.2, inset).

A similar approach of coating SBA-15 with magnesium oxide was previously reported by Zukał *et al.*[30] Although the amount of MgO deposited on the silica surface was significantly lower, they demonstrated that coating of the surface did not lead to a collapse of the porous SBA-15 structure. Wei *et al.* introduced an alternative preparation method via *in situ* coating of SBA-15 by adding magnesium acetate salt to the initial mixture of raw materials for SBA-15 synthesis.[28] Samples with a Si:Mg atomic ratio between 2.6 and 7.1 were claimed to possess a better stability and higher surface areas compared to MgO-coating by post-synthesis impregnation. However, minor amounts of MgCl₂ that are likely to form during the preparation are not desirable for the application in catalysis described within this work.

The weight portion of MgO in *MgO/SBA-15* amounted to about 15 wt.% as determined by X-ray fluorescence (XRF) measurements. This resulted in an atomic ratio of Si to Mg of 4.4.

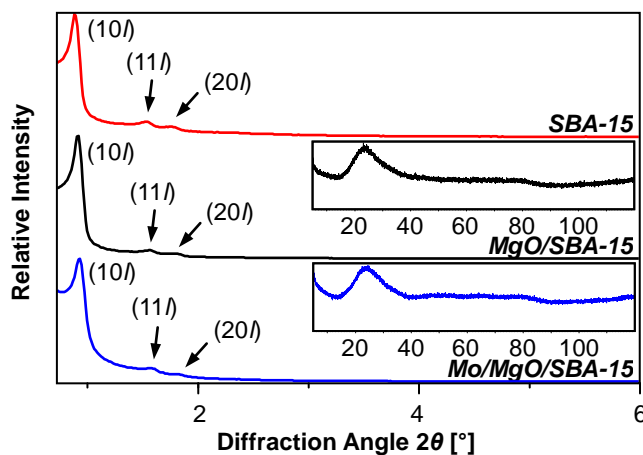


Fig. 4.2 Low-angle X-ray diffraction patterns of parent SBA-15 (top), *MgO/SBA-15* (middle), and molybdenum oxide supported on *MgO/SBA-15* (bottom). (10 l), (11 l), and (20 l) diffraction peaks are indicated. The inset shows wide-angle XRD patterns, which exhibited no peaks of any crystalline substances.

Table 4.1 Textural properties of *nano-MgO*, *MgO/SBA-15*, and parent SBA-15: specific surface area, a_{BET} (calculated by BET method), external surface area, a_{Ext} (calculated as the difference between a_{BET} and a_{Meso}), area corresponding to the mesopores, a_{Meso} , average pore diameter, d_{Meso} (calculated by NLDFT method), meso- and micropore volume, V_{Meso} , and V_{Micro} , respectively, d_{10l} -value (derived from low-angle XRD), unit cell constant, a_0 (corresponding to the hexagonal pore arrangement), and wall thickness, t_w , between the mesopores (calculated as the difference between a_0 and d_{Meso}).

| | a_{BET} | a_{Ext}^a | a_{Meso}^a | d_{Meso} | V_{Meso}^a | V_{Micro}^a | d_{10l} | a_0 | t_w |
|-------------------|---------------------|---------------------|---------------------|------------|----------------------|----------------------|-----------|-------|-------|
| | [m ² /g] | [m ² /g] | [m ² /g] | [nm] | [cm ³ /g] | [cm ³ /g] | [nm] | [nm] | [nm] |
| <i>nano-MgO</i> | 302 | 32 | 270 | 3.3 | 0.197 | - | - | - | - |
| <i>MgO/SBA-15</i> | 402 | 23 | 379 | 7.6 | 0.606 | 0.022 | 10.3 | 11.8 | 4.2 |
| <i>SBA-15</i> | 710 | 32 | 679 | 8.8 | 1.083 | 0.055 | 10.3 | 11.8 | 3.0 |

^a Values were calculated from t -plot analysis.

Nitrogen Physisorption

Both support materials exhibited a high specific surface area with a narrow pore size distribution. Fig. 4.3 shows the N₂ adsorption/desorption isotherms of *nano-MgO* and *MgO/SBA-15*,

together with the corresponding pore size distribution derived from NLDFT analysis (Fig. 4.3, inset). A comparison of experimental and simulated isotherm, resulting from NLDFT calculation, is given in the Appendix (Fig. A 1.3). *Nano-MgO* gave rise to an isotherm of mainly type I, which is typical for microporous materials. However, the appearance of a hysteresis loop between adsorption and desorption branches was indicative of a mesoporous structure. NLDFT calculation of the pore size distribution from the adsorption branch gave a maximum at a pore diameter of 3.3 nm. The material possessed a high surface area of approximately 300 m²/g, which was even higher than that of ordered mesoporous MgO obtained by using a CMK-3 exotemplate.[21,98]

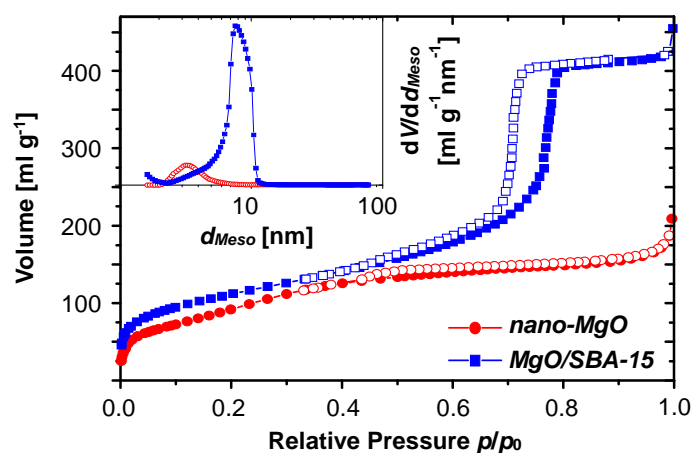


Fig. 4.3 Nitrogen adsorption/desorption isotherms and pore size distribution (inset) of the two support materials *nano-MgO* (circles) and *MgO/SBA-15* (squares). Filled symbols represent the adsorption branch, open symbols the desorption branch. The pore size distribution (logarithmic scale) was derived from NLDFT calculations assuming a cylindrical pore shape.

The isotherm of *MgO/SBA-15* was of type IV indicative of mesoporous materials. Adsorption and desorption branches in hysteresis range were nearly parallel as expected for regularly shaped pores. The mesopores of *MgO/SBA-15* with an average diameter of 7.6 nm were larger than those of *nano-MgO*. To estimate the mesopore area and external surface area a *t*-plot analysis was performed.[84] (*t*-Plots are given in the Appendix, Fig. A 1.1 and Fig. A 1.2.) Table 4.1 summarizes the surface areas (*i.e.*, BET surface area, external surface area, mesopore surface area) and pore volumes (micro- and mesopore volume). About 90% of the calculated BET surface area of *nano-MgO* was present as internal surface area within the

mesopores. Therefore, the external surface area formed only a minor fraction of the overall surface.

For *MgO/SBA-15* and parent SBA-15 a certain amount of micropores in addition to mesopores was determined. The presence of micropores or surface corrugations is known to cause a corona of reduced mean density around the cylindrical mesopores.[29,103] Amount and size of the micropores strongly depend on synthesis procedure.[104,105] The applied synthesis procedure resulted only in a small amount of micropores representing under 5% of the total pore volume. Coating of SBA-15 with MgO led to a decrease in micropore volume, thus causing a smoothing of the surface. Similar observations were reported in the literature for grafting of SBA-15 with alumina.[29,106] Furthermore, Zukal *et al.* correlated the growth of the alumina layer with a decreasing external surface area.[29] The slight decrease in external surface area and micropore volume were thus indicative of a layer of MgO on the SBA-15 surface. MgO loading of 15 wt.% corresponds to a calculated surface density of 3.7 Mg atoms per nm² (SBA-15). Based on Raman data of the *MgO/SBA-15* support a complete covering of the SBA-15 surface with MgO could be assumed, due to the absence of any characteristic SBA-15 bands.[107]

4.2.2 Chemical Properties – Applicability in Catalytic Reaction

The catalytic performance of the support materials in selective oxidation of propene was tested at 450 °C in 5% propene and 5% oxygen. The results obtained are shown in Table 4.2. They were compared to the data of the pure diluting material boron nitride (BN) and silica SBA-15. The support materials exhibited low catalytic activity with only minor selectivity to selective oxidation products. Major products corresponded to total oxidation of propene. Comparison of catalytic activity led to the order:

$$MgO/SBA-15 > nano-MgO \approx SBA-15 > BN.$$

The alkaline surface character apparently led to an increased activity compared to acidic silica SBA-15. The higher catalytic activity of *MgO/SBA-15* compared to *nano-MgO* was most probably due to the higher specific surface area of *MgO/SBA-15*. Bare SBA-15 and the diluent boron nitride (BN) exhibited a rather high selectivity towards acrolein but at a low

overall catalytic activity. In total, catalytic activity tests of the support materials and boron nitride showed that their catalytic performance was negligible.

Table 4.2 Catalytic performance of supports and diluting material boron nitride (BN) in selective propene oxidation at 450 °C. (^a sum of propionic aldehyde, acetone, isopropyl alcohol, allyl alcohol, and acrylic acid; ^b sum of acetic aldehyde and acetic acid)

| | C₃H₆ Conversion [%] | Selectivity [%] | | | CO₂ [%] | CO [%] |
|-------------------|--|------------------------|--------------------------------------|--------------------------------------|------------------------------|------------------|
| | | Acrolein [%] | C₃ | C₂ | | |
| | | | Oxygenates^a [%] | Oxygenates^b [%] | | |
| <i>nano-MgO</i> | 0.7 | 4 | 0 | 1 | 42 | 53 |
| <i>MgO/SBA-15</i> | 1.7 | 2 | 1 | 3 | 59 | 34 |
| SBA-15 | 0.6 | 34 | 11 | 9 | 31 | 15 |
| BN | 0.4 | 26 | 1 | 7 | 47 | 19 |

4.2.3 Physical Properties – Thermal Stability

To study the thermal stability of the support materials with respect to surface area and pore structure molybdenum oxide was deposited on the supports. Calcination of the molybdenum oxide precursor required thermal treatment under static air at temperatures up to 450 °C.

Nanostructured MgO (nano-MgO)

Deposition of molybdenum oxides on *nano-MgO* resulted in broad X-ray diffraction (XRD) peaks corresponding to magnesium hydroxide (compare Fig. 4.1). Thus, a partial transformation of the supporting *nano-MgO* to the hydroxide took place during incipient wetness. This is not surprising because the incipient wetness procedure was done with an aqueous molybdenum oxide precursor solution where small MgO particles exposed on the surface should readily form Mg(OH)₂. Upon calcination of the samples magnesium oxide was formed again.

A comparison of the results from physisorption measurements before and after calcination of the molybdenum oxide precursor on the supporting *nano-MgO* revealed severe changes in textural properties. Physisorption data are summarized in Table 4.3. Apparently, BET

surface area and mesopore volume decreased after molybdenum oxide deposition, while the external surface area considerably increased. Therefore, a partial clogging of the pores during calcination seemed likely. The overall shape of the physisorption isotherm of molybdenum oxide supported on *nano-MgO* (*Mo/nano-MgO*) compared to parent *nano-MgO* changed significantly (Fig. 4.4).

Table 4.3 Textural properties of *nano-MgO*, and molybdenum oxide supported on *nano-MgO* after calcination at 450 °C: specific surface area, a_{BET} (calculated by BET method), external surface area, a_{Ext} (calculated as the difference between a_{BET} and a_{Meso}), area corresponding to the mesopores, a_{Meso} , average pore diameter, d_{Meso} (calculated by NLDFT method), and mesopore volume, V_{Meso} .

| | a_{BET} [m ² /g] | a_{Ext} ^a [m ² /g] | a_{Meso} ^a [m ² /g] | d_{Meso} [nm] | V_{Meso} ^a [cm ³ /g] |
|--------------------|----------------------------------|---|--|--------------------|---|
| <i>nano-MgO</i> | 302 | 32 | 270 | 3.3 | 0.197 |
| <i>Mo/nano-MgO</i> | 249 | 102 | 146 | 3.4 | 0.100 |

^a Values were calculated from *t*-plot analysis.

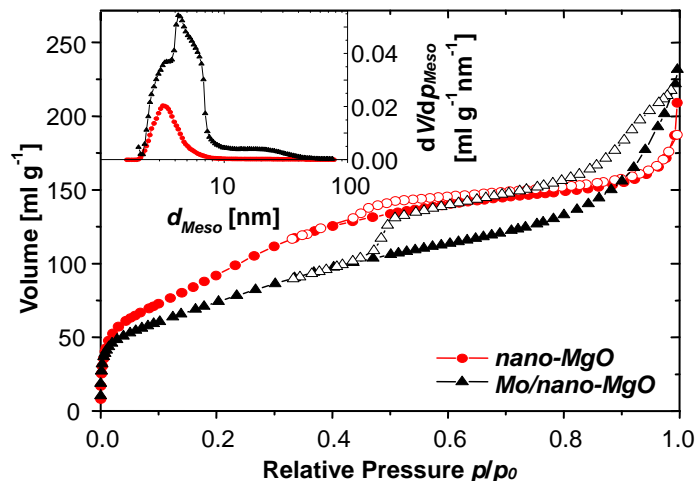


Fig. 4.4 Nitrogen adsorption/desorption isotherms and pore size distribution (inset) of *nano-MgO* (red circles) and molybdenum oxide supported on *nano-MgO* (black triangles). Filled symbols represent the adsorption branch, open symbols the desorption branch. Pore size distribution (logarithmic scale) was derived from NLDFT calculation.

The isotherm of *Mo/nano-MgO* remained mainly of type I but with a rather undefined hysteresis loop between adsorption and desorption branch. A well-defined mesopore structure with-

in the material could not be assumed, because closure of adsorption and desorption branch took place at a relative pressure close to 0.42. A closure at this pressure is generally considered to be caused by percolation effects.[83] Hence, pore diameter distribution varied over a broad range (Fig. 4.4, inset).

During calcination the molybdenum oxide species diffused into the surface of *nano-MgO* and formed a rather undefined phase mixture with a strong interaction between molybdenum centers and MgO support. A similar occlusion of vanadium catalyst particles in bulk MgO after calcination has been previously reported by Blasco *et al.*[69] It is likely that besides diffusion of molybdenum ions a rearrangement of the pore structure within *nano-MgO* occurred during calcination. Transformation of magnesium oxide to magnesium hydroxide corresponds to a conversion from a cubic face-centered to a hexagonal closed-packed structure. This structural transformation may induce changes on the macroscopic scale. New pores were generated while other pores were clogged. Therefore, a partially new surface was generated and the molybdenum containing phase was occluded in the bulk. Possible changes in textural properties of the bare support material were tested during temperature programmed treatment under oxidizing conditions. Thermal analysis of *nano-MgO* under 20% O₂/He was carried out in a temperature range between 30 °C and 450 °C. A representative thermogravimetry (TG) profile is depicted in Fig. 4.5.

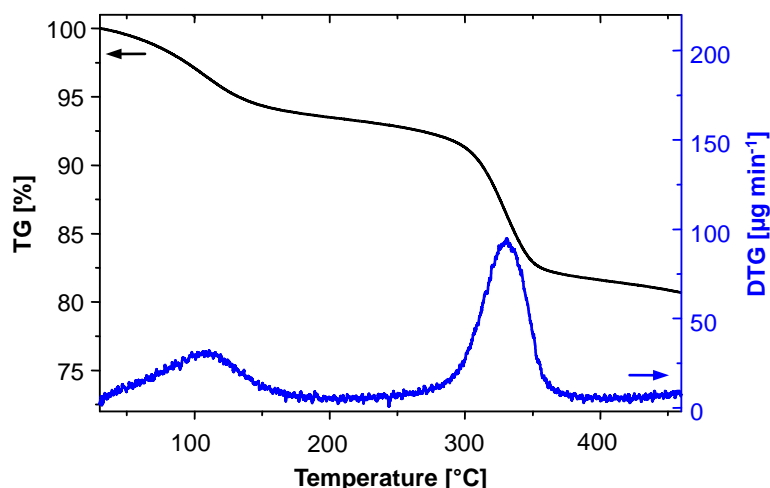


Fig. 4.5 TG/DTG profile of *nano-MgO* in the temperature range between 30 °C and 450 °C (reaction atmosphere: 20% O₂/He).

The derivative thermogravimetric (DTG) signal resolved two peaks in the temperature range between 90–110 °C, and 280–360 °C, respectively. The first peak was related to desorption of physically adsorbed water on the MgO surface and resulted in a mass loss of 5–7%. The second peak was ascribed to the decomposition of magnesium hydroxide Mg(OH)₂ to magnesium oxide. Storage of the samples under ambient conditions supposedly led to the partial hydration of the MgO surface to Mg(OH)₂. Endothermic dehydration of Mg(OH)₂ to MgO takes place at temperatures above 350 °C.[108] A complete conversion of Mg(OH)₂ to MgO theoretically results in a weight loss of 30.9%. The observed weight loss of about 9% in a temperature range between 280–360 °C indicated that about 30% of the *nano-MgO* sample was present as Mg(OH)₂ under ambient conditions. This was most probably due to the high surface area of *nano-MgO* which was exposed to ambient environment. Thermal stability was tested by *in situ* X-ray diffraction (XRD) measurements under synthetic air in a temperature range between 50 °C and 450 °C. Evolution of the diffraction patterns in the 2θ -range between 33° and 68° is given in the Appendix (Fig. A 1.4). The highly dispersed Mg(OH)₂ particles on the surface of pure *nano-MgO* assumed from thermal analysis were not detectable by XRD. MgO crystallite sizes approximated by Scherrer's formula (eq. (3-9)) changed from 4.9 nm before to 6.3 nm after thermal treatment. Hence, a crystallite growth of approximately 30% was observed.

MgO-coated SBA-15 (MgO/SBA-15)

Deposition and calcination of molybdenum oxide on *MgO/SBA-15* did not lead to a change in textural properties. Hence, thermal stability of molybdenum oxide dispersed on the support was tested under catalytic propene oxidizing conditions in a fixed-bed reactor at 450 °C. Fig. 4.6 depicts the N₂ physisorption isotherms before and after catalytic reaction in 5% propene and 5% oxygen. Overall shape of the isotherms before and after reaction remained similar. Both isotherms exhibited a hysteresis loop with nearly parallel adsorption and desorption branch. Therefore, the mesopores within the material remained well-ordered with a narrow pore size distribution, which was similar before and after catalytic reaction (Fig. 4.6, inset).

BET surface and mesopore area, given in Table 4.4, only slightly decreased after reaction resulting in a smoothing of the surface. Hence, no major structural changes of the support material were observed during catalytic reaction at elevated temperatures. Low-angle X-ray

diffraction (XRD) patterns before and after catalytic reaction confirmed that the hexagonal ordering of the pore structure was preserved. Hence, cell parameters remained constant (compare Table 4.4).

Table 4.4 Textural Properties of molybdenum oxide supported on MgO/SBA-15 before and after catalytic reaction: specific surface area, a_{BET} (calculated by BET method), external surface area, a_{Ext} (calculated as the difference between a_{BET} and a_{Meso}), area corresponding to the mesopores, a_{Meso} , average pore diameter, d_{Meso} (calculated by NLDFT method), meso- and micropore volume, V_{Meso} , and V_{Micro} , respectively, d_{10l} -value (derived from low-angle XRD), unit cell constant, a_0 (corresponding to the hexagonal pore arrangement), and wall thickness, t_w , between the mesopores (calculated as the difference between a_0 and d_{Meso}).

| | a_{BET} | a_{Ext}^a | a_{Meso}^a | d_{Meso} | V_{Meso}^a | V_{Micro}^a | d_{10l} | a_0 | t_w |
|----------------------|---------------------|---------------------|---------------------|------------|----------------------|----------------------|-----------|-------|-------|
| | [m ² /g] | [m ² /g] | [m ² /g] | [nm] | [cm ³ /g] | [cm ³ /g] | [nm] | [nm] | [nm] |
| Mo/MgO/SBA-15 | | | | | | | | | |
| As-Prepared | 243 | 78 | 165 | 7.3 | 0.257 | 0.030 | 10.1 | 11.6 | 4.3 |
| After React. | 180 | 78 | 102 | 7.3 | 0.215 | 0.014 | 10.1 | 11.6 | 4.3 |

^a Values were calculated from t -plot analysis.

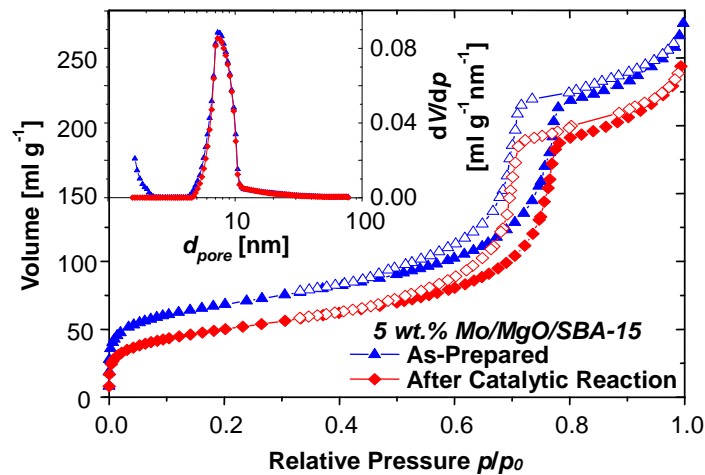


Fig. 4.6 Nitrogen adsorption/desorption isotherms and pore size distribution (inset) of molybdenum oxides supported on MgO/SBA-15 before (blue triangles) and after catalytic reaction (red diamonds). Filled symbols represent the adsorption branch, open symbols the desorption branch. Pore size distribution (logarithmic scale) was derived from NLDFT calculations assuming a cylindrical pore shape.

4.3 Conclusions

Two different MgO-based materials were studied as support material. The support materials were characterized by X-ray diffraction, N₂ physisorption, and thermal analysis with respect to their catalytic applicability. Both support materials were reproducibly prepared with a high surface area and a narrow pore size distribution in the mesopore range. Pore size and specific BET surface area of *nano-MgO* were smaller than those of *MgO/SBA-15*. Although both materials were prepared with the triblock copolymer P-123 as structure directing agent, only *MgO/SBA-15* exhibited a hexagonal long range ordering. It was shown that for *MgO/SBA-15* coating of silica SBA-15 with magnesium oxide led to highly dispersed MgO on the silica surface. Thus, surface properties of the parent SBA-15 were altered by introducing MgO without a collapse of the porous system.

Reactivity of *nano-MgO* and *MgO/SBA-15* during catalytic reaction were tested for selective propene oxidation. Both support materials exhibited only poor catalytic activity and selectivity. Therefore, they were considered to be inert under reaction conditions. The materials exhibited considerably different thermal stabilities under catalytic propene oxidizing conditions. The structure of *nano-MgO* collapsed during treatment at elevated temperatures. About 30% of the material was present as Mg(OH)₂ under ambient conditions. Thermal treatment led to a transformation of Mg(OH)₂ to MgO and thus, to the generation of a strongly altered surface with a broad pore size distribution. Hence, *nano-MgO* was not convenient as support material in catalytic application. The material proved to be instable after deposition of molybdenum oxides and subsequent calcination. Therefore, in the following *MgO/SBA-15* will be used as support material.

In *MgO/SBA-15* the MgO surface on SBA-15 was stabilized by the SiO₂ framework. Only a slight increase in external surface area, accompanied by a decreasing mesopore area, was observed after deposition of molybdenum oxides. Furthermore, *MgO/SBA-15* remained stable under catalytic reaction conditions. The specific BET surface area only slightly decreased at elevated temperatures, while the mesoporous structure remained stable.

5 Structural Characterization of Supported Oxide Catalysts

Studying structure activity correlations of catalyst systems requires a detailed knowledge of the catalyst structure. Therefore, the oxide catalysts were investigated by a combination of various characterization techniques, such as X-ray spectroscopy, DR-UV-Vis spectroscopy, and X-ray diffraction. The vanadium and molybdenum oxide were supported on alkaline high surface area *MgO/SBA-15*. The oxides supported on *nano-MgO* will not be discussed here because the material proved to be unsuitable as support (refer to Chap. 4). An in-depth discussion of the differences regarding molybdenum oxides supported on *nano-MgO* and *MgO/SBA-15* has been previously reported.[109] As it will be shown the properties of the support material have a huge impact on the local structure of the supported oxides. Therefore, this chapter closes with a comparison of vanadium and molybdenum oxides supported on alkaline *MgO/SBA-15* to the oxides supported on more acidic silica SBA-15 and carbon CMK-3. Details on preparation and characterization of the oxide catalysts supported on SBA-15 can be found elsewhere.[41,110-112]

5.1 Experimental

5.1.1 Sample Preparation

Vanadium and molybdenum oxides supported on *MgO/SBA-15* with loadings between 1–10 wt.% vanadium or molybdenum were prepared. Oxide deposition on the support material was carried out by incipient wetness. An aqueous oxide precursor solution, containing ammonium decavanadate $(\text{NH}_4)_6\text{V}_{10}\text{O}_{28}\cdot x\text{H}_2\text{O}$ or ammonium heptamolybdate $(\text{NH}_4)_6\text{Mo}_7\text{O}_{24}\cdot 4\text{H}_2\text{O}$ (Fluka, 99.0%) was used for vanadium, and molybdenum oxide, respectively. Samples were dried at room temperature overnight and calcined in static air at 450 °C for 5 h. Metal oxide loadings of the *V/MgO/SBA-15* and *Mo/MgO/SBA-15* samples were quantified by X-ray fluorescence (XRF) spectroscopy.

Uncalcined supported vanadium oxides were colorless at loadings of 1 wt.% V. With increasing catalyst loading the color of the *V/MgO/SBA-15* samples turned to light yellow.

After calcination the yellow color turned to a darker brownish yellow. Supported molybdenum oxides were colorless independent of catalyst loading. The color did not change upon calcination. Fig. 5.1 depicts the supported vanadium and molybdenum oxides with various catalyst loadings.

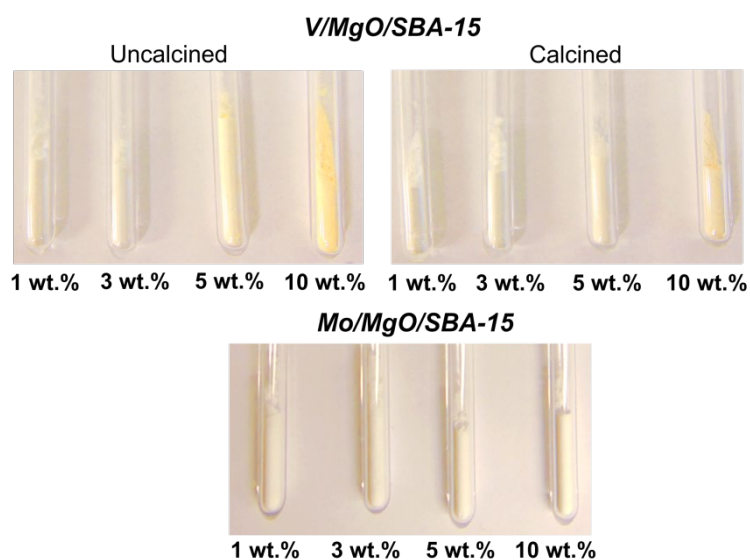


Fig. 5.1 Top: Vanadium oxide supported on *MgO/SBA-15* at various vanadium loadings before (uncalcined) and after calcination at 450 °C. Bottom: Calcined molybdenum oxide supported on *MgO/SBA-15* at various molybdenum loadings.

For comparison vanadium and molybdenum oxides were supported on carbon CMK-3. Therefore, mesoporous CMK-3 was prepared according to a modified procedure introduced by Vinu *et al.*[19] In a typical synthesis 2.0 g of template SBA-15 were added to a solution obtained by dissolving 3.0 g of sucrose (Aldrich) and 0.34 g of H₂SO₄ (98%, Roth) in 10.0 g of deionized water. The suspension was dried at 100 °C for 6 h. Subsequently, the oven temperature was raised to 160 °C and held at that temperature for another 6 h. The dark-brown powder was homogenized and added to a second solution obtained by dissolving 2.0 g of sucrose (Aldrich) and 0.2 g of H₂SO₄ (98%, Roth) in 10.0 g of deionized water. The suspension was again subjected to the thermal treatment described above. After homogenization the obtained powder was heated with a heating rate of 5 K/min to 700 °C under nitrogen flow. In order to fully carbonize the polymer the sample was kept under these conditions for 6 h. The silica template was dissolved by adding the carbonized sample to 50 ml of a 2-M solution of sodium hydroxide with an H₂O/EtOH ratio of 1:1. Subsequently, the product was filtered off, washed

with deionized H₂O, ethanol, and ether and dried at 110 °C. To fully remove the silica framework the procedure was repeated. A detailed analysis of the physico-chemical properties of the obtained CMK-3 support is reported elsewhere.[98]

Vanadium and molybdenum oxides supported on carbon CMK-3 with loadings of 10 wt.% vanadium or molybdenum were prepared in a similar procedure as described for the oxides supported on *MgO/SBA-15*. Oxide deposition was carried out by incipient wetness with an aqueous oxide precursor solution of (NH₄)₆V₁₀O₂₈·xH₂O or (NH₄)₆Mo₇O₂₄·4H₂O (Fluka, 99.0%). Samples were dried at room temperature overnight and calcined in static air at 300 °C for 5 h. Bulk vanadium and molybdenum oxides used as references are listed in the Appendix (Table A 2.1) together with their synthesis procedure or information on the commercial provider.

5.1.2 Sample Characterization

X-Ray Absorption Spectroscopy

Transmission X-ray absorption spectroscopy (XAS) was performed at the V K edge (5.465 keV) and the Mo K edge (19.999 keV) at beamline C, and X1, respectively, at the Hamburg Synchrotron Radiation Laboratory, HASYLAB, using a Si(111) (V K edge) or Si(311) (Mo K edge) double crystal monochromator. For *ex situ* measurements samples were diluted with wax (Hoechst wax C micropowder, Merck) or polyethylene (PE, Induchem Switzerland) and pressed into self-supporting pellets with a diameter of 13 mm. Sample masses were calculated to result in an edge jump around $\Delta\mu(d) = 1.0$. Spectra of the X-ray absorption fine structure (XAFS) at the V K edge (5.4–6.3 keV) were measured in approximately 21 min. At the Mo K edge the energy range for a XAFS scan was 19.9–21.0 keV (~12 min).

XAFS analysis was performed using the software package WinXAS v3.2.[113] For analysis of the EXAFS, background subtraction and normalization were carried out by fitting a linear polynomial and a third degree polynomial to the pre-edge, and the post-edge region of an absorption spectrum, respectively. The EXAFS, $\chi(k)$, was extracted by using cubic splines to obtain a smooth atomic background, $\mu_0(k)$. The $\text{FT}(\chi(k)\cdot k^3)$ was calculated according to eq. (3-3) by Fourier transformation of the k^3 -weighted experimental $\chi(k)$ function, multiplied by a Bessel window, into the R space. For analysis of the XANES, background subtraction

and normalization were carried out by fitting linear polynomials to the pre-edge and the post-edge region of an absorption spectrum in the energy range of 5.4–5.7 keV (V K edge) or 19.95–20.10 keV (Mo K edge).

Diffuse Reflectance UV-Vis Spectroscopy

DR-UV-Vis measurements were conducted on a two-beam spectrometer (V670, JASCO) using an integration sphere coated with barium sulfate or a Praying Mantis™ cell (Harrick Scientific Products, Inc.) for *in situ* measurements. Powder samples were measured in the spectral region of 200–2000 nm with the integration sphere and a region of 220–890 nm with the Praying Mantis™ cell. Pure support material or commercial magnesium oxide (ABCR, 99.95%) was used as reflectance standard for baseline correction. Samples were measured as is or diluted with the reflectance standard. Reference materials were diluted with commercial magnesium oxide. For comparison vanadium oxides supported on pure SBA-15 (V/SBA-15) were measured as well. Dehydration of V/SBA-15 was carried out in the *in situ* cell in 20% oxygen in helium (Air Liquide, 20% O₂ (4.8) in He (5.0), total flow 50 ml/min) in a temperature range from 20 °C to 280 °C using a heating rate of 4 K/min.

The DR-UV-Vis spectra were transferred into the Kubelka-Munk function, $F(R_\infty)$ (eq. (3-4)). For determination of the edge energy data were plotted $(F(R_\infty) \cdot h\nu)^2$ against $h\nu$ according to Gao *et al.*[114] The edge energy, E_g , was determined from the intercept of a straight line fitted to the low-energy rise. The intercept of the linear function with the abscissa was taken as edge energy, E_g . An example of the fitting procedure is given in the Appendix (Fig. A 2.1). The uncertainty of this approach was estimated to be approximately 3%.

Nitrogen Physisorption

Nitrogen adsorption/desorption isotherms were measured at -196 °C using a BELSORP-Mini II (BEL Inc. Japan). Prior to measurement samples were degassed under reduced pressure ($\sim 10^{-2}$ kPa) at 110 °C for 30 min and kept under the same pressure overnight at 200 °C. Data analysis was performed as described above (refer to Chap. 4.1.2).

Powder X-Ray Diffraction

Powder X-ray diffraction patterns were collected with a diffractometer (X'Pert PRO MPD, PANalytical) in theta/theta geometry. Cu K alpha radiation (40 kV/40 mA) and a solid state multi-channel (PIXcel[®]) detector were used. Low-angle and wide-angle diffraction patterns were measured in the transmission, and reflection mode, respectively. Details on measurement parameters and data analysis are described above (refer to Chap. 4.1.2).

Thermal Analysis

Thermogravimetry (TG) and differential thermal analysis (DTA) were conducted with a thermobalance (SSC 5200, Seiko Instruments). The oven was purged with a predefined reaction gas mixture consisting of 20% oxygen (Air Liquide, 4.5) and 80% helium (Air Liquide, 5.0). The total flow was kept low to avoid mass transport of the light mesoporous particles. It was adjusted to 50 ml/min. Sample and reference underwent a temperature programmed heat treatment between 30 °C and 450 °C. The heating rate was varied between 2 K/min and 10 K/min. Beforehand, samples were kept under O₂/He atmosphere to dry for 1 h.

The apparent activation energy of water desorption, E_D , was determined by a Kissinger plot.[115] Therefore, the quantity of $\ln(\beta/T_{max}^2)$ was plotted against $1/T$, with the heating rate, β , and the temperature, T_{max} , of the maximum in the DTA signal. The maximum of the DTA curve was determined from a smoothed signal. The apparent activation energy, E_D , was calculated from the slope of the linearized plot according to the equation

$$\ln\left(\frac{\beta}{T_{max}^2}\right) = \frac{E_D}{RT} + \ln\left(\frac{E_D}{AR}\right) \quad (5-1)$$

where R is the ideal gas constant and A is a pre-exponential factor.

Raman Spectroscopy

Raman spectra were recorded on a FT-RAMAN spectrometer (RFS 100, Bruker). A Nd:YAG laser with a wavelength of 1064 nm was used for excitation. Samples were measured in a glass sample holder with a resolution of 1 cm⁻¹. The laser power at the sample position was

adjusted to 150 mW. All samples were measured three times, whereas every measurement consisted of 500 scans. Scans were averaged for improvement of the signal-to-noise ratio.

X-Ray Fluorescence Analysis

Elemental analysis was performed to quantify vanadium and molybdenum oxide loadings. X-ray fluorescence spectroscopy was conducted on an X-ray spectrometer (AXIOS, 2.4 kW model, PANalytical) equipped with a Rh X-ray tube, a gas flow detector, and a scintillation detector. Sample preparation and data analysis was performed as described above (refer to Chap. 4.1.2).

5.2 Supported Vanadium Oxides

5.2.1 Vanadium Oxide Catalyst Dispersion and Surface Properties

After deposition of the vanadium oxides the support material exhibited a hexagonal ordering similar to the initial *MgO/SBA-15*. However, the corresponding low-angle X-ray diffraction (XRD) peaks, shown in Fig. 5.2, were broadened and of lower intensity than those of the pure support. The deposition of vanadium oxide on the support not only led to a decreased intensity but also to a shift of the $(10l)$ peak to higher 2θ -values. This indicated shrinkage of the unit cell.

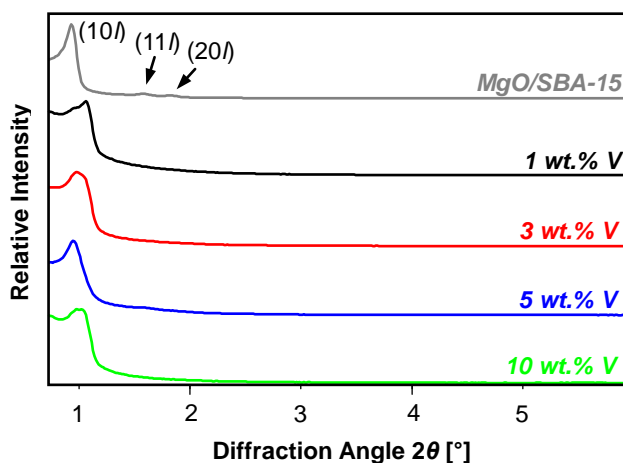


Fig. 5.2 Low-angle X-ray diffraction (XRD) patterns of bare *MgO/SBA-15* and the supported vanadium oxides at various vanadium loadings. $(10l)$, $(11l)$, and $(20l)$ diffraction peaks are indicated.

Surface area and mesopore size of the supported oxides was characterized by N₂ physisorption. The specific surface area systematically decreased with increasing vanadium loading. Specific surface area of the samples, a_{BET} , and relative decrease in surface area with respect to the originating support material are summarized in Table 5.1 together with pore diameter, d_{pore} , d_{10l} -values, unit cell constant, a_0 , and wall thickness, t_{wall} , between the mesopores. In conjunction with the decreasing surface area a shrinking mesopore size and volume was observed.

Table 5.1 Textural properties of MgO/SBA-15 and vanadium oxides supported on MgO/SBA-15 at various catalyst loadings: specific surface area, a_{BET} (calculated by BET method), average pore diameter, d_{pore} , and pore volume, V_{pore} (calculated by NLDFT method), d_{10l} -values (derived from low-angle XRD), unit cell constant, a_0 (corresponding to the hexagonal pore arrangement), and wall thickness, t_{wall} , between the mesopores ($t_{wall} = a_0 - d_{pore}$).

| | a_{BET}^a [m ² /g] | d_{pore} [nm] | V_{pore} [ml/g] | d_{10l} [nm] | a_0 [nm] | t_{wall} [nm] |
|---------------------|------------------------------------|--------------------|----------------------|-------------------|---------------|--------------------|
| MgO/SBA-15 | 535 | 7.9 | 0.67 | 9.9 | 11.4 | 3.5 |
| V/MgO/SBA-15 | | | | | | |
| 1 wt.% V | 330 (-11%) | 5.3 | 0.35 | 8.7 | 10.0 | 4.7 |
| 3 wt.% V | 321 (-29%) | 5.9 | 0.32 | 9.2 | 10.7 | 4.8 |
| 5 wt.% V | 316 (-41%) | 7.3 | 0.41 | 9.8 | 11.3 | 4.0 |
| 10 wt.% V | 201 (-46%) | 5.7 | 0.19 | 9.2 | 10.6 | 4.9 |

^a Relative decrease in surface area with respect to the originating support material is given in parantheses.

Fig. 5.3 depicts the wide-angle XRD patterns of the supported vanadium oxides. Weakly pronounced peaks detected for 5 wt.% V were attributed to Mg₂V₂O₇. Only at the highest loading (10 wt.% V) small diffraction peaks of V₂O₅ were observed. This indicated the partial formation of crystalline vanadium oxide phases on the support. Compared to a physical mixture of V₂O₅ (5 wt.% V) and MgO/SBA-15 the V₂O₅ diffraction peaks in the pattern of the supported vanadium oxide (10 wt.% V) were very weak, indicating only a small fraction of crystalline V₂O₅.

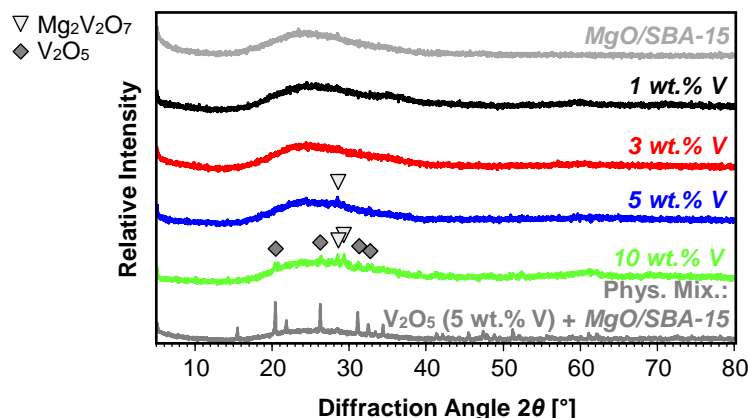


Fig. 5.3 Wide-angle X-ray diffraction patterns of bare *MgO/SBA-15* and supported vanadium oxides at various catalyst loadings. Diffraction peaks in the patterns of *V/MgO/SBA-15* with 5 wt.% and 10 wt.% V were identified as crystalline $\text{Mg}_2\text{V}_2\text{O}_7$, and V_2O_5 phases, respectively. For comparison the diffraction pattern of a physical mixture of crystalline V_2O_5 (5 wt.% V) and *MgO/SBA-15* is shown.

Vanadium oxide surface coverage, summarized in Table 5.2, varied depending on catalyst loading between 0.4 and 5.9 V atoms per nm^2 . These values were still considered to be below monolayer coverage on the basis of the theoretical space requirement of a “ $\text{VO}_{2.5}$ ” unit in bulk V_2O_5 as proposed by Roozeboom *et al.* Accordingly, monolayer coverage would be achieved at ten vanadium atoms per nm^2 . [116] However, the maximum coverage (*i.e.*, prior to formation of V_xO_y nanocrystallites) is known to be dependent on the characteristics of the oxide support. Wachs *et al.* summarized investigations on various support materials and concluded a maximum coverage of approximately 7–8 V atoms per nm^2 [36], which is still above surface coverage of the *V/MgO/SBA-15* sample with a weight loading of 10 wt.% V. In contrast, silica as support material exhibited a different behavior. Due to the requirement of available hydroxyl groups on the surface, the maximum coverage is limited to 2–3 V atoms per nm^2 . According to the authors, supported vanadium oxide species would preferentially bind to other oxide surfaces than silica, if available. [36] Thus, on the MgO-coated SBA-15 the MgO surface can be considered as preferential anchoring site for the supported vanadium oxides.

Table 5.2 Surface coverage, $\Phi_{V\ atoms}$ (V atoms per nm^2), UV-Vis edge energy, E_g , and approximated No. of V–O–V bonds for vanadium oxides supported on *MgO/SBA-15* at various catalyst loadings and for vanadium oxides supported on bare SBA-15 (4.1 wt.% V).

| V loading | $\Phi_{V\ atoms}$ [V atoms/ nm^2] | Edge Energy, E_g [eV] | No. (V-O-V) |
|-----------------------|--|----------------------------|-------------|
| 1 wt.% | 0.4 | 4.12 | 0 |
| 3 wt.% | 1.1 | 3.96 | 0.25 |
| 5 wt.% | 1.9 | 3.66 | 0.99 |
| 10 wt.% | 5.9 | 3.45 | 1.56 |
| V/SBA-15 (4.1 wt.% V) | 1.1 | 3.42 | 1.59 |

5.2.2 Diffuse Reflectance UV-Vis and Raman Spectroscopy

Supported vanadium oxides exhibit UV-Vis absorption bands that can be used to investigate the chemical environment of the vanadium centers. The strong absorption results from charge transfer (CT) transitions between the oxygen ligands (O^{2-}) and the central vanadium (V^{5+}) atom. Fig. 5.4 shows the DR-UV-Vis spectra of supported vanadium oxides at various vanadium loadings before and after calcination at elevated temperatures.

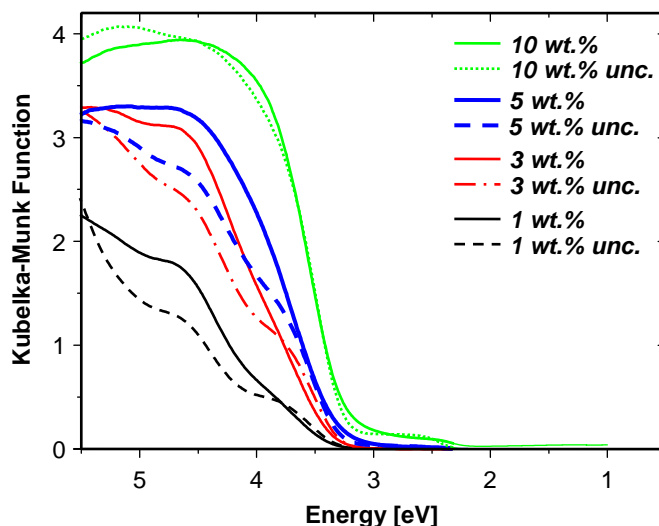


Fig. 5.4 DR-UV-Vis spectra of supported vanadium oxides at loadings of 1, 3, 5, and 10 wt.% V before and after calcination in air at 450 °C. Spectra were recorded at room temperature under ambient conditions with an integration sphere.

Only one broad band is visible as a result of overlapping absorption features. The spectrum of $V/MgO/SBA-15$ with a loading of 10 wt.% V exhibited an additional shoulder in the range of 2–3 eV, which is indicative of V_2O_5 . This corroborated the presence of V_2O_5 nanocrystallites as already assumed from the peaks in the X-ray diffraction pattern (compare Fig. 5.3). The overall shape of the spectra of the uncalcined and calcined state shown in Fig. 5.4 was very similar. This indicated a similar structure of the supported oxides before and after calcination.

To differentiate between overlapping bands, the spectra of the calcined and uncalcined oxide catalysts were fitted with Pseudo-Voigt functions in the wavelength range between 220 nm and 450 nm. For all spectra three Pseudo-Voigt functions were necessary to describe the absorption band. The fitted curves together with the spectra of the samples are shown in Fig. 5.5. Positions and full width at half maximum (FWHM) of the fitted Pseudo-Voigt functions are listed in Table 5.3. Fit results for the spectra of the uncalcined vanadium oxides are given in the Appendix (Table A 3.1).

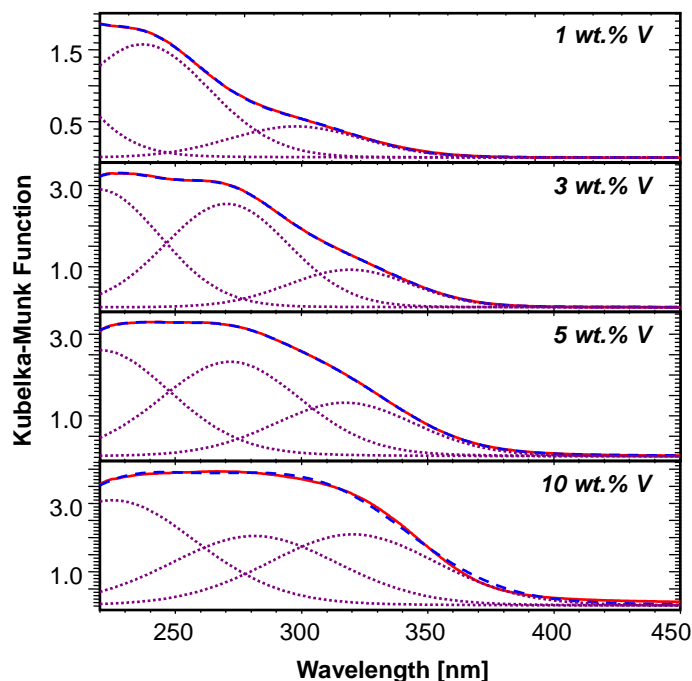


Fig. 5.5 Refinement of sum (dashed) of three fitted Pseudo-Voigt functions (dotted) to the DR-UV-Vis spectra (solid line) of the supported oxides at various vanadium loadings. Resulting fit parameters are given in Table 5.3.

With increasing vanadium loading the absorption bands shifted to higher wavelengths. Avdeev *et al.* calculated the absorption spectrum of a VO_4^{3-} ion stabilized on a silica surface with an ideally tetrahedral geometry of the oxygen atoms around the vanadium center. They determined a band at 212 nm and two strongly overlapping bands at 244 nm and 257 nm.[117] The calculation corresponded well to the first two fitted absorption bands at 211 nm and 266 nm in the spectrum of 1 wt.% $\text{V}/\text{MgO}/\text{SBA-15}$. However, the shift of the bands at higher catalyst loadings possibly indicated a distortion of the tetrahedral geometry. This might be caused by formation of oligomerized $[\text{VO}_4]$ units. Furthermore, an additional third absorption band had to be fitted to the spectra. Thus, a higher coordinated vanadium atom with more than four oxygen ligands might be present. According to Morey *et al.* a band around 330 nm is indicative of a pseudo-tetrahedral geometry with an additional coordination of a water molecule to the vanadium center.[118] Hence, the coordination of a water or hydroxyl group, which is bound to the support material, seemed reasonable. This can be explained by the tendency of isolated vanadium(V) species to extend their coordination sphere. According to the literature this can occur either by oligomerization of the vanadium oxide units or by adding water and hydroxyl ligands.[118,119]

Table 5.3 Position and full width at half maximum (FWHM) of the fitted UV-Vis absorption bands shown in Fig. 5.5.

| | 1 wt.% V | | | 3 wt.% V | | | 5 wt.% V | | | 10 wt.% V | | |
|----------------------|----------|-----|-----|----------|-----|-----|----------|-----|-----|-----------|-----|-----|
| Position [nm] | 211 | 266 | 318 | 219 | 270 | 319 | 221 | 272 | 318 | 225 | 281 | 320 |
| FWHM [nm] | 53 | | | 58 | | | 66 | | | 79 | | |
| Residual | 1.1 | | | 0.4 | | | 0.3 | | | 2.3 | | |

The overall band position of the CT transitions is commonly used to estimate the degree of oligomerization of the vanadium oxide units.[62,114] Hence, the shift of the band position to higher wavelength (lower energy) indicated a higher number of V–O–V bonds ($No.(V-O-V)$). The edge energies of several measured reference compounds followed an inverse proportional relationship. The correlation between edge energy, E_g , and $No.(V-O-V)$ is illustrated in Fig. 5.6 and can be expressed by

$$No.(V-O-V) = 13.26(\pm 1.02) - 3.61(\pm 0.32) \text{ eV}^{-1} \cdot E_g. \quad (5-2)$$

face coverage and vanadium loading the sample color changed from colorless at 1 wt.% V to dark brownish yellow at 10 wt.% V (compare Fig. 5.1).

Raman spectra of $V/MgO/SBA-15$ in the uncalcined and calcined state are shown in Fig. 5.7. At loadings below 5 wt.% V only weakly pronounced bands, that could hardly be assigned to any vanadium oxide species, were observed. The spectrum of the $MgO/SBA-15$ support itself was featureless. The peaks at 145, 286, 700, and 995 cm^{-1} observed for the calcined state at higher loadings (≥ 5 wt.% V) could be attributed to V_2O_5 .^[48,120] For comparison, the spectrum of a physical mixture of 3 wt.% V_2O_5 and SBA-15 is shown in Fig. 5.7 (right). The remaining signals in the spectra of 5 wt.% and 10 wt.% $V/MgO/SBA-15$ at 175 cm^{-1} and 923 cm^{-1} could not be assigned to any reference vanadates, such as *ortho*- $Mg_2V_2O_8$, *pyro*- $Mg_2V_2O_7$, or *meta*- MgV_2O_6 . However, Went *et al.* suggested that broad features in the region of 920–945 cm^{-1} were due to polyvanadate groups bound to the support.^[121] In the spectrum of the uncalcined samples (Fig. 5.7, left) weak bands at 182, 252, 320, 959, and 998 cm^{-1} were observed at a loading of 10 wt.% V. These bands were characteristic for ammonium decavanadate ($(NH_4)_6V_{10}O_{28}$), which was used as vanadium oxide precursor during incipient wetness.

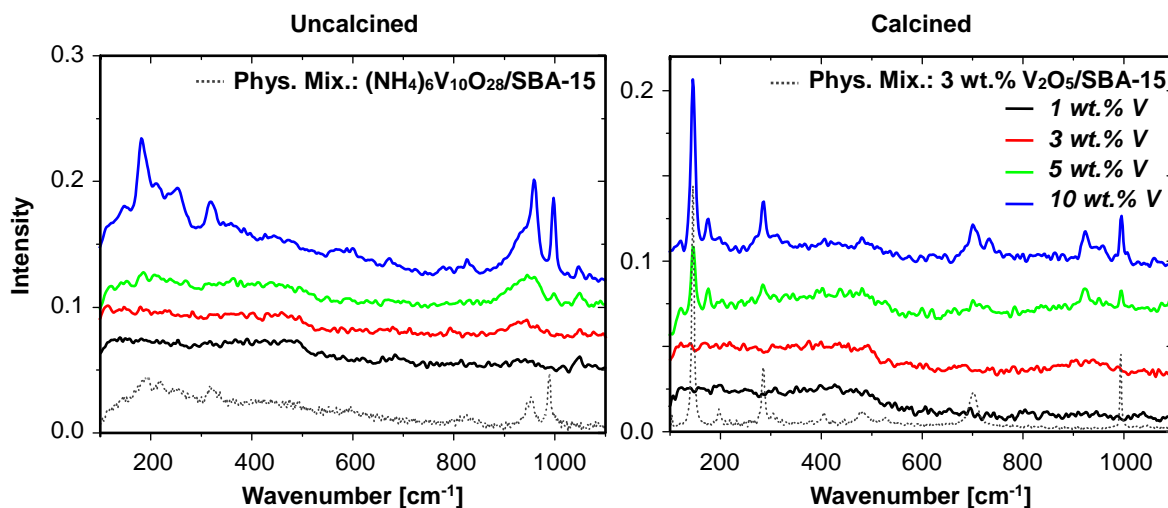


Fig. 5.7 Raman spectra of uncalcined (left) and calcined (right) $V/MgO/SBA-15$ with various catalyst loadings. For comparison the spectra of a physical mixture of ammonium decavanadate ($(NH_4)_6V_{10}O_{28}$), and vanadium pentoxide (V_2O_5), respectively, with SBA-15 are shown as well. Spectra were offset for clarity.

5.2.3 X-Ray Absorption Near Edge Structure

All supported vanadium oxides exhibited a similar X-ray absorption near edge structure (XANES, Fig. 5.8). Apparently, the local structure around the vanadium atoms corresponded to a structure similar to that of the tetrahedrally coordinated reference vanadate $\text{Ca}_3\text{V}_2\text{O}_8$ (also shown in Fig. 5.8). The tetrahedral coordination was corroborated by the distinct XANES pre-edge peak. The pre-edge peak height decreased with increasing catalyst loading, indicating a distorted tetrahedral geometry around the vanadium center. Wong *et al.* investigated the dependency of the pre-edge peak height on the “size of the molecular cage”. They correlated the average bond length with the intensity of the pre-edge peak. The smaller the “cage size” the higher was the pre-edge peak intensity.[65] In oligomerized vanadates the average bond length progressively increases with increasing degree of oligomerization. Therefore, it seemed reasonable, that the “cage size” of the supported vanadium oxide tetrahedra increased with increasing surface coverage. Consequently, a decreasing pre-edge peak was observed. These results nicely confirmed the findings from UV-Vis data analysis discussed above (Chap. 5.2.2), where an increasing degree of oligomerization was observed with increasing surface coverage.

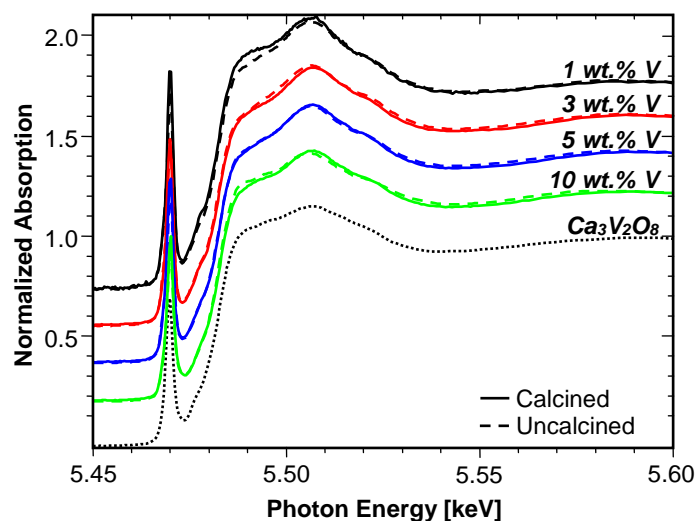


Fig. 5.8 Normalized V K edge XANES spectra of uncalcined (dashed) and calcined (solid line) supported vanadium oxide catalysts together with the spectrum of a calcium orthovanadate reference ($\text{Ca}_3\text{V}_2\text{O}_8$).

5.2.4 X-Ray Absorption Fine Structure

The extended X-ray absorption fine structure (EXAFS) of the supported vanadium oxides closely resembled that of crystalline calcium orthovanadate ($\text{Ca}_3\text{V}_2\text{O}_8$). The structure of $\text{Ca}_3\text{V}_2\text{O}_8$ is built of isolated $[\text{VO}_4]$ units with a tetrahedral coordination of oxygen atoms around the vanadium center. The pseudo-radial distribution function, $\text{FT}(\chi(k)\cdot k^3)$, of $\text{Ca}_3\text{V}_2\text{O}_8$ exhibited one prominent peak at a distance in the range from 1–2 Å. Fig. 5.9 depicts the X-ray absorption fine structure (XAFS), $\chi(k)\cdot k^3$, of the supported vanadium oxides and the orthovanadate reference together with the Fourier transformed XAFS, $\text{FT}(\chi(k)\cdot k^3)$.

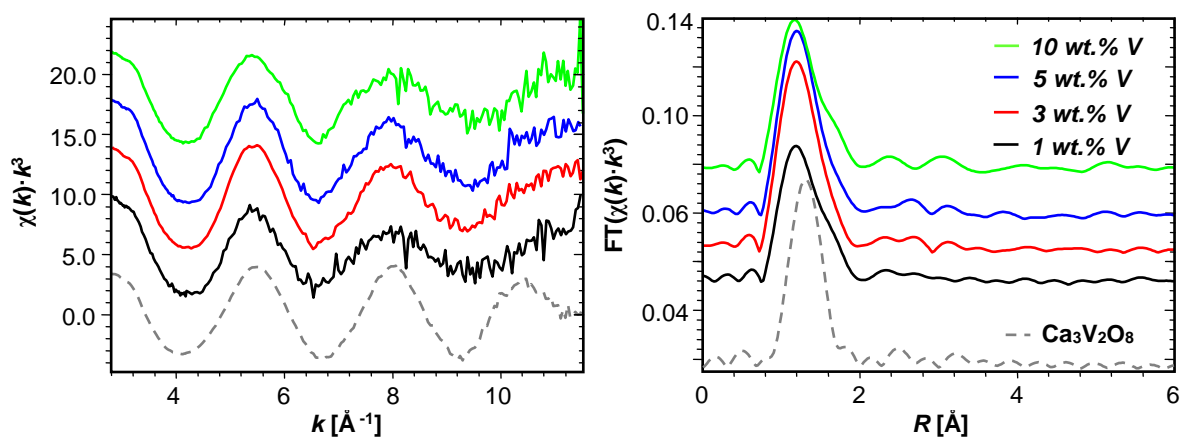


Fig. 5.9 V K edge XAFS, $\chi(k)\cdot k^3$ (left), and pseudo-radial distribution function, $\text{FT}(\chi(k)\cdot k^3)$ (right, not phase-shift corrected), of vanadium oxide catalysts supported on *MgO/SBA-15* at various catalyst loadings compared to the data of a calcium orthovanadate reference ($\text{Ca}_3\text{V}_2\text{O}_8$).

Apparently, data quality permitted reliable data analysis up to 11.5 \AA^{-1} . The distinct peak in the $\text{FT}(\chi(k)\cdot k^3)$ was in good agreement with peak position and amplitude in the reference spectrum of $\text{Ca}_3\text{V}_2\text{O}_8$. To further elucidate the local structure around the vanadium centers a structure refinement was performed. From UV-Vis and XANES data a local structure of distorted, partially connected $[\text{VO}_4]$ tetrahedra was assumed. Hence, a theoretical XAFS function calculated for a magnesium pyrovanadate ($\alpha\text{-Mg}_2\text{V}_2\text{O}_7$) model structure, consisting of $[\text{V}_2\text{O}_7]$ units, was refined to the $\text{FT}(\chi(k)\cdot k^3)$ of the samples. A good agreement between theoretical and experimental $\text{FT}(\chi(k)\cdot k^3)$ of the supported vanadium oxides was achieved.

Fig. 5.10 depicts the resulting theoretical and experimental $FT(\chi(k) \cdot k^3)$. Significance of the fitted parameters was determined by calculating confidence limits and statistical F parameters. The number of free running parameters in the fitting procedure was kept far below the number of independent parameters according to the Nyquist theorem. In order to achieve reasonable fit results, the smallest sets of required distances were used in each fit. Corresponding fitting parameters are given in Table 5.4.

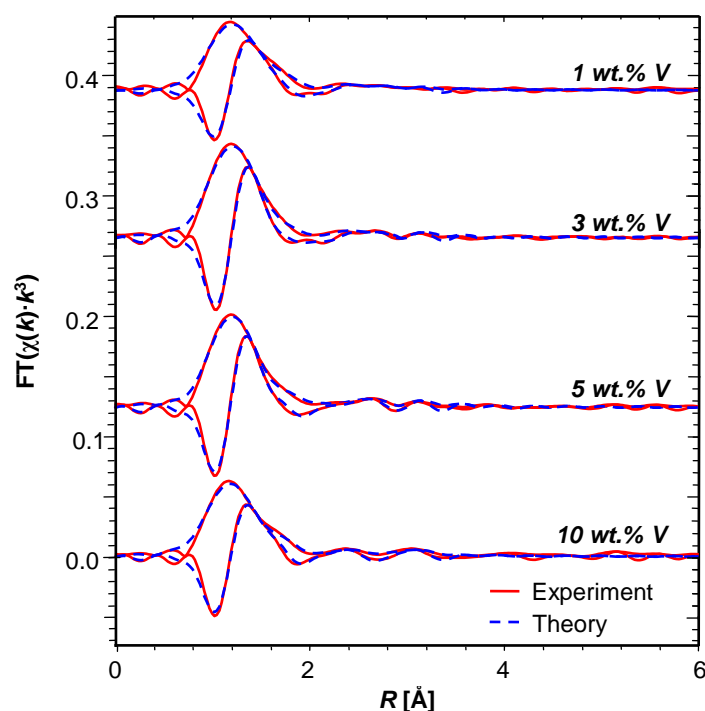


Fig. 5.10 Experimental (red) V K edge $FT(\chi(k) \cdot k^3)$ of vanadium oxide catalysts supported on *MgO/SBA-15* together with a theoretical XAFS function (blue). Corresponding fitting results are given in Table 5.4.

Two short and two long V-O distances were used to refine the tetrahedral units. These results are in agreement with the crystallographic data of vanadium metavanadates (KVO_3 , NH_4VO_3), where a chainlike structure of adjacent $[VO_4]$ tetrahedra is present. Evans *et al.* determined two long V-O distances, which link the tetrahedra together, and two equally short V-O distances around 1.66 Å for the non-bridging oxygen atoms.[122] The short distance was identified by several authors as V=O vanadyl bond, whereas distances above 1.8 Å are indicative of V-O-support bonds or bridging V-O-V bonds between $[VO_4]$ tetrahedrons.[55,65] The presence of two equally short V-O bonds in *V/MgO/SBA-15* can be at-

tributed to a partial hybrid formation with the empty $3d$ orbitals of the vanadium.[123] Participation of the $3d$ orbitals in formation of π bonds, which causes a shortening in the V–O bond, has been reported in the literature.[65,122]

Table 5.4 Number, N , of atoms at a distance, R , from the absorbing vanadium atom in the local structure of the oxides supported on MgO/SBA-15 at various catalyst loadings. Experimental distances and XAFS disorder parameters, σ^2 , were obtained from the refinement of a α -Mg₂V₂O₇ model structure to the experimental V K edge XAFS FT($\chi(k) \cdot k^3$) of the samples (Fig. 5.10) (k range from 2.8–11.5 Å⁻¹, R range 0.7–3.8 Å, $N_{ind} = 19$, $N_{free} = 8$ –10).

| Type | N | 1 wt.% V | | 3 wt.% V | | 5 wt.% V | | 10 wt.% V | |
|-----------------|----------------|----------|------------------------------|-------------------|------------------------------|-------------------|------------------------------|-------------------|------------------------------|
| | | R [Å] | σ^2 [Å ²] | R [Å] | σ^2 [Å ²] | R [Å] | σ^2 [Å ²] | R [Å] | σ^2 [Å ²] |
| V–O | 2 _f | 1.68 | 0.0033 _c | 1.67 | 0.0007 _c | 1.67 | 0.0005 _c | 1.66 | 0.0018 _c |
| V–O | 1 _f | 1.81 | 0.0033 _c | 1.78 | 0.0007 _c | 1.80 | 0.0005 _c | 1.80 | 0.0018 _c |
| V–O | 1 _f | 1.88 | 0.0033 _c | 1.86 | 0.0007 _c | 1.88 | 0.0005 _c | 1.87 | 0.0018 _c |
| V–O | 1 _f | 2.75 | 0.0076 _f | 2.76 | 0.0051 _f | 2.73 | 0.0075 _f | 2.71 | 0.0076 _f |
| V–V | 1 _f | - | - | - | - | - | - | 3.45 _c | 0.0252 _c |
| V–V | 1 _f | - | - | 3.15 | 0.0112 | 3.32 | 0.0028 | 3.45 _c | 0.0252 _c |
| V–Mg | 1 _f | 3.25 | 0.0056 _c | 3.21 _c | 0.0045 _c | 3.36 _c | 0.0083 _c | 3.47 _c | 0.0103 _c |
| V–Mg | 1 _f | 3.46 | 0.0056 _c | 3.21 _c | 0.0045 _c | 3.36 _c | 0.0083 _c | 3.47 _c | 0.0103 _c |
| V–Mg | 1 _f | - | - | 3.43 | 0.0045 _c | 3.36 _c | 0.0083 _c | - | - |
| Residual | | 9.3 | | 9.0 | | 7.2 | | 8.7 | |

Note: Subscript c indicates parameters that were correlated, subscript f parameters that were fixed in the refinement.

Interaction of the vanadium oxides with the support was confirmed by V–Mg distances between 3.2 Å and 3.5 Å. With increasing vanadium loading an increasing influence of V–V distances was observed within the refinement. At loadings ≥ 3 wt.% V an additional V–V distance was necessary to fully account for the amplitude in the FT($\chi(k) \cdot k^3$) at higher distances. At a loading of 10 wt.% V, two V–V distances were required to achieve good fit results. The increasing influence of linking V–V distances was in good agreement with the UV-Vis data (Fig. 5.6). This confirmed an increasing degree of oligomerization with increased vanadium loading. Interestingly, no change in V–O distances was observed with increasing

oligomerization. The formation of adjacent VO_x units is usually accompanied by a distortion of the tetrahedral structure [124,125] and a lengthened V–O–V bond. In the case of vanadium oxides supported on *MgO/SBA-15* no distortion of the tetrahedra was observed. This was attributed to a stronger vanadium oxide-support interaction compared to the interaction between the vanadium oxide tetrahedra. In addition to the four V–O distances attributed to the $[\text{VO}_4]$ tetrahedra, the coordination of a fifth oxo-ligand as predicted from UV-Vis absorption bands was confirmed by a weak amplitude at 2.7–2.8 Å. This could only be accounted for by considering an additional V–O distance in the refinement. The results corroborated the coordination of a hydroxyl group, which is anchored to the support, to the vanadium center.

5.3 Supported Molybdenum Oxides

5.3.1 Molybdenum Oxide Catalyst Dispersion and Surface Properties

The supported molybdenum oxides were prepared with a surface coverage that was kept below monolayer coverage in the range of 0.2 to 4.2 molybdenum atoms per nm^2 . Theoretical monolayer coverage based on the space requirement of a " MoO_3 " unit as proposed by van Hengstum *et al.* would be achieved at seven molybdenum atoms per nm^2 . [126] Wide-angle X-ray diffraction (XRD) patterns of molybdenum oxide supported on *MgO/SBA-15* showed no peaks of crystalline molybdenum oxide phases, like MoO_3 or MgMoO_4 (Appendix, Fig. A 4.1). This may indicate that the molybdenum oxide species were highly dispersed on the support.

After deposition of the molybdenum oxides the hexagonal ordering of the support material remained. Fig. 5.11 depicts the corresponding low-angle XRD patterns. Compared to the diffraction peaks of the bare support, those of *Mo/MgO/SBA-15* exhibited a decreased intensity together with a shift of the $(10l)$ peak to higher 2θ -values. Hence, shrinkage of the unit cell was observed. Surface area and mesopore size of the supported oxides, characterized by N_2 physisorption, systematically decreased with increasing molybdenum loading. Table 5.5 summarizes specific surface area, a_{BET} , and relative decrease in surface area with respect to the original support material together with surface coverage, $\Phi_{\text{Mo atoms}}$, pore diameter, d_{pore} ,

unit cell constant, a_0 , and wall thickness, t_{wall} , between the mesopores. Consistent with the shrinking surface area at higher catalyst loading pore diameters decreased while wall thicknesses increased.

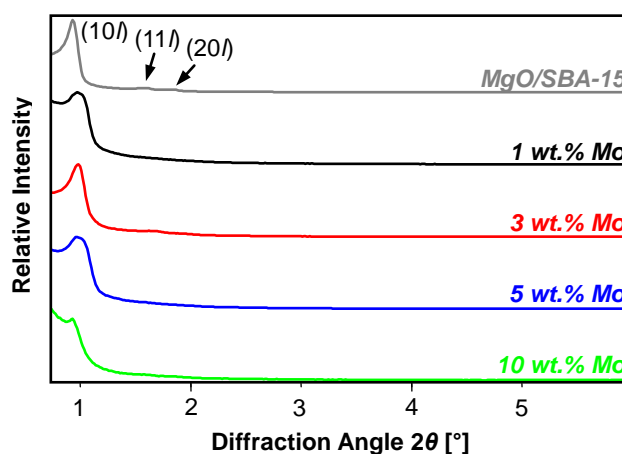


Fig. 5.11 Low-angle X-ray diffraction patterns of bare *MgO/SBA-15* and the supported molybdenum oxides at various catalyst loadings. (10*l*), (11*l*), and (20*l*) peaks are indicated.

Table 5.5 Textural properties of molybdenum oxides on *MgO/SBA-15* and of bare *MgO/SBA-15*: specific surface area, a_{BET} (calculated by BET method), molybdenum oxide surface coverage, $\Phi_{Mo\ atoms}$, average pore diameter, d_{pore} (calculated by NLDFT method), unit cell constant, a_0 (corresponding to the hexagonal pore arrangement), and wall thickness, t_{wall} , between the mesopores ($t_{wall} = a_0 - d_{pore}$).

| | a_{BET}^a [m ² /g] | $\Phi_{Mo\ atoms}$ [Mo atoms/nm ²] | d_{pore} [nm] | a_0 [nm] | t_{wall} [nm] |
|----------------------|------------------------------------|---|--------------------|---------------|--------------------|
| <i>MgO/SBA-15</i> | 394 | - | 7.6 | 11.8 | 3.5 |
| <i>Mo/MgO/SBA-15</i> | | | | | |
| 1 wt.% Mo | 311 (-20%) | 0.2 | 7.0 | 10.8 | 3.8 |
| 3 wt.% Mo | 306 (-22%) | 0.6 | 6.8 | 10.9 | 4.1 |
| 5 wt.% Mo | 242 (-39%) | 1.3 | 7.3 | 11.6 | 4.3 |
| 10 wt.% Mo | 149 (-62%) | 4.2 | 6.6 | 11.5 | 4.9 |

^a Relative decrease in surface area with respect to the originating support material is given in parantheses.

5.3.2 Diffuse Reflectance UV-Vis and Raman Spectroscopy

UV-Vis spectra of *Mo/MgO/SBA-15* exhibited a similar shape independent of molybdenum loading. Fig. 5.12 depicts the DR-UV-Vis spectra of supported molybdenum oxides compared to the spectra of reference compounds. The supported molybdenum oxides exhibited only one broad band in the UV-range, comparable to spectra of the molybdenum oxide references, such as $\text{Na}_2\text{MoO}_4 \cdot 2\text{H}_2\text{O}$ with isolated $[\text{MoO}_4]$ units.

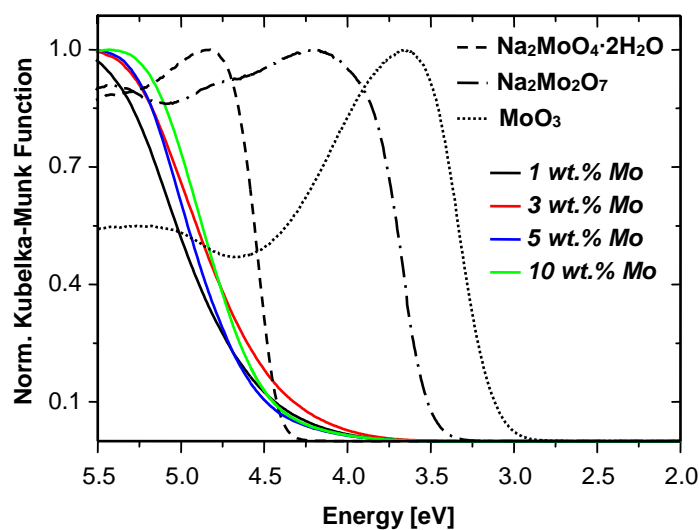


Fig. 5.12 Normalized DR-UV-Vis spectra of supported molybdenum oxides together with those of various molybdenum oxide references.

Average number of covalent Mo–O–Mo bonds of the dispersed molybdenum oxide particles was investigated by analyzing the optical band gap energy, which was determined from the position of the low-energy rise in UV-Vis spectra. According to Weber an inverse proportional correlation between edge energy and number of nearest neighbors is given.[37] Therefore, isolated molybdenum centers, as in Li_2MoO_4 , $\text{Na}_2\text{MoO}_4 \cdot 2\text{H}_2\text{O}$ or MgMoO_4 , exhibit high edge energies, whereas lower edge energies indicate adjacent molybdenum centers as in MoO_3 . The correlation between edge energy, E_g , and number of covalent Mo–O–Mo bonds ($No.(Mo-O-Mo)$) is illustrated in Fig. 5.13 and can be described by

$$No.(Mo-O-Mo) = 18.05(\pm 0.77) - 4.11(\pm 0.20) \text{ eV}^{-1} \cdot E_g. \quad (5-3)$$

Edge energies of the uncalcined supported molybdenum oxides on *MgO/SBA-15* amounted to approximately 4.9 eV, which was high compared to the edge energy of reference compounds (see Fig. 5.13). Calcination of the samples led to a minor shift of the edge energy to 4.8 eV. Huang *et al.* investigated molybdenum oxides supported on SBA-15.[41] In contrast to MgO-coated SBA-15, pure silica apparently led to higher associated molybdenum oxide units. The edge energy of the molybdenum oxides supported on SBA-15 was about 3.9 eV, which is typical for higher connected metal centers. Edge energies of the oxides supported on *MgO/SBA-15* were independent of catalyst loading. A list of the edge energies of *Mo/MgO/SBA-15* at various molybdenum loadings and of the reference molybdenum oxides is given in the Appendix (Table A 4.1 and Table A 4.2). However, a clear distinction, especially between dimeric and isolated molybdenum oxide units, is not possible on the basis of UV-Vis absorption data. This is due to a significant overlap of UV-Vis band positions, and thus, edge energy region as it has previously been discussed in the literature.[77,127,128] To further elucidate the local structure of the supported molybdenum oxides, other investigation techniques, like X-ray absorption spectroscopy, had to be used.

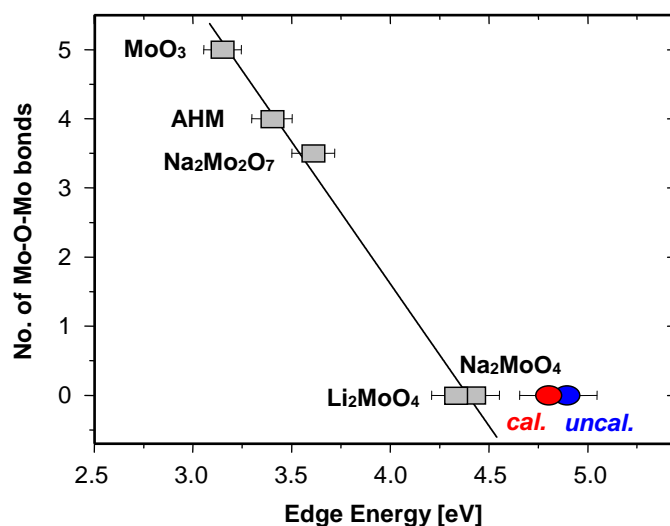


Fig. 5.13 Number of covalent Mo–O–Mo bonds as a function of edge energy. Shown are the edge energies of supported molybdenum oxides in the calcined (red) and uncalcined state (blue) in comparison to those of measured molybdenum oxide references (AHM: ammonium heptamolybdate).

Raman spectra of *Mo/MgO/SBA-15* (Appendix, Fig. A 4.2) before calcination and in the calcined state were very similar. At low loadings (1–3 wt.% Mo) the spectra were featureless.

At higher loadings (5–10 wt.% Mo) the spectra exhibited only broad bands of weak intensity in the region of 290–360 cm^{-1} and 880–955 cm^{-1} . The observed bands could not be assigned to any molybdate reference. However, Tian *et al.* related Raman bands in the region of 820–920 cm^{-1} to the asymmetric stretching of various $[\text{MoO}_4]$ units. Additionally, they assigned a broad band around 531 cm^{-1} to the corresponding $[\text{MoO}_4]$ bending modes.[129] The spectrum of molybdenum trioxide (MoO_3) exhibits characteristic bands (668, 819, and 996 cm^{-1}) [129,130] even at low concentration, due to a high Raman cross-section. Therefore, a physical mixture of MgO and MoO_3 with a loading of 3 wt.% Mo resulted in strong Raman peaks, which were clearly identifiable (compare Appendix, Fig. A 4.2). The absence of these peaks in the spectra of *Mo/MgO/SBA-15* demonstrated the fine dispersion of the supported molybdenum oxides even at high catalyst loading without the formation of crystalline MoO_3 .

5.3.3 X-Ray Absorption Near Edge Structure

The X-ray absorption near edge structure (XANES) of *Mo/MgO/SBA-15* was similar for all supported molybdenum oxides independent of catalyst loadings. Mo K edge XANES spectra of the supported oxides together with two molybdate references are given in the Appendix (Fig. A 4.3). Apparently, the local structure around the molybdenum atoms corresponded to a structure similar to tetrahedrally coordinated reference molybdates (also shown in Fig. A 4.3). The tetrahedral coordination was corroborated by a distinct pre-edge peak. The local structure of the calcined *Mo/MgO/SBA-15* samples resembled that of the molybdenum oxides in the uncalcined state. Therefore, no major changes in local geometry around the molybdenum center were induced upon calcination of the material. For quantification of the tetrahedral structure a XANES simulation was performed by using XANES spectra of appropriate references. Therefore, the XANES spectra of an ideally tetrahedral (Na_2MoO_4) and octahedral ($\alpha\text{-MoO}_3$) reference structure were fitted to the experimental data. Fig. 5.14 shows the refinement results of the sum of the reference XANES spectra to those of the supported molybdenum oxide species. The uncalcined samples contained a tetrahedral fraction of 86–87% and an octahedral fraction of 12–13% (see fitting results in Table 5.6). Upon calcination of *Mo/MgO/SBA-15* the octahedral fraction of the molybdenum oxide was minimized to 7%. Hence, the supported oxides were mainly arranged in tetrahedral $[\text{MoO}_4]$ units on the *MgO/SBA-15* support.

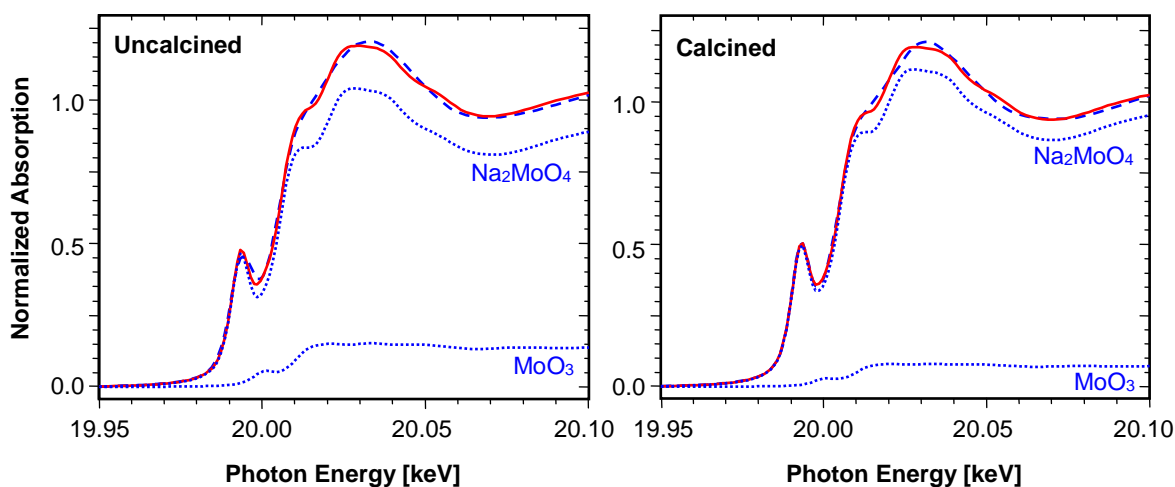


Fig. 5.14 Refinement of sum (dashed) of XANES spectra of a tetrahedral (Na_2MoO_4) and octahedral (MoO_3) reference to the Mo K edge XANES spectra (solid line) of uncalcined (left) and calcined (right) molybdenum oxide supported on *MgO/SBA-15* (5 wt.% Mo).

Table 5.6 Tetrahedral and octahedral fractions calculated from XANES spectra of the supported molybdenum oxides before and after calcination (XANES components shown in Fig. 5.14). Na_2MoO_4 and $\alpha\text{-MoO}_3$ were used as reference compounds for a tetrahedral, and octahedral structure, respectively.

| | Uncalcined | Calcined |
|---------------------------------|------------|----------|
| Tetrahedral Fraction [%] | 86 | 93 |
| Octahedral Fraction [%] | 14 | 7 |

5.3.4 X-Ray Absorption Fine Structure

The extended X-ray absorption fine structure (EXAFS) of molybdenum oxide supported on *MgO/SBA-15* at various molybdenum loadings did not exhibit any significant differences. The pseudo-radial distribution function, $\text{FT}(\chi(k) \cdot k^3)$, of the uncalcined samples corresponded to that of isolated molybdenum centers without neighboring metal atoms. Only one prominent peak at distances in the range from 1–2 Å was observed. Fig. 5.15 depicts the X-ray absorption fine structure (XAFS), $\chi(k) \cdot k^3$, of uncalcined and calcined supported molybdenum oxide at a loading of 5 wt.% Mo together with the Fourier transformed XAFS, $\text{FT}(\chi(k) \cdot k^3)$. XAFS and $\text{FT}(\chi(k) \cdot k^3)$ corresponding to the samples with catalyst loadings of 1, 3, and 10 wt.% Mo are given in the Appendix (Fig. A 4.4).

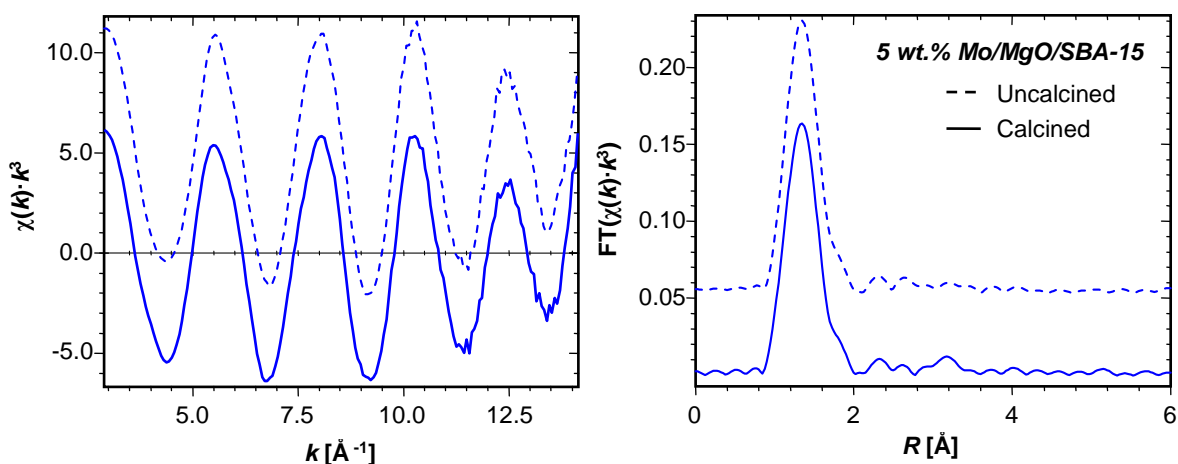


Fig. 5.15 Mo K edge XAFS, $\chi(k) \cdot k^3$ (left), and pseudo-radial distribution function, $\text{FT}(\chi(k) \cdot k^3)$ (right, not phase-shift corrected), of calcined (solid line) and uncalcined (dashed) *Mo/MgO/SBA-15* (5 wt.% Mo).

Apparently, data quality of the XAFS, $\chi(k) \cdot k^3$, shown in Fig. 5.15, permitted reliable data analysis up to 14 \AA^{-1} . The prominent peak around 1–2 \AA was in good agreement with peak position and amplitude in the reference spectrum of MgMoO_4 . Hence, a theoretical XAFS function calculated for a MgMoO_4 model structure was refined to the $\text{FT}(\chi(k) \cdot k^3)$ of the samples. Fig. 5.16 depicts the resulting theoretical and experimental $\text{FT}(\chi(k) \cdot k^3)$ for *Mo/MgO/SBA-15* before and after calcination. The corresponding fitting parameters are given in Table 5.7. A good agreement between theoretical and experimental $\text{FT}(\chi(k) \cdot k^3)$ of uncalcined *Mo/MgO/SBA-15* was achieved. Within the limits of distance resolution in XAFS refinements ($dR = \pi/2k_{\text{max}} = 0.11 \text{ \AA}$, with $k_{\text{max}} = 14 \text{ \AA}^{-1}$) only one Mo–O distance was resolved. Therefore, an ideal tetrahedral geometry was assumed for the local structure around the molybdenum atoms in *Mo/MgO/SBA-15*. The refinement was improved by considering additional Mo–Mg paths at higher distances. Characteristic Mo–O and Mo–Mg paths in the local structure of the uncalcined samples and the corresponding single scattering $\text{FT}(\chi(k) \cdot k^3)$ are also shown in Fig. 5.16 (left). The Mo–Mg distances required to describe the experimental $\text{FT}(\chi(k) \cdot k^3)$ indicated a linkage to the MgO surface via two Mo–O–Mg bonds. The $\text{FT}(\chi(k) \cdot k^3)$ of calcined *Mo/MgO/SBA-15* resembled that of the uncalcined species. Nevertheless, the refinement revealed an additional Mo–Mo distance indicating a possible dimeric molybdenum oxide species. From XANES analysis discussed above the fraction of octahedral molybdenum oxide units was estimated to $\sim 7\%$. Hence, the influence of oligomerized octahedral units on the amplitude in the experimental $\text{FT}(\chi(k) \cdot k^3)$ was considered to be insignificant.

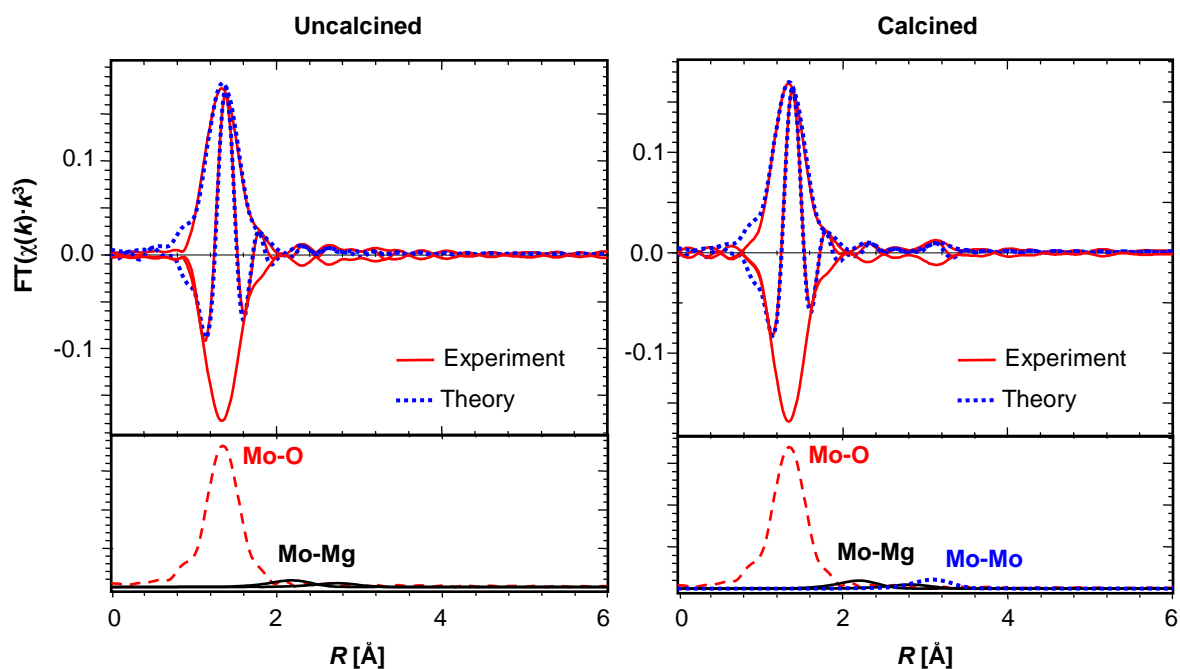


Fig. 5.16 Experimental (solid line) Mo K edge $\text{FT}(\chi(k) \cdot k^3)$ of molybdenum oxide catalysts supported on *MgO/SBA-15* in the uncalcined (left) and calcined (right) state, together with a theoretical XAFS function (dotted). Corresponding fitting results are given in Table 5.7. $\text{FT}(\chi(k) \cdot k^3)$ of the individual scattering paths are displayed below each fit.

Table 5.7 Number, N , of atoms at distance, R , from the absorbing molybdenum atom in the local structure of *Mo/MgO/SBA-15* before and after calcination. Experimental distances, R , and XAFS disorder parameters, σ^2 , were obtained from the refinement of a MgMoO_4 model structure to the experimental Mo K edge XAFS $\text{FT}(\chi(k) \cdot k^3)$ of the samples (Fig. 5.16) (k range from 2.9–14.2 \AA^{-1} , R range 0.9–4.1 \AA , $N_{\text{ind}} = 24$, $N_{\text{free}} = 8$).

| Type | N | Uncalcined | | Calcined | | |
|-----------------|----------------|----------------------|-------------------------------|----------------|----------------------|-------------------------------|
| | | R [\AA] | σ^2 [\AA^2] | N | R [\AA] | σ^2 [\AA^2] |
| Mo–O | 4 _f | 1.77 | 0.0006 | 4 _f | 1.78 | 0.0011 |
| Mo–Mg | 1 _f | 2.67 | 0.0090 _c | 1 _f | 2.67 | 0.0081 _c |
| Mo–Mg | 1 _f | 3.25 | 0.0090 _c | 1 _f | 3.33 | 0.0081 _c |
| Mo–Mo | - | - | - | 1 _f | 3.46 | 0.0081 _c |
| Residual | | | 8.8 | | | 8.4 |

Note: Subscript *c* indicates parameters that were correlated, subscript *f* parameters that were fixed in the refinement.

To estimate the fraction of dimeric tetrahedral species on the support, the $\text{FT}(\chi(k)\cdot k^3)$ was simulated for a theoretical molybdenum oxide dimer model system “ Mo_2O_7 ”. Therefore, two adjacent $[\text{MoO}_4]$ tetrahedrons were assumed, with a Mo-Mo distance comparable to the fitting results above (Table 5.7). The disorder parameter, σ^2 , was taken from an MoO_3 EXAFS refinement to obtain a reasonable value for the Mo-Mo distance ($\sigma^2 = 0.0035 \text{ \AA}^2$).^[131] Fig. 5.17 depicts a comparison of the $\text{FT}(\chi(k)\cdot k^3)$ of $\text{Mo}/\text{MgO}/\text{SBA-15}$ and of the dimer simulation.

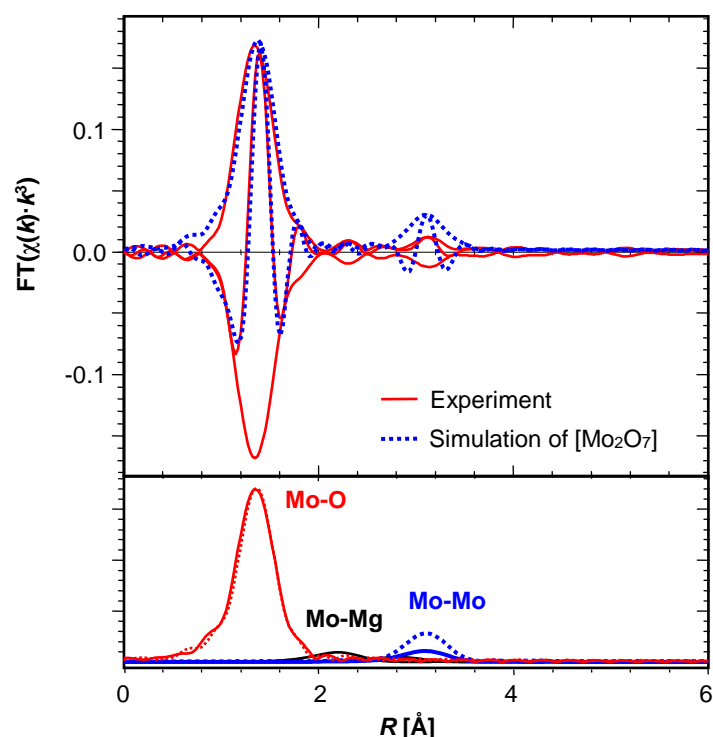


Fig. 5.17 Experimental Mo K edge $\text{FT}(\chi(k)\cdot k^3)$ of molybdenum oxide supported on $\text{MgO}/\text{SBA-15}$ (solid line) compared to a simulated XAFS function of a $[\text{MoO}_4]$ dimer (dotted). $\text{FT}(\chi(k)\cdot k^3)$ of the individual scattering paths of the experimental (solid) and simulated (dotted) data are displayed below.

Apparently, the amplitude of the Mo-Mo path is significantly higher for the simulated molybdenum oxide dimer. The reduced amplitude of the experimental spectrum may have two different reasons. Either a phase mixture of monomeric and dimeric molybdenum oxide species was present on the $\text{MgO}/\text{SBA-15}$ support or the supported oxide species exhibited a substantially higher disorder compared to the unsupported bulk oxide. A distinction between the two effects was not possible. However, assuming a mixture of monomeric and dimeric tetrahedral units, quantification of the dimeric species was attempted. Therefore, an EXAFS refinement was performed to determine the number, N , of neighboring molybdenum atoms. To obtain

reasonable results for the number, N , the disorder parameter, σ^2 , had to be fixed in the refinement. Resulting theoretical and experimental $\text{FT}(\chi(k)\cdot k^3)$ together with the corresponding fitting parameters are given in the Appendix (Fig. A 4.5 and Table A 4.3). The uncertainty in the determination of the number, N , of neighboring molybdenum atoms must be considered high due to the unknown disorder of the supported molybdenum oxide species. Nevertheless, quantification of the dimeric molybdenum oxide tetrahedra amounted to approximately 40%, resulting in a monomer to dimer ratio of $\sim 3:2$.

5.4 Influence of Support Material

5.4.1 MgO-coated SBA-15 (*MgO/SBA-15*)

The choice of the support material plays an important role for the structure of the supported oxides. Within the scope of this work a MgO-based support material with alkaline surface properties was chosen. The behavior of the vanadium and molybdenum oxides supported on alkaline *MgO/SBA-15* differed considerably from that on other support materials, such as acidic silica SBA-15 or carbon CMK-3. Under ambient conditions the observed structure of the supported vanadium and molybdenum oxides is similar to that in aqueous solution. The oxide species formed depend on vanadium or molybdenum oxide concentration and pH value of the solution. For supported oxides the net pH of the oxide support at which the oxide surface possesses no surface charge (point of zero charge, PZC) corresponds to the pH value of a solution of vanadium or molybdenum oxides.

The presence of minor amounts of remaining silica domains on the surface of *MgO/SBA-15* cannot be excluded. However, it can be assumed that the vanadium and molybdenum oxide species preferentially anchored to the MgO layer due to strong acid-base interactions between the supported metal oxides and MgO. The low density and reactivity of remaining silanol groups restrained the possibility of vanadium or molybdenum oxides binding to the silica surface. A similar conclusion was drawn by Wachs *et al.* when comparing the reactivity of several oxide surfaces.[132] The results of this work showed that coating of silica SBA-15 with magnesium oxide (*MgO/SBA-15*) yielded in a transformation of the previously

acidic to an alkaline surface. As it will be shown in the following, the characteristics of coated and uncoated SBA-15 as support material were clearly distinguishable.

5.4.2 Influence on Supported Vanadium Oxides

Vanadium Oxides on Silica SBA-15

Following the behavior of vanadium oxides in aqueous solution, the tendency to form monomeric $[\text{VO}_4]$ species increases at low vanadium oxide concentration and high net pH of the oxide surface, whereas oligomerized species tend to form at high vanadium oxide concentrations and low net pH.[5] The impregnation of the alkaline *MgO/SBA-15* surface with ammonium decavanadate solution resulted in dissociation of the $\text{V}_{10}\text{O}_{28}^{6-}$ ions into $[\text{VO}_4]$ units. This behavior nicely resembled the characteristics of vanadium oxides under alkaline conditions, as the $[\text{VO}_4]$ tetrahedra were more stable on the alkaline support material than the high oligomerized precursor species. The structure of the supported vanadium oxides persisted during calcination at elevated temperatures. Vanadium oxides supported on more acidic silica SBA-15 tend to form a hydrated structure in the presence of water. Thus, the supported vanadium oxides form a network of small cluster with a square-pyramidal coordination of oxygen atoms around the vanadium center. Upon calcination at elevated temperatures the structure is dehydrated, resulting in a dimeric or chainlike structure of $[\text{VO}_4]$ tetrahedrons.[4,111] Conversely, on alkaline *MgO/SBA-15* the vanadium oxides did not show a hydrated state. The oxide structure described was present after initial calcination of the samples and proved to be stable under ambient conditions.

A comparison of the DR-UV-Vis spectra of vanadium oxides supported on *MgO/SBA-15* and bare SBA-15 is given in Fig. 5.18. The spectrum of as-prepared (hydrated) vanadium oxides on SBA-15 was clearly distinguishable from that of the vanadium oxides on *MgO/SBA-15*. In contrast, the spectra of the dehydrated V/SBA-15 samples resembled those of vanadium oxides supported on *MgO/SBA-15* at higher loadings, indicating the presence of adjacent $[\text{VO}_4]$ units. Furthermore, the UV-Vis edge energies of dehydrated oxides supported on SBA-15 were considerably lower compared to the edge energies of the oxides supported on *MgO/SBA-15* at similar vanadium loadings (compare Fig. 5.6). This confirmed a higher degree of oligomerization of the dehydrated vanadium oxides supported on SBA-15.

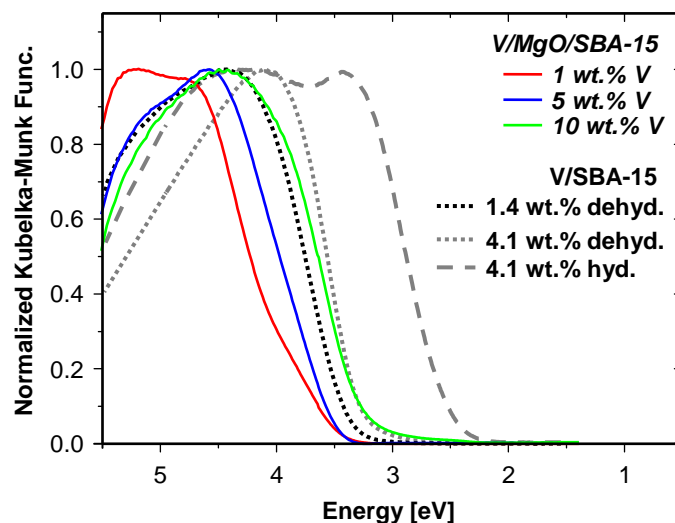


Fig. 5.18 Normalized DR-UV-Vis spectra of supported vanadium oxides at weight loadings of 1, 5, and 10 wt.% V (solid lines) together with two spectra of vanadium oxides supported on bare SBA-15. Depicted are the spectra of the hydrated (dashed line) and dehydrated (dotted) state of the oxides supported on SBA-15. All spectra were recorded at room temperature in helium atmosphere with an *in situ* cell.

Vanadium Oxides on Carbon CMK-3

Vanadium oxides supported on carbon CMK-3 exhibited a structure similar to that of the dehydrated state of V/SBA-15 consisting of a two-dimensional V_2O_5 -type layer on the support. A similar V_2O_5 -type structure for vanadium oxide catalysts supported on activated carbon was reported by Zhu *et al.* who investigated vanadium oxide catalysts supported on activated carbon for NO reduction with ammonia.[133] Fig. 5.19 depicts the X-ray absorption near edge structure (XANES) of vanadium oxide on CMK-3 compared to that of V/SBA-15 and of a bulk V_2O_5 reference. The XANES features in the three spectra were similar. All spectra featured a strong pre-edge peak which is related to a forbidden $1s-3d$ transition caused by overlapping of the vanadium $3d$ orbitals with the $2p$ orbitals of the oxygen ligands.[65] The intensity of the pre-edge peak increases with proceeding deviation from perfect octahedral symmetry. Therefore, the XANES spectra of V_2O_5 , where a structure of distorted square-pyramidal $[VO_5]$ units is present, exhibited a strong pre-edge feature. The pre-edge peak intensity decreased from V_2O_5 over V/SBA-15 to V/CMK-3. This indicated a less distinctive disorder in the two-dimensional V_2O_5 -type structure of V/CMK-3.

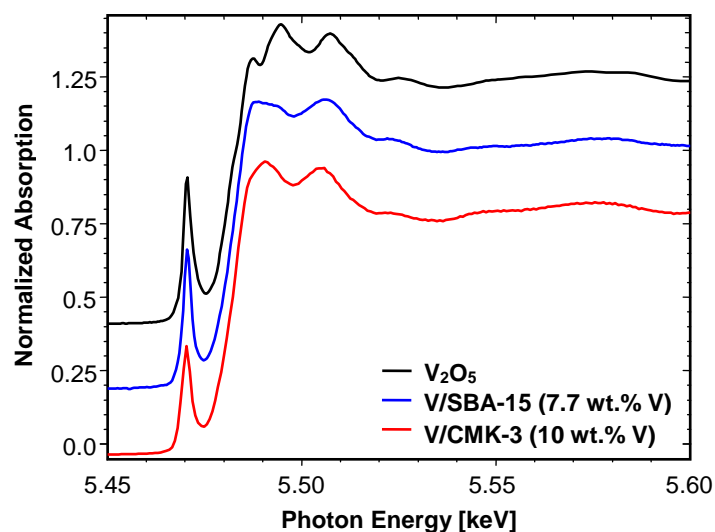


Fig. 5.19 Normalized V K edge XANES spectra of vanadium oxide on CMK-3 (10 wt.% V, red) compared to that of V/SBA-15 (7.7 wt.% V, blue) and of a bulk V_2O_5 reference (black).

The higher ordered structure of the vanadium oxides supported on CMK-3 compared to that of V/SBA-15 might possibly be due to a weaker oxide-support interaction in V/CMK-3. This weak interaction was attributed to the non-oxide nature of CMK-3. Structural formation of the supported vanadium oxides was most reasonably influenced by the presence of physisorbed water on the CMK-3 surface. Therefore, the vanadium oxide structure on CMK-3 resembled that of the oxide structure in aqueous solution at neutral pH.

5.4.3 Influence on Supported Molybdenum Oxides

Molybdenum Oxides on Silica SBA-15

Comparable to the behavior of vanadium oxides supported on silica SBA-15, molybdenum oxides supported on SBA-15 are reported to exhibit a dehydrated and a hydrated state. The latter exists in the presence of water under ambient conditions.[134] On the one hand, the structure of the hydrated state was shown to resemble that of the metastable hexagonal modification of molybdenum trioxide (hex- MoO_3). It was claimed that this structure was stabilized due to the interaction of the oxide species with the SBA-15 support.[41] On the other hand, the dehydrated state of molybdenum oxide species on SBA-15 consisted of a large fraction of connected molybdenum oxide species composed of oligomeric Mo_xO_y species and $[MoO_4]$ tetrahedrons.[128] Conversely, on the *MgO/SBA-15* support no such differentiation between

hydrated and dehydrated state was observed. The molybdenum oxide structure obtained after initial calcination remained stable under ambient conditions. It consisted of isolated or partially dimeric tetrahedral molybdenum oxide units on the *MgO/SBA-15* support. The structure of the molybdenum oxide supported on *MgO/SBA-15* and bare SBA-15 was again comparable to the behavior of the oxides in aqueous solution. At high pH values MoO_4^{2-} units are formed, whereas under acidic conditions polyoxomolybdates (*e.g.*, heptamolybdate $\text{Mo}_7\text{O}_{24}^{6-}$) are favored.[5,6] A comparison of the refinement results of the X-ray absorption fine structure (XAFS) presented above (Chap. 5.3.4) to those of the dehydrated molybdenum oxide species formed on SBA-15 (Fig. 5.20, right) confirmed this assumption.

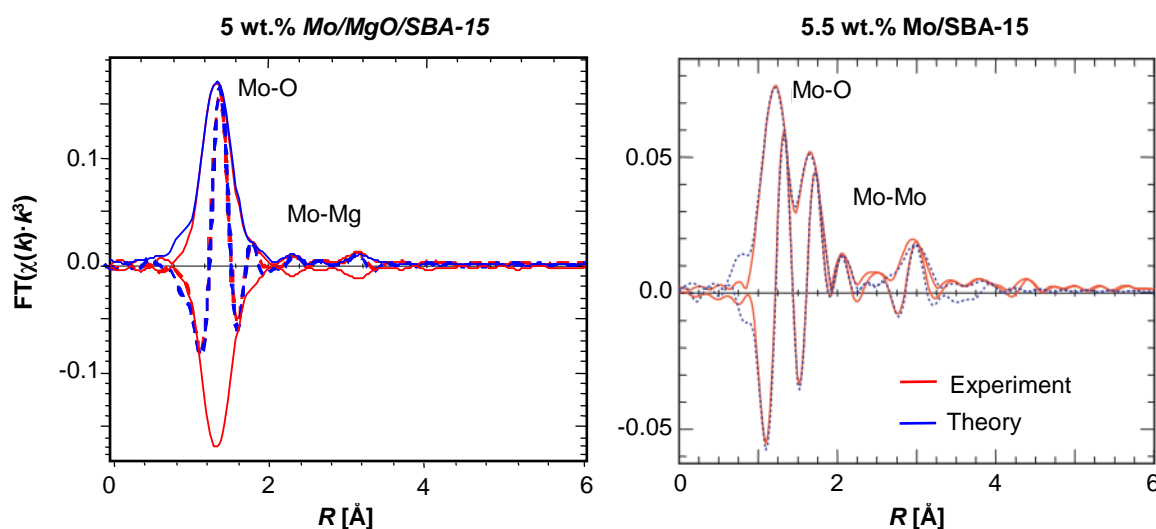


Fig. 5.20 Comparison of the Mo K edge $\text{FT}(\chi(k) \cdot k^3)$ of molybdenum oxide supported on *MgO/SBA-15* (5 wt.% Mo, left) and of the dehydrated molybdenum oxide species supported on bare SBA-15 at similar catalyst loading (5.5 wt.% Mo, right, adapted from [128]).

The formation of predominantly isolated tetrahedral molybdenum oxide units on the alkaline *MgO/SBA-15* support stood in contrast to the oligomeric oxide species on the more acidic SBA-15. Hence, impregnation of the MgO surface with ammonium heptamolybdate (AHM) solution resulted in dissociation of the heptamolybdate anions into $[\text{MoO}_4]$ units, which are more stable under alkaline conditions. Results from analysis of the extended X-ray absorption fine structure (EXAFS) revealed significant differences in the molybdenum oxide structure on *MgO/SBA-15* compared to the structure formed on bare SBA-15. On SBA-15 a structure of adjacent octahedral and tetrahedral molybdenum oxide species is present.[128] However,

these structural features typically present in molybdenum oxides supported on SBA-15 were absent in the oxide species on *MgO/SBA-15*. Hence, given the detection limit and accuracy of the EXAFS analysis, the contribution of molybdenum oxide species located on remaining silica domains should not exceed 5–10%.

Molybdenum Oxides on Carbon CMK-3

The structure of molybdenum oxide supported on carbon CMK-3 was similar to that of the molybdenum oxide species on SBA-15 in the hydrated state which resembled that of hex- MoO_3 . As it was already discussed above for vanadium oxides supported on CMK-3, the non-oxide nature of CMK-3 promoted the formation of an oxide structure similar to that of vanadium or molybdenum oxide in aqueous solution at natural pH. Fig. 5.21 shows a comparison of the X-ray absorption near edge structure (XANES) of Mo/SBA-15 and Mo/CMK-3 at comparable molybdenum loadings to that of an $\alpha\text{-MoO}_3$ reference.

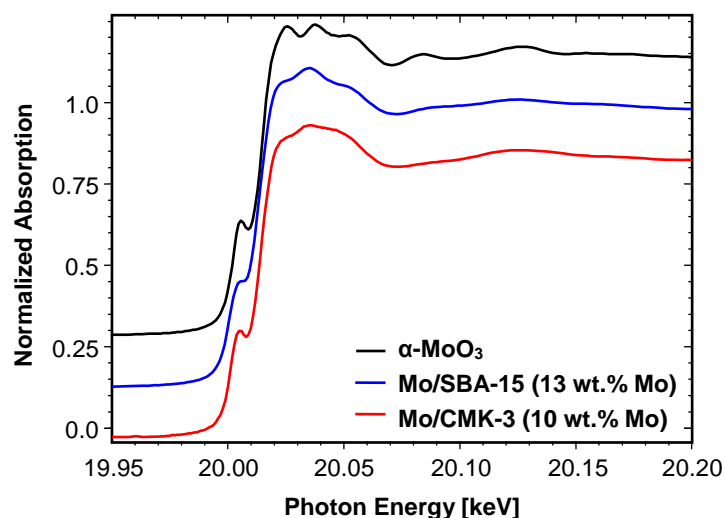


Fig. 5.21 Normalized Mo K edge XANES spectra of molybdenum oxides supported on silica SBA-15 (13 wt.% Mo, blue) and on carbon CMK-3 (10 wt.% Mo, red) compared to the spectra of an $\alpha\text{-MoO}_3$ reference.

The similarity of the local structure around the molybdenum center was visible in a similar near edge structure. However, characteristically for the hex- MoO_3 structure, the first XANES feature behind the adsorption edge (~ 20.03 keV) in the spectra of Mo/SBA-15 and Mo/CMK-3 appeared to be more reduced than the feature in the spectrum of $\alpha\text{-MoO}_3$. A similar hex- MoO_3 -type structure was previously observed for molybdenum oxide supported on

hollow carbon nanofibers (CNF). The as-prepared structure on CNF was shown to be stable up to a temperature of 350 °C.[131]

5.4.4 Dehydration/Dehydroxylation of Support Material

For a comprehensive description of the *MgO/SBA-15* surface understanding of dehydration (removal of physically adsorbed water) and dehydroxylation (removal of hydroxyl groups from the surface) processes is of importance. Many researches address the investigation of silanol groups bound to an amorphous silica surface, such as, for instance, SBA-15.[135,136] According to Zhuravlev, the water desorption process on silica during temperature programmed heat treatment can basically be divided into three steps. First, the physically adsorbed water is removed in a dehydration process up to a temperature of 190 °C. The activation energy of this process amounts to ~ 50 kJ/mol. In a second step vicinal silanol groups are removed during dehydroxylation. The third step includes another dehydroxylation process where isolated silanol groups are consecutively removed with increasing temperature. The activation energy of the dehydroxylation also increases with increasing temperature.[135] On *MgO/SBA-15* the surface silanol groups are predominantly replaced by MgO and Mg(OH)₂ groups. Hence, a change in dehydration and dehydroxylation behavior seemed likely. Thermogravimetric (TG) measurements were conducted to compare dehydration processes of *MgO/SBA-15* before and after deposition of vanadium and molybdenum oxides with the results from the measurement of SBA-15. After an initial phase of one hour, where the samples were left to dry at 30 °C, the temperature was raised with various heating rates to 400 °C and kept at the temperature for 30 min. Fig. 5.22 (left) depicts a typical TG/DTG profile.

Basically, three steps of mass loss were distinguished in all thermograms. The first mass loss, which already occurred at room temperature, was ascribed to desorption of water present in a multilayer on the surface. This was in accordance with Zhuravlev who described a similar behavior for amorphous silica.[135] The second and most prominent step took place in a temperature range between 70 °C and 200 °C. The process was ascribed to desorption of physically adsorbed water in a monolayer coverage on the surface. The adjacent third step ranged from 200 °C up to the maximum temperature of 400 °C. The mass loss is most probably due to the dehydroxylation of surface Mg(OH)₂ groups and formation of MgO. As already reported for *nano-MgO* this transformation usually takes place at temperatures around

350 °C.[108] The dehydroxylation step was not very well resolved as it was only visible as broad shoulder at the right-hand side of the derivative thermogravimetric (DTG) peak assigned to the dehydration step.

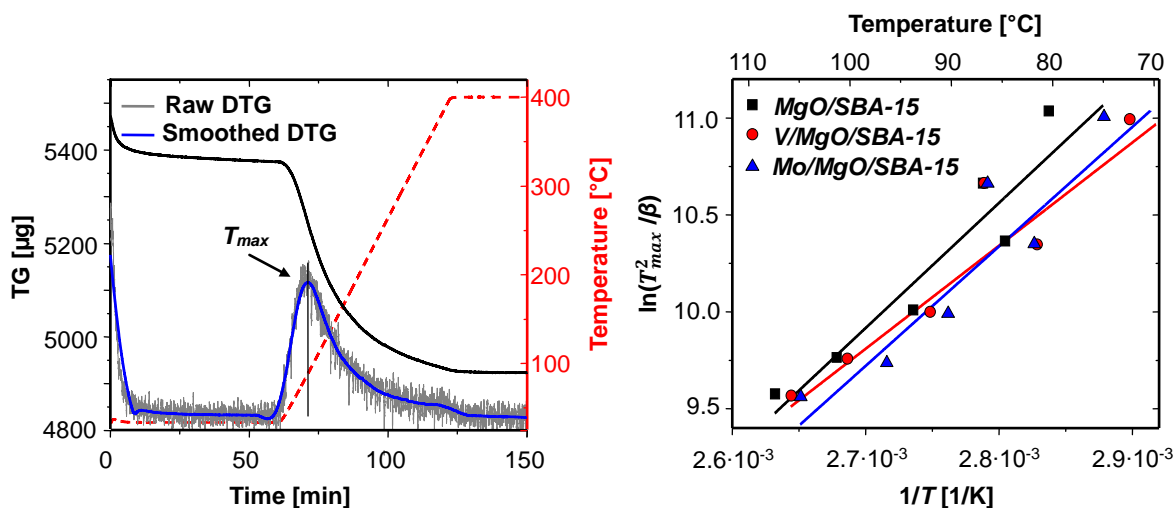


Fig. 5.22 Typical profile for *MgO/SBA-15* during thermal treatment under 20% O_2/He (left) and the obtained Kissinger plot (right) for the determination of the apparent activation energy of water desorption, E_D , for bare *MgO/SBA-15*, 5 wt.% *V/MgO/SBA-15*, and 5 wt.% *Mo/MgO/SBA-15*. The heating rate for the exemplary TG/DTG profile (left) was 6 K/min.

To reveal the influence of the supported vanadium and molybdenum oxide catalyst on the dehydration behavior the apparent activation energy of water desorption, E_D , was calculated from an Arrhenius-type (Kissinger) plot according to eq. (5-1). Therefore, the temperature, T_{max} , of the maximum in the DTG signal was determined for various heating rates, β , and plotted in a linearized form in Fig. 5.22 (right). Calculated activation energies for unloaded *MgO/SBA-15*, *V/MgO/SBA-15*, and *Mo/MgO/SBA-15* are listed in Table 5.8. For all samples the activation energy of water desorption amounted to approximately 50 kJ/mol. Therefore, dehydration seemed to be independent on catalyst deposition on the *MgO/SBA-15* surface.

The activation energy was well below the energy determined for the dehydration of the SBA-15 surface. Thus, water adsorbed on the surface of *MgO/SBA-15* was only weakly bonded compared to water on bare SBA-15. In contrast to the behavior of *MgO/SBA-15* the deposition of vanadium oxide on SBA-15 led to a decrease in activation energy. This was interpreted as a change in desorption behavior due to the influence of the hydrated vanadium oxide structure

present on SBA-15.[110] As it was already discussed above no formation of a hydrated oxide structure was observed on *MgO/SBA-15*.

Table 5.8 Apparent activation energies of water desorption, E_D , of bare *MgO/SBA-15* and vanadium or molybdenum oxide supported on *MgO/SBA-15* determined from a Kissinger plot (Fig. 5.22, right). Results were compared to the data of the SBA-15 analog (taken from [110]).

| | E_D [kJ/mol] | Total Mass Loss [%] |
|----------------------------------|----------------|---------------------|
| <i>MgO/SBA-15</i> | 53 ± 10 | 15.5 |
| <i>V/MgO/SBA-15</i> (3 wt.% V) | 73 ± 14 | 14.0 |
| <i>V/MgO/SBA-15</i> (5 wt.% V) | 44 ± 5 | 9.5 |
| <i>V/MgO/SBA-15</i> (10 wt.% V) | 44 ± 4 | 14.5 |
| <i>Mo/MgO/SBA-15</i> (5 wt.% Mo) | 51 ± 8 | 15.3 |
| SBA-15 | 100–110 | 3.6 |
| V/SBA-15 (7.7 wt.% V) | 72–83 | 6–10 |

The overall mass loss during dehydration/dehydroxylation of *MgO/SBA-15* amounted to 15–16%. This was considerably higher than the mass loss detected for bare SBA-15. The affinity to water is significantly higher for magnesium oxide than for silica. This was explicitly visible for *nano-MgO* where a large amount of the MgO surface was transformed to $\text{Mg}(\text{OH})_2$ under ambient conditions (refer to Chap. 4). Thus, it seemed reasonable that a higher amount of physically adsorbed water on *MgO/SBA-15* led to a higher overall mass loss.

5.5 Conclusions

Vanadium and molybdenum oxides supported on *MgO/SBA-15* have been examined by a combination of various characterization techniques. Coating of silica SBA-15 with magnesium oxide (*MgO/SBA-15*) altered the previously more acidic silica surface to a surface with alkaline properties. The vanadium and molybdenum oxide species formed on coated and uncoated SBA-15 were clearly distinguishable. Structure formation of the supported oxides was comparable to the behavior of the oxides in aqueous solution. The dehydration behavior of *MgO/SBA-15* was in contrast to the behavior of parent silica SBA-15. The activation energy of water desorption of *MgO/SBA-15* was approximately 50 kJ/mol. No changes in activation

energy were observed upon deposition of vanadium or molybdenum oxide catalysts on *MgO/SBA-15*. Therefore, water desorption seemed to proceed independent of catalyst loading. In contrast, the activation energy of *SBA-15* was significantly higher. Thus, a stronger interaction of the adsorbed water molecules with the *SBA-15* surface was assumed.

The structure of vanadium oxide supported on *MgO/SBA-15* strongly depended on catalyst loading and surface coverage. At low surface coverage in the range of 0.5 vanadium atoms per nm^2 predominantly monomeric $[\text{VO}_4]$ tetrahedra were present. The alkaline surface of the support material *MgO/SBA-15* stabilized the formation of low oligomerized tetrahedral vanadium oxide species even under ambient conditions. Fig. 5.23 schematically depicts the suggested configurations of the supported vanadium oxides.

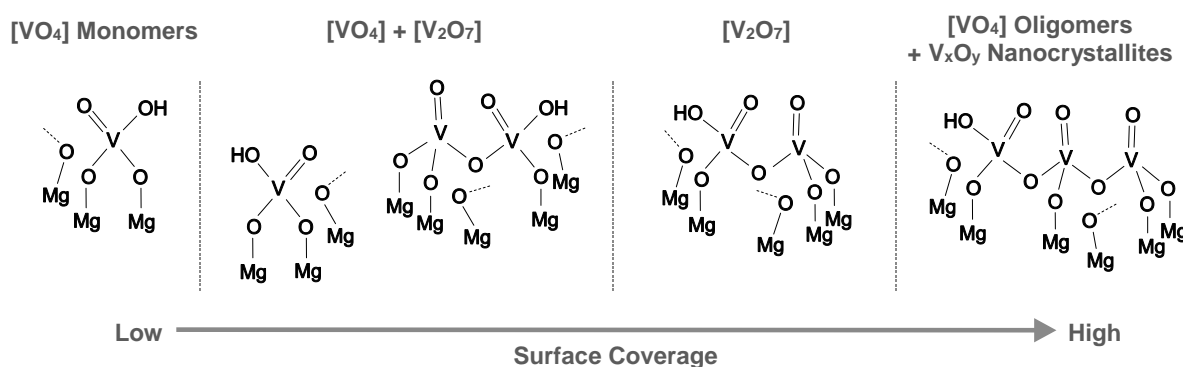


Fig. 5.23 Schematic representation of molecular configurations for vanadium oxide supported on *MgO/SBA-15*. The degree of oligomerization increased with increasing surface coverage. The configurations can schematically be divided into four sections with a majority phase of a) monomeric $[\text{VO}_4]$ tetrahedra, b) $[\text{VO}_4]$ monomers and dimers, c) $[\text{V}_2\text{O}_7]$ units, and d) $[\text{VO}_4]$ oligomers and V_xO_y nanocrystallites. The coordination of a fifth oxo-ligand to the vanadium center is indicated.

With increasing surface coverage the degree of oligomerization of the tetrahedral vanadium oxide units increased. Accordingly, configurations can roughly be divided into four majority phases. At low surface coverage (< 0.5 V atoms/ nm^2) predominately monomeric $[\text{VO}_4]$ tetrahedra were present. In the range of one vanadium atom per nm^2 a mixture of monomeric and dimeric $[\text{VO}_4]$ units was assumed. At higher coverage (≥ 2 V atoms/ nm^2) $[\text{V}_2\text{O}_7]$ units constituted the majority phase. In the range of maximum coverage (~ 6 V atoms/ nm^2) $[\text{VO}_4]$ oligomers and partial formation of V_xO_y nanocrystallites were observed. The possible coordi-

nation of a fifth oxo-ligand as proposed from UV-Vis and EXAFS data is indicated in the structural model (Fig. 5.23).

A change between hydrated and dehydrated state, as commonly observed for vanadium oxides supported on oxide supports, such as silica, titania, and alumina, was not detected. A comparison of the oxide structure with the dehydrated structure of vanadium oxides supported on silica SBA-15 showed that the acidity of the support had a great impact on the structure of the supported oxide species. The degree of oligomerization of supported vanadium oxide units increased with increasing surface coverage. However, to achieve a comparable degree of oligomerization on SBA-15 and *MgO/SBA-15* the vanadium oxide loadings had to be in a different range. The alkaline character of *MgO/SBA-15* allowed the dispersion of low oligomerized, tetrahedral vanadium oxide units even at comparatively high loadings (10 wt.% V). Conversely, on SBA-15 substantially higher oligomerized units were achieved at similar amounts of vanadium oxide. The vanadium oxide structure on carbon CMK-3 resembled that of the hydrated state on silica SBA-15. Hence, the oxide species consisted of a two-dimensional V_2O_5 -type layer on the CMK-3 support. The vanadium oxide structure on CMK-3 was comparable to the oxide structure in aqueous solution at neutral pH. This effect was attributed to the presence of physisorbed water on the surface of CMK-3. A low oxide-support interaction on the non-oxide CKM-3 support was assumed to cause a low distortion of the octahedral vanadium oxide units.

In contrast to the supported vanadium oxides, where the structure was strongly dependent on surface coverage, the structure of the molybdenum oxides supported on *MgO/SBA-15* was largely independent of catalyst loading and surface coverage. The formation of the $[MoO_4]$ tetrahedra took place without calcination after deposition and drying of the ammonium heptamolybdate precursor on the alkaline surface. A difference between hydrated and dehydrated state as for molybdenum oxides supported on bare SBA-15 was not observed. However, upon initial calcination the molybdenum oxide species remained stable on the surface, predominately preserving the isolated tetrahedra with a partial generation of $[Mo_2O_7]$. The ratio between monomeric and dimeric tetrahedral molybdenum oxide units on the

MgO/SBA-15 support determined by EXAFS analysis was estimated to 3:2. Fig. 5.24 schematically represents the molecular structure of the supported molybdenum oxides.

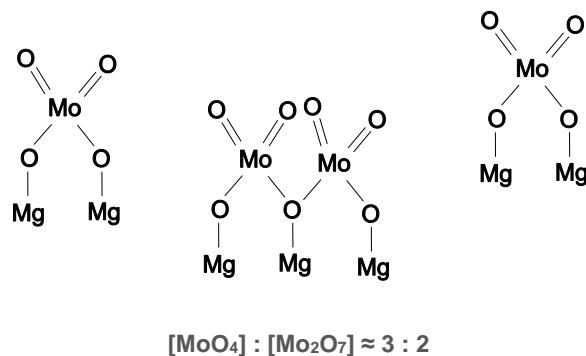


Fig. 5.24 Schematic representation of molecular configurations for molybdenum oxide supported on *MgO/SBA-15*. The molybdenum oxide structure was independent of catalyst loading and consisted of a mixture of monomeric and dimeric $[\text{MoO}_4]$ tetrahedra. The ratio between monomers and dimers was $\sim 3:2$.

The molybdenum oxide species supported on *MgO/SBA-15* differed considerably from that of molybdenum oxides supported on acidic support materials like silica SBA-15, where oligomeric molybdenum oxide species were formed. Similar to the behavior of supported vanadium oxides the structure of molybdenum oxides supported on carbon CMK-3 was comparable to that of the hydrated state of molybdenum oxide on SBA-15. The molybdenum oxide species on CMK-3 was present in a structure resembling that of the hexagonal modification of molybdenum trioxide (hex- MoO_3).

6 Catalytic Properties / *In Situ* Characterization of Supported Oxide Catalysts

Catalytic activity of vanadium and molybdenum oxide catalysts supported on *MgO/SBA-15* was investigated. Therefore, the supported vanadium and molybdenum oxide catalysts were studied during selective oxidation of propene (SOP). To directly compare the results obtained for SOP with the behavior of the catalysts in a different type of selective oxidation reaction the supported vanadium oxides were additionally tested in oxidative dehydrogenation (ODH) of propane. By using different *in situ* characterization techniques structural and electronic changes within the metal oxide catalysts were directly correlated to their properties in catalytic selective oxidation reaction. Comparison to oxide catalysts supported on other supporting materials, like silica SBA-15 and carbon CMK-3, emphasized the severe influence of the nature of the support and the metal oxide-support interaction on the catalytic behavior.

6.1 Experimental

6.1.1 Sample Characterization

X-Ray Absorption Spectroscopy

In situ and *ex situ* transmission X-ray absorption spectroscopy (XAS) was performed at the V K edge (5.465 keV) and the Mo K edge (19.999 keV) at the Hamburg Synchrotron Radiation Laboratory, HASYLAB (beamline C, X1, and A) using a Si(111) (V K edge) or Si(311) (Mo K edge) double crystal monochromator. For *ex situ* measurements samples were diluted with wax (Hoechst wax C micropowder, Merck) or polyethylene (PE, Induchem Switzerland) and pressed into self-supporting pellets with a diameter of 13 mm. *In situ* XAS measurements were performed in an *in situ* cell described earlier.[137] Therefore, powder samples were diluted with boron nitride (Alfa Aesar, 99.5%) and pressed into self-supporting pellets with a diameter of 5 mm. Sample masses were calculated to result in an edge jump around $\Delta\mu(d) = 1.0$.

At the V K edge the energy range used for scans of the X-ray absorption near edge structure (XANES) and the extended X-ray absorption fine structure (EXAFS) were 5.4–5.7 keV (~ 3.5 min/scan), and 5.4–6.3 keV (~ 21 min/scan), respectively. For fast measurements "quick EXAFS" (QEXAFS) scans were performed (5.4–5.8 keV, ~ 2.5 min/scan). At the Mo K edge the energy range for an EXAFS scan was 19.9–21.0 keV (~ 12 min/scan). QEXAFS measurements were conducted in the range between 19.9–20.3 eV (~ 0.8 min/scan). *In situ* measurements were conducted in 5% propene and 5% oxygen in helium (total flow 40 ml/min) in a temperature range from 20 °C to 450 °C at a heating rate of 4 K/min. The gas atmosphere was analyzed using an online mass spectrometer (Omnistar, Pfeiffer) in a multiple ion detection mode. If not stated otherwise ion currents were normalized to the helium current.

X-ray absorption fine structure analysis was performed using the software package WinXAS v3.2.[113] For analysis of the EXAFS, background subtraction and normalization were performed by fitting a linear polynomial and a third degree polynomial to the pre-edge, and the post-edge region of an absorption spectrum, respectively. The EXAFS, $\chi(k)$, was extracted by using cubic splines to obtain a smooth atomic background, $\mu_0(k)$. The $\text{FT}(\chi(k) \cdot k^3)$ was calculated according to eq. (3-3) by Fourier transformation of the k^3 -weighted experimental $\chi(k)$ function, multiplied by a Bessel window, into the R space. For analysis of the XANES, background subtraction and normalization were performed by fitting linear polynomials to the pre-edge and the post-edge region of an absorption spectrum in the energy range of 5.4–5.7 keV (V K edge) or 19.95–20.10 keV (Mo K edge). The position of the V K absorption edge was measured according to Wong *et al.* at the edge energy half way up the normalized edge step.[65] To determine the edge position in an analyzing routine an arctangent (atan) function was fitted to the absorption step. An example of the fitting procedure is given in the Appendix (Fig. A 2.2). For pre-edge peak analysis of Mo K edge XANES spectra a Gaussian and an atan function were fitted to the pre-edge peak, and the adsorption edge, respectively. Details on fit parameters are given in the Appendix (Fig. A 2.3).

Diffuse Reflectance UV-Vis Spectroscopy

DR-UV-Vis measurements were conducted on a two-beam spectrometer (V670, JASCO) using a Praying Mantis™ *in situ* cell (Harrick Scientific Products, Inc.). Powder samples were measured in the spectral region of 220–890 nm. Boron nitride (Alfa Aesar, 99.5%) was used for sample dilution and as reflectance standard for baseline correction. *In situ* measurements were conducted in 5% propene (Linde Gas, 10% propene (3.5) in He (5.0)) and 5% oxygen (Linde Gas, 20% O₂ (5.0) in He (5.0)) in helium (Air Liquide, 6.0) in a temperature range from 20 °C to 425 °C at a heating rate of 4.25 K/min. The total gas flow was adjusted to 40 ml/min. The gas atmosphere was analyzed using an online mass spectrometer (Omnistar, Pfeiffer) in a multiple ion detection mode. The DR-UV-Vis spectra were transferred to the Kubelka-Munk function, $F(R_{\infty})$, according to eq. (3-4).

Kinetic analysis of hydrocarbon adsorption was performed by using an isoconversional method. These model free kinetics introduced by Friedman[138] and developed by Vyazovkin[139] allow the determination of the activation energy, E_a , without choosing a reaction model. The basic assumption of this approach is that the reaction model, $f(\alpha)$, does not depend on temperature, T , or heating rate, β . Under isothermal conditions the kinetic equation for various temperatures, T_i , can be described in its logarithmic form as

$$\ln \frac{d\alpha}{dt} = \ln(A_{\alpha}f(\alpha)) - \frac{E_a}{RT_i} \quad (6-1)$$

where t is the time at a given extent of conversion, α , A is a pre-exponential factor, and R is the gas constant. The apparent activation energy, E_a , as a function of extent of conversion, α , is obtained from the slope of the plot $-\ln t_{\alpha,i}$ against T_i^{-1} . Hydrocarbon adsorption was measured at four different temperatures in 5% propene (Linde Gas, 10% propene (3.5) in He (5.0)) and 5% oxygen (Linde Gas, 20% O₂ (5.0) in He (5.0)) in helium (Air Liquide, 6.0) under isothermal conditions. Before reaction, the *in situ* cell was heated with a heating rate of 17 K/min to the desired temperature under nitrogen atmosphere. After temperature stabilization the atmosphere was switched to reaction gases. The extent of conversion was developed from the normalized absorption band intensity at 450 nm. Intensities were normalized to the maximum of the charge transfer (CT) transition band at room temperature.

CHNS Element Analysis

Elemental contents of C, H, N, and S were determined by using an analyzer (FlashEA 1112 NC, ThermoFinnigan/ThermoElectron) with CHNS-O configuration. Measurements were performed to investigate the amount of residual carbon within the supported metal oxide catalysts after catalytic reaction.

Catalytic Activity Tests

Quantitative catalysis measurements were performed in a laboratory fixed-bed reactor connected to an online gas chromatography system (CP-3800, Varian). The fixed-bed reactor consisted of a SiO₂ tube (30 cm length, 9 mm inner diameter) placed vertically in a tube furnace. The sample was placed on a frit in the center of the isothermal zone. The catalyst bed in the reactor was approximately 2.5 cm in height. In order to achieve a constant volume in the reactor and to reduce thermal effects, catalyst samples (between 10 mg and 233 mg) were diluted with boron nitride (Alfa Aesar, 99.5%) to result in an overall sample mass of 400 mg. The reactor was operated at low propene conversion levels (4–6%). Thus, secondary reactions were avoided and heat or mass transfer limitations were minimized. Hydrocarbons and oxygenated reaction products were analyzed using a Carbowax 52CB capillary column connected to an Al₂O₃/MAPD capillary column, and a fused silica restriction (25 m·0.32 mm), respectively. Each column was connected to a flame ionization detector. Permanent gases (O₂, N₂, CO₂, CO) were separated and analyzed using a “Permanent Gas Analyzer” (CP-3800, Varian) connected to a thermal conductivity detector.

For catalytic tests in selective propene oxidation a mixture of 5% propene (Linde Gas, 10% propene (3.5) in He (5.0)) and 5% oxygen (Linde Gas, 20% O₂ (5.0) in He (5.0)) in helium (Air Liquide, 6.0) was used in a temperature range of 20–450 °C. Reactant gas flow rates of oxygen, propene, and helium were adjusted through separate mass flow controllers (Bronkhorst) to a total flow of 40 ml/min. For catalytic tests in oxidative dehydrogenation (ODH) of propane a mixture of 5% propane (Linde Gas, 10% propene (3.5) in He (5.0)) and 7.5% oxygen (Linde Gas, 20% O₂ (5.0) in He (5.0)) in helium (Air Liquide, 6.0) was used in a temperature range of 20–500 °C. Flow rates of oxygen, propane, and helium were adjusted to

a total flow of 20 ml/min. To continuously monitor reactant and product gas flow a mass spectrometer (Omnistar, Pfeiffer) was connected in a multiple ion detection mode.

Conversion and product selectivity were determined on the basis of the measured volume fractions, Vol%. Conversion, X , of a key component, k , and selectivity, S , towards the desired product, p_n , were calculated by the following equations

$$X(k) = \frac{\text{Vol}\%(k)_{\text{in}} - \text{Vol}\%(k)_{\text{out}}}{\text{Vol}\%(k)_{\text{in}}} \quad (6-2)$$

$$S(p_n) = \frac{a(p_n)}{a(k)} \cdot \frac{\text{Vol}\%(p_n)_{\text{out}} - \text{Vol}\%(p_n)_{\text{in}}}{\sum \left(\frac{a(p_x)}{a(k)} \cdot \text{Vol}\%(p_x)_{\text{out}} \right)} \quad (6-3)$$

where $a(p_n)/a(k)$ is the fraction of carbon atoms in the desired product molecule, $a(p_n)$, relative to the carbon atoms in propene or propane ($a(k) = 3$). The selectivity of a product, p_n , calculated by eq. (6-3) was based on the sum of volume fractions, Vol%, of all other measured products, p_x . To ensure reasonable results for the calculated selectivities carbon balances were determined by the equation

$$\frac{\text{Vol}\%(C)_{\text{out}}}{\text{Vol}\%(C)_{\text{in}}} = \frac{\sum \left(a(p_x) \cdot \text{Vol}\%(p_x)_{\text{out}} + 3 \cdot \text{Vol}\%(C_3H_y)_{\text{out}} \right)}{3 \cdot \text{Vol}\%(C_3H_y)_{\text{in}}} \quad (6-4)$$

where $\text{Vol}\%(C_3H_y)$ is the volume fraction of propene for selective propene oxidation or propane for ODH, respectively. Carbon balances were always higher than 0.98.

Catalytic activity is reported in terms of turnover frequencies (TOF), *i.e.*, acrolein TOF for selective propene oxidation and propane-to-propene TOF for ODH reaction. Therefore, it was assumed that the catalytically active sites corresponded to transition metal surface atoms. In case of supported metal oxides, where the metal oxide species were supposed to be finely dispersed on the surface of the support, all metal atoms were considered as surface atoms. Hence, TOF values were calculated as number of acrolein, or propene molecules, formed per transition metal surface atom (V; Mo) per second. The experimental error of the given reaction rates was estimated from the relative errors of reactant gas flow rates, catalyst sample masses, and quantification of the transition metal content.

6.2 Influence of Heat and Mass Transport Limitations

When chemical reactions are accompanied by heat evolution, concentration and temperature gradients may occur between the catalyst particles. Analysis of such a system becomes rather complicated because reactant concentration and rate constant become a function of the position within the particle. Since selective propene oxidation and propane dehydrogenation are exothermic reactions it had to be ensured that the rates were measured without interference of heat or concentration gradients. Therefore, the Koros-Nowak test was performed. According to the Koros-Nowak criterion the reaction rate or turnover frequency (TOF; moles reacted per surface mole of the active material per second) must be invariant as the concentration of the active material is changed.[140] Table 6.1 gives the test results for selective propene oxidation and ODH reaction for catalysts with differing surface coverages at various catalyst concentrations.

Table 6.1 Results of the Koros-Nowak test to estimate the influence of heat and concentration gradients on the reaction rate during selective propene oxidation and oxidative propane dehydrogenation.

| Selective Propene Oxidation | | | |
|--|----------------------|---------------------------|---|
| V loading | Catalyst Mass | Propene Conversion | Acrolein TOF |
| | [mg] | [%] | [10⁻³ s⁻¹] |
| 5 wt.% | 29.7 | 6.0 | 0.33 |
| | 75.0 | 17.1 | 0.28 |
| 7 wt.% | 16.0 | 5.9 | 0.52 |
| | 27.6 | 9.4 | 0.49 |
| Oxidative Propane Dehydrogenation | | | |
| V loading | Catalyst Mass | Propane Conversion | Propane-to-Propene |
| | [mg] | [%] | TOF [10⁻³ s⁻¹] |
| 5 wt.% | 79.7 | 5.1 | 0.26 |
| | 131.5 | 8.5 | 0.25 |
| 8 wt.% | 69.2 | 5.4 | 0.24 |
| | 159.0 | 12.8 | 0.23 |

Apparantly, TOF values were not affected by changing catalyst concentrations. Hence, it was assumed that kinetic data were free of mass transport and heat limitations. Koros-Nowak test results are only shown for the supported vanadium oxide catalysts. Since reaction rates for supported molybdenum oxides were generally lower, it was assumed that mass transport and heat limitations were also negligible for *Mo/MgO/SBA-15*.

To ensure the absence of significant diffusion effects Weisz and Prater developed a criterion which is independent of the rate constant of the reaction.[141] The Weisz-Prater criterion provides a dimensionless number, C_{WP} , which contains only observable parameters. This is particularly useful since these parameters can easily be measured or calculated. For negligible diffusional limitations the Weisz-Prater criterion is given as

$$C_{WP} = \frac{r_{propene} \cdot \rho_{cat} \cdot L_{cat}^2}{C_{propene} D_{eff}} \ll 1 \quad (6-5)$$

with the observed reaction rate, $r_{propene}$, the catalyst density, ρ_{cat} , the length, L_{cat} , of a catalyst particle, the surface concentration, $C_{propene}$, of the reactant, and the Knudsen diffusivity, D_{eff} , within the pores. At 450 °C the diffusivity of propene was calculated to be $1.2 \cdot 10^{-6} \text{ m}^2 \text{ s}^{-1}$ at an average pore diameter of 6 nm (refer to the Appendix, A5). Assuming a particle length, L_{cat} , of 50 μm eq. (6-5) gives a Weisz-Prater criterion of $C_{WP} = 0.0008$. Since C_{WP} was well below one, influences of diffusional effects on catalytic reaction were neglected. Details on the estimation of the various parameters used in the calculation are given in the Appendix (A5).

6.3 Supported Vanadium Oxides

6.3.1 Catalytic Performance in Selective Propene Oxidation

The catalytic activity of the supported vanadium oxides was tested for selective propene oxidation at comparable propene conversions between 4–6%. Table 6.2 gives the product distribution during selective propene oxidation at 440 °C for vanadium oxide supported on *MgO/SBA-15* at various catalyst loadings compared to the product distribution for vanadium oxide supported on SBA-15, and bulk V_2O_5 , respectively. Besides acrolein, carbon oxides

were the main reactions products for *V/MgO/SBA-15*. Acrolein selectivity increased with increasing vanadium loading up to a loading of 7 wt.% V. At higher loadings acrolein selectivity remained constant. In contrast to the reaction products determined for vanadium oxide supported on *MgO/SBA-15*, vanadium oxide supported on SBA-15 presented a higher selectivity to acrolein. The selectivity was comparable to that of bulk V_2O_5 but with a higher formation of other unwanted oxygenates.

Table 6.2 Product distribution of propene oxidation for vanadium oxides supported on *MgO/SBA-15* at various catalyst loadings under isoconversional conditions in 5% propene and 5% oxygen at 440 °C. For comparison catalytic results of V/SBA-15 and bulk V_2O_5 are shown as well.

| V loading | Selectivity ^a [%] | | | | | Ratio | |
|-------------------------|------------------------------|----|----|--------|-----------------|-------|---------------------|
| | Acro | AA | PA | Others | CO ₂ | CO | CO ₂ /CO |
| 1 wt. % | 3 | 4 | 1 | 1 | 58 | 33 | 1.8 |
| 3 wt. % | 9 | 4 | 1 | - | 56 | 30 | 1.9 |
| 5 wt. % | 10 | 5 | 1 | 2 | 55 | 27 | 2.0 |
| 7 wt. % | 14 | 13 | 3 | 2 | 45 | 23 | 2.0 |
| 8 wt. % | 13 | 11 | 2 | 2 | 47 | 25 | 1.9 |
| 10 wt. % | 14 | 8 | 1 | 1 | 48 | 28 | 1.7 |
| V/SBA-15 (7.7 wt. %) | 23 | 19 | 29 | 5 | 12 | 12 | 1.0 |
| V_2O_5 | 26 | 20 | 2 | 2 | 27 | 23 | 1.2 |

^a Acro: acrolein; AA: acetic aldehyde; PA: propionic aldehyde; Others: mainly isopropyl alcohol and acetone.

To investigate the overall catalytic activity in terms of propene conversion of the various *V/MgO/SBA-15* catalysts, selective propene oxidation was carried out for similar quantities of vanadium oxide species. Therefore, catalyst masses used in the fixed-bed reactor were calculated to result in similar vanadium contents ($\sim 40 \mu\text{mol V}$). Fig. 6.1 depicts the propene conversion as a function of vanadium oxide surface coverage. Propene conversion exhibited a maximum at a surface coverage of 2–4 V atoms per nm^2 . Smaller conversions at low surface coverage can be explained by the presence of predominantly monomeric vanadium oxide tetrahedra. Isolated $[\text{VO}_4]$ units are considered to be inactive in propene oxidation.[142] This

observation is consistent with theoretical calculations by Witko *et al.* on propene adsorption on the V_2O_5 surface. They showed that a propene molecule preferentially adsorbed with its C–H group on the bridging oxygen atom between two vanadium centers, leading to the formation of a C–O bond.[143] At surface coverages above 4 V atoms per nm^2 the higher degree of oligomerization did not lead to a higher catalytic activity. Conversely, propene conversion even decreased at higher surface coverages due to the presence of crystalline V_xO_y species.

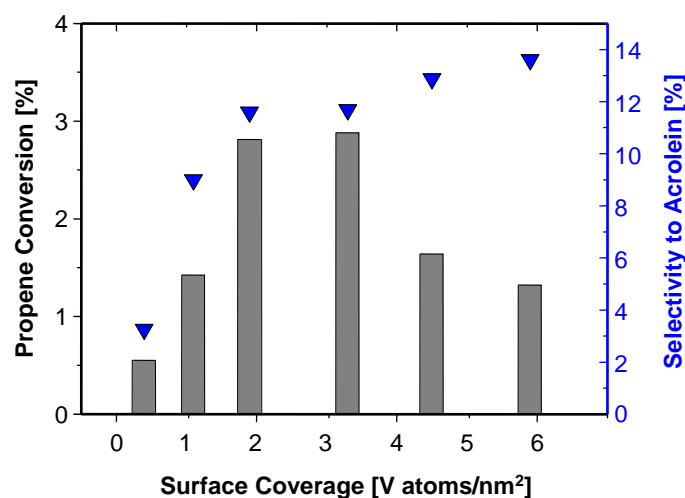


Fig. 6.1 Propene conversion (left axis), and selectivity towards acrolein (right axis) of $V/MgO/SBA-15$ as a function of vanadium oxide surface coverage. Data were measured in a fixed-bed reactor at 400 °C. Sample masses were calculated to result an equal amount of vanadium ($\sim 40 \mu\text{mol V}$).

In contrast to the observed propene conversion, selectivity towards the selective oxidation product acrolein followed a different trend. At surface coverages up to approximately 2 V atoms per nm^2 selectivity increased with increasing coverage. Beyond this point only a slight increase in selectivity was observed. These findings were further investigated by studying the relationship between acrolein formation and vanadium oxide surface coverage.

Acrolein TOF as a Function of Surface Coverage

The acrolein turnover frequency (TOF) was correlated to the vanadium oxide surface coverage. Fig. 6.2 shows a comparison of the acrolein TOF of vanadium oxide supported on $MgO/SBA-15$ and of oxides supported on bare SBA-15. TOF values strongly varied as a function of surface coverage. A similar dependency on surface coverage and number of oligomeric

vanadium oxide units was reported by Zhao and Wachs for vanadium oxide supported on various supports. They observed increasing acrolein TOF values with increasing surface coverage.[144] The acrolein TOF as a function of surface coverage of vanadium oxide supported on *MgO/SBA-15* and SBA-15 (Fig. 6.2) exhibited a “volcano type” behavior. Initially, acrolein formation increased with increasing surface coverage and then decreased at higher coverage. A maximum TOF seemed to be present for an optimal surface coverage of 3–4 V atoms per nm² on *MgO/SBA-15*.

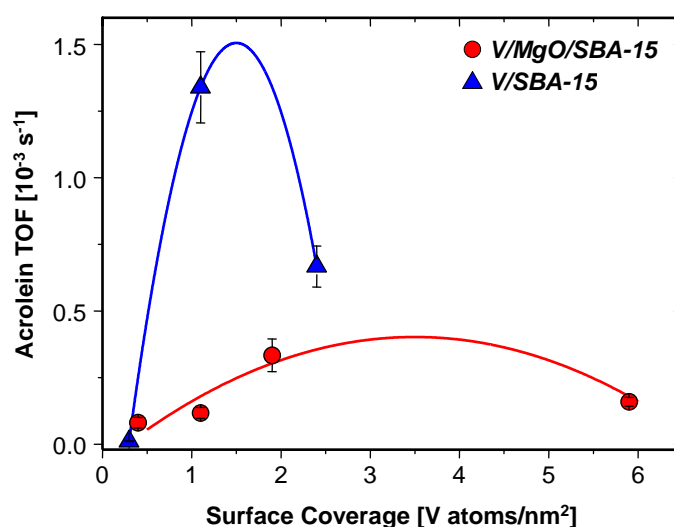


Fig. 6.2 Acrolein turnover frequency (TOF) of vanadium oxide catalysts supported on *MgO/SBA-15*, and on bare SBA-15 as a function of surface coverage. Rates were measured under isoconversional conditions in 5% propene and 5% O₂ at 440 °C.

As already discussed above, the vanadium oxide units became proceedingly oligomerized with increasing surface coverage (refer to Chap. 5.2). Therefore, the catalytic activity was strongly influenced by the degree of oligomerization of the catalyst oxide units. For the *MgO/SBA-15* support a degree of oligomerization of 1–2 V–O–V bonds was estimated at the optimal surface coverage (compare structure configuration in Chap. 5, Fig. 5.23). Apparently, oxidation of propene to acrolein requires active sites consisting of at least dimeric vanadium oxide units. This assumption is in agreement with the literature.[142] Hence, for a catalytic reaction exhibiting a transfer of more than two electrons, multiple linked [VO₄] sites need to be involved.[145] Solsona *et al.* studied the oxidation of propene for unsupported and SiO₂-supported VMgO catalysts. Significant acrolein selectivities in the range of 3–9% were de-

ected only for catalysts containing *pyro*- $\text{Mg}_2\text{V}_2\text{O}_7$ or *meta*- MgV_2O_6 . *Ortho*- $\text{Mg}_3\text{V}_2\text{O}_8$, which consists of isolated $[\text{VO}_4]$ tetrahedra, mainly produced carbon oxides without detectable acrolein formation.[120] These findings corroborate the observation that acrolein formation only took place in the presence of oligomerized vanadium oxide units.

At higher loading maximum coverage of the vanadium oxide units on the surface of the support was reached. Apparently, this led to a decreasing acrolein TOF. Above or close to monolayer coverage nanocrystalline vanadium oxide species, *e.g.*, V_2O_5 , may form. The decreasing acrolein formation was caused either by the formation of a less selective vanadium oxide species or, more likely, by a lower number of accessible active sites in nanocrystalline oxides. At loadings of 10 wt.% V on *MgO/SBA-15* broad diffraction peaks of nanocrystalline V_2O_5 were observed in the X-ray diffraction patterns, thus corroborating the assumption of crystalline V_xO_y species (Chap. 5, Fig. 5.3).

Influence of Catalyst Structure

The optimal surface coverage was dependent on the oxide support. Hence, according to the “volcano curve” (Fig. 6.2), the optimal vanadium oxide coverage on SBA-15 could be estimated to approximately 1.5 V atoms per nm^2 . Conversely, the optimal surface coverage on the *MgO/SBA-15* support shifted to a higher value of 3–4 V atoms per nm^2 . This effect was attributed to the higher tendency of the vanadium oxide units to form oligomeric species on acidic SBA-15 than on alkaline *MgO/SBA-15*. A comparison of the UV-Vis absorption edge energy of dehydrated V/SBA-15 and V/*MgO/SBA-15* was presented in Chap. 5 (Fig. 5.18). Apparently, a smaller degree of oligomerization was observed for vanadium oxides on *MgO/SBA-15* at similar vanadium concentrations. However, for both support materials the optimal surface coverage necessary for a maximum acrolein TOF implied a degree of oligomerization in the same range of 1–2 V–O–V bonds.

The Optimal Surface Coverage

In an attempt to design the optimal surface coverage with a maximum in acrolein formation, two additional V/*MgO/SBA-15* samples were prepared with a surface coverage of 3.3 and 4.5 V atoms per nm^2 . It was shown that the measured acrolein turnover frequency (TOF) at a surface coverage of 3.3 V atoms per nm^2 was indeed located at the maximum of the “volcano

curve”. Fig. 6.3 depicts the acrolein TOF as a function of surface coverage with the two additional points. The maximum of the “volcano plot” turned out to be located in a narrow range of surface coverage between 3 and 3.5 V atoms per nm². Considering the additional point at 4.5 V atoms per nm² the existence of the relatively sharp maximum was confirmed by a decrease in catalytic activity for more than 50% after exceeding the optimal range.

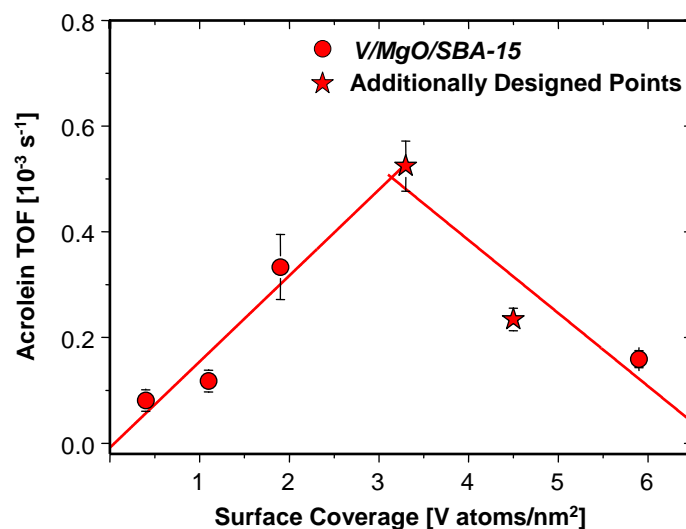


Fig. 6.3 Acrolein TOF of vanadium oxide catalysts supported on *MgO/SBA-15* as a function of surface coverage with the rates of the additionally designed catalysts. The additional points gave rise to a sharpened “volcano plot”.

6.3.2 Behavior under Propene Oxidizing Conditions

During treatment of the vanadium oxide supported on *MgO/SBA-15* in propene/oxygen the structural characteristics of the vanadium oxide persisted in the temperature range between 25 °C and 450 °C. The X-ray absorption near edge structure (XANES) with its pronounced pre-edge peak resembled that of a tetrahedrally coordinated vanadium center (compare Chap. 5.2.3). In the measured temperature range no structural changes were observed. Evolution of the V K edge XANES and the Fourier transformed X-ray absorption fine structure (XAFS) $\chi(k)$ under propene oxidizing conditions is depicted in the Appendix (Fig. A 3.1).

To investigate electronic changes of the vanadium center under catalytic reaction conditions *in situ* DR-UV-Vis spectroscopy was conducted under similar reaction conditions. DR-UV-Vis spectroscopy is known to be a useful tool to estimate the extent of reduction of dis-

persed metal oxides.[64] Weak bands corresponding to $d-d$ transitions of partially reduced vanadium oxide species can be sensitively detected in the region around 700 nm. Fig. 6.4 shows the evolution of the absorption band intensity at 700 nm during temperature programmed reaction in propene and oxygen. The overall DR-UV-Vis spectra measured during reaction are depicted in the inset of Fig. 6.4. The main absorption band around 280 nm was attributed to the V–O charge transfer transition and exhibited a band broadening with increasing temperature accompanied by an intensity increase. This temperature dependency was observed to be reversible. Therefore, changes in the main absorption band were ascribed to temperature induced effects.

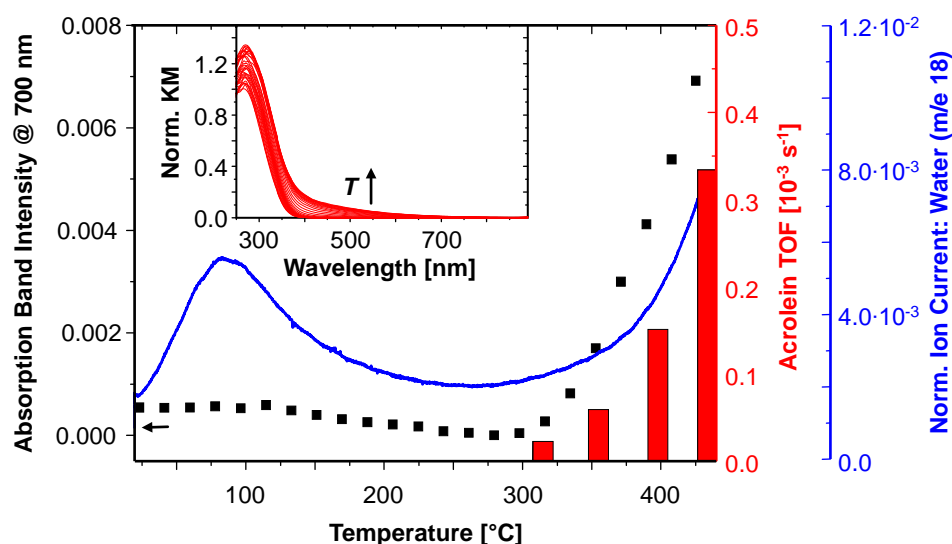


Fig. 6.4 Evolution of the absorption band intensity at 700 nm (black squares) correlated to acrolein TOF (red bars), and water signal (blue line) detected by online mass spectrometry. Absorption band intensity was evaluated from the DR-UV-Vis spectra (shown in the inset) during temperature programmed reaction in propene/oxygen (RT \rightarrow 425 °C, 4.25 K/min, 5% propene, 5% oxygen in He).

The absorption band intensity at 700 nm increased at 300 °C indicating a partial reduction of the vanadium oxide species. Together with the increasing band intensity, formation of water was detected by mass spectrometry. This confirmed the ongoing reduction process. Evolution of water at lower temperature (\sim 100 °C) was assigned to the release of physisorbed water from the surface of the support material as commonly observed for high surface area oxides. The reduction of the vanadium oxide species at temperatures above 300 °C was directly correlated to the onset of catalytic activity. The selective oxidation product acrolein was formed at

an onset temperature of 300 °C. Acrolein TOF measured by gas chromatography increased with proceeding reduction. Therefore, a certain degree of reduction seemed to be required for catalytic reaction. It is widely accepted that the active sites during catalysis involve mixed valence compounds, as for instance V^{5+} – V^{4+} . [54] Commonly, a certain degree of reduction of vanadium oxide catalysts is observed in selective oxidation of hydrocarbons. [146] The degree of reduction depended on the hydrocarbon-to-oxygen ratio as well as on the C–H bond strength. For selective oxidation of *o*-xylene a degree of reduction of 20–30% has been observed for vanadium oxides supported on titania, resulting in an average oxidation state between 4.7 and 4.8. [56]

From *in situ* investigations of *V/MgO/SBA-15* during selective oxidation of propene it was concluded that the overall structure of the supported catalysts remained unchanged in the measured temperature range up to 450 °C. The onset of catalytic activity, *i.e.*, acrolein formation, correlated to a partial reduction of the vanadium oxide species. Reduction was initiated at an onset temperature around 300 °C.

6.3.3 Catalyst Reducibility

Reducibility of the catalyst species directly influences catalytic performance in selective oxidation reactions. [55,70,147] Thus, reduction studies provide indirect information about the ability of the catalyst to insert oxygen into a hydrocarbon molecule. Oxygen insertion is an essential step in selective oxidation reactions. In order to characterize reducibility of the supported vanadium oxide catalysts, *in situ* X-ray absorption spectroscopy (XAS) was conducted under reducing conditions. Evolution of V K edge X-ray absorption near edge structure (XANES) of 5 wt.% *V/MgO/SBA-15* during temperature programmed treatment in propene is depicted in Fig. 6.5 (left). The overall XANES shape remained unchanged up to a temperature of 250 °C. Higher temperatures led to a decreasing pre-edge peak (Fig. 6.5, right), indicating either a change of tetrahedral geometry or a reduction of the vanadium oxide species. The decreasing pre-edge peak height coincided with a shift of the absorption edge position to lower energies.

A dependency of the shift in V K edge position on a change in oxidation state was previously reported by Chaurand *et al.* [148] In order to determine the evolution of the average

vanadium oxidation state during reduction a calibration curve was constructed from V K edge shifts of various vanadium oxide references. Following the procedure described by Chaurand *et al.* the shift of the absorption edge position of the references was plotted against their average oxidation state.[148] Fig. 6.6 depicts the linear relationship between average vanadium oxidation state (Ox) and shift of absorption edge position ($E_{1/2}-E_0$) of the measured references. The obtained relationship could be expressed by

$$E_{1/2}-E_0 = 6.09(\pm 0.55) + 2.02(\pm 0.13) \text{ eV}^{-1} \cdot Ox. \quad (6-6)$$

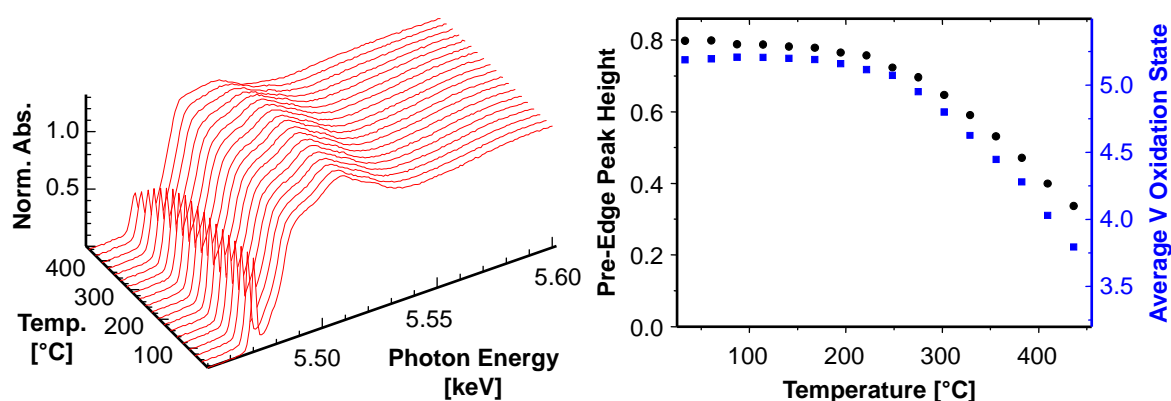


Fig. 6.5 Left: evolution of V K edge XANES spectra of *V/MgO/SBA-15* (5 wt.% V) and right: comparison of the decreasing pre-edge peak height (left axis) to the average V oxidation state (right axis) during temperature programmed reduction in propene (RT → 440 °C, 4 K/min, 5% propene in He).

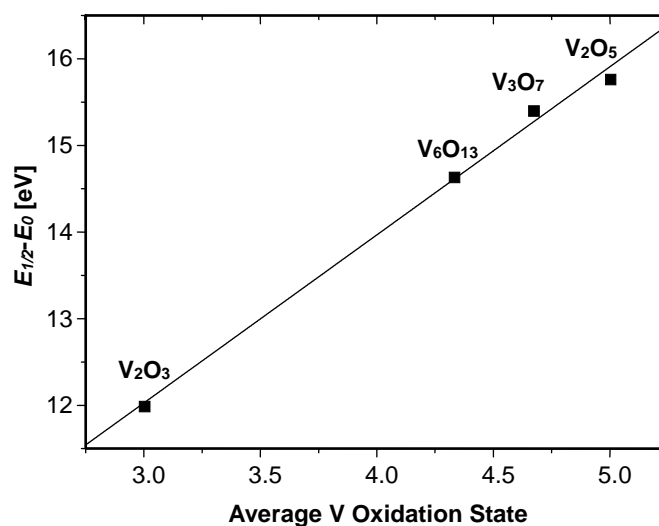


Fig. 6.6 Absorption edge energy shift as a function of average oxidation state for various vanadium oxide references. The energy shift was calculated as the difference between tabulated vanadium K edge energy, E_0 (5.465 keV), and measured energy half way up the normalized edge step, $E_{1/2}$.

The linear correlation obtained for the references (eq. (6-6)) was directly applied to the shift of absorption edge position in the XANES of *V/MgO/SBA-15* under reducing atmosphere. At temperatures above 250 °C the V^{5+} oxide species was reduced to an average oxidation state of ~ 3.7 . The degree of reduction followed a trend similar to that of the decreasing pre-edge peak height (compare Fig. 6.5, right). Hence, the decreased pre-edge peak height is more likely caused by a reduction of the vanadium oxide species rather than a change in local geometry. A mixed valence state of fully oxidized V^{5+} centers and reduced V^{4+} , and V^{3+} centers, respectively, was assumed. However, since the oxidation state evaluated by XANES analysis only reflects an average value a differentiation between V^{4+} and V^{3+} centers was not possible.

Onset temperature and degree of reduction of the vanadium oxide species was found to be dependent on catalyst loading and degree of oligomerization. Table 6.3 summarizes onset temperature for the reduction in propene and average vanadium oxidation state of the supported vanadium oxides at various catalyst loadings together with their average number of covalent V–O–V bonds (*No. (V-O-V)*), derived from DR-UV-Vis data (refer to Chap. 5.2.2).

Table 6.3 Average number of covalent V–O–V bonds (*No. (V-O-V)*, derived from DR-UV-Vis data) together with the average oxidation state of the vanadium centers in *V/MgO/SBA-15* at various catalyst loadings after temperature programmed reduction in 5% propene in He. The average V oxidation state was derived from XANES data (for details see text).

| V loading | Average <i>No. (V-O-V)</i> | Average V Oxidation State | Reduction Onset Temperature [°C] |
|------------------|---------------------------------------|--------------------------------------|---|
| 1 wt. % | 0 | 4.2 | 355 |
| 3 wt. % | 0.25 | 4.1 | 354 |
| 5 wt. % | 0.99 | 3.7 | 317 |
| 10 wt. % | 1.56 | 3.6 | 247 |

With increasing catalyst loading the average oxidation state decreased while the reduction onset temperature shifted to lower values. Vanadium oxide oligomerization progressively increased with increasing catalyst loading. Therefore, the achievable degree of reduction was higher for higher oligomerized vanadium oxides. A similar trend was observed by Went *et al.* for reduction of vanadium oxide supported on titania with ammonia. They reported that adja-

cent vanadium oxide units were necessary for reduction. Vanadyl bonds, *i.e.*, $V^{5+}=O$, were not reduced.[149] It was concluded that bridging V–O–V bonds facilitated reduction. The isolated $[VO_4]$ units present on the 1 wt.% $V/MgO/SBA-15$ sample were only slightly reduced to an average oxidation state of 4.2 at the highest onset temperature of approximately 350 °C. Reduction of the higher oligomerized $[VO_4]$ units with an average number of 1.56 V–O–V bonds present on the 10 wt.% $V/MgO/SBA-15$ sample was initiated at a significantly lower temperature of about 250 °C leading to an average oxidation state of 3.6.

6.3.4 Redox Properties of the Catalyst

After investigating the reducibility of the supported vanadium oxides, *in situ* X-ray absorption spectroscopy (XAS) was performed to study the redox behavior of the catalysts. Evolution of the V K edge X-ray absorption near edge structure (XANES) during reduction and reoxidation is depicted in Fig. 6.7. The $V/MgO/SBA-15$ catalyst underwent a temperature programmed reaction in propene/oxygen in a temperature range between 30 °C and 450 °C (Fig. 6.7, I.). To induce partial reduction of the vanadium oxide catalysts, the gas atmosphere was temporarily changed to reducing conditions by switching off the oxygen under isothermal conditions at 450 °C (Fig. 6.7, II.).

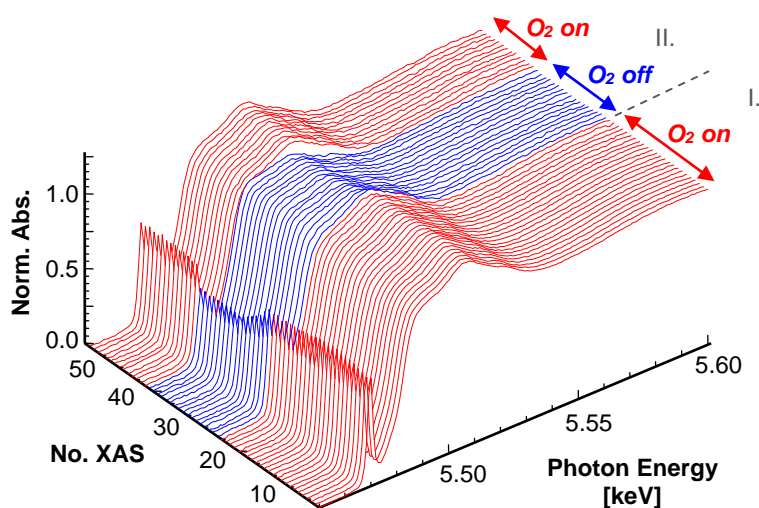


Fig. 6.7 Evolution of V K edge XANES spectra of $V/MgO/SBA-15$ (10 wt.% V). I.) During temperature programmed reaction in propene/oxygen (RT \rightarrow 450 °C, 4 K/min, 5% propene, 5% oxygen in He). II.) After reaching the target temperature of 450 °C a reduction/reoxidation cycle was conducted by temporarily switching off the oxygen. After a time period of \sim 20 min the oxygen was switched back on.

As it was already discussed above no major structural changes were observed during temperature programmed treatment in propene oxidizing atmosphere. During isothermal reduction in propene a decreasing pre-edge peak indicated reduction of the vanadium centers in *V/MgO/SBA-15*. The degree of reduction was obtained by analyzing the shift in absorption edge position as described above (Chap. 6.3.3). Fig. 6.8 shows the evolution of the average V oxidation state. During the reduction period of ~ 20 min the average oxidation state was reduced from 5 to approximately 3.8. These results were similar to the oxidation state obtained after temperature programmed reduction (compare Fig. 6.5, right). Reduction and reoxidation of the supported vanadium oxide species exhibited different reaction rates. While reduction took place over a time period of 20 minutes, reoxidation very rapidly occurred after addition of oxygen. Within the accessible time resolution (84 seconds per spectrum) no intermediate steps were recorded. However, the initial oxidation state was not completely recovered after reoxidation (Fig. 6.8). Thus, partially reduced vanadium oxide species remained under catalytic reaction conditions after the oxidation treatment.

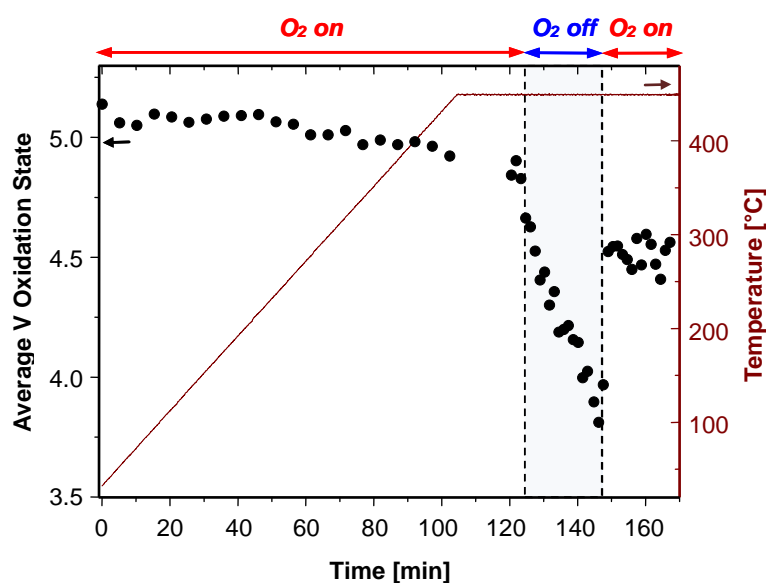


Fig. 6.8 Evolution of the average V oxidation state of *V/MgO/SBA-15* (10 wt.% V) evaluated from the *in situ* XANES measurements shown in Fig. 6.7 during temperature programmed reaction in propene/oxygen atmosphere and during isothermal reduction/reoxidation cycle at 450 °C.

To further elucidate the correlation of reduced species and catalytic activity with better time resolution, *in situ* DR-UV-Vis spectroscopy was performed. Evolution of DR-UV-Vis spectra

of a supported vanadium oxide (5 wt.% V) under isothermal propene oxidizing conditions is depicted in the Appendix (Fig. A 3.2). Two reduction/reoxidation cycles were carried out by periodically switching the gas atmosphere from propene oxidizing (5% propene, 5% O₂) to reducing conditions (5% propene). Under reducing atmosphere absorption bands corresponding to *d-d* transitions of partially reduced vanadium centers appeared around 700 nm. Thus, a reduction of the supported vanadium oxide species was indicated. Evolution of the band intensity at 700 nm under reducing conditions and during reoxidation is shown in Fig. 6.9 together with the ion current of acrolein.

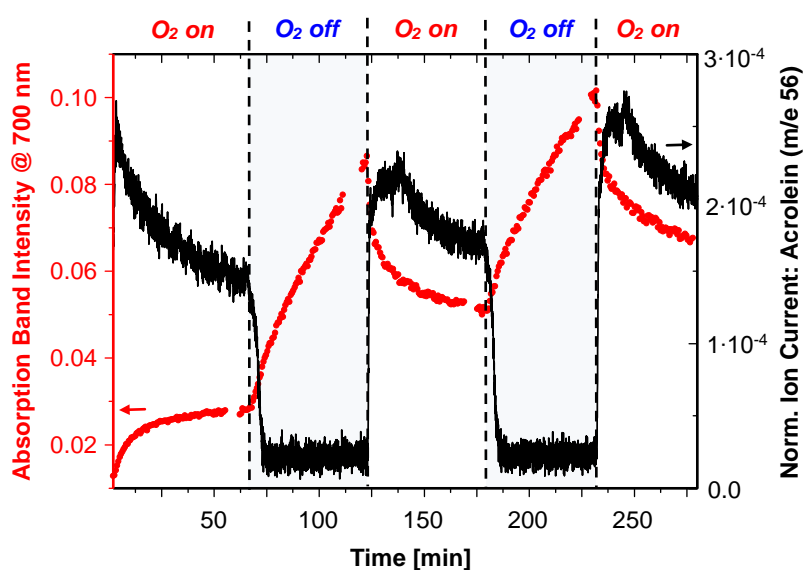


Fig. 6.9 Evolution of the absorption band intensity at 700 nm of *V/MgO/SBA-15* (5 wt.% V) evaluated from the DR-UV-Vis spectra shown in Fig. A 3.2 during reduction/reoxidation cycles. Band intensities (left axis) were correlated to acrolein formation (right axis).

Upon reoxidation of the vanadium oxides the absorption bands around 700 nm did not completely disappear. Hence, an offset in absorption band intensity after each reduction/reoxidation cycle was visible. The enhanced degree of reduction correlated to an increasing acrolein formation. Thus, conducting redox cycles led to an active vanadium oxide species with partially reduced vanadium centers. Therefore, it might be assumed that selectivity to acrolein correlated to the transformation of the fully oxidized vanadium oxide species to lower valent oxides. An enhanced catalytic activity for the reduced oxide V₆O₁₃ in selective oxidation reactions compared to fully oxidized V₂O₅ was documented in the literature.[150] A similar behavior was reported by Haber in selective oxidation of *o*-xylene over V₂O₅/TiO₂

catalysts. He claimed that the active catalyst consists of a mixture of V^{5+} and V^{4+} , resembling a V_6O_{13} -type structure. Under reaction conditions the vanadium suboxides were stabilized by the presence of potassium. Conversely, pure V_2O_5 under similar reaction conditions was reoxidized to V^{5+} . [146] Therefore, it seemed likely that the presence of magnesium in the $V/MgO/SBA-15$ samples may stabilize the partially reduced vanadium ions under reducing atmosphere and inhibited reoxidation in the presence of oxygen. For bulk vanadium oxides a stabilization effect is caused by the ability of vanadium oxide to form bronze-like structures by intercalation of alkali or alkaline earth metals (M). A variety of nonstoichiometric $M_xV_2O_5$ compounds exist with vanadium being in the mixed valence states +IV and +V. [151] These compounds usually form at temperatures around 800 °C in a solid state reaction.

6.3.5 Catalytic Performance in Oxidative Dehydrogenation of Propane

In addition to investigating catalytic activity in selective propene oxidation, the $V/MgO/SBA-15$ catalysts were studied in the oxidative dehydrogenation (ODH) of propane. In order to avoid misunderstandings with the results for propene oxidation, catalytic activity, *i.e.*, turnover frequency (TOF), for ODH reaction is reported as propane-to-propene TOF. TOF values were calculated as propene molecule formed per surface vanadium atom per second. Catalytic test results obtained under isoconversional conditions (~ 5% propane conversion) at 500 °C are presented in Fig. 6.10. A correlation between vanadium oxide surface coverage and catalytic activity as for the selective oxidation of propene was not observed. Propane-to-propene TOF showed no trend for the measured catalysts with surface coverages between 0.4 and 5.9 V atoms per nm^2 but varied between $0.15 \cdot 10^{-3} s^{-1}$ and $0.30 \cdot 10^{-3} s^{-1}$.

At a propane conversion of ~ 5% oxidative dehydrogenation to propene was the major reaction with propene selectivities between 55–69% for all $V/MgO/SBA-15$ catalysts. Besides propene and the total oxidation products CO_2 and CO , small quantities of acrolein were detected (~ 1%). Selectivity to propene was considerably higher than for bulk vanadium-magnesium mixed oxide catalysts reported in the literature.

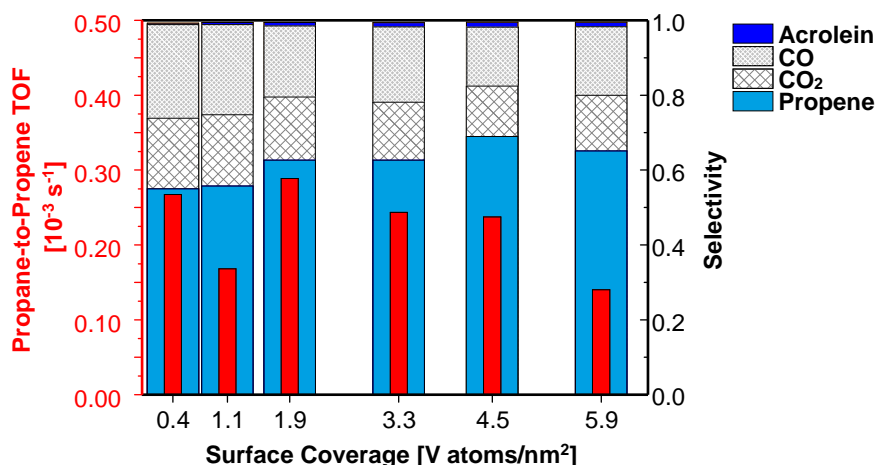


Fig. 6.10 Comparison of propane-to-propene TOF (left axis) and product distribution (right axis) in ODH reaction at similar propane conversions ($\sim 5\%$) for vanadium oxide supported on *MgO/SBA-15* at various surface coverages (reaction conditions: 5% propane, 7.5% O₂ in He, $T = 500$ °C).

Balderas-Tapia *et al.* observed selectivities to propene between 23–31% at similar conversions for VMgO catalysts with differing amounts of vanadium oxide. Major reaction products were carbon oxides. Conversely, no acrolein formation was detected.[68] Differences in product selectivity might be due to the higher quantities of vanadium oxide within the catalysts used by Tapia and coworkers. However, a more reasonable explanation was the higher dispersion of the surface vanadium oxides on *MgO/SBA-15*, thus leading to a better separation of the "active catalyst sites". A similar conclusion has been drawn by Solsona *et al.* who investigated the catalytic activity in propane ODH of silica-supported V-Mg mixed oxides. They reported the highest selectivities to propene at high Mg/V ratios where magnesium orthovanadate Mg₃V₂O₈ formed the majority phase.[120] It has been proposed that tetrahedral [VO₄] units are the active sites in oxidative dehydrogenation.[68,152] A high dispersion of these units, thus leading to isolated sites, was reported to be beneficial for propene formation, while oligomeric vanadium oxide species may lead to consecutive propene combustion reactions.[153] In contrast to the selective oxidation of propene, with four electrons being transferred in order to yield acrolein, ODH of propane is a two-electron transfer reaction. Theoretically, this process requires only one active site.[145] Therefore, it seemed reasonable that propane-to-propene TOF did not exhibit a dependency on surface coverage. In contrast to propene oxidation, oligomerized vanadium oxide species did not lead to an enhanced catalytic activity in ODH. The lowest propane-to-propene TOF value observed for the highest surface

coverage (5.9 V atoms/nm^2) was most likely due to the partial formation of crystalline V_2O_5 (compare Chap. 5.2). The vanadium oxide species within the crystallites did not contribute in ODH reaction. Therefore, a lower dispersion of the vanadium oxide species led to a smaller number of accessible surface sites.

Influence of Vanadium Oxide-Support Interaction on ODH Reaction

Selectivity during selective oxidation of propene was shown to strongly correlate to the nature of the vanadium oxide-support interaction. Accordingly, differences in catalytic activity for propane ODH of vanadium oxide supported on *MgO/SBA-15* and silica SBA-15 were expected. A comparison of the catalytic test results showed a similar selectivity to propene for both catalysts. Catalytic data of V/SBA-15 are given in the Appendix (Fig. A 3.4). Selectivities to consecutive reaction products (mainly acrolein; other: acetic aldehyde and acetone) ranged between 4–7% and were higher for vanadium oxide supported on SBA-15 than those observed for *V/MgO/SBA-15*. Liu *et al.* observed substantial amounts of ethene when investigating propane ODH on V/SBA-15 catalysts.[154] Conversely, no ethene formation as a result of propane cracking was detected here. Differences in product distribution were most likely due to deviating reaction parameters used by Liu and coworkers. They operated at substantially higher propane conversions ($\sim 30\%$) and a higher reaction temperature of $600 \text{ }^\circ\text{C}$.[154]

Similar to the differences in catalytic activity for propene oxidation, propane-to-propene TOF in ODH reaction differed considerably for the oxide catalysts supported on SBA-15 compared to that of *V/MgO/SBA-15*. Fig. 6.11 depicts a comparison between TOF values for varying vanadium oxide surface coverages on both support materials. Catalytic activity in terms of propane-to-propene TOF for V/SBA-15 was more than twice as high as that of vanadium oxide supported on *MgO/SBA-15*. The higher catalytic activity of V/SBA-15 was most likely due to a better reducibility of the supported vanadium oxide units (refer to Chap. 6.5.1). Furthermore, the acidic nature of SBA-15 may also enhance consecutive reaction of the electron-rich propene molecule. Hence, for V/SBA-15 significantly higher quantities of oxygenates like acrolein were detected than for the oxides supported on alkaline *MgO/SBA-15*.

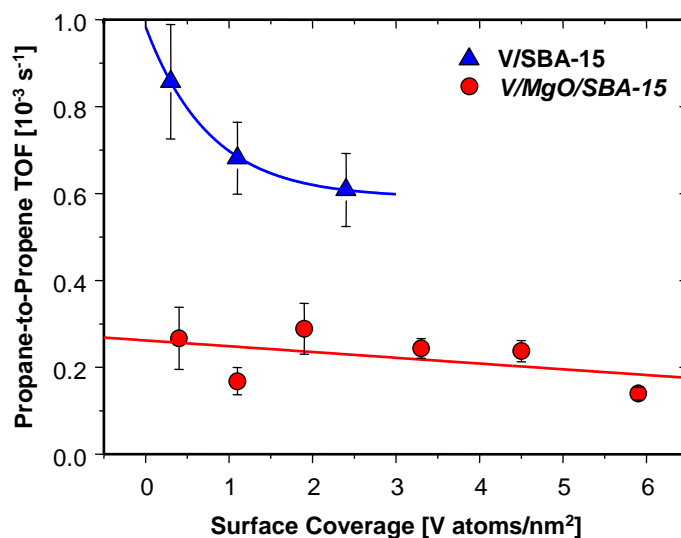


Fig. 6.11 Propane-to-propene TOF in ODH reaction of vanadium oxide catalysts supported on *MgO/SBA-15* (red circles) and silica *SBA-15* (blue triangles) as a function of surface coverage. Reaction conditions: 5% propane, 7.5% O₂ in He, $T = 500$ °C.

Interestingly, catalytic performance of V/SBA-15 seemed to increase with decreasing surface coverage. Regarding the given error bars and the few data points, a reliable trend could not be concluded. However, a similar observation was reported for vanadium oxides supported on SBA-15 and MCM-41. A higher catalytic activity at higher overall surface area was ascribed to the better dispersion of the catalyst units on the surface of the support.[154] Therefore, lower propane-to-propene TOF values at higher surface coverage, observed in Fig. 6.11, were most likely due to the presence of higher oligomerized vanadium oxide units. Blasco *et al.* suggested that selectivity in ODH reaction depended on the distance between the catalytically active sites. Accordingly, a sufficiently large alkane molecule might react with two adjacent vanadium oxide units, resulting in deeper oxidation of the alkane.[69] This effect presumably caused the decreasing propane-to-propene TOF at higher surface coverage. Additionally, formation of nano-crystalline V₂O₅ led to a decreasing number of catalytically active surface sites. UV-Vis data of the V/SBA-15 samples with surface coverages of 1.1 and 2.4 V atoms per nm² confirmed the presence of small amounts of V₂O₅ crystallites.[110]

6.4 Supported Molybdenum Oxides

6.4.1 Catalytic Performance in Selective Propene Oxidation

Catalytic activity in selective propene oxidation was tested for molybdenum oxides supported on *MgO/SBA-15* at various catalyst loadings. Results were compared to the data of molybdenum oxide supported on silica SBA-15 (5 wt.% Mo) and a magnesium molybdate (MgMoO_4) reference. Fig. 6.12 shows a comparison of product distribution and acrolein turnover frequency (TOF) at similar propene conversions (4–6%) at 440 °C.

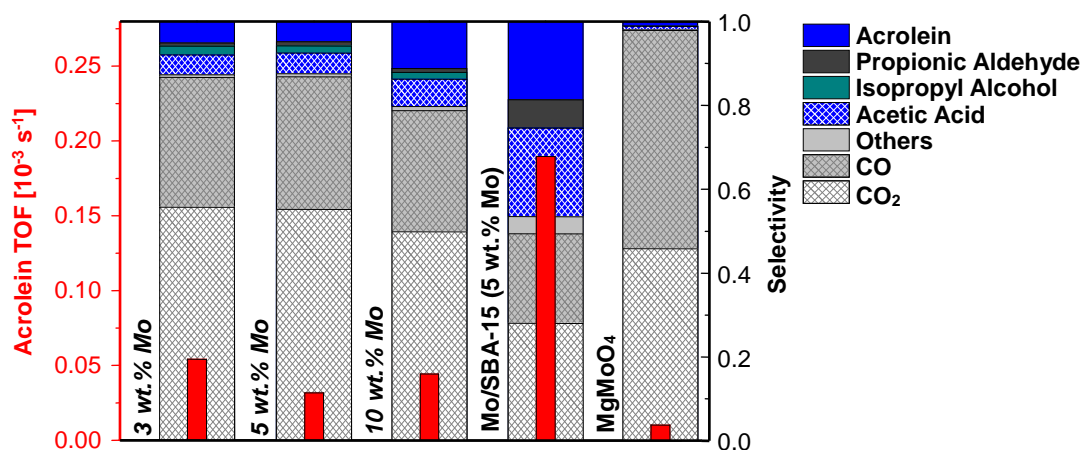


Fig. 6.12 Acrolein TOF (left axis) and product distribution (right axis) at similar propene conversions for molybdenum oxide on *MgO/SBA-15* at various catalyst loadings. Data were compared to the catalytic results of molybdenum oxide supported on SBA-15 (5 wt.% Mo) and bulk magnesium molybdate (MgMoO_4).

Propene conversion of *Mo/MgO/SBA-15* with a loading of 1 wt.% Mo was too low to yield reliable results. Hence, product distribution for 1 wt.% *Mo/MgO/SBA-15* has been omitted. The acrolein TOF remained similar for the evaluated *Mo/MgO/SBA-15* samples with loadings between 3 wt.% and 10 wt.% Mo. Therefore, a correlation between molybdenum oxide surface coverage and acrolein formation was not observed. The similar acrolein TOF values were attributed to the similar structure of the supported molybdenum oxides. Degree of oligomerization and local geometry of the $[\text{MoO}_4]$ units were largely independent of molybdenum oxide loading and surface coverage (refer to Chap. 5.3).

During selective propene oxidation carbon oxides were the main oxidation products. Table 6.4 summarizes the product distribution for *Mo/MgO/SBA-15* compared to the data of

molybdenum oxide supported on silica SBA-15 (5 wt.% Mo) and a MgMoO_4 reference. The predominately isolated tetrahedral $[\text{MoO}_4]$ units on MgO/SBA-15 were rather inactive in selective oxidation. In addition to acrolein, acetic acid, isopropyl alcohol, and propionic aldehyde were formed by selective oxidation. A comparison to molybdenum oxide supported on SBA-15 showed a significantly higher catalytic activity of Mo/SBA-15 . Acrolein TOF values of Mo/SBA-15 were about three times higher than those for Mo/MgO/SBA-15 .

Table 6.4 Product distribution of propene oxidation on molybdenum oxide supported on MgO/SBA-15 at various catalyst loadings and surface coverage, $\Phi_{\text{Mo atoms}}$, compared to the data of molybdenum oxide on SBA-15 and a MgMoO_4 reference (propene conversion: 4–6%). Additionally, the CO_2/CO ratio is given. For 1 wt.% Mo/MgO/SBA-15 a sufficient propene conversion could not be achieved under the given experimental conditions (5% propene, 5% O_2 in He, $T = 440^\circ\text{C}$).

| Mo loading | $\Phi_{\text{Mo atoms}}$ [Mo atoms/nm ²] | Selectivity ^a [%] | | | | | | | Ratio CO_2/CO |
|-------------------------------|---|------------------------------|----|-----|----|--------|---------------|----|----------------------------------|
| | | Acro | PA | Iso | AA | Others | CO_2 | CO | |
| 1 wt. % | 0.2 | - | - | - | - | - | - | - | - |
| 3 wt. % | 0.6 | 5 | 1 | 2 | 5 | - | 55 | 32 | 1.7 |
| 5 wt. % | 1.3 | 5 | 1 | 2 | 5 | - | 55 | 32 | 1.7 |
| 10 wt. % | 4.2 | 11 | 1 | 2 | 7 | - | 50 | 29 | 1.7 |
| Mo/SBA-15 (5 wt. % Mo) | | 19 | 7 | - | 21 | 4 | 28 | 21 | 1.3 |
| MgMoO₄ | | 1 | - | - | 1 | - | 46 | 52 | 0.9 |

^a Acro: acrolein; PA: propionic aldehyde; Iso: isopropyl alcohol; AA: acetic aldehyde; Others: mainly acetone and acetic acid.

It is assumed that the structure of the molybdenum oxide species built on the different support materials played a crucial role. Grasselli *et al.* considered the concept of site isolation fundamental for selective oxidation catalysts. Accordingly, for selective oxidation of alkenes the reactive surface oxygen groups must be spatially isolated, ideally containing two to five oxygen atoms per group.[51] However, the site isolation hypothesis does not consider the case of single, isolated metal centers. The low acrolein TOF for molybdenum oxide supported on MgO/SBA-15 probably originated from the presence of a few dimeric molybdenum oxide species (compare Chap. 5.3). Gryzbowska-Swierkosz proposed a correlation between catalytic activity and character of the metal oxygen bond (M–O bond). Thus, selective oxidation takes

place only in the presence of bridging M–O–M bonds.[155] The activated molybdenum oxide species on SBA-15 constituted a mixture of octahedral $[\text{MoO}_6]$ and tetrahedral $[\text{MoO}_4]$ species with corner-sharing $[\text{MoO}_6]$ units.[112] Hence, selectivity towards selective oxidation of propene to acrolein was considerably higher for the Mo/SBA-15 sample than for the molybdenum oxide on the alkaline support. Magnesium molybdate MgMoO_4 as bulk reference consists of isolated $[\text{MoO}_4]$ tetrahedra without any bridging Mo–O–Mo motifs. Therefore, it showed only very low activity in selective oxidation. Main products (~ 98%) were total oxidation products CO and CO_2 .

6.4.2 Structural Evolution under Catalytic Conditions

Behavior of the molybdenum oxide catalysts supported on *MgO/SBA-15* under catalytic reaction conditions was investigated by *in situ* X-ray absorption spectroscopy (XAS). Evolution of the X-ray absorption near edge structure (XANES) and the Fourier transformed X-ray absorption fine structure (XAFS), $\text{FT}(\chi(k) \cdot k^3)$, during temperature programmed, selective propene oxidation are shown in the Appendix (Fig. A 4.6). Overall shape of Mo K edge XANES spectra and XAFS $\text{FT}(\chi(k) \cdot k^3)$ of the supported molybdenum oxides remained unchanged. Hence, the structure of molybdenum oxide supported on *MgO/SBA-15* during thermal treatment under catalytic reaction conditions was considered stable up to 450 °C.

Further investigations of the molybdenum oxide catalysts under propene oxidizing conditions were performed by *in situ* DR-UV-Vis spectroscopy. Fig. 6.13 depicts the DR-UV-Vis spectra of *Mo/MgO/SBA-15* (5 wt.% Mo) under catalytic reaction conditions at 425 °C measured over a time period of six hours. With proceeding time on stream increasing absorption band intensities in the spectral region around 340 nm and 450 nm were observed. Besides the possibility of tracking electronic changes within the catalyst oxides, UV-Vis spectroscopy possesses a very high sensitivity in the detection of molecules with conjugated double bonds, aromatics, and allylic ions.[156] Detection of these molecules may provide additional information on the surface reaction of propene on the supported molybdenum oxides. Adsorption of propene on the catalyst surface is strongly influenced by the acid-base properties of the catalyst. The first step in selective oxidation, *i.e.*, hydrogen abstraction, requires the activation of a C–H bond. In case of heterolytic activation the presence of an acid or alkaline site is

needed. Hence, acidic sites promote the dissociation to give a carbocation, while alkaline sites facilitate proton abstraction resulting in the formation of a carbanion.[157]

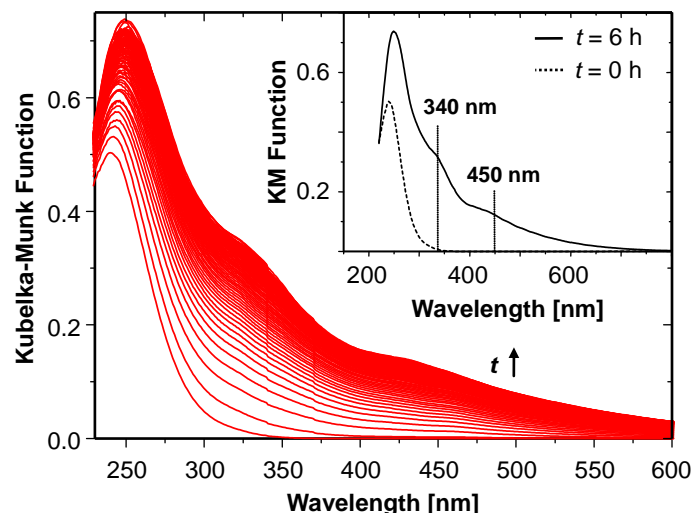


Fig. 6.13 Evolution of the DR-UV-Vis spectra of *Mo/MgO/SBA-15* (5 wt.% Mo) under propene oxidizing conditions (5% propene, 5% O₂ in He) at 425 °C during a period of time on stream, *t*, of 6 h.

Bands in the spectral region around 340 nm and 450 nm have previously been observed by various authors during the reaction of hydrocarbons on zeolite type catalysts.[158,159] Kiricsi *et al.* proposed the formation of a π -complex involving the C=C double bond of propene and the acid site of a zeolite. Accordingly, the primary surface species is formed by donation of a proton from the Brønsted acid site of a zeolite resulting in a carbocation.[159] The alkaline surface properties of *MgO/SBA-15* most reasonably led to the abstraction of a proton by alkaline surface hydroxyl groups rather than proton donation to a Brønsted acid site. Thus, the chemisorbed species on *Mo/MgO/SBA-15* might form by generation of an allyl anion.

To ensure that the absorption bands originated from a hydrocarbon species rather than from electronic changes within the catalyst subsequent oxidation was conducted in 20% oxygen in He. Reoxidation was monitored by online mass spectrometry. Fig. 6.14 shows the ion currents of water and carbon dioxide before and during reoxidation.

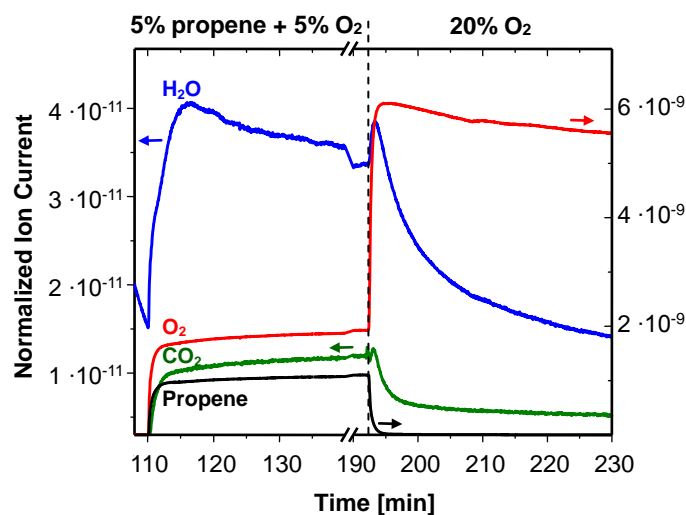


Fig. 6.14 Ion currents of the reaction products (left axis) water (m/e 18) and carbon dioxide (m/e 44) and the reactants (right axis) propene (m/e 41) and oxygen (m/e 32) during isothermal catalytic reaction at 425 °C in 5% propene and 5% oxygen and subsequent oxidation in 20% oxygen.

An immediate increase in water and carbon dioxide formation was observed after switching the gas atmosphere to 20% oxygen in He. Formation of water and carbon dioxide was accompanied by vanishing absorption band intensities in the spectral region above 300 nm. Hence, the presence of chemisorbed hydrocarbon species on the catalyst surface seemed reasonable. This was confirmed by elemental analysis of the supported molybdenum oxide catalysts. As a result a carbon content between 3–4 wt.% was detectable after catalytic reaction.

6.4.3 Hydrocarbon Chemisorption and Coke Formation

The formation of hydrocarbon species on the surface of *Mo/MgO/SBA-15* as discussed above was further studied by analyzing the absorption band intensities of the apparent maxima at 340 nm and 450 nm. Absorption band intensities were measured under isothermal reaction conditions at various temperatures. The increasing absorption intensity at 450 nm with time was assumed to correspond to the adsorption of hydrocarbon molecules on the catalyst surface. For evaluation, the extend of hydrocarbon adsorption was normalized to the highest band intensity observed at 410 °C. Fig. 6.15 (left) depicts the extend of adsorption during isothermal reaction in propene/oxygen atmosphere at 410 °C, 400 °C, 390 °C, and 375 °C. Experimental curves were described by a deceleratory kinetic model where the reaction rate de-

creases with increasing extend of reaction. Therefore, data were linearized by a "two-dimensional diffusion" rate law according to the relationship

$$kt = ((1 - \alpha)\ln(1 - \alpha)) + \alpha \quad (6-7)$$

with the rate constant, k , reaction time, t , and the extend of reaction, α . [160] Resulting rate constants, k , were plotted as $\ln(k)$ against $1/T$ in Fig. 6.15 (right).

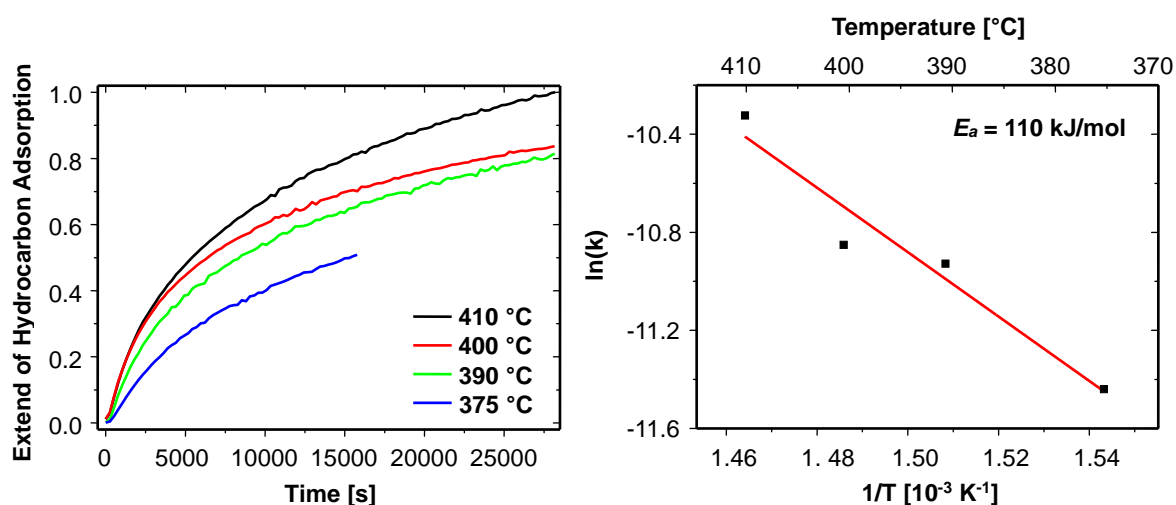


Fig. 6.15 Left: Extend of hydrocarbon adsorption derived from isothermal evolution of absorption band intensity at 450 nm. Right: Arrhenius-type diagram constructed from the rate constants, k , determined from the extend of hydrocarbon adsorption (left) assuming a "two-dimensional diffusion" rate law.

The Arrhenius-type diagram gave a straight line in the measured temperature range. From linear regression an apparent activation energy, E_a , of approximately 110 kJ/mol was obtained. The activation energy was in the range for formation of CO_2 (105 kJ/mol) and acrolein (120 kJ/mol) as proposed by Abon *et al.* for catalytic oxidation of propene on MoO_3 catalysts. [161]

Transformation of the adsorbed hydrocarbon species supposedly led to coke formation on the catalyst surface. This may result in deactivation of the catalyst. Therefore, the reaction was further investigated by an isoconversional kinetic analysis. This model-free approach allows determining the activation energy, E_a , without choosing a reaction model. To confirm a similar reaction process independent of reaction temperature, the extend of reaction, α , was plotted against the ratio of reaction time, t , and half time, $t_{1/2}$, at which $\alpha = 1/2$. The experi-

mental curves measured at four different temperatures were congruent up to an extend of reaction of $\alpha \approx 0.6$ (Fig. 6.16, inset). This confirmed that the reaction up to this point was governed by similar kinetic processes. Fig. 6.16 depicts the dependency of the apparent activation energy, E_a , on the extend of reaction, α . With proceeding reaction the apparent activation energy increased from approximately 30 kJ/mol to an average value of 120 kJ/mol. At reaction extends higher than $\alpha = 0.3$ the apparent energy exhibited no further increase but varied constantly around 120 kJ/mol.

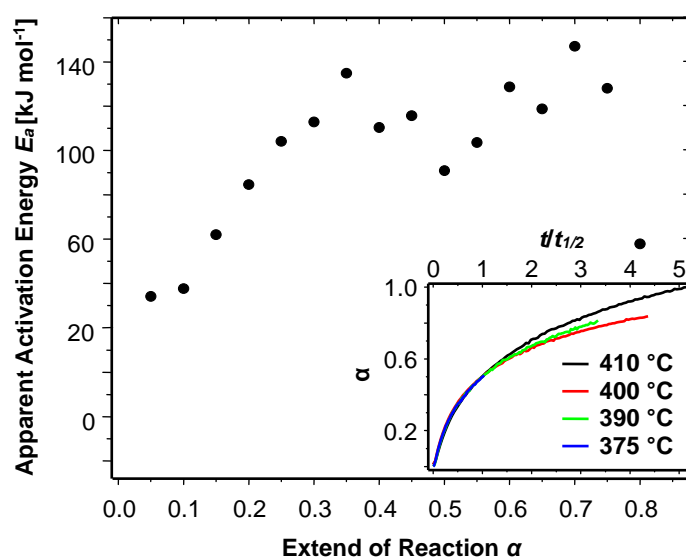


Fig. 6.16 Apparent activation energy, E_a , as a function of reaction extend, α . Inset: Half-life normalized extend of hydrocarbon adsorption, α , at the corresponding temperatures derived from *in situ* DR-UV-Vis data of *Mo/MgO/SBA-15* (5 wt.% Mo) during isothermal reaction in propene/oxygen (5% propene, 5% O₂ in He).

Van Sint Annaland *et al.* investigated coke formation from propene adsorption on zeolite type catalysts. According to them coke formation was initiated by oligomerization of adsorbed propene molecules. The formation of these so-called coke precursors gave rise to calculated activation energies in the range of 40 to 150 kJ/mol. For multilayer coke formation activation energies were determined to about 200 kJ/mol.[162] In agreement with the reported results the determined activation energy of approximately 120 kJ/mol indicated the formation of oligomerized propene molecules forming a submono- or monolayer on the surface of the supported molybdenum oxide catalysts. The lower activation energy at the beginning of the reac-

tion was attributed to the formation of allylic π -complexes with the alkaline catalyst surface or gas phase transport.

6.4.4 Catalyst Reducibility

Reduction experiments of the molybdenum oxide supported on *MgO/SBA-15* with propene were performed using *in situ* X-ray absorption spectroscopy (XAS). In a temperature range between 25 °C and 450 °C the X-ray absorption near edge structure (XANES) and the Fourier transformed X-ray absorption fine structure (XAFS), $FT(\chi(k) \cdot k^3)$, exhibited no major changes (see Appendix, Fig. A 4.7). However, analysis of the XANES pre-edge peak revealed a decreasing intensity. For pre-edge peak analysis a Gaussian and an atan function were fitted to the pre-edge peak, and the absorption edge, respectively (for details see Appendix, Fig. A 2.3). Fig. 6.17 depicts the evolution of the pre-edge peak intensity of *Mo/MgO/SBA-15* during reduction in propene compared to the data of a magnesium molybdate reference.

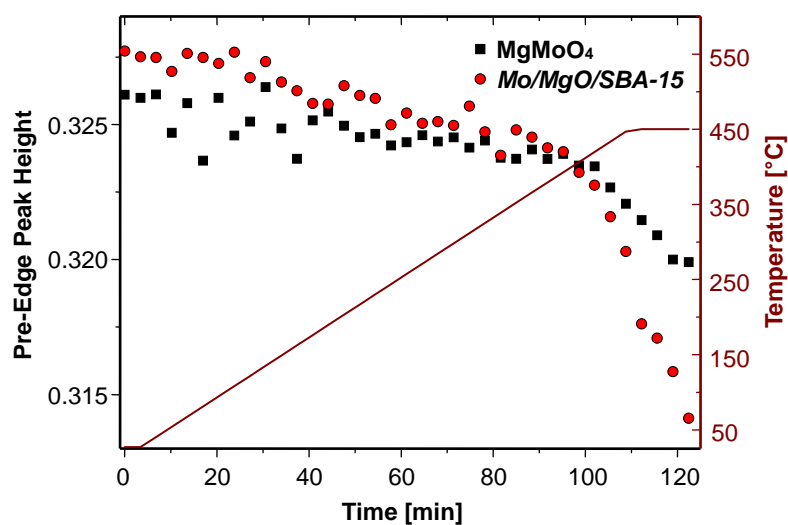


Fig. 6.17 Evolution of the pre-edge peak height of *Mo/MgO/SBA-15* (5 wt.% Mo, red circles) compared to the data of a *MgMoO₄* reference (black squares) during temperature programmed reduction in propene (RT → 450 °C, 4 K/min, 5% propene in He).

In the spectra of sample and reference a decreasing pre-edge peak height was observed at an onset temperature of approximately 350 °C. A decreasing pre-edge peak height might be caused by two different reasons; either a change in tetrahedral geometry around the molybdenum center or by reduction of the average Mo oxidation state. In order to differentiate be-

tween the two effects a structure refinement to the experimental $FT(\chi(k) \cdot k^3)$ of *Mo/MgO/SBA-15* and $MgMoO_4$ was performed and applied to the data of the *in situ* measurements. Therefore, a theoretical XAFS function calculated for a $MgMoO_4$ model structure consisting of $[MoO_4]$ tetrahedra was refined to the first shell of the $FT(\chi(k) \cdot k^3)$ of the sample and reference. Within the limits of distance resolution the first coordination shell could be refined by four equally long Mo-O distances in both cases. Distance, R , and disorder parameter, σ^2 , increased with increasing temperature. Evolution of relative Mo-O distances during reduction is shown in the Appendix (Fig. A 4.8). Only minor changes were observed and the variation in R ranged within the calculated confidence limits of $\pm 0.001 \text{ \AA}$. Hence, increasing distance values were attributed to a proceeding disorder of the tetrahedral units with increasing temperature. A change from a tetrahedral to an octahedral coordination sphere around the molybdenum center could thus be neglected. Therefore, the decreasing pre-edge peak height during temperature programmed reaction in propene was most likely caused by reduction of the average Mo oxidation state.

Unfortunately, no information on actual values of the Mo oxidation state could be drawn from XANES data. Several XANES features, such as K edge position or pre-edge peak position, height and position of the XANES maxima, were correlated to the oxidation state of known molybdenum oxide references as proposed in the literature.[65,148,163] However, none of these XANES features could be correlated to the Mo oxidation state of the *Mo/MgO/SBA-15* catalysts. Hence, the degree of reduction during temperature programmed treatment in propene could not be quantified but only qualitatively monitored.

Aritani *et al.* studied the reducibility of Mo-Mg mixed oxides with hydrogen. They reported that the reducibility strongly depended on the Mo/Mg atomic ratio. At low ratios where only $MgMoO_4$ was present no reduction of the molybdenum phase was observed.[164] Thus, for the measured $MgMoO_4$ reference the slight decrease in pre-edge peak height (Fig. 6.17) indicated only minor reduction under propene atmosphere. However, the supported molybdenum oxide exhibited a stronger decrease in pre-edge peak height than the magnesium molybdate reference. This indicated a higher degree of reduction of the *Mo/MgO/SBA-15* catalyst. The higher reducibility of the supported molybdenum oxides compared to bulk $MgMoO_4$ was attributed to a higher dispersion of the $[MoO_4]$ units and the presence of

[Mo₂O₇] units with bridging Mo–O–Mo bonds in *Mo/MgO/SBA-15*. To confirm electronic changes of the molybdenum centers under reducing conditions *in situ* DR-UV-Vis spectroscopy was performed. As it was already shown for supported vanadium oxides (Chap. 6.3.2) weak bands corresponding to *d–d* transitions of partially reduced metal centers can be used to estimate the degree of reduction. Fig. 6.18 depicts the evolution of the absorption band intensity at 700 nm derived from the spectra of *Mo/MgO/SBA-15* (10 wt.% Mo) during isothermal reduction in propene at 425 °C. The increasing intensity with time confirmed the reduction of the molybdenum oxide species as already assumed from XAFS data. Changes in the tetrahedral geometry of the supported oxide units were not observed under reducing conditions.

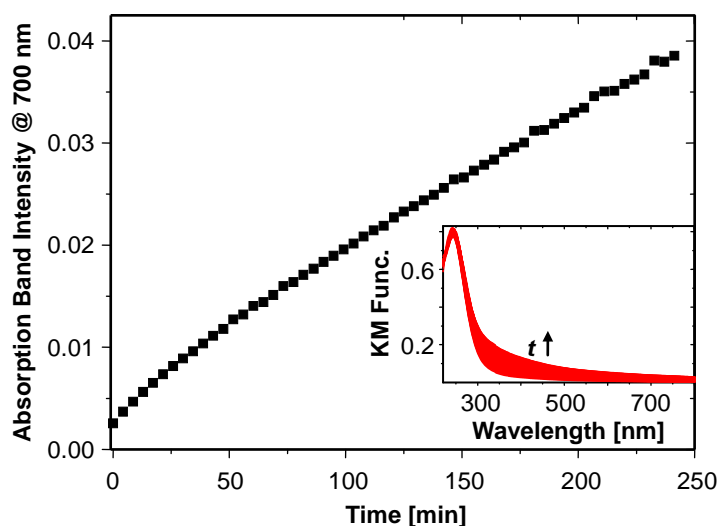


Fig. 6.18 Evolution of the absorption band intensity at 700 nm derived from the DR-UV-Vis spectra (inset) of *Mo/MgO/SBA-15* (10 wt.% Mo) during isothermal reduction at 425 °C in 5% propene in He.

6.4.5 Redox Properties of the Catalyst

To elucidate the relationship between reducibility of the catalyst and its catalytic activity the redox behavior of the molybdenum oxides supported on *MgO/SBA-15* was studied by *in situ* X-ray absorption spectroscopy (XAS). Therefore, the X-ray absorption near edge structure (XANES) was recorded during temperature programmed reaction in propene/oxygen in a temperature range between 25 °C and 450 °C. At 450 °C a reduction/reoxidation cycle was conducted by temporarily switching off the oxygen. To evaluate the degree of reduction of the molybdenum oxides, the XANES pre-edge peak height was analyzed as described above

(Chap. 6.4.4). Fig. 6.19 depicts the pre-edge peak height during temperature programmed reaction and during the isothermal redox experiment at 450 °C.

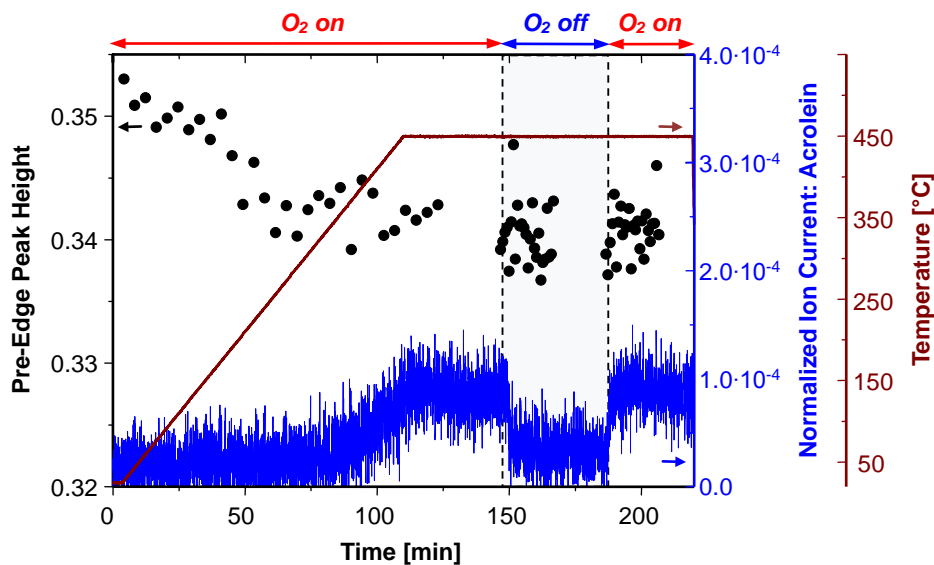


Fig. 6.19 Evolution of the pre-edge peak height (left axis) evaluated from *in situ* XANES measurements at the Mo K edge and measured ion current of acrolein (right axis, m/e 56) during temperature programmed reaction in propene/oxygen atmosphere and during isothermal reduction/reoxidation cycle at 450 °C.

After initial reduction of the molybdenum oxide species under reaction conditions as it was already discussed above (Chap. 6.4.2) no further changes were observed. During isothermal reduction (O₂ off) over a time period of approximately 40 min and subsequent reoxidation (O₂ on) the pre-edge peak height remained constant. Thus, no further reduction of the molybdenum oxide catalysts occurred under reducing conditions. Acrolein formation before and after the reduction period remained similar.

6.5 Influence of Support Material

6.5.1 Silica SBA-15 as Support Material

Vanadium Oxides on SBA-15

A comparison of catalytic activity in terms of acrolein turnover frequency (TOF, Fig. 6.2) indicated a substantially higher catalytic performance of the vanadium oxides supported on

SBA-15 than the oxide species supported on *MgO/SBA-15*. While acrolein TOF for *V/MgO/SBA-15* reached a maximum value of approximately $0.5 \cdot 10^{-3} \text{ s}^{-1}$, TOF values for vanadium oxide supported on SBA-15 ranged between $0.7 \cdot 10^{-3} \text{ s}^{-1}$ and $1.4 \cdot 10^{-3} \text{ s}^{-1}$. The latter was comparable to the values reported by Zhao and Wachs for vanadium oxide supported on silica and Al_2O_3 .^[144] In the catalytically active range a similar structural motif, *i.e.*, tetrahedral vanadium oxide oligomers, was present on both *MgO/SBA-15* and SBA-15. Therefore, the higher catalytic activity of *V/SBA-15* was attributed to the influence of the vanadium oxide-support interaction, *i.e.*, differences in character of the V–O–Si and V–O–Mg bond. The lower catalytic performance of vanadium oxide supported on *MgO/SBA-15* can be attributed to the alkaline surface sites, which impede initial adsorption of the olefin. Conversely, the acidic surface of SBA-15 facilitates adsorption of the reactant, and thus, may enhance catalytic performance. Generally, the transformation of the adsorbed intermediate to the selectively oxidized product has to be quick in order to avoid premature desorption or over-oxidation.^[157] Moreover, the redox behavior of the catalyst plays a crucial role. Hence, for vanadium oxide supported on SBA-15 a higher reducibility would be expected allowing a fast transformation of the reactants.

To gain deeper insight into the influence of the vanadium oxide-support interaction on catalytic activity, reducibility of vanadium oxide supported on bare SBA-15 was investigated. Evolution of V K edge X-ray absorption near edge structure (XANES) of vanadium oxide supported on SBA-15 (7.7 wt.% V) during temperature programmed reduction in propene is depicted in the Appendix (Fig. A 6.1). The overall XANES shape changed at an onset temperature of 210 °C. The pre-edge peak decreased considerably, indicating a reduction of the vanadium oxide species.

In Fig. 6.20 (left) the evolution of the average oxidation state of vanadium oxide supported on SBA-15 is compared to that of *V/MgO/SBA-15*. The average V oxidation state was determined according to eq. (6-6) (for details refer to Chap. 6.3.3). Deviation from an initial average oxidation state of +5 for both catalysts was attributed to the use of bulk vanadium oxide references for calibration (see Chap. 6.3.3). These bulk oxides differed from the supported oxides in local geometry and dispersion of the metal centers. Next to the average oxidation state, these properties influence the position of the V K edge, which was used for cali-

bration. Therefore, the average oxidation state estimated for the supported vanadium oxides rather describes a trend than actual values. However, under the assumption that *V/MgO/SBA-15* and *V/SBA-15* were in a fully oxidized state before reaction the initial oxidation state of both catalysts was normalized to +5 (Fig. 6.20, right). Hence, differences in the evolution of the average oxidation state of the vanadium oxides supported on *MgO/SBA-15* and bare *SBA-15* during reduction could be evaluated. Vanadium oxides supported on *SBA-15* were reduced at a lower temperature (~ 235 °C) compared to the oxides on *MgO/SBA-15* (~ 247 °C). Furthermore, the degree of reduction of *V/SBA-15* was significantly higher resulting in an average oxidation state of +3 (compare Table 6.3).

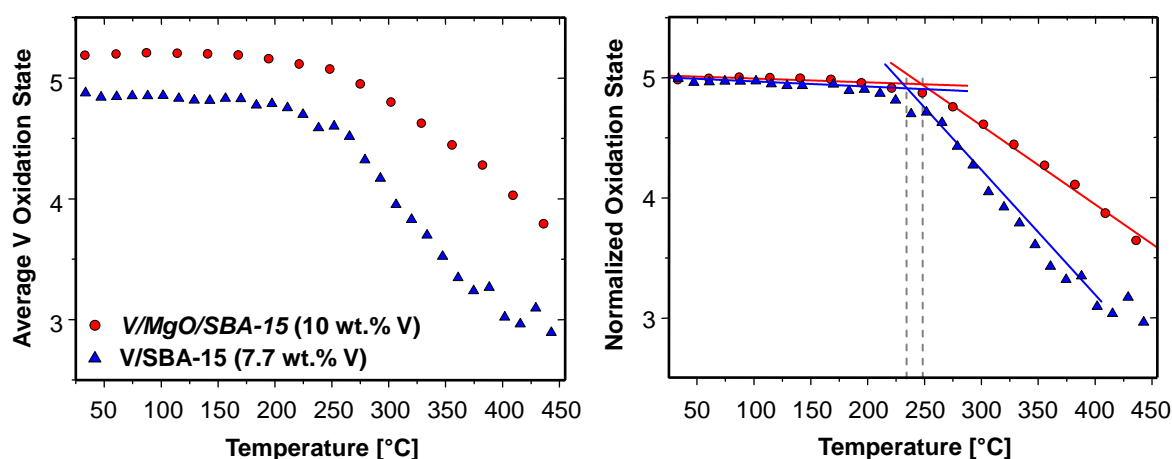


Fig. 6.20 Left: evolution of the average V oxidation state of *V/MgO/SBA-15* (red circles) and *V/SBA-15* (blue triangles) and right: average oxidation state of both catalysts normalized to +5. Data were evaluated from *in situ* XANES measurements at the V K edge during temperature programmed reduction in 5% propene in He.

A higher reduction onset temperature and significantly lower degree of reduction of *V/MgO/SBA-15* compared to *V/SBA-15* was most likely due to the different acid-base properties of both supports. A similar trend has been observed by Lemonidou *et al.*[66] They determined onset temperature and degree of reduction of vanadium oxides supported on several supporting oxides during temperature programmed reduction in H_2 . According to them, reducibility of the supported vanadium oxide species increased with increasing acidity of the support.[66] The better reducibility of the oxides supported on acidic *SBA-15* was attributed to a weaker vanadium oxide-support interaction of *V/SBA-15* compared to the strongly bond vanadium oxide species on alkaline *MgO/SBA-15*.

It was proposed that the vanadyl bond, $V^{5+}=O$, was very active in total combustion.[165] The highly dispersed vanadium oxide species on the *MgO/SBA-15* support exhibited a low connectivity of the oxide units. Accordingly, concentration of vanadyl bonds was high while only few bridging $V-O-V$ bonds were present. Therefore, the low selectivity to oxygenates and high activity in carbon oxide formation of *V/MgO/SBA-15* might be due to the lack of more selective bridging $V-O-V$ bonds. Conversely, acrolein formation was significantly higher for the higher oligomerized vanadium oxide units on SBA-15.

Molybdenum Oxides on SBA-15

The molybdenum oxide species on silica SBA-15 showed a significantly higher selectivity to acrolein than the oxides supported on *MgO/SBA-15* (compare Table 6.4). In contrast to the isolated $[MoO_4]$ tetrahedra present on *MgO/SBA-15*, the as-prepared structure on silica SBA-15 resembled that of a two-dimensional layer of hexagonal MoO_3 (hex- MoO_3 , refer to Chap. 5.4.3). The *Mo/SBA-15* catalyst has already been reported to be highly active and selective in propene oxidation.[112] To correlate changes in structure to catalytic activity, *in situ* X-ray absorption spectroscopy (XAS) was conducted under propene oxidizing conditions. Fig. 6.21 (left) depicts the evolution of the X-ray absorption near edge structure (XANES) during temperature programmed reaction in propene/oxygen atmosphere.

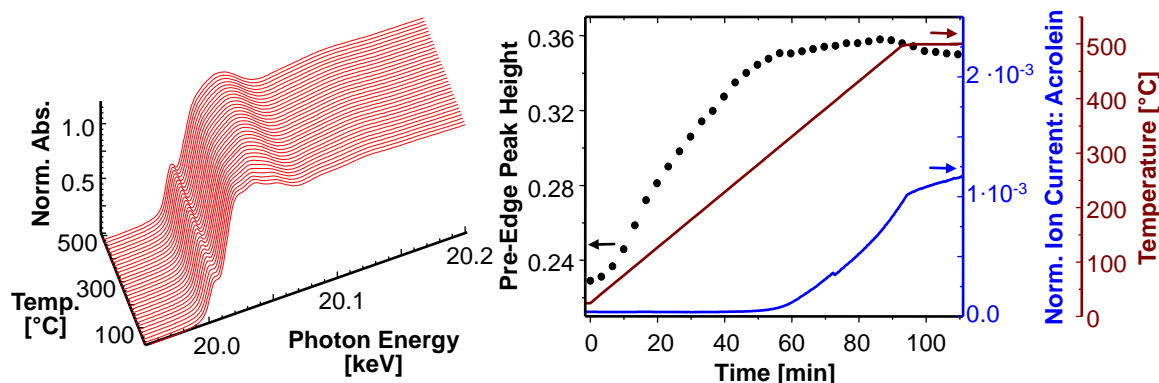


Fig. 6.21 Left: evolution of Mo K edge XANES spectra of *Mo/SBA-15* (13 wt.% Mo) and right: evolution of the pre-edge peak height evaluated from *in situ* XANES (left axis) together with the measured ion current of acrolein (*m/e* 56; right axis) during temperature programmed reaction in propene/oxygen (RT \rightarrow 500 °C, 5 K/min, 5% propene, 5% O_2 in He, total gas flow 30 ml/min).

As it was already shown by Ressler *et al.* the hex-MoO₃ like structure of Mo/SBA-15 remained stable up to 500 °C.[112] Nevertheless, an increasing XANES pre-edge peak was observed (Fig. 6.21, right). This indicated an increasing distortion of the local Mo-O coordination with a partial formation of tetrahedral molybdenum oxide units. Hence, a proceeding disorder within the two-dimensional hex-MoO₃ structure with increasing temperature was assumed. At a temperature of approximately 330 °C completion of structural rearrangement was indicated by a constant pre-edge peak height. This point coincided with the onset of catalytic activity, *i.e.*, formation of acrolein.

Reducibility and redox properties of the Mo/SBA-15 catalyst were investigated by temperature programmed reduction in propene and subsequent reoxidation at 450 °C. To qualitatively monitor the degree of reduction during reaction the XANES pre-edge peak height was evaluated. Fig. 6.22 shows the evolution of the pre-edge peak height together with the ion current of acrolein.

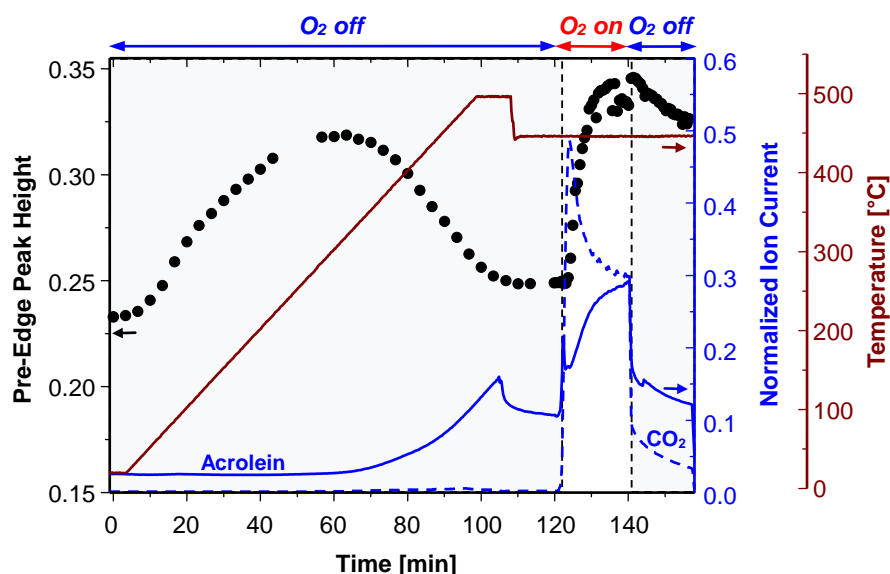


Fig. 6.22 Evolution of the pre-edge peak height (left axis) evaluated from *in situ* XANES measurements at the Mo K edge and measured ion currents (right axis) of acrolein (m/e 56) and carbon dioxide (m/e 44) during temperature programmed reduction in propene and during isothermal reoxidation/re-reduction cycle at 450 °C. (After normalization to the ion current of He, the ion currents were normalized to one. The maximum of the ion current of acrolein between 100–110 min was attributed to the temperature cool down from 500 °C to 450 °C and was thus considered as an artifact.)

Structural rearrangement in a temperature range between 25 °C and 325 °C as described above was indicated by an increasing pre-edge peak. A subsequent decrease in pre-edge peak height at a temperature of about 325 °C was interpreted as reduction of the molybdenum oxide species. The average Mo oxidation state was estimated by the position of the "second XANES feature" according to the procedure described by Ressler *et al.*[163] Details on the evaluation can be found in the Appendix (Fig. A 6.2 and Fig. A 6.3). Accordingly, the molybdenum oxide species was reduced to an average oxidation state of +5. Subsequent reoxidation in 5% propene and 5% oxygen led to a fully reoxidized species with an average Mo oxidation state of +6. Full reoxidation was achieved within 5–7 min. During reoxidation acrolein formation simultaneously increased reaching its maximum at the time of complete reoxidation (Fig. 6.22). Conversely, the ion current of the total oxidation product carbon dioxide exhibited the opposite trend. The ion current of CO₂ sharply increased after switching to oxygen atmosphere and then decreased. Hence, it was assumed that catalytic activity correlated to the degree of molybdenum oxide reduction. As it has already been reported this behavior most probably corresponded to an increasing selectivity during reoxidation.[112] During re-reduction the pre-edge peak height slowly decreased indicating a slow reduction of the molybdenum oxide species. The reduced average Mo oxidation state was confirmed by a simultaneous decrease in the position of "second XANES feature" (compare Appendix, Fig. A 6.3)

6.5.2 Carbon CMK-3 as Support Material

Vanadium and molybdenum oxides supported on carbon CMK-3 were shown to exhibit a similar as-prepared structure as the oxides supported on silica SBA-15 (refer to Chap. 5.4). The structure of the vanadium oxides resembled that of hydrated V/SBA-15 which consists of a two-dimensional V₂O₅-type structure. The molybdenum oxide species on CMK-3 were present in a structure that resembled that of molybdenum trioxide in the hexagonal modification (hex-MoO₃).

Vanadium Oxides on CMK-3

The behavior of vanadium oxide supported on SBA-15 and CMK-3 observed under catalytic reaction conditions differed considerably from each other. In order to investigate structural changes of V/CMK-3 under catalytic reaction conditions *in situ* X-ray absorption spectroscopy

py (XAS) at the V K edge was performed in a temperature range between 20 °C and 400 °C. Unlike V/SBA-15 where a transformation of the hydrated to the dehydrated state took place in a temperature range below 280°C [110], the structure of the vanadium oxides supported on CMK-3 remained unchanged. The X-ray absorption near edge structure (XANES) of V/CMK-3 in the measured temperature range between 20 °C and 400 °C resembled that of a two-dimensional V_2O_5 -type structure. Similar observations were reported by Zhu *et al.* They did not detect any changes in the structure of vanadium oxide supported on activated carbon during NO reduction with ammonia at 350 °C. The structure of the as-prepared and used catalyst resembled that of V_2O_5 . [133] A comparison of the XANES spectra of V/CMK-3 to that of a V_2O_5 reference during temperature programmed reaction in propene/oxygen is given in the Appendix (Fig. A 3.3). The XANES of the V_2O_5 reference exhibited significant changes at an onset temperature of 350 °C indicating a partial reduction of the vanadium oxide species via a V_6O_{13} -type intermediate. To evaluate the degree of reduction of the vanadium oxide species in V_2O_5 and V/CMK-3, the shift in V K edge position was analyzed as described above (Chap. 6.3.3). Fig. 6.23 depicts the evolution of the average V oxidation state during temperature programmed reaction together with the measured ion currents of acrolein.

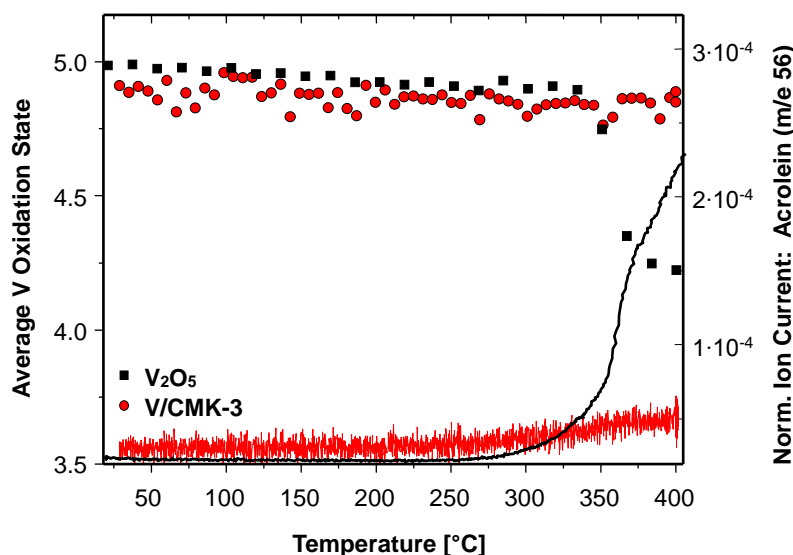


Fig. 6.23 Evolution of the average V oxidation state (left axis) evaluated from *in situ* XANES spectra (Fig. A 3.3) and simultaneously measured ion current of acrolein (right axis) of V/CMK-3 (10 wt.% V, red) compared to the data of a V_2O_5 reference (black) during temperature programmed reaction in propene/oxygen (5% propene, 5% O_2 in He).

For the V_2O_5 reference a reduction of the average oxidation state from +5 to +4.3 was observed. Reduction occurred at an onset temperature of 350 °C and directly correlated to the onset of catalytic activity, *i.e.*, an increasing acrolein formation. These observations were in agreement with the literature where V_6O_{13} is claimed to be the catalytically active species for selective hydrocarbon species.[150] Conversely, for the vanadium oxide species on CMK-3 no reduction of the average vanadium oxidation state was observed in the measured temperature range. The ion current of acrolein exhibited only a minor increase at 350 °C, thus indicating poor catalytic activity of V/CMK-3.

Structural changes of the vanadium oxide catalysts supported on CMK-3 were analyzed by the change in XANES pre-edge peak. Fig. 6.24 shows the evolution of the pre-edge peak height under catalytic reaction conditions. At an onset temperature of 350 °C the pre-edge peak sharply increased.

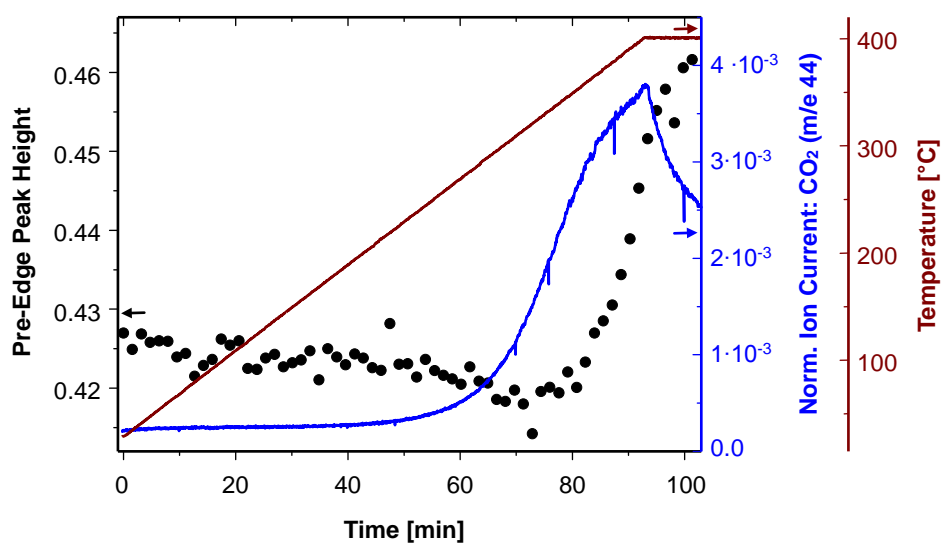


Fig. 6.24 Evolution of the pre-edge peak height (left axis) evaluated from *in situ* XANES of V/CMK-3 (10 wt.% V) together with the measured ion current of CO_2 (right axis) during temperature programmed reaction in propene/oxygen (RT \rightarrow 400 °C, 4 K/min, 5% propene, 5% O_2 in He).

It was previously shown that thermal decomposition of the bare support CMK-3 occurred in a temperature range between 330 °C and 400 °C.[98] Therefore, the increasing ion current of carbon dioxide, also shown in Fig. 6.24, was attributed to the combustion of the support. Carbon dioxide formation exhibited a maximum around 350 °C while the change in pre-edge

peak height was slightly delayed to higher temperatures. Hence, the increasing pre-edge peak in the XANES of V/CMK-3 was most likely caused by CMK-3 decomposition rather than by catalytically induced structure changes. Without the influence of the support material the structure of the remaining vanadium oxide species became highly distorted presumably changing from an octahedral to a tetrahedral coordination sphere.

Molybdenum Oxides on CMK-3

Since the structure of molybdenum oxide supported on silica SBA-15 and carbon CMK-3 were comparable to each other the catalytic behavior of both catalysts was expected to be similar as well. In order to investigate structural changes under catalytic reaction conditions *in situ* X-ray absorption spectroscopy (XAS) was performed in a temperature range between 25 °C and 400 °C. Fig. 6.25 (left) depicts the evolution of the X-ray absorption near edge structure (XANES) of molybdenum oxide supported on CMK-3 (10 wt.% Mo) during temperature programmed reaction in propene/oxygen atmosphere.

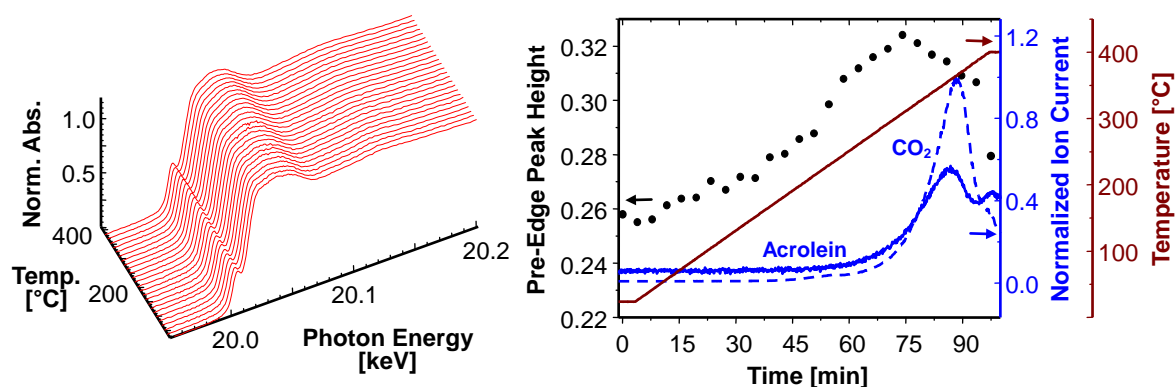


Fig. 6.25 Left: evolution of Mo K edge XANES spectra and right: evolution of the pre-edge peak height (left axis) evaluated from *in situ* XANES of Mo/CMK-3 (10 wt.% Mo) together with the normalized ion currents (right axis) of acrolein (m/e 56) and carbon dioxide (m/e 44) during temperature programmed reaction in propene/oxygen (RT → 400 °C, 4 K/min, 5% propene, 5% O₂ in He). (After normalization to the ion current of He, the ion currents were normalized to one.)

No major structural changes were observed during reaction. Similar to Mo/SBA-15 the XANES pre-edge peak height, shown in Fig. 6.25 (right), increased with increasing temperature. Thus, it was assumed that a comparable structural disorder of the molybdenum oxide units on CMK-3 occurred. The increasing ion current of carbon dioxide (Fig. 6.25, right) was

attributed to thermal combustion reaction of the support. Similar observations were already discussed above for V/CMK-3. Hence, the decreasing pre-edge peak in the XANES of the supported molybdenum oxides was most likely caused by oxidation of CMK-3 rather than by catalytically induced structure changes. As it was already assumed for the V/CMK-3 catalysts, the combustion of the support material led to a distortion of the remaining molybdenum oxide species. Previously investigated molybdenum oxides supported on thermally more stable hollow carbon nanofibers (CNF) exhibited a similar molybdenum oxide structure. However, since the support material was stable up to 500 °C catalytically induced structure changes could be analyzed. It was shown that the hex-MoO₃-type structure present on CNF was reducible to a MoO₂ intermediate under catalytic reaction conditions at temperatures around 450 °C.[131]

6.5.3 Influence of Support on Catalytic Behavior

The higher catalytic activity of the vanadium oxide catalysts on SBA-15 compared to the oxides on *MgO/SBA-15* correlated to a better reducibility of V/SBA-15 compared to *V/MgO/SBA-15*. This behavior might be attributed to the acidic nature of the silica support. Conversely, V/CMK-3 exhibited only poor acrolein formation. During catalytic reaction no structural or electronic changes were observed for the vanadium oxide species on CMK-3. Molybdenum oxide supported on silica SBA-15 and carbon CMK-3 exhibited a significantly higher reducibility and re-oxidizability than the oxide supported on *MgO/SBA-15*. The enhanced redox properties of Mo/SBA-15 and Mo/CMK-3 might be caused by a synergetic effect between the different structural molybdenum oxide motifs. Ozkan *et al.* reported an oxygen spillover effect during selective hydrocarbon oxidation on a two-phase catalyst consisting of "simple" manganese molybdates (MnMoO₄) and molybdenum trioxide (MoO₃). Accordingly, the lattice oxygen of the MoO₃ phase was incorporated into the hydrocarbon. Molecular oxygen from the gas phase was then chemisorbed at the "simple" molybdate allowing it to "spill over" to the reduced MoO₃ site.[166] The higher reducibility of molybdenum oxide supported on CNF compared to Mo/SBA-15 was attributed to a considerably weaker molybdenum oxide-support interaction in Mo/CNF, which was not sufficient to stabilize the hex-MoO₃ structure at elevated temperatures (≥ 450 °C).[131] Conversely, the molybdenum oxide-support interaction in *Mo/MgO/SBA-15* was considered to be strong. Therefore, reduci-

bility and catalytic activity of *Mo/MgO/SBA-15* was rather low. Reducibility of supported molybdenum oxide was shown to be strongly dependent on the properties of the support material. A similar trend was observed by Brito and Laine. They investigated the reducibility of molybdenum oxides supported on $\text{SiO}_2/\text{Al}_2\text{O}_3$ materials. Accordingly, the weaker oxide-support interaction of molybdenum oxides on silica led to a better reducibility in hydrogen compared to the reducibility of the strongly bound oxides on alumina.[167]

The metal oxide-support interaction has a large impact on redox properties and acid-base character of the supported oxide catalysts. Critical steps in selective oxidation reactions are adsorption and desorption of the gaseous reactants, and products, respectively. Adsorption and desorption probability of the reactants on the catalyst surface is governed by its acid-base characteristics. The influence of the support material on the catalytic performance of the supported metal oxides has frequently been described in the literature and is still under debate.[62,66,145,168,169]. Apparently, a change of support material significantly altered the properties of the supported vanadium and molybdenum oxide catalysts. Strong acid-base interactions between the vanadium and molybdenum oxide and the alkaline *MgO/SBA-15* support supposedly resulted in a strong metal oxide-support interaction. A similar conclusion was drawn by Kim *et al.* when comparing the reactivity of different oxide surfaces.[132] Hence, on the more acidic SBA-15 support the metal oxide-support interaction was considered to be weak, while on CMK-3 the absence of any surface hydroxyl groups most likely resulted in an even weaker oxide-support interaction. The supposed metal oxide-support interaction led to the order:

carbon (CMK-3; CNF) < silica (SBA-15) << magnesium oxide (*MgO/SBA-15*).

From the results discussed above a correlation between the metal oxide-support interaction and the reducibility of the catalysts was assumed. Therefore, the weaker the metal oxide-support interaction, the higher was the reducibility of the catalyst. Certainly, the nature of the support influences both, oxide-support interaction and structure of the supported metal oxides. Therefore, the higher reducibility of the metal oxides supported on silica and carbon compared to the oxides on *MgO/SBA-15* was most likely additionally enhanced by the presence of oligomerized $[\text{MO}_x]$ units. Thus, the reduced species might be stabilized by neighboring metal

centers, which share bridging oxygen atoms. These oligomerized oxide units were proposed to better compensate the excess negative charge than isolated $[\text{MO}_x]$ units.[59,167]

6.5.4 Water-Gas Shift Reaction Proceeding as Side-Reaction

A major difference in product distribution between vanadium and molybdenum oxide catalysts supported on *MgO/SBA-15* and the measured references, such as V/SBA-15 and V_2O_5 , was a significantly higher CO_2/CO ratio for the catalysts supported on *MgO/SBA-15* (compare Table 6.2 and Table 6.4). For bulk V_2O_5 and vanadium oxide supported on SBA-15 the ratio between CO_2 and CO was approximately 1. Conversely, reaction of oxide catalysts on *MgO/SBA-15* led to a CO_2/CO ratio of 2. This was attributed to the different properties of the oxide support. It has previously been reported in the literature that for alkali-promoted oxide supports a lower amount of CO was formed during selective oxidation.[170] The excessive formation of CO_2 might be explained by the water-gas shift (WGS) reaction proceeding as side-reaction. In the presence of water, CO is converted to CO_2 while hydrogen is formed from the water reactant. The assumption was confirmed by the observation of an increasing hydrogen ion current during propene oxidation on *MgO/SBA-15* based catalysts (Fig. 6.26).

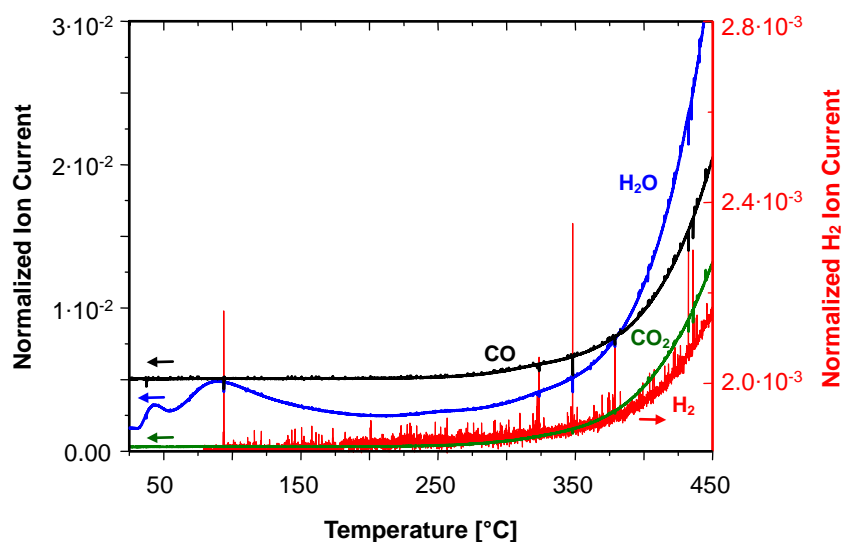
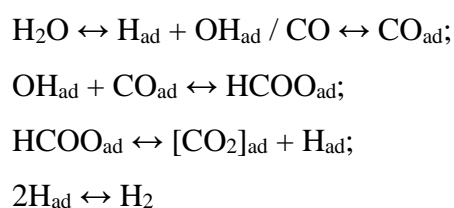


Fig. 6.26 Evolution of the ion currents of H_2O (m/e 18), CO (m/e 28), CO_2 (m/e 44) (left axis), and H_2 (m/e 2, right axis) detected by online mass spectrometry during temperature programmed propene oxidation on *V/MgO/SBA-15* (5 wt.% V) in a fixed-bed reactor (RT \rightarrow 450 °C, 4 K/min, 5% propene, 5% O_2 in He).

Hydrogen formation started at a temperature of approximately 325 °C and coincided with the formation of the oxidation products H₂O, CO₂, and CO. The comparably low intensity of the ion current of hydrogen was due to a generally lower sensitivity of the mass spectrometer to oxygen-free components. Therefore, intensities of the measured ion currents cannot be used for quantitative comparison. The water-gas shift reaction was most likely enhanced by the ability of magnesium oxide to adsorb water on its surface. The high affinity of the *MgO/SBA-15* surface to water adsorption has already been discussed above (refer to Chap. 5.4.4). After water adsorption the hydroxyl groups on the MgO surface might react with CO. It has been reported in the literature that the reaction proceeds on the MgO surface via a formate intermediate. The authors furthermore claimed, that the formate decomposition to CO₂ and H₂ only takes place in the presence of water.[171] The reaction mechanism on the MgO surface was proposed to proceed via the following steps according to a Langmuir-Hinshelwood type mechanism [172,173]:



On the surface of silica SBA-15 no water adsorption took place during reaction. The low affinity of SBA-15 compared to *MgO/SBA-15* to adsorb water on its surface has already been discussed above (Chap. 5.4.4). Hence, a conversion of CO to CO₂ via WGS reaction was not detected for vanadium or molybdenum oxides supported on SBA-15.

6.6 Catalytic Activity – A Comparison between Vanadium and Molybdenum Oxide Catalysts

Catalytic performance, *i.e.*, acrolein turnover frequency (TOF) and propene conversion, of vanadium and molybdenum oxides supported on *MgO/SBA-15* was compared under steady-state conditions at 400 °C. Fig. 6.27 depicts the evolution of acrolein TOF and propene conversion under isothermal conditions over a period of 20 h time on stream. During the first hour propene conversion of both catalysts exhibited a considerable decrease. Acrolein formation of *V/MgO/SBA-15* followed the trend of propene conversion and slightly decreased

during initial reaction time. Acrolein TOF for *Mo/MgO/SBA-15* strongly increased during the first hour of time on stream, thus opposing the trend of propene conversion. This behavior might indicate the presence of highly active oxygen species adsorbed on the catalyst surface. These highly active species most likely led to chemisorption of hydrocarbon species on the surface of *Mo/MgO/SBA-15* as it was previously discussed (refer to Chap. 6.4.3). The formation of oligomerized hydrocarbon surface species occurred on the same time scale as the observed catalyst deactivation process for *Mo/MgO/SBA-15*. Remaining unoccupied catalytic sites were more selective, thus leading to higher acrolein TOF values and less carbon oxide formation. On vanadium oxide supported on *MgO/SBA-15* a similar hydrocarbon adsorption process was not observed. Hence, a significant increase in acrolein TOF after initial catalytic reaction as for the supported molybdenum oxides was not detected. However, acrolein TOF for *V/MgO/SBA-15* was approximately five times higher than for *Mo/MgO/SBA-15*.

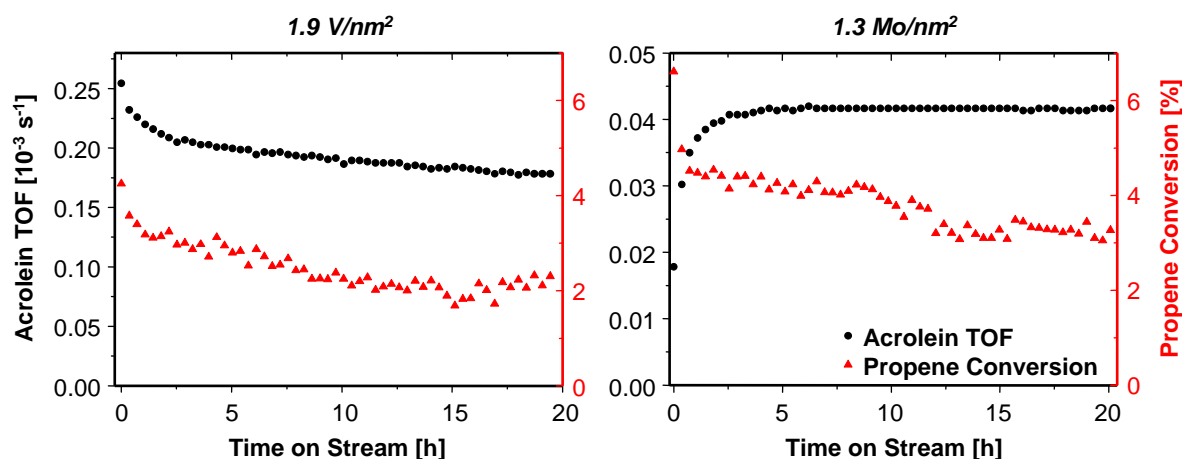


Fig. 6.27 Evolution of acrolein TOF (black circles) and propene conversion (red triangles) with time on stream during a time period of 20 h for vanadium (left) and molybdenum oxide (right) supported on *MgO/SBA-15* (reaction conditions: 5% propene, 5% O₂ in He, *T* = 400 °C). TOF values were calculated as acrolein molecule formed per transition metal surface atom (V; Mo) per second.

The structure of vanadium and molybdenum oxide supported on *MgO/SBA-15* was shown to consist of tetrahedral metal(M)-oxide(O) [MO₄] units. At comparable surface concentrations (1.9 V/nm² and 1.3 Mo/nm²) a similar degree of oligomerization of the oxide units was assumed (refer to Chap. 5). Hence, differences in catalytic performance could directly be correlated to the influence of chemical properties rather than structural effects. To elucidate the role played by the metal oxygen M–O bond in selective oxidation reaction and to explain the rela-

tive catalytic activities of both oxides their catalytic performance in selective propene oxidation was compared. Fig. 6.28 shows the selectivity towards acrolein as a function of propene conversion.

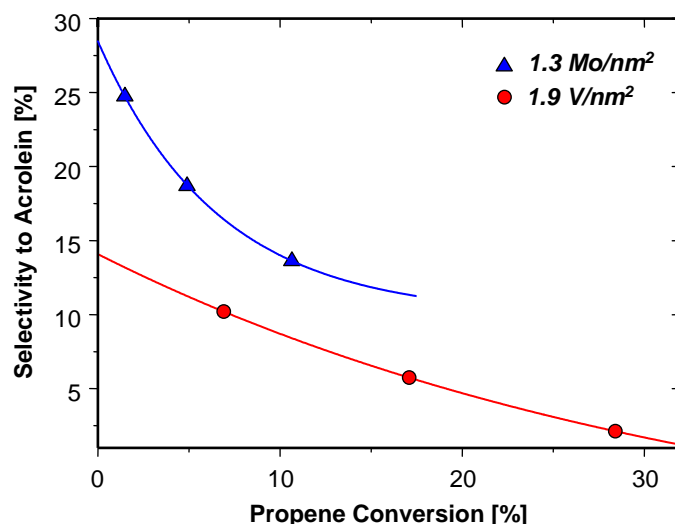


Fig. 6.28 Selectivity to acrolein for 5 wt.% V/MgO/SBA-15 (1.9 V/nm²) and 5 wt.% Mo/MgO/SBA-15 (1.3 Mo/nm²) as a function of propene conversion (reaction conditions: 5% propene, 5% O₂ in He, $T = 440$ °C).

In addition to acrolein, acetic aldehyde, propionic aldehyde, isopropyl alcohol, and acetone were the main selective oxidation products for propene oxidation on both catalysts. Formation of total oxidation products (CO, CO₂) was in the same range (~85%). With increasing propene conversion selectivity to acrolein decreased for both oxide catalysts. However, selectivity was always higher for molybdenum oxides compared to that of vanadium oxides. A similar trend was observed by Faraldos *et al.* when investigating the selective oxidation of methane on MoO₃ and V₂O₅ catalysts supported on silica. They observed a higher selectivity to formaldehyde for supported molybdenum oxide while the overall reactivity was higher for the V₂O₅ catalysts.[174]

A comparison of catalytic activity in terms of acrolein formation showed that supported vanadium oxides exhibited turnover frequencies (TOF) about five times higher than those of Mo/MgO/SBA-15. The differences observed for the two oxide catalysts might be explainable by their different reducibility. Generally, differences in the catalytic behavior of V₂O₅ and MoO₃ can be attributed to their inherent redox properties. These properties are proposed to

originate from the following characteristics: higher reducibility of V_2O_5 compared to MoO_3 , a lower Tammann temperature of V_2O_5 , thus implying higher lattice oxygen mobility, and the difference in the redox potentials of V^{5+}/V^{4+} and Mo^{6+}/Mo^{5+} . [3] For both oxides catalytic activity correlated with a partial reduction of the active metal oxide species during reaction. Apparently, reducibility required the presence of bridging M–O–M bonds. These bridging bonds are considered to be more nucleophilic and therefore exhibit a higher reactivity than terminal M=O groups. [155] In accordance with their higher catalytic activity, *V/MgO/SBA-15* catalysts exhibited a considerably higher reducibility than the supported molybdenum oxides. While no changes during redox cycles were observed in the average valence state of *Mo/MgO/SBA-15* the supported vanadium oxides were reduced in propene atmosphere to an average oxidation state of +IV. Reoxidation of the vanadium oxide units occurred on a considerably faster time scale than reduction. However, upon reoxidation the initial oxidation state was not completely recovered. The vanadium oxide species remained in a partially reduced state under catalytic reaction condition. This behavior most likely resulted in higher acrolein selectivity, since selective hydrocarbon oxidation requires fast reoxidation of the active site. Slow transformation of gas phase oxygen to lattice oxygen may otherwise result in highly active oxygen intermediates which lead to total oxidation of the reactants. [175]

6.7 Conclusions

The catalytic properties of the supported vanadium and molybdenum oxides were studied under selective propene oxidizing conditions. Additionally, the working catalysts were investigated by *in situ* spectroscopy. Therefore, it was possible to deduce structure activity correlations from the structural and functional characterization of the model catalyst system. Vanadium oxide dispersion and the nature of the support strongly affected the performance of supported vanadium oxides in selective propene oxidation. Acrolein turnover frequency (TOF) was found to be a function of vanadium surface coverage, resembling a "vulcano type" curve. The optimal surface coverage for a maximum acrolein TOF was in the range of 3–3.5 V atoms/nm² for vanadium oxide on *MgO/SBA-15* and at approximately 1.5 V atoms/nm² for vanadium oxide supported on SBA-15. Isolated $[VO_4]$ species exhibited only little catalytic activity on both support materials. In the optimal range of catalytic performance adjacent $[VO_4]$ tetrahedra with an average number of 1–2 V–O–V bonds were present. Therefore, se-

lective oxidation of propene, being a four-electron redox reaction, was assumed to involve two surface $[\text{VO}_4]$ units. The obtained relationship was used to synthesize a $V/\text{MgO}/\text{SBA-15}$ catalyst with the optimal surface coverage. Thus, the predicted maximum acrolein TOF was reached. Therefore, it was possible to improve the investigated $V/\text{MgO}/\text{SBA-15}$ catalyst system in terms of "rational catalyst design" by applying the knowledge from structure activity correlations.

Under reaction conditions the $[\text{VO}_4]$ tetrahedral units were partially reduced. Reducibility of the catalysts correlated to their catalytic activity and increased with increasing degree of oligomerization of the vanadium oxide units. Hence, selectivity to acrolein increased at higher surface coverage up to approximately 2 V atoms per nm^2 . Beyond this point only a slight increase in selectivity was observed. Combination of the data from *in situ* spectroscopy with catalytic activity during redox experiments revealed that the catalytically active site consisted of a partially reduced vanadium oxide species with an average oxidation state between +IV and +V. Hence, the reaction was assumed to proceed via a redox type or Mars-van-Krevelen mechanisms. Compared to the alkaline $\text{MgO}/\text{SBA-15}$, a more acidic oxide support, such as silica SBA-15, enhanced selective oxidation of propene to acrolein by a factor of five. The weaker oxide-support interaction in $V/\text{SBA-15}$ led to a higher reducibility, and consequently to a higher catalytic activity, of the catalysts. Thus, by modification of the vanadium oxide-support interaction it was possible to alter the acid-base and redox properties of the model catalyst system which directly influenced catalytic performance. Moreover, knowledge on structure activity correlations of the catalysts in selective oxidation of propane was transferred to oxidative dehydrogenation (ODH) of propane on $V/\text{MgO}/\text{SBA-15}$ catalysts. This two-electron redox reaction was found to proceed independent of the surface coverage. Therefore, and in contrast to selective propene oxidation, only one $[\text{VO}_4]$ unit needed to be involved in ODH reaction. Consistent with the results for propene oxidation, a change of the oxide support from $\text{MgO}/\text{SBA-15}$ to bare silica SBA-15 led to a higher catalytic activity. Higher reducibility of the vanadium oxide units on SBA-15 and the acidic nature of the support not only resulted in higher propane-to-propene TOF values, but also enhanced consecutive reaction of propene to oxygenation products like acrolein.

Catalytic activity of molybdenum oxide supported on *MgO/SBA-15* was found to be independent of catalyst loading and surface coverage. This behavior was attributed to the fact that molybdenum oxide structure and degree of oligomerization of the tetrahedral $[\text{MoO}_4]$ units did not change at varying surface coverage. Conversely, the nature of the support material strongly influenced catalytic performance. Changing the support from *MgO/SBA-15* to silica SBA-15 enhanced acrolein TOF by the factor of four. The lower catalytic activity of *Mo/MgO/SBA-15* catalysts emphasized the requirement of bridging Mo–O–Mo bonds with redox properties for selective oxidation. Isolated $[\text{MoO}_4]$ tetrahedra showed hardly any catalytic activity. The observed selectivity to acrolein for *Mo/MgO/SBA-15* was attributed to the presence of dimeric tetrahedral units besides the predominant $[\text{MoO}_4]$ monomers. The significantly higher amount of bridging units within the molybdenum oxide species supported on SBA-15 led to an increase in catalytic activity and selectivity. Comparable to the catalytic behavior of supported vanadium oxide catalysts, catalytic performance of the molybdenum oxides correlated to the reduction of the catalyst species. Reducibility and redox properties of the catalysts not only depended on the degree of oligomerization of the molybdenum oxide units but also on the nature of the oxide-support interaction. It was assumed that reducibility increased with decreasing strength of the oxide-support interaction. Therefore, molybdenum oxide supported on silica SBA-15 and carbon CMK-3 exhibited a significantly higher reducibility and re-oxidizability than those supported on *MgO/SBA-15*, where the molybdenum oxide was considered to be strongly bond to the support.

Vanadium and molybdenum oxides supported on *MgO/SBA-15* exhibited a similar structure consisting of tetrahedral metal(M)-oxide(O) $[\text{MO}_4]$ units. For both supported oxides the presence of bridging M–O–M bonds was required in order to achieve reducibility of the catalysts. Partial reduction of the active species during reaction was correlated to catalytic activity. However, a comparison of the catalytic properties of the two catalysts revealed several differences. During catalytic reaction of *Mo/MgO/SBA-15* at 400 °C formation of adsorbed hydrocarbon species was observed on the catalyst surface. The apparent activation energy was in the range between 110 kJ/mol and 120 kJ/mol. Thus, formation of polymerized hydrocarbon molecules on the surface eventually led to the deactivation of the catalyst by coke formation. Propene conversion during the first hour of time on stream considerably decreased while se-

lective oxidation to acrolein increased. It was assumed that hydrocarbon adsorption predominantly occurred on highly active but unselective catalyst surface sites. Deactivation of the unselective sites led to an acceleration of acrolein turnover frequency (TOF) by the factor of approximately two. In contrast to the supported molybdenum oxides, catalytic reaction of *V/MgO/SBA-15* did not result in any observable coke formation. Acrolein TOF and propene conversion only slightly decreased over initial time on stream.

At similar surface coverage selectivity to acrolein was always higher for molybdenum oxides compared to vanadium oxides. Conversely, catalytic activity, expressed in terms of acrolein TOF, was approximately five times higher for vanadium oxide catalysts than for supported molybdenum oxides. Differences in catalytic behavior were attributed to the different inherent redox properties, *i.e.*, higher reducibility of vanadium oxide compared to molybdenum oxide, lower Tammann temperature of V_2O_5 , implying a higher lattice oxygen mobility within the supported vanadium oxide species, and the difference in the redox potentials of V^{5+}/V^{4+} and Mo^{6+}/Mo^{5+} .

7 Summary and Outlook

The relation between catalytic performance and structure of a catalyst system is a fundamental issue in academic and industrial studies. Structure and chemical composition of commercially employed catalysts are usually very complex. Therefore, investigations of suitable catalyst model systems are required. Such model systems allow the separate investigation of the influence of individual chemical or structural motifs on catalytic performance. The objectives of this work were the preparation and detailed characterization of vanadium or molybdenum oxides supported on an alkaline oxide support. Vanadium and molybdenum oxides supported on MgO-coated SBA-15 (*MgO/SBA-15*) were prepared in a loading range between 1 wt.% and 10 wt.% vanadium or molybdenum (0.2 to 5.9 metal atoms per nm²). Structural characterization of the metal oxide catalysts was performed by X-ray absorption spectroscopy, diffuse reflectance UV-Vis spectroscopy, nitrogen physisorption, Raman spectroscopy, and X-ray diffraction. The study aimed at investigating the influence of the alkaline support properties on structure and catalytic activity of the supported oxides. Therefore, the *V/MgO/SBA-15* and *Mo/MgO/SBA-15* catalysts were compared to vanadium and molybdenum oxides supported on other support materials, such as SBA-15 and CMK-3. Catalytic activity of these model systems was tested in selective propene oxidation and oxidative dehydrogenation of propane. To deduce structure activity correlations the catalysts were investigated under reaction conditions by *in situ* spectroscopy. Catalytic performance, *i.e.*, gas phase composition, conversion, and product selectivity, was analyzed using a laboratory fixed-bed reactor.

7.1.1 Support Material

Alkaline oxide supports based on magnesium oxide were synthesized via two different approaches. First, nanostructured magnesium oxide (*nano-MgO*) was obtained by a direct route with the triblock copolymer P-123 as structure-directing agent. Second, *MgO/SBA-15* was prepared by coating of SBA-15 with magnesium oxide. Hence, the acidic silica surface of SBA-15 was altered to an alkaline surface by a MgO layer. The support materials were investigated in terms of surface area and pore size distribution, activity during catalytic reaction, and thermal stability. Both synthetic approaches resulted in a high surface area material with a narrow pore size distribution in the mesopore range. Catalytic activity of the bare supports in

selective propene oxidation was negligible. However, the structure of *nano-MgO* collapsed at elevated temperatures (450 °C). Under ambient conditions, about 30% of the material was present as $\text{Mg}(\text{OH})_2$. Thermal treatment led to a transformation of $\text{Mg}(\text{OH})_2$ to MgO and thus, to a strongly altered surface species. Conversely, *MgO/SBA-15* remained stable under catalytic reaction conditions. Therefore, only *MgO/SBA-15* proved to be a suitable support material for this work.

Dehydration of the *MgO/SBA-15* support required an activation energy of approximately 50 kJ/mol. No changes in activation energy were observed upon deposition of vanadium or molybdenum oxide catalysts on *MgO/SBA-15*. Therefore, the dehydration process seemed to proceed independent of catalyst deposition. Compared to bare SBA-15 the activation energy of the dehydration step was considerably lower for *MgO/SBA-15*, indicating a weaker interaction of the adsorbed water molecules on the *MgO/SBA-15* surface.

7.1.2 Structure of Supported Vanadium and Molybdenum Oxides

Vanadium and molybdenum oxides supported on *MgO/SBA-15* were prepared by an incipient wetness procedure. Calcination of the *V/MgO/SBA-15* and *Mo/MgO/SBA-15* catalysts led to fine dispersion of the metal oxides on the *MgO/SBA-15* surface. Formation of crystalline vanadium or molybdenum oxide species was only observed at high loadings (10 wt.%). The local structure of the supported metal oxides was directly correlated to the net pH at point of zero charge (PZC) of the surface of the oxide support. The structure was therefore comparable to that of the corresponding oxides in aqueous solution at similar pH. Thus, the alkaline surface of *MgO/SBA-15* resulted in the formation of predominantly isolated, tetrahedral vanadium or molybdenum oxide units.

A schematic representation of the local structure of the supported vanadium and molybdenum oxides derived from structural analysis is given in Fig. 7.1. The degree of oligomerization of vanadium oxides supported on *MgO/SBA-15* was strongly dependent on catalyst loading and surface coverage. With increasing surface coverage the degree of oligomerization of the tetrahedral vanadium oxide units increased. Therefore, at low surface coverage ($< 0.5 \text{ V atoms/nm}^2$) predominately monomeric $[\text{VO}_4]$ tetrahedra were present. The degree of oligomerization of the tetrahedral units progressively increased until maximum sur-

face coverage (~ 6 V atoms/nm²) was reached. At maximum coverage partial formation of V_xO_y nanocrystallites was observed in addition to the formation of [VO₄] oligomers. The tetrahedral coordination sphere around the vanadium atoms was most likely extended by the coordination of an additional fifth oxo-ligand to the metal center. This additional oxo-ligand presumably was provided by a hydroxyl group bound to the *MgO/SBA-15* support. In contrast to the supported vanadium oxides, the degree of oligomerization of the supported molybdenum oxides was largely independent of catalyst loading and surface coverage. The molybdenum oxide species were present as predominantly isolated [MoO₄] tetrahedra. Upon initial calcination the partial formation of [Mo₂O₇] units was observed in addition to the tetrahedral monomers. The ratio between monomeric and dimeric molybdenum oxide units on the *MgO/SBA-15* support was estimated to 3:2.

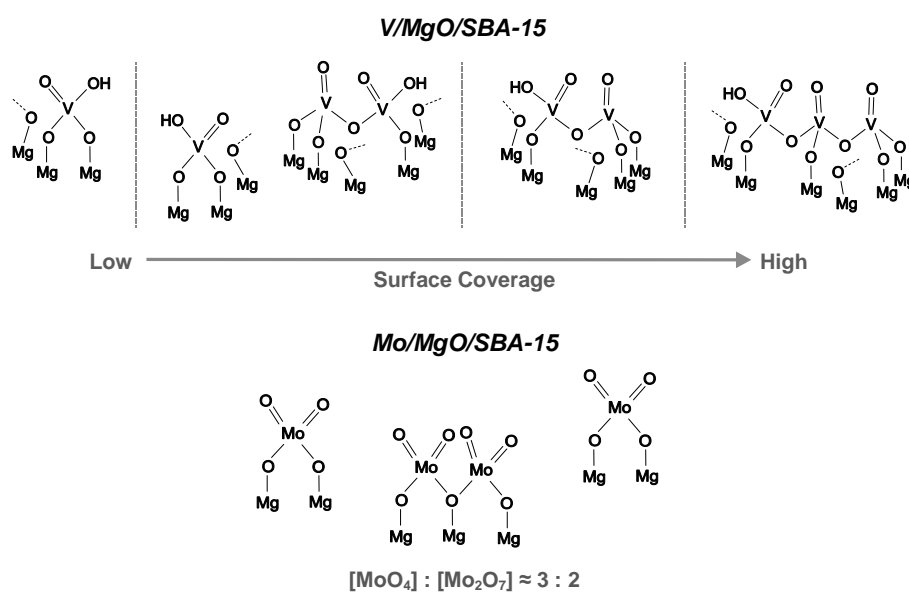


Fig. 7.1 Schematic representation of molecular configurations for vanadium and molybdenum oxides supported on *MgO/SBA-15*. The degree of oligomerization of the vanadium oxides increased with increasing surface coverage from monomeric to oligomeric [VO₄] tetrahedra. The molybdenum oxide species consisted of a mixture of monomeric and dimeric [MoO₄] tetrahedra with a ratio of monomers to dimers of \sim 3:2.

The structure of the vanadium and molybdenum oxides supported on *MgO/SBA-15* was preserved under ambient conditions in the presence of water. A change between hydrated and dehydrated state was not detected. This was in contrast to vanadium and molybdenum oxides supported on oxide materials, such as silica or alumina, where hydrated and dehydrated states

are commonly observed. On SBA-15 a hydrated state of highly oligomerized metal oxide species is formed under ambient conditions. Hence, the structures of vanadium and molybdenum oxide supported on coated and uncoated SBA-15 were clearly distinguishable. This was attributed to different net pH at PZC of the surface of SBA-15 and *MgO/SBA-15*. A comparison of the oxide structure on alkaline *MgO/SBA-15* to the dehydrated structure of vanadium oxides supported on the more acidic silica SBA-15 revealed significant differences. Therefore, it was shown that the acidity of the supporting oxide had a great impact on the structure of the supported metal oxide species. On more acidic SBA-15 substantially higher oligomerized metal oxide units were formed than on alkaline *MgO/SBA-15* at similar catalyst loadings. In addition to investigating vanadium and molybdenum oxides supported on SBA-15, the *V/MgO/SBA-15* and *Mo/MgO/SBA-15* catalysts were compared to the oxide species supported on carbon CMK-3. The non-oxide support CMK-3 led to a vanadium and molybdenum oxide structure that was comparable to the oxide structure in aqueous solution at neutral pH. This effect was most likely due to the presence of physisorbed water on the surface of CMK-3. The structure of *V/CMK-3* and *Mo/CMK-3* resembled that of the hydrated state on silica SBA-15. Hence, the metal oxide species consisted of a two-dimensional layer of octahedral metal oxide units on the CMK-3 support. A weaker oxide-support interaction compared to that on SBA-15 was assumed to cause a low distortion of the octahedrally coordinated metal oxide units on CMK-3.

7.1.3 Catalytic Properties and Structure Activity Correlations

Reactivity of the vanadium and molybdenum oxide catalysts was tested for selective oxidation of propene to acrolein. This study focused on elucidating structure activity correlations by investigating the well-characterized *V/MgO/SBA-15* and *Mo/MgO/SBA-15* catalyst model systems with *in situ* techniques under reaction conditions. To verify the structure activity correlations obtained for propene oxidation, the *V/MgO/SBA-15* catalysts were additionally tested for oxidative dehydrogenation of propane, where a different reaction mechanism was assumed.

Redox properties of the vanadium and molybdenum oxides were shown to play an important role for their catalytic performance. Partial reduction of the active species during reaction was directly correlated to catalytic activity. Bridging metal(M)-oxide(O) M–O–M

bonds were found to be required in order to achieve reducibility of the metal oxide species. Isolated $[\text{MO}_4]$ units were only slightly reduced under catalytic reaction conditions. Combination of the data from *in situ* spectroscopy with catalytic activity revealed that the catalytically active site consisted of partially reduced metal oxide species. Hence, reaction was assumed to proceed via a Mars-van-Krevelen or redox type mechanisms. For *V/MgO/SBA-15* the most active species were observed to contain vanadium centers in the mixed oxidation state between +IV and +V. Reducibility of the supported oxide catalysts was enhanced with increasing degree of oligomerization of the vanadium oxide units. Therefore, the higher reducibility observed at higher vanadium oxide surface coverage and higher degree of oligomerization correlated to an increasing selectivity to acrolein.

The nature of the support had a tremendous impact on the structure of the supported metal oxide, and therefore, influenced their catalytic properties. By modification of the metal oxide-support interaction it was possible to alter the acid-base and redox properties of the model catalyst system. Hence, a change from *MgO/SBA-15* to silica SBA-15 and carbon CMK-3 directly influenced catalytic performance. Metal oxides supported on SBA-15 and CMK-3 exhibited a significantly higher reducibility and re-oxidizability than those supported on *MgO/SBA-15*. This behavior was attributed to a weaker oxide-support interaction for the metal oxides supported on SBA-15 or CMK-3 compared to the oxides supported on *MgO/SBA-15*. On *MgO/SBA-15* the oxide species were considered to be strongly bond to the support, due to strong acid-base interactions between alkaline support and metal oxides.

Vanadium and molybdenum oxides supported on *MgO/SBA-15* exhibited a similar structure of tetrahedral metal(M)-oxide(O) $[\text{MO}_4]$ units. Therefore, the influence of a change in chemical composition on catalytic performance at an invariant structural motif could be studied. It was pointed out, that catalytic activity and selectivity in propene oxidation for vanadium and molybdenum oxides differed considerably from each other. At similar catalyst loadings acrolein turnover frequency (TOF) of *V/MgO/SBA-15* was approximately five times higher than that for *Mo/MgO/SBA-15*. Conversely, selectivity to acrolein was always higher for the supported molybdenum oxides. Differences in the catalytic behavior of *V/MgO/SBA-15* and *Mo/MgO/SBA-15* might be caused by their different inherent redox properties, such as reduci-

bility, Tammann temperature of the corresponding oxides, and redox potentials of V^{5+}/V^{4+} and Mo^{6+}/Mo^{5+} . Both catalyst systems, $V/MgO/SBA-15$ and $Mo/MgO/SBA-15$, were tested under long-term reaction conditions during a period of 20 h time on stream at 400 °C. For supported molybdenum oxides propene conversion over the first hour of time on stream decreased considerably while selective oxidation to acrolein increased. This was attributed to the formation of adsorbed hydrocarbon species on the catalyst surface. The formation of coke eventually led to the deactivation of highly active but unselective catalyst surface sites. Hence, acrolein TOF for $Mo/MgO/SBA-15$ was nearly doubled after the first hour of time on stream. Conversely, acrolein TOF and propene conversion for supported vanadium oxides only slightly decreased over initial time on stream. No coke formation was observed.

The structural variation observed for the vanadium oxide species supported on $MgO/SBA-15$ permitted to study the influence of catalyst structure on catalytic properties. With increasing vanadium oxide surface coverage the degree of oligomerization of the vanadium oxide units increased. It was shown that the degree of oligomerization strongly affected catalytic activity in propene oxidation. Acrolein turnover frequency (TOF) as a function of surface coverage resembled a "vulcano type" curve (Fig. 7.2).

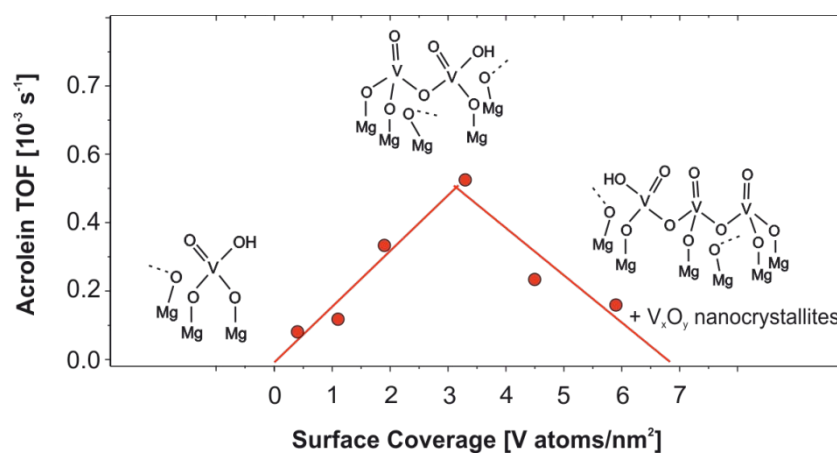


Fig. 7.2 Acrolein TOF of vanadium oxide catalysts supported on $MgO/SBA-15$ as a function of surface coverage. The optimal surface coverage for a maximum acrolein TOF was in the range of 3–3.5 V atoms/nm². In this range the vanadium oxide species were present as adjacent $[VO_4]$ tetrahedra with an average number of 1–2 V–O–V bonds.

Isolated $[\text{VO}_4]$ units exhibited only little catalytic activity, whereas higher oligomerized vanadium oxide units yielded higher acrolein TOF values. In the range of maximum coverage acrolein TOF decreased, due to the formation of nanocrystalline V_xO_y species. An invariant structure, as it was observed for the molybdenum oxide supported on *MgO/SBA-15* at various catalyst loadings, *i.e.*, 1–10 wt.% Mo, resulted in a similar catalytic activity in selective propene oxidation independent of molybdenum oxide surface coverage.

The correlation between surface coverage and catalytic activity obtained for the first set of *V/MgO/SBA-15* catalysts was used to prepare the optimal surface coverage meeting the predicted maximum of the "vulcano curve" (Fig. 7.2). Hence, in a second set of samples a maximum acrolein TOF for *V/MgO/SBA-15* was achieved at medium coverage in the range of 3–3.5 V atoms/nm². In this range the supported vanadium oxide species consisted of linked $[\text{VO}_4]$ tetrahedra with an average number of 1–2 V–O–V bonds. These results confirmed the assumption of at least two surface $[\text{VO}_4]$ units being involved in the selective oxidation of propene. The necessity of two vanadium centers in the catalytic reaction is most likely due to the fact that selective oxidation of propene to acrolein requires the transfer of four electrons. Conversely, the oxidative dehydrogenation (ODH) of propane involves only two electrons. Therefore, in the range below formation of V_xO_y nanocrystallites propane-to-propene turnover frequency (TOF) was found to be independent of surface coverage. This behavior thus indicated the requirement of only one $[\text{VO}_4]$ unit in ODH reaction.

7.1.4 Outlook

The results of this work on structural and functional characterization of the *V/MgO/SBA-15* and *Mo/MgO/SBA-15* model systems will add to understanding structure activity correlations in working metal oxide catalysts. The rational improvement of selective oxidation catalysts still remains a challenge. Therefore, continuative fundamental research on catalyst model systems is needed. A short-term objective for future research is a systematic catalytic testing of the catalyst systems to extend the knowledge on the reaction pathway in selective oxidation reactions. Therefore, further *in situ* investigations should be performed under dynamic reaction conditions. *In situ* Raman spectroscopy, for instance, offers the possibility of studying the local structure of the supported oxide catalysts under working conditions. Especially the influence of the metal oxide-support interaction on the redox properties of the catalysts are of

interest. Because this interaction is still not well understood further studies in this field are necessary. The work on the non-oxide support material CMK-3 presented here has emphasized the impact of the metal oxide-support interaction. The presumably weaker oxide-support interaction on a non-oxide support might enhance reducibility and reoxidizability of the catalysts. This assumption needs further research on the oxide-support bond strength for metal oxides supported on various support material. As non-oxide support materials non-oxide ceramics, *i.e.*, carbides or nitrides, with high specific surface areas and ordered pore structures might be suitable.

Selective oxidation of propene was shown to require the presence of at least dimeric metal oxide units. The next step in elucidating structure activity correlations will require the investigation of dimeric or oligomeric metal oxide units with increased chemical complexity. Therefore, research should be extended to the investigation of mixed vanadium and molybdenum oxides supported on various support materials. As long-term objective, chemical complexity can further be increased by the addition of other components, like tungsten, niobium, or bismuth. Therefore, a step-by-step development from understanding model catalyst systems to the understanding of systems, that are close to the "real" catalysts, can be achieved. Hence, investigation of selected model systems in selective oxidation has still much to offer to the science of heterogeneous catalysis.

Bibliography

1. Thomas, J.M., *Turning Points in Catalysis*. *Angew. Chem. Int. Ed.* **1994**. 33(9): p. 913–937.
2. *Chemische Industrie kurz gefasst*. Verband der Chemischen Industrie e. V. **2012**.
3. Fierro, J.L.G., *Metal Oxides: Chemistry and Applications*. **2010**: Taylor & Francis Group.
4. Deo, G., Wachs, I.E., and Haber, J., *Supported Vanadium Oxide Catalysts: Molecular Structural Characterization and Reactivity Properties*. *Crit. Rev. Surf. Chem.* **1994**. 4(3/4): p. 141–187.
5. Jahr, K.F. and Fuchs, J., *Neue Wege und Ergebnisse der Polysäureforschung*. *Angew. Chem.* **1966**. 78(15): p. 725–735.
6. Jander, G. and Winkel, A., *Über amphotere Oxydhydrate, deren wäßrige Lösungen und kristallisierende Verbindungen. XII Mitteilung. Hydrolysierende Systeme und ihre Aggregationsprodukte mit besonderer Berücksichtigung der Erscheinungen in wäßrigen Aluminiumsalzlösungen*. *Z. Anorg. Allg. Chem.* **1931**. 200(1): p. 257–278.
7. Corma, A., *From Microporous to Mesoporous Molecular Sieve Materials and Their Use in Catalysis*. *Chem. Rev.* **1997**. 97(6): p. 2373–2420.
8. Tüysüz, H., Lehmann, C.W., Bongard, H., et al., *Direct Imaging of Surface Topology and Pore System of Ordered Mesoporous Silica (MCM-41, SBA-15, and KIT-6) and Nanocast Metal Oxides by High Resolution Scanning Electron Microscopy*. *J. Amer. Chem. Soc.* **2008**. 130(34): p. 11510–11517.
9. Zhao, D., Huo, Q., Feng, J., et al., *Nonionic Triblock and Star Diblock Copolymer and Oligomeric Surfactant Syntheses of Highly Ordered, Hydrothermally Stable, Mesoporous Silica Structures*. *J. Amer. Chem. Soc.* **1998**. 120: p. 6024–6036.
10. Zhao, D., Feng, J., Huo, Q., et al., *Triblock Copolymer Syntheses of Mesoporous Silica with Periodic 50 to 300 Angstrom Pores*. *Science* **1998**. 279(5350): p. 548–552.

11. Beck, J.S., Vartuli, J.C., Roth, W.J., et al., *A new family of mesoporous molecular sieves prepared with liquid crystal templates*. J. Amer. Chem. Soc. **1992**. 114(27): p. 10834–10843.
12. Fuertes, A.B. and Nevskaja, D.M., *Control of mesoporous structure of carbons synthesised using a mesostructured silica as template*. Microporous Mesoporous Mater. **2003**. 62(3): p. 177–190.
13. Fuertes, A.B., *Template synthesis of mesoporous carbons with a controlled particle size*. J. Mater. Chem. **2003**. 13(12): p. 3085–3088.
14. Zhou, L., Ren, Q., Zhou, X., et al., *Comprehensive understanding on the formation of highly ordered mesoporous tungsten oxides by X-ray diffraction and Raman spectroscopy*. Microporous Mesoporous Mater. **2008**. 109(1–3): p. 248–257.
15. Jiao, F., Jumas, J.-C., Womes, M., et al., *Synthesis of Ordered Mesoporous Fe₃O₄ and γ -Fe₂O₃ with Crystalline Walls Using Post-Template Reduction/Oxidation*. J. Amer. Chem. Soc. **2006**. 128(39): p. 12905–12909.
16. Dickinson, C., Zhou, W., Hodgkins, R.P., et al., *Formation Mechanism of Porous Single-Crystal Cr₂O₃ and Co₃O₄ Templated by Mesoporous Silica*. Chem. Mater. **2006**. 18(13): p. 3088–3095.
17. Wang, Y.-g. and Xia, Y.-y., *Electrochemical capacitance characterization of NiO with ordered mesoporous structure synthesized by template SBA-15*. Electrochim. Acta **2006**. 51(16): p. 3223–3227.
18. Zhu, S., Zhou, Z., Zhang, D., et al., *Synthesis of mesoporous amorphous MnO₂ from SBA-15 via surface modification and ultrasonic waves*. Microporous Mesoporous Mater. **2006**. 95(1–3): p. 257–264.
19. Vinu, A., Srinivasu, P., Takahashi, M., et al., *Controlling the textural parameters of mesoporous carbon materials*. Microporous Mesoporous Mater. **2007**. 100(1–3): p. 20–26.
20. Fuertes, A.B., *Synthesis of ordered nanoporous carbons of tunable mesopore size by templating SBA-15 silica materials*. Microporous Mesoporous Mater. **2004**. 67(2–3): p. 273–281.

21. Roggenbuck, J., Koch, G., and Tiemann, M., *Synthesis of Mesoporous Magnesium Oxide by CMK-3 Carbon Structure Replication*. Chem. Mater. **2006**. 18(17): p. 4151–4156.
22. Li, J., Dai, W.-L., and Fan, K., *Formation of Ordered Mesoporous MgO with Tunable Pore Diameter and Its Application As Excellent Alkaline Catalyst in Baeyer-Villiger Oxidation*. J. Phys. Chem. C **2008**. 112(45): p. 17657–17663.
23. Wagner, T., Waitz, T., Roggenbuck, J., et al., *Ordered mesoporous ZnO for gas sensing*. Thin Solid Films **2007**. 515(23): p. 8360–8363.
24. Roggenbuck, J., Schäfer, H., Tsoncheva, T., et al., *Mesoporous CeO₂: Synthesis by nanocasting, characterisation and catalytic properties*. Microporous Mesoporous Mater. **2007**. 101(3): p. 335–341.
25. Schwickardi, M., Johann, T., Schmidt, W., et al., *High-Surface-Area Oxides Obtained by an Activated Carbon Route*. Chem. Mater. **2002**. 14(9): p. 3913–3919.
26. Xiong, G., Luo, L., Li, C., et al., *Synthesis of Mesoporous ZnO (m-ZnO) and Catalytic Performance of the Pd/m-ZnO Catalyst for Methanol Steam Reforming*. Energy Fuels. **2009**. 23(3): p. 1342–1346.
27. Yu, J.C., Xu, A., Zhang, L., et al., *Synthesis and Characterization of Porous Magnesium Hydroxide and Oxide Nanoplates*. J. Phys. Chem. B **2003**. 108(1): p. 64–70.
28. Wei, Y., Wang, Y., Zhu, J., et al., *In-Situ Coating of SBA-15 with MgO: Direct Synthesis of Mesoporous Solid Bases from Strong Acidic Systems*. Adv. Mater. **2003**. 15(22): p. 1943–1945.
29. Zukal, A., Siklová, H., and Čejka, J., *Grafting of Alumina on SBA-15: Effect of Surface Roughness*. Langmuir **2008**. 24(17): p. 9837–9842.
30. Zukal, A., Pastva, J., and Čejka, J., *MgO-modified mesoporous silicas impregnated by potassium carbonate for carbon dioxide adsorption*. Microporous Mesoporous Mater. **2013**. 167(0): p. 44–50.
31. Bérubé, F., Kleitz, F., and Kaliaguine, S., *Surface properties and epoxidation catalytic activity of Ti-SBA15 prepared by direct synthesis*. J. Mater. Sci. **2009**. 44(24): p. 6727–6735.

32. Gao, X., Bare, S., Weckhuysen, B., et al., *In Situ Spectroscopic Investigation of Molecular Structures of Highly Dispersed Vanadium Oxide on Silica under Various Conditions*. *J. Phys. Chem. B* **1998**. 102: p. 10842–10852.
33. Xie, S., Iglesia, E., and Bell, A.T., *Effects of Hydration and Dehydration on the Structure of Silica-Supported Vanadia Species*. *Langmuir* **2000**. 16(18): p. 7162–7167.
34. Hess, C., *Direct correlation of the dispersion and structure in vanadium oxide supported on silica SBA-15*. *J. Catal.* **2007**. 248(1): p. 120–123.
35. García, H., López Nieto, J., Palomares, E., et al., *Photoluminescence of supported vanadia catalysts: linear correlation between the vanadyl emission wavelength and the isoelectric point of the oxide support*. *Catal. Lett.* **2000**. 69(3): p. 217–221.
36. Wachs, I.E. and Weckhuysen, B.M., *Structure and reactivity of surface vanadium oxide species on oxide supports*. *Appl. Catal. A* **1997**. 157(1–2): p. 67–90.
37. Weber, R.S., *Effect of Local Structure on the UV-Visible Absorption Edges of Molybdenum Oxide Clusters and Supported Molybdenum Oxides*. *J. Catal.* **1995**. 151(2): p. 470–474.
38. Topka, P., Balcar, H., Rathouský, J., et al., *Metathesis of 1-octene over MoO₃ supported on mesoporous molecular sieves: The influence of the support architecture*. *Microporous Mesoporous Mater.* **2006**. 96(1–3): p. 44–54.
39. Rossel, R.A.V., McGlynn, R.N., and McBratney, A.B., *Determining the composition of mineral-organic mixes using UV-vis-NIR diffuse reflectance spectroscopy*. *Geoderma* **2006**. 137(1–2): p. 70–82.
40. Debecker, D.P., Hauwaert, D., Stoyanova, M., et al., *Opposite effect of Al on the performances of MoO₃/SiO₂-Al₂O₃ catalysts in the metathesis and in the partial oxidation of propene*. *Appl. Catal. A* **2011**. 391(1–2): p. 78–85.
41. Huang, Z., Bensch, W., Sigle, W., et al., *The modification of MoO₃ nanoparticles supported on mesoporous SBA-15: characterization using X-ray scattering, N₂ physisorption, transmission electron microscopy, high-angle annular darkfield technique, Raman and XAFS spectroscopy*. *J. Mater. Sci.* **2008**. 43(1): p. 244–253.

42. Hu, H., Wachs, I.E., and Bare, S.R., *Surface Structures of Supported Molybdenum Oxide Catalysts: Characterization by Raman and Mo L3-Edge XANES*. J. Phys. Chem. **1995**. 99(27): p. 10897–10910.
43. Williams, C.C., Ekerdt, J.G., Jehng, J.M., et al., *A Raman and ultraviolet diffuse reflectance spectroscopic investigation of silica-supported molybdenum oxide*. J. Phys. Chem. **1991**. 95(22): p. 8781–8791.
44. Llorente, J.M., Rives, V., Malet, P., et al., *MoO₃/MgO systems: Effect of preparation method on their physicochemical properties*. J. Catal. **1992**. 135(1): p. 1–12.
45. Chang, S.C., Leugers, M.A., and Bare, S.R., *Surface chemistry of magnesium oxide-supported molybdenum oxide: an in situ Raman spectroscopic study*. J. Phys. Chem. **1992**. 96(25): p. 10358–10365.
46. Bare, S.R., *Surface Structure of Highly Dispersed MoO₃ on MgO Using in Situ Mo L3-Edge XANES*. Langmuir **1998**. 14(6): p. 1500–1504.
47. Aritani, H., Tanaka, T., Funabiki, T., et al., *Study of the Local Structure of Molybdenum–Magnesium Binary Oxides by Means of Mo L3-Edge XANES and UV–Vis Spectroscopy*. J. Phys. Chem. **1996**. 100(50): p. 19495–19501.
48. Deo, G. and Wachs, I.E., *Predicting molecular structures of surface metal oxide species on oxide supports under ambient conditions*. J. Phys. Chem. **1991**. 95(15): p. 5889–5895.
49. Stampfl, S.R., Chen, Y., Dumesic, J.A., et al., *Interactions of molybdenum oxide with various oxide supports: Calcination of mechanical mixtures*. J. Catal. **1987**. 105(2): p. 445–454.
50. Eley, D.D., Pines, H., and Weisz, P.B., *Advances in Catalysis*. **1981**: Elsevier Science.
51. Grasselli, R.K., *Fundamental Principles of Selective Heterogeneous Oxidation Catalysis*. Top. Catal. **2002**. 21(1): p. 79–88.
52. Mars, P. and van Krevelen, D.W., *Oxidations carried out by means of vanadium oxide catalysts*. Chemical Engineering Science **1954**. 3: p. 41–59.

53. Centi, G., Cavani, F., and Trifiró, F., *Selective oxidation by heterogeneous catalysis*. Fundamental and Applied Catalysis, Ed. Twigg, M.V. and Spencer, M.S. **2000**, New York: Kluwer Academic/Plenum Publishers
54. Krylov, O.V. and Margolis, L.Y., *Selectivity of Partial Hydrocarbon Oxidation*. Int. Rev. Phys. Chem. **1983**. 3(3): p. 305–333.
55. Weckhuysen, B.M. and Keller, D.E., *Chemistry, spectroscopy and the role of supported vanadium oxides in heterogeneous catalysis*. Catal. Today **2003**. 78(1–4): p. 25–46.
56. Grzybowska-Świerkosz, B., *Vanadia-titania catalysts for oxidation of o-xylene and other hydrocarbons*. Appl. Catal. A **1997**. 157(1–2): p. 263–310.
57. Liu, T.-C., Forissier, M., Coudurier, G., et al., *Properties of molybdate species supported on silica*. J. Chem. Soc., Faraday Trans. I **1989**. 85(7): p. 1607–1618.
58. Ohler, N. and Bell, A.T., *Selective oxidation of methane over MoO_x/SiO₂: isolation of the kinetics of reactions occurring in the gas phase and on the surfaces of SiO₂ and MoO_x*. J. Catal. **2005**. 231(1): p. 115–130.
59. Chen, K., Xie, S., Bell, A.T., et al., *Structure and Properties of Oxidative Dehydrogenation Catalysts Based on MoO₃/Al₂O₃*. J. Catal. **2001**. 198(2): p. 232–242.
60. Abello, M.C., Gomez, M.F., and Cadus, L.E., *Selective oxidation of propane on MgO/γ-Al₂O₃-supported molybdenum catalyst: influence of promoters*. Catal. Lett. **1998**. 53(3): p. 185–192.
61. Debecker, D.P., Schimmoeller, B., Stoyanova, M., et al., *Flame-made MoO₃/SiO₂-Al₂O₃ metathesis catalysts with highly dispersed and highly active molybdate species*. J. Catal. **2011**. 277(2): p. 154–163.
62. Tian, H., Ross, E.I., and Wachs, I.E., *Quantitative Determination of the Speciation of Surface Vanadium Oxides and Their Catalytic Activity*. J. Phys. Chem. B **2006**. 110(19): p. 9593–9600.
63. Gao, X., Bañares, M.A., and Wachs, I.E., *Ethane and n-Butane Oxidation over Supported Vanadium Oxide Catalysts: An in Situ UV-Visible Diffuse Reflectance Spectroscopic Investigation*. J. Catal. **1999**. 188(2): p. 325–331.

64. Argyle, M.D., Chen, K., Iglesia, E., et al., *In situ UV-Visible Spectroscopic Measurements of Kinetic Parameters and Active Sites for Catalytic Oxidation of Alkanes on Vanadium Oxides*. *J. Phys. Chem. B* **2004**. 109(6): p. 2414–2420.
65. Wong, J., Lytle, F., Messmer, R., et al., *K-edge absorption spectra of selected vanadium compounds*. *Phys. Rev. B* **1984**. 30: p. 5596–5610.
66. Lemonidou, A.A., Nalbandian, L., and Vasalos, I.A., *Oxidative dehydrogenation of propane over vanadium oxide based catalysts: Effect of support and alkali promoter*. *Catal. Today* **2000**. 61(1–4): p. 333–341.
67. Zhao, Z., Yamada, Y., Ueda, A., et al., *The roles of redox and acid–base properties of silica-supported vanadia catalysts in the selective oxidation of ethane*. *Catal. Today* **2004**. 93–95: p. 163–171.
68. Balderas-Tapia, L., Hernández-Pérez, I., Schacht, P., et al., *Influence of reducibility of vanadium–magnesium mixed oxides on the oxidative dehydrogenation of propane*. *Catal. Today* **2005**. 107–108: p. 371–376.
69. Blasco, T. and Nieto, J.M.L., *Oxidative dehydrogenation of short chain alkanes on supported vanadium oxide catalysts*. *Appl. Catal. A* **1997**. 157(1–2): p. 117–142.
70. Ozkan, U.S. and Watson, R.B., *The structure–function relationships in selective oxidation reactions over metal oxides*. *Catal. Today* **2005**. 100(1–2): p. 101–114.
71. Zazhigalov, V.A., Pyatnitskaya, A.I., Bacherikova, I.V., et al., *Dependence of the activity of vanadium-phosphorus catalysts on the V⁴⁺/V⁵⁺ ratio in oxidation of butane*. *React. Kinet. Catal. Lett.* **1983**. 23(1–2): p. 119–123.
72. Cadus, L.E., Gomez, M.F., and Abello, M.C., *Synergy effects in the oxidative dehydrogenation of propane over MgMoO₄-MoO₃ catalysts*. *Catal. Lett.* **1997**. 43(3–4): p. 229–233.
73. Weckhuysen, B.M., *In-situ Spectroscopy of Catalysts*. **2004**: American Scientific Publishers.
74. Niemantsverdriet, J.W., *Spectroscopy in Catalysis: An Introduction*. 3rd Ed. **2007**, Weinheim: Wiley-VCH Verlag GmbH & Co. KGaA.

75. Koningsberger, D.C. and Prins, R., *X-Ray Absorption - Principles, Applications, Techniques of EXAFS, SEXAFS and XANES*. **1988**: John Wiley & Sons, Inc.
76. Koningsberger, D.C., Mojet, B.L., van Dorssen, G.E., et al., *XAFS spectroscopy; fundamental principles and data analysis*. *Top. Catal.* **2000**. 10(3): p. 143–155.
77. Fournier, M., Louis, C., Che, M., et al., *Polyoxometallates as models for oxide catalysts: Part I. An UV-visible reflectance study of polyoxomolybdates: Influence of polyhedra arrangement on the electronic transitions and comparison with supported molybdenum catalysts*. *J. Catal.* **1989**. 119(2): p. 400–414.
78. Atkins, P.W., De Paula, J., and Bär, M., *Physikalische Chemie*. 4th Ed. **2006**, Weinheim: Wiley-VCH Verlag GmbH.
79. Kortüm, G. and Lohr, J.E., *Reflectance Spectroscopy: Principles, Methods, Applications*. **2012**: Springer London, Limited.
80. Kubelka, P. and Munk, F., *Ein Beitrag zur Optik der Farbanstriche*. *Zeitschrift für technische Physik* **1931**. 12(112): p. 593–601.
81. Harrick Scientific Products, I., *The Praying MantisTM - User's Manual*, **2004**.
82. Sing, K.S.W., Everett, D.H., Haul, R.A.W., et al., *Reporting Physisorption Data for Gas/Solid Systems with Special Reference to the Determination of Surface Area and Porosity*. *Pure & Appl. Chem.* **1985**. 57(4): p. 603–619.
83. Gregg, S.G. and Sing, K.S.W., *Adsorption, Surface Area and Porosity*. 2nd Ed. **1982**, London: Academic Press Inc.
84. Lippens, B.C. and de Boer, J.H., *Studies on Pore Systems in Catalysts: V. The t Method*. *J. Catal.* **1965**. 4(3): p. 319–323.
85. Rouquerol, F., Rouquerol, J., and Sing, K., *Adsorption by Powders and Porous Solids*. **1999**, London: Academic Press.
86. Brunauer, S., Emmett, P.H., and Teller, E., *Adsorption of Gases in Multimolecular Layers*. *J. Amer. Chem. Soc.* **1938**. 60(2): p. 309–319.
87. Allmann, R., *Röntgenpulverdiffraktometrie: Rechnergestützte Auswertung, Phasenanalyse und Strukturbestimmung*. 2nd Ed. **2003**, Berlin Heidelberg: Springer-Verlag.

88. Dinnebier, R.E. and Billinge, S.J.L., *Powder Diffraction Theory and Practice*. **2008**, Cambridge: The Royal Society of Chemistry.
89. *DIN 51005: Thermische Analyse (TA) - Begriffe*. **2005** [cited 2013 20.05.2013]; Available from: <http://www.beuth.de/langanzeige/DIN+51005/81449381.html>.
90. Haines, P.J., *Principles of Thermal Analysis and Calorimetry*. **2002**, Cambridge: The Royal Society of Chemistry.
91. Haw, J.F., *In-Situ Spectroscopy in Heterogeneous Catalysis*. **2002**, Weinheim: Wiley-VCH Verlag GmbH & Co. KGaA.
92. Skoog, D.A. and Leary, J.J., *Instrumentelle Analytik: Grundlagen, Geräte, Anwendungen*. 4th Ed. **1996**, Berlin Heidelberg: Springer-Verlag.
93. Beckhoff, B., Kanngieber, B., Langhoff, N., et al., *Handbook of Practical X-ray Fluorescence Analysis*. **2006**: Springer-Verlag Berlin Heidelberg.
94. Haber, J., Block, J.H., and Delmon, B., *Methods and Procedures for Catalyst Characterization*, in *Handbook of Heterogeneous Catalysis*, Ertl, G., Knözinger, H., Schüth, F., et al. Editors. **2008**, Wiley-VCH Verlag GmbH: Weinheim. p. 1230–1258.
95. Hagen, J., *Industrial Catalysis - A Practical Approach*. 2nd Ed. **2006**, Weinheim: Wiley-VCH Verlag GmbH & Co. KGaA.
96. Hübschmann, H.-J., *Handbuch der GC/MS - Grundlagen und Anwendung*. **1996**, Weinheim: VCH Verlagsgesellschaft mbH.
97. Grob, R.L. and Barry, E.F., *Modern Practice of Gas Chromatography*. 4th Ed. **2004**, Hoboken: John Wiley & Sons, Inc.
98. Scholz, J., *Struktur-Aktivitätsrelationen von Molybdänoxidkatalysatoren geträgert auf nanostrukturiertem Magnesiumoxid*. Technische Universität Berlin, Fakultät II – Mathematik und Naturwissenschaften **2009**. Diploma Thesis: p. 1–107.
99. Lippens, B.C., Linsen, B.G., and Boer, J.H.d., *Studies on pore systems in catalysts I. The adsorption of nitrogen; apparatus and calculation*. *J. Catal.* **1964**. 3(1): p. 32–37.
100. Wang, G., Zhang, L., Dai, H., et al., *PI23-Assisted Hydrothermal Synthesis and Characterization of Rectangular Parallelepiped and Hexagonal Prism Single-*

- Crystalline MgO with Three-Dimensional Wormholelike Mesopores*. Inorg. Chem. **2008**. 47(10): p. 4015–4022.
101. Sasaki, S., Fujino, K., Tak, et al., *X-Ray Determination of Electron-Density Distributions in Oxides, MgO, MnO, CoO, and NiO, and Atomic Scattering Factors of their Constituent Atoms*. Proc. Jpn. Acad., Ser. B **1979**. 55(2): p. 43–48.
102. Catti, M., Ferraris, G., Hull, S., et al., *Static compression and H disorder in brucite, Mg(OH)₂, to 11 GPa: a powder neutron diffraction study*. Phys. Chem. Miner. **1995**. 22(3): p. 200–206.
103. Gommes, C.J., Friedrich, H., Wolters, M., et al., *Quantitative Characterization of Pore Corrugation in Ordered Mesoporous Materials Using Image Analysis of Electron Tomograms*. Chem. Mater. **2009**. 21(7): p. 1311–1317.
104. Yang, C.-M., Zibrowius, B., Schmidt, W., et al., *Stepwise Removal of the Copolymer Template from Mesopores and Micropores in SBA-15*. Chem. Mater. **2004**. 16(15): p. 2918–2925.
105. Ravikovitch, P.I. and Neimark, A.V., *Characterization of Micro- and Mesoporosity in SBA-15 Materials from Adsorption Data by the NLDFIT Method*. J. Phys. Chem. B **2001**. 105(29): p. 6817–6823.
106. Gurinov, A.A., Rozhkova, Y.A., Zukal, A.t., et al., *Mutable Lewis and Brønsted Acidity of Aluminated SBA-15 as Revealed by NMR of Adsorbed Pyridine-15N*. Langmuir **2011**. 27(19): p. 12115–12123.
107. Nitsche, D. and Hess, C., Personal Communication: *Raman data of V/MgO/SBA-15*. **2013**.
108. Holleman, A.F., Wiberg, E., and Wiberg, N., *Lehrbuch der anorganischen Chemie*. **1995**: W. de Gruyter.
109. Scholz, J., Walter, A., Hahn, A.H.P., et al., *Molybdenum oxide supported on nanostructured MgO: Influence of the alkaline support properties on MoO_x structure and catalytic behavior in selective oxidation*. Microporous Mesoporous Mater. **2013**. 180(0): p. 130–140.

110. Walter, A., *Spectroscopic and catalytic investigations of supported $V_xO_y/SBA-15$ and magnesium vanadate model catalysts for selective propene oxidation*. Technischen Universität Berlin, Fakultät II – Mathematik und Naturwissenschaften **2011**. Dissertation: p. 1–225.
111. Walter, A., Herbert, R., Hess, C., et al., *Structural characterization of vanadium oxide catalysts supported on nanostructured silica SBA-15 using X-ray absorption spectroscopy*. Chem. Cent. J. **2010**. 4: p. 3.
112. Ressler, T., Walter, A., Huang, Z., et al., *Structure and properties of a supported MoO_3 –SBA-15 catalyst for selective oxidation of propene*. J. Catal. **2008**. 254(2): p. 170–179.
113. Ressler, T., *WinXAS: a Program for X-ray Absorption Spectroscopy Data Analysis under MS-Windows*. J. Synchrotron Rad. **1998**. 5: p. 118–122.
114. Gao, X. and Wachs, I.E., *Investigation of Surface Structures of Supported Vanadium Oxide Catalysts by UV-vis-NIR Diffuse Reflectance Spectroscopy*. J. Phys. Chem. B **2000**. 104(6): p. 1261–1268.
115. Kissinger, H.E., *Reaction Kinetics in Differential Thermal Analysis*. Analytical Chemistry **1957**. 29(11): p. 1702–1706.
116. Roozeboom, F., Fransen, T., Mars, P., et al., *Vanadium oxide monolayer catalysts. I. Preparation, characterization, and thermal stability*. Z. Anorg. Allg. Chem. **1979**. 449(1): p. 25–40.
117. Avdeev, V.I. and Zhidomirov, G., *Models of finely dispersed MgO and V_2O_5 on silica. Theoretical analysis of optical properties using TDDFT*. Res. Chem. Intermed. **2004**. 30(1): p. 41–64.
118. Morey, M., Davidson, A., Eckert, H., et al., *Pseudotetrahedral $O_3/2V=O$ Centers Immobilized on the Walls of a Mesoporous, Cubic MCM-48 Support: Preparation, Characterization, and Reactivity toward Water As Investigated by $51V$ NMR and UV–Vis Spectroscopies*. Chem. Mater. **1996**. 8(2): p. 486–492.
119. Anpo, M., Sunamoto, M., and Che, M., *Preparation of highly dispersed anchored vanadium oxides by photochemical vapor deposition method and their photocatalytic activity for isomerization of trans-2-butene*. J. Phys. Chem. **1989**. 93: p. 1187–1189.

120. Solsona, B., Dejoz, A., Vázquez, M.I., et al., *SiO₂-supported vanadium magnesium mixed oxides as selective catalysts for the oxydehydrogenation of short chain alkanes*. Appl. Catal. A **2001**. 208(1–2): p. 99–110.
121. Went, G.T., Oyama, S.T., and Bell, A.T., *Laser Raman spectroscopy of supported vanadium oxide catalysts*. J. Phys. Chem. **1990**. 94(10): p. 4240–4246.
122. Evans, H.T., *Crystal structure refinement and vanadium bonding in the metavanadates KVO₃, NH₄VO₃ and KVO₃·H₂O**. Z. Kristallogr. **1960**. 114(1–6): p. 257–277.
123. Griffith, J.S. and Orgel, L.E., *Ligand-field theory*. Q. Rev., Chem. Soc. **1957**. 11(4): p. 381–393.
124. Gopal, R. and Calvo, C., *Crystal Structure of α -Zn₂V₂O₇*. Can. J. Chem. **1973**. 51(7): p. 1004–1009.
125. Gopal, R. and Calvo, C., *Crystal structure of magnesium divanadate, Mg₂V₂O₇*. Acta Crystallogr., Sect. B **1974**. 30(10): p. 2491–2493.
126. Van Hengstum, A.J., Van Ommen, J.G., Bosch, H., et al., *Preparation of supported vanadium and molybdenum oxide catalysts using metal acetylacetonate complexes*. Applied Catalysis **1983**. 5(2): p. 207–217.
127. Jeziorowski, H. and Knoezinger, H., *Raman and ultraviolet spectroscopic characterization of molybdena on alumina catalysts*. J. Phys. Chem. **1979**. 83(9): p. 1166–1173.
128. Thielemann, J.P., Ressler, T., Walter, A., et al., *Structure of molybdenum oxide supported on silica SBA-15 studied by Raman, UV-Vis and X-ray absorption spectroscopy*. Appl. Catal. A **2011**. 399(1–2): p. 28–34.
129. Tian, H., Wachs, I.E., and Briand, L.E., *Comparison of UV and Visible Raman Spectroscopy of Bulk Metal Molybdate and Metal Vanadate Catalysts*. J. Phys. Chem. B **2005**. 109(49): p. 23491–23499.
130. Dieterle, M., Weinberg, G., and Mestl, G., *Raman spectroscopy of molybdenum oxides*. Phys. Chem. Chem. Phys. **2002**. 4(5): p. 812–821.

131. Ressler, T., Walter, A., Scholz, J., et al., *Structure and properties of a Mo oxide catalyst supported on hollow carbon nanofibers in selective propene oxidation*. J. Catal. **2010**. 271(2): p. 305–314.
132. Kim, D.S., Wachs, I.E., and Segawa, K., *Molecular Structures and Reactivity of Supported Molybdenum Oxide Catalysts*. J. Catal. **1994**. 149(2): p. 268–277.
133. Zhu, Z., Liu, Z., Niu, H., et al., *Mechanism of SO₂ Promotion for NO Reduction with NH₃ over Activated Carbon-Supported Vanadium Oxide Catalyst*. J. Catal. **2001**. 197(1): p. 6–16.
134. Thielemann, J., *Synthesis, Characterization and in situ Catalysis of Silica SBA-15 Supported Molybdenum Oxide Model Catalysts*. Technischen Universität Darmstadt, Fachbereich VII – Chemie **2011**. Dissertation: p. 1–188.
135. Zhuravlev, L.T., *The surface chemistry of amorphous silica. Zhuravlev model*. Colloids and Surfaces A: Physicochem. Eng. Aspects **2000**. 173(1–3): p. 1–38.
136. Nawrocki, J., *The silanol group and its role in liquid chromatography*. J. Chromatogr. A **1997**. 779(1–2): p. 29–71.
137. Ressler, T., *Application of time-resolved in-situ X-ray absorption spectroscopy in solid-state chemistry*. Anal. Bioanal. Chem. **2003**. 376(5): p. 584–593.
138. Friedman, H.L., *Kinetics of thermal degradation of char-forming plastics from thermogravimetry. Application to a phenolic plastic*. J. Polym. Sci., Part C: Polym. Symp. **1964**. 6(1): p. 183–195.
139. Vyazovkin, S. and Wight, C.A., *Model-free and model-fitting approaches to kinetic analysis of isothermal and nonisothermal data*. Thermochim. Acta **1999**. 340–341(0): p. 53–68.
140. Madon, R.J. and Boudart, M., *Experimental criterion for the absence of artifacts in the measurement of rates of heterogeneous catalytic reactions*. Ind. Eng. Chem. Fundam. **1982**. 21(4): p. 438–447.
141. Weisz, P.R. and Prater, C.D., in *Advances in Catalysis*, Frankenburg, W.G., Komarewsky, V.V.I., and Rideal, E.E.K. Editors. **1954**, Elsevier Science: New York. p. 143.

142. Grasselli, R., *Genesis of site isolation and phase cooperation in selective oxidation catalysis*. Top. Catal. **2001**. 15(2–4): p. 93–101.
143. Witko, M., Hermann, K., and Tokarz, R., *Adsorption and reactions at the (001) V₂O₅ surface: cluster model studies*. Catal. Today **1999**. 50(3–4): p. 553–565.
144. Zhao, C. and Wachs, I.E., *Selective oxidation of propylene over model supported V₂O₅ catalysts: Influence of surface vanadia coverage and oxide support*. J. Catal. **2008**. 257(1): p. 181–189.
145. Wachs, I.E., *The generality of surface vanadium oxide phases in mixed oxide catalysts*. Appl. Catal. A **2011**. 391(1–2): p. 36–42.
146. Haber, J., *Fifty years of my romance with vanadium oxide catalysts*. Catal. Today **2009**. 142(3–4): p. 100–113.
147. Bettahar, M.M., Costentin, G., Savary, L., et al., *On the partial oxidation of propane and propylene on mixed metal oxide catalysts*. Appl. Catal. A **1996**. 145(1–2): p. 1–48.
148. Chaurand, P., Rose, J., Briois, V., et al., *New methodological approach for the vanadium K-edge X-ray absorption near-edge structure interpretation: Application to the speciation of vanadium in oxide phases from steel slag*. J. Phys. Chem. B **2007**. 111(19): p. 5101–5110.
149. Went, G.T., Leu, L.J., Lombardo, S.J., et al., *Raman spectroscopy and thermal desorption of ammonia adsorbed on titania (anatase)-supported vanadia*. J. Phys. Chem. **1992**. 96(5): p. 2235–2241.
150. Andersson, A., *An oxidized surface state model of vanadium oxides and its application to catalysis*. J. Solid State Chem. **1982**. 42(3): p. 263–275.
151. Millet, P., Satto, C., Sciau, P., et al., *MgV₂O₅ and δ -Li_xV₂O₅: A Comparative Structural Investigation*. J. Solid State Chem. **1998**. 136(1): p. 56–62.
152. Kung, H.H. and Kung, M.C., *Oxidative dehydrogenation of alkanes over vanadium-magnesium-oxides*. Appl. Catal. A **1997**. 157(1–2): p. 105–116.
153. Cavani, F., Ballarini, N., and Cericola, A., *Oxidative dehydrogenation of ethane and propane: How far from commercial implementation?* Catal. Today **2007**. 127(1–4): p. 113–131.

154. Liu, Y.-M., Cao, Y., Yi, N., et al., *Vanadium oxide supported on mesoporous SBA-15 as highly selective catalysts in the oxidative dehydrogenation of propane*. *J. Catal.* **2004**. 224(2): p. 417–428.
155. Grzybowska-Świerkosz, B., *Thirty years in selective oxidation on oxides: what have we learned?* *Top. Catal.* **2000**. 11–12(1): p. 23–42.
156. Hunger, M. and Weitkamp, J., *In situ IR, NMR, EPR, and UV/Vis spectroscopy: Tools for new insight into the mechanisms of heterogeneous catalysis*. *Angew. Chem. Int. Ed.* **2001**. 40(16): p. 2954–2971.
157. Albonetti, S., Cavani, F., and Trifirò, F., *Key Aspects of Catalyst Design for the Selective Oxidation of Paraffins*. *Catal. Rev.* **1996**. 38(4): p. 413–438.
158. Hunger, M., *Moderne Methoden der In-situ-Festkörper-NMR-Spektroskopie in der heterogenen Katalyse*. *Chemie Ingenieur Technik* **2007**. 79(6): p. 781–793.
159. Kiricsi, I., Foerster, H., Tasi, G., et al., *ChemInform Abstract: Generation, Characterization, and Transformations of Unsaturated Carbenium Ions in Zeolites*. *Chem. Rev.* **1999**. 30(46): p. 2085–2114.
160. Khawam, A. and Flanagan, D.R., *Solid-State Kinetic Models: Basics and Mathematical Fundamentals*. *J. Phys. Chem. B* **2006**. 110(35): p. 17315–17328.
161. Abon, M., Massardier, J., Mingot, B., et al., *New unsupported [100]-oriented MoO₃ catalysts II. Catalytic properties in propylene oxidation*. *J. Catal.* **1992**. 134(2): p. 542–548.
162. van Sint Annaland, M., Kuipers, J.A.M., and van Swaaij, W.P.M., *A kinetic rate expression for the time-dependent coke formation rate during propane dehydrogenation over a platinum alumina monolithic catalyst*. *Catal. Tod.* **2001**. 66(2–4): p. 427–436.
163. Ressler, T., Wienold, J., Jentoft, R.E., et al., *Bulk Structural Investigation of the Reduction of MoO₃ with Propene and the Oxidation of MoO₂ with Oxygen*. *J. Catal.* **2002**. 210(1): p. 67–83.
164. Aritani, H., Tanaka, T., Funabiki, T., et al., *Structure of Mo-Mg Binary Oxides in Oxidized/Reduced States Studied by X-ray Absorption Spectroscopy at the Mo K Edge and Mg K Edge*. *J. Phys. Chem.* **1996**. 100(13): p. 5440–5446.

165. Centi, G., Trifiró, F., Ebner, J.R., et al., *Mechanistic Aspects of Maleic Anhydride Synthesis from C4 Hydrocarbons over Phosphorus Vanadium Oxide*. Chem. Rev. **1988**. 88(1): p. 55–80.
166. Ozkan, U.S., Smith, M.R., and Driscoll, S.A., *Investigation of synergy effects in selective oxidation catalysts through in situ laser raman spectroscopy / isotopic labeling technique*. J. Catal. **1992**. 134(1): p. 24–35.
167. Brito, J. and Laine, J., *Characterization of supported MoO₃ by temperature-programmed reduction*. Polyhedron **1986**. 5(1–2): p. 179–182.
168. Hamilton, N., Wolfram, T., Tzolova Muller, G., et al., *Topology of silica supported vanadium-titanium oxide catalysts for oxidative dehydrogenation of propane*. Catal. Sci. Technol. **2012**. 2(7): p. 1346–1359.
169. Beck, B., Harth, M., Hamilton, N.G., et al., *Partial oxidation of ethanol on vanadia catalysts on supporting oxides with different redox properties compared to propane*. J. Catal. **2012**. 296(0): p. 120–131.
170. Courcot, D., Ponchel, A., Grzybowska, B., et al., *Effect of the sequence of potassium introduction to V₂O₅/TiO₂ catalysts on their physicochemical properties and catalytic performance in oxidative dehydrogenation of propane*. Catal. Today **1997**. 33(1–3): p. 109–118.
171. Shido, T., Asakura, K., and Iwasawa, Y., *Reactant-promoted reaction mechanism for catalytic water-gas shift reaction on MgO*. J. Catal. **1990**. 122(1): p. 55–67.
172. Ueno, A., Onishi, T., and Tamaru, K., *Dynamic technique to elucidate the reaction intermediate in surface catalysis. Water-gas shift reaction*. Trans. Faraday Soc. **1970**. 66(0): p. 756–763.
173. Duarte de Farias, A.M., Barandas, A.P.M.G., Perez, R.F., et al., *Water-gas shift reaction over magnesia-modified Pt/CeO₂ catalysts*. J. Power Sources **2007**. 165(2): p. 854–860.
174. Faraldos, M., Bañares, M.A., Anderson, J.A., et al., *Comparison of Silica-Supported MoO₃ and V₂O₅ Catalysts in the Selective Partial Oxidation of Methane*. J. Catal. **1996**. 160(2): p. 214–221.

-
175. Sokolovskii, V.D., *Principles of Oxidative Catalysis on Solid Oxides*. Catal. Rev. **1990**. 32(1–2): p. 1–49.
176. Gao, X., Ruiz, P., Xin, Q., et al., *Preparation and characterization of three pure magnesium vanadate phases as catalysts for selective oxidation of propane to propene*. Catal. Lett. **1994**. 23(3): p. 321–337.
177. Selim, S.A., Philip, C.A., and Mikhail, R.S., *Thermal decomposition of ammonium metavanadate*. Thermochim. Acta **1980**. 36(3): p. 287–297.
178. Chaklanabish, N. and Maiti, H., *Thermal stability of pure and lithium intercalated non-stoichiometric V₆O₁₃*. J. Therm. Anal. Calorim. **1986**. 31(6): p. 1243–1251.
179. Brückner, W., Oppermann, H., Reichelt, T., et al., *Vanadiumoxide: Darstellung, Eigenschaften, Anwendung*. **1983**: Akademie-Verlag.
180. Yoon, Y.S., Ueda, W., and Moro-oka, Y., *Oxidative dehydrogenation of propane over magnesium molybdate catalysts*. Catal. Lett. **1995**. 35(1): p. 57–64.
181. Seleborg, M., *A Refinement of the Crystal Structure of Disodium Dimolybdate*. Acta Chem. Scand. **1967**. 21: p. 499–504.

Appendix

A1 Support Material

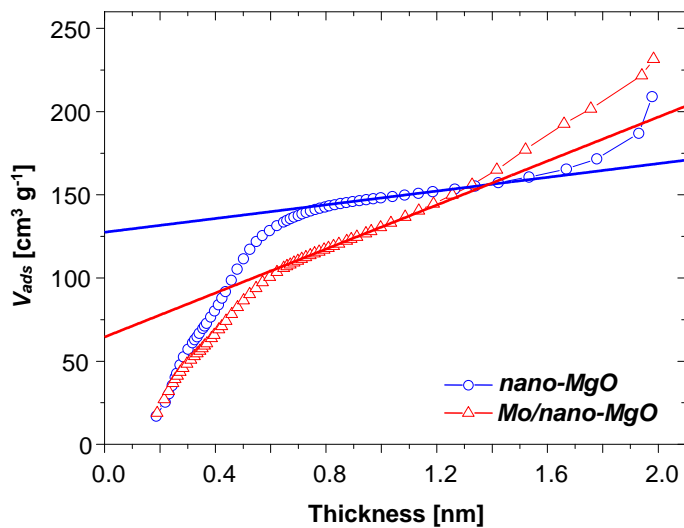


Fig. A 1.1 t -Plots of nano-MgO (circles) and Mo/nano-MgO (triangles). The Harkins-Jura thickness equation was used as reference isotherm.

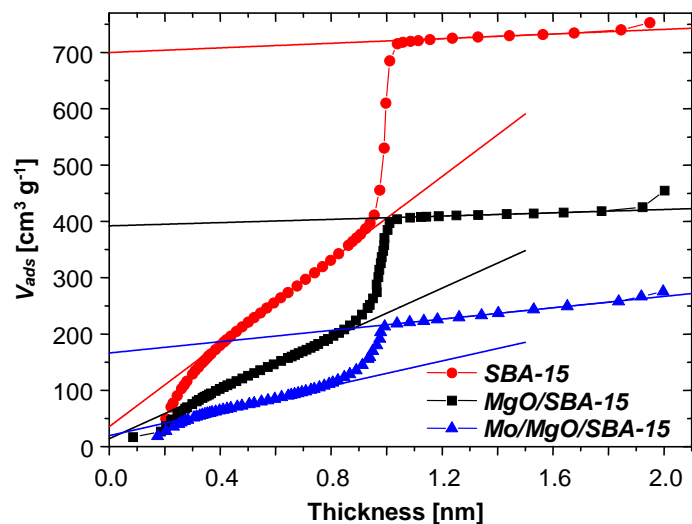


Fig. A 1.2 t -Plots of parent SBA-15 (circles), MgO/SBA-15 (squares), and Mo/MgO/SBA-15 (triangles). The Harkins-Jura thickness equation was used as reference isotherm.

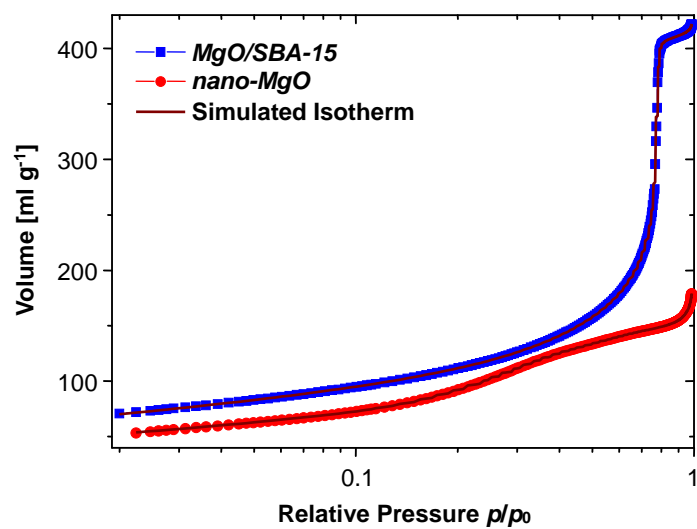


Fig. A 1.3 Nitrogen physisorption adsorption/desorption isotherms of *MgO/SBA-15* and *nano-MgO* together with the simulated isotherms derived from NLDFT calculations (logarithmic scale).

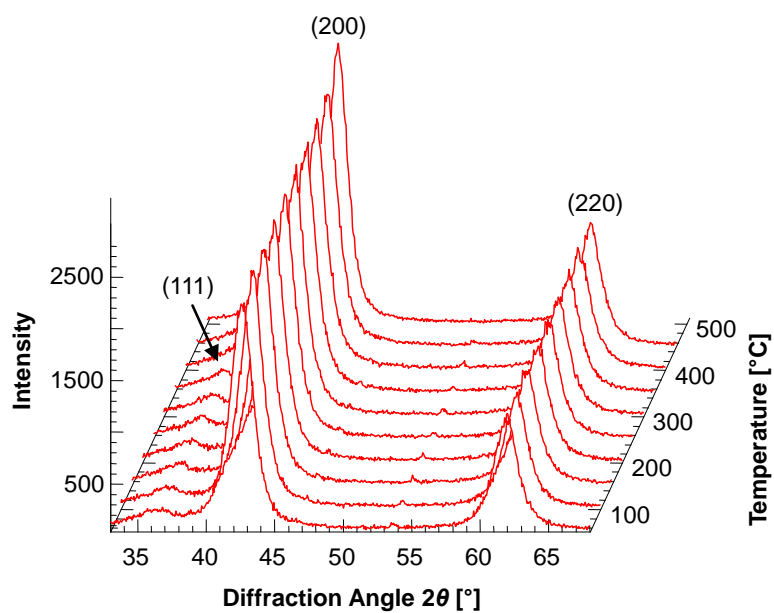


Fig. A 1.4 Evolution of X-ray diffraction patterns of *nano-MgO* during heat treatment between 50 °C and 450 °C in 20% O₂/He.

A2 Experimental

Table A 2.1 Vanadium and molybdenum oxides used as reference compounds together with their purchase information or synthesis procedure.

| | Provider / Synthesized | Synthesis |
|------------------------------------|---|---|
| Vanadium Oxides | | |
| V_2O_5 | Alfa Aesar, 99.8% | |
| $(NH_4)_6V_{10}O_{28} \cdot xH_2O$ | Synthesized (TU Berlin, Ressler group) | 1 g of NH_4VO_3 was dissolved in 33 ml of water and heated to 70 °C for 24 h. The residue was filtered off and 1.4 ml of 50% acetic acid was added dropwise to the resulting yellow solution. After addition of 26.5 ml of ethanol the deep orange solution was cooled with a mixture of 1:1 acetone and dry ice. The resulting orange powder was filtered off and washed with ethanol and diethyl ether.[110] |
| K_3VO_4 | Alfa Aesar, 99.9% | |
| Na_3VO_4 | Alfa Aesar, 99.9% | |
| $Mg_3V_2O_8$ | Synthesized (TU Berlin, Ressler group) | Prepared by the citrate method according to Gao <i>et al.</i> [176] $Mg(NO_3)_2 \cdot 6H_2O$ (Fluka, 99%) or $Ca(NO_3)_2 \cdot 4H_2O$ (Fluka, 99%) and NH_4VO_3 (Fluka, 99%) were used as metal precursors in the concentrations required for the desired Mg/V, and Ca/V ratio, respectively. The salts were dissolved in 500 ml of water. The mixture was heated to 90 °C for 2 h until a clear yellow solution was obtained. After cooling to 27 °C 2 ml of 65% HNO_3 were added to avoid precipitation. Subsequently, citric acid (Roth 99.5%) was added to neutralize the positive charges of Mg^{2+}/Ca^{2+} and V^{5+} . Water was removed by evaporation in two steps to avoid the formation of NO_x gases. The resulting amorphous solid was calcined in two steps: 18 h at 380 °C and 6–8.5 h at 550–750 °C either in a muffle furnace or an open tube furnace.[110] |
| $\alpha\text{-}Mg_2V_2O_7$ | Synthesized (TU Berlin, Ressler group) | |
| MgV_2O_6 | Synthesized (TU Berlin, Ressler group) | |
| $Ca_3V_2O_8$ | Synthesized (TU Berlin, Ressler group) | |
| $Ca_2V_2O_7$ | Synthesized (TU Berlin, Ressler group) | |
| CaV_2O_6 | Synthesized (TU Berlin, Ressler group) | |
| $NaVO_3$ | Aldrich, 99.9% | |
| KVO_3 | Alfa Aesar, 99.9% | |
| NH_4VO_3 | Fluka, 99% | |

| | Provider / Synthesized | Synthesis |
|--------------------------|---|--|
| V_3O_7 | Synthesized (TU Berlin, Lerch group) | Synthesis procedure adapted from [177]. 5 g of NH_4VO_3 (Merck, p.a.) were placed in aluminum oxide vessel and put into a tube furnace. Combustion reaction was conducted at 450 °C for 30 h under continuous argon (Air Liquide, 5.0) gas flow (5 l/h) to remove gaseous by-products. Subsequently, the furnace was opened to allow the reactants to cool down quickly. V_3O_7 was obtained quantitatively as black powder. |
| V_6O_{13} | Synthesized (TU Berlin, Lerch group) | Synthesis procedure adapted from [178]. 5 g of NH_4VO_3 (Merck, p.a.) were placed in aluminum oxide vessel and put into a tube furnace. Combustion reaction was conducted at 650 °C for 12 h under continuous argon (Air Liquide, 5.0) gas flow (5 l/h) to remove gaseous by-products. Subsequently, the furnace was opened to allow the reactants to cool down quickly. A mixture of V_6O_{13} and V_2O_5 was obtained. To remove V_2O_5 the mixture was boiled for 10 min in sodium hydroxide solution (1 mol/l). The residue was filtered off and washed with ethanol. The resulting black powder was dried over night at 110 °C. |
| V_2O_5 | Synthesized (TU Berlin, Lerch group) | Synthesis procedure adapted from [179]. 5 g of V_2O_5 (Merck, p.a.) were placed in aluminum oxide vessel and put into a tube furnace. Reduction was conducted at 800 °C for 16 h. As reducing agent hydrogen (Air Liquide, 3.0) was used with a continuous gas flow of 3 l/h. |
| Molybdenum Oxides | | |
| MoO_3 | Sigma-Aldrich, 99.5% | |
| $MgMoO_4$ | Synthesized (TU Berlin, Ressler group) | Prepared according to Yoon <i>et al.</i> [180] An aqueous solution of ammonium heptamolybdate (Fluka, 99%) at pH = 9 was mixed with an aqueous solution of $Mg(NO_3)_2 \cdot 6H_2O$ (Fluka, 99%) at pH = 2. The Mg/Mo ratio was kept at 0.9. The pH value of the mixed solution was adjusted to ~ 5. The precipitates were solidified by evaporation of water at 80 °C. The resulting slurry was dried at 110 °C for 20 h. Calcination in air was performed in three steps at 200 °C, 250 °C, and 300 °C for 0.5 h, 0.5 h, and 3 h, respectively. The yellow solid was ground to a fine powder and calcined again at 600 °C for 9 h. The raw product was suspended in aqueous ammonia solution (pH ≥ 15) and stirred for 2 h. The insoluble residue was filtered off. The filtrate was solidified by evaporation and again dissolved in ammonia solution. The solution was heated to 100 °C and kept at that temperature without stirring until the solution was evaporated. The resulting white powder was dried at 120 °C.[98] |

| | Provider / Synthesized | Synthesis |
|---|---|--|
| Li_2MoO_4 | Aldrich, 99.9% | |
| $\text{Na}_2\text{MoO}_4 \cdot 2\text{H}_2\text{O}$ | Sigma-Aldrich, 99+% | |
| $\text{Na}_2\text{Mo}_2\text{O}_7$ | Synthesized (TU Berlin, Ressler group) | Prepared according to Seleborg.[181] 3.14 g of $\text{Na}_2\text{MoO}_4 \cdot 2\text{H}_2\text{O}$ (Sigma-Aldrich, 99+%) and 1.87 g of MoO_3 (Sigma-Aldrich, 99.5%) were ground thoroughly. The mixture was heated to 650 °C and held at that temperature for 42 h under static air. White rod-shaped crystals were obtained. |
| $(\text{NH}_4)_6\text{Mo}_7\text{O}_{24} \cdot 4\text{H}_2\text{O}$ | Fluka, 99.0% | |

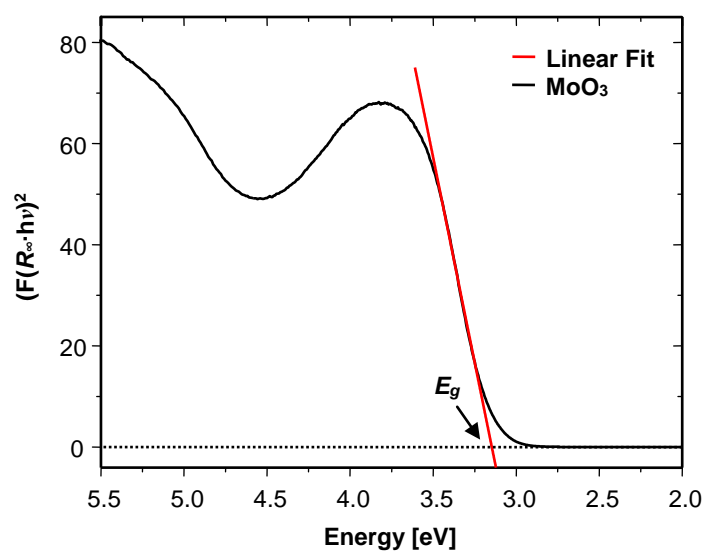


Fig. A 2.1 Determination of the edge energy, E_g , with a linear fit function from the UV-Vis spectrum of MoO_3 . The edge energy, E_g , was determined at the intercept of the linear fit function with the abscissa.

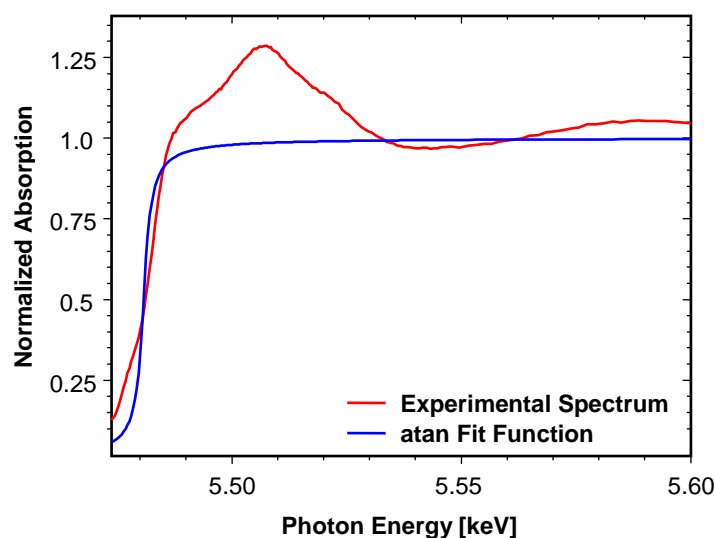


Fig. A 2.2 Fitting routine to determine the V K edge position, $E_{1/2}$, at the edge energy half way up the normalized edge step of an experimental XANES spectrum (e.g., 5 wt.% V/MgO/SBA-15) with an atan fit function in the spectral region between 5.474–5.600 keV. Within the fitting procedure only the position was allowed to vary while height and half width of the function were fixed to 1, and 0.01, respectively. Resulting position of the fit function was taken as $E_{1/2}$.

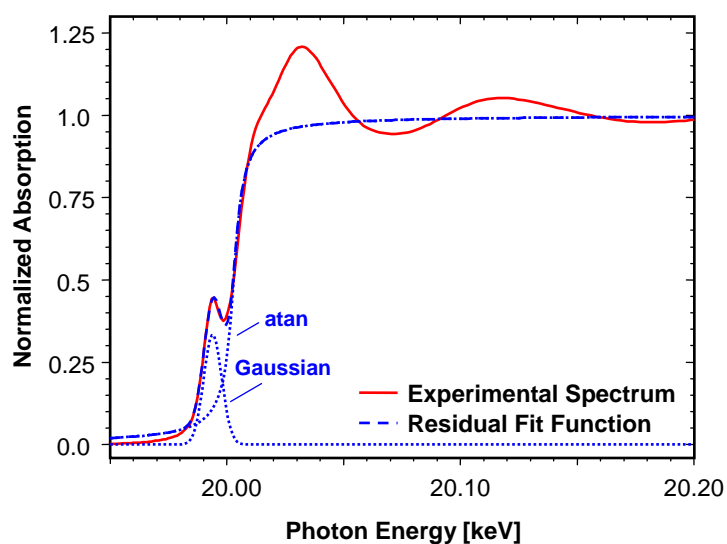


Fig. A 2.3 Fitting routine to determine the pre-edge peak height from a Mo K edge XANES spectrum (e.g., 5 wt.% Mo/MgOSBA-15) with a Gaussian function to resemble the pre-edge peak and an atan function to fit the edge step. The fit was performed in the spectral region between 19.95–20.20 keV. Within the fitting procedure all parameters of the Gaussian function (position, height, and full width at half maximum) were allowed to vary. For the atan function only the position was allowed to vary while height and half width were fixed to 1, and 0.01, respectively. The height of the Gaussian function was taken as pre-edge peak height.

A3 Supported Vanadium Oxides

Table A 3.1 Position and full width at half maximum (FWHM) of the fitted UV-Vis absorption bands for uncalcined *V/MgO/SBA-15*.

| | 1 wt.% V unc. | | | 3 wt.% V unc. | | | 5 wt.% V unc. | | | 10 wt.% V unc. | | |
|----------------------|---------------|-----|-----|---------------|-----|-----|---------------|-----|-----|----------------|-----|-----|
| Position [nm] | 202 | 263 | 324 | 217 | 270 | 326 | 220 | 272 | 325 | 223 | 275 | 325 |
| FWHM [nm] | 55 | | | 57 | | | 59 | | | 66 | | |
| Residual | 0.7 | | | 0.5 | | | 0.7 | | | 1.8 | | |

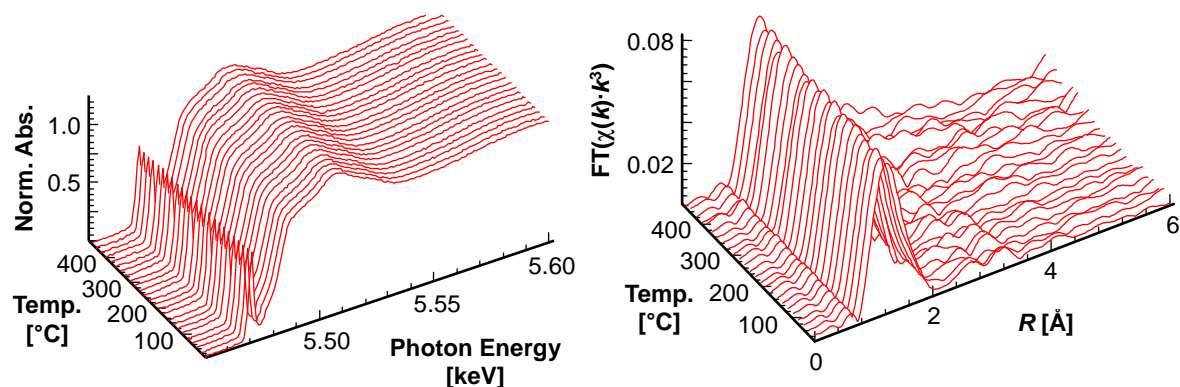


Fig. A 3.1 Evolution of V K edge XANES spectra (left) and of the Fourier transformed XAFS $\chi(k)$ (right), of *V/MgO/SBA-15* during temperature programmed treatment in propene and oxygen (RT \rightarrow 450 °C, 4 K/min, 5% propene, 5% oxygen in He).

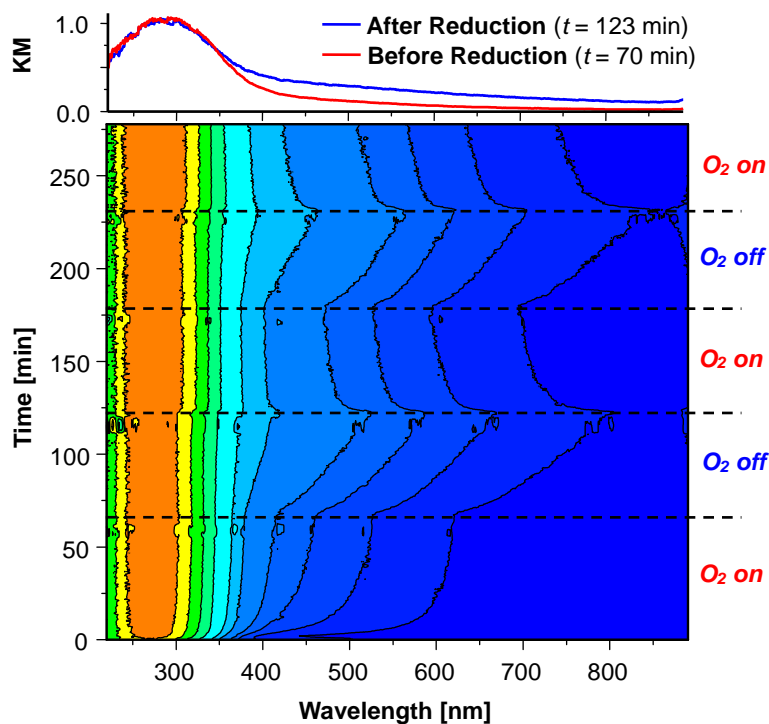


Fig. A 3.2 *In situ* DR-UV-Vis spectra of *V/MgO/SBA-15* (5 wt.% V) under isothermal catalytic reaction conditions ($T = 425$ °C, 5% propene, 5% oxygen in He). Two reduction/reoxidation cycles were conducted by periodically changing the gas atmosphere from propene oxidizing (5% propene, 5% O₂) to reducing conditions (5% propene).

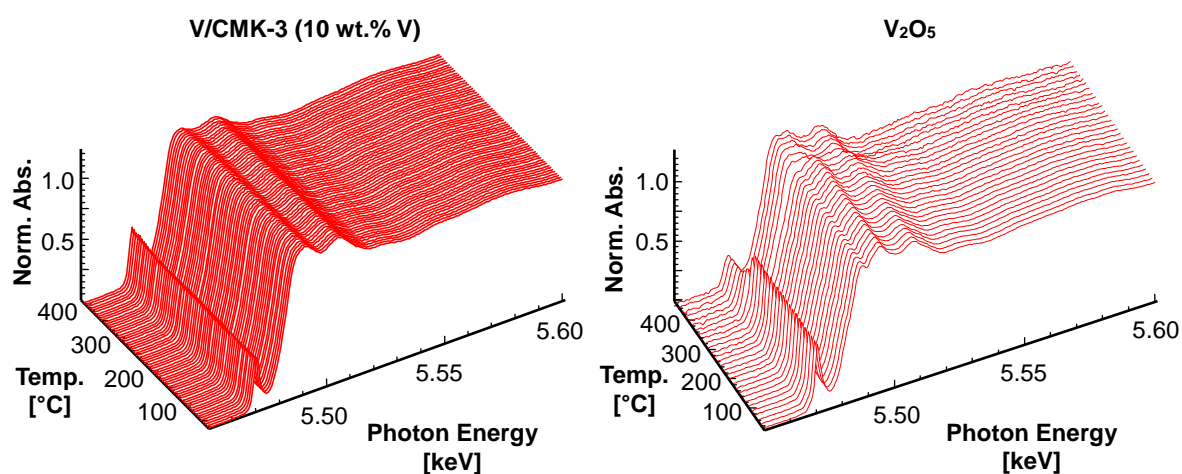


Fig. A 3.3 Evolution of V K edge XANES spectra of *V/CMK-3* (10 wt.% V) (left) and *V₂O₅* (right) during temperature programmed reaction in propene/oxygen (5% propene, 5% O₂ in He).

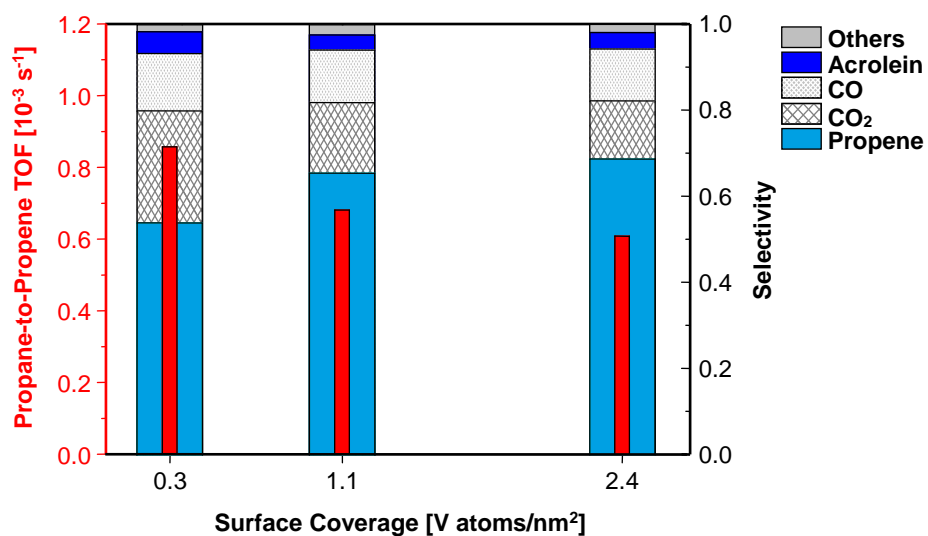


Fig. A 3.4 Comparison of propane-to-propene TOF (left axis) and product distribution in ODH reaction (right axis) at similar propane conversions (~5%) for vanadium oxide supported on silica SBA-15 at various surface coverages (reaction conditions: 5% propane, 7.5% O₂ in He, $T = 500$ °C). Reaction products denoted as "others" refer to acetic aldehyde and acetone.

A4 Supported Molybdenum Oxides

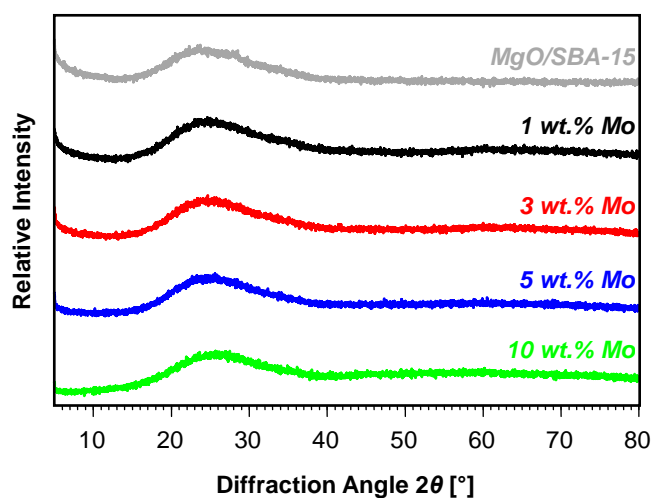


Fig. A 4.1 Wide-angle X-ray diffraction patterns of bare *MgO/SBA-15* and supported molybdenum oxides at various catalyst loadings.

Table A 4.1 Molybdenum oxide surface coverage, $\Phi_{Mo\ atoms}$, and UV-Vis edge energy of molybdenum oxides on *MgO/SBA-15*.

| | $\Phi_{Mo\ atoms}$ [Mo atoms/nm ²] | Edge Energy [eV] |
|-------------------|--|------------------|
| 1 wt.% Mo | 0.2 | 4.86 |
| 3 wt.% Mo | 0.6 | 4.76 |
| 5 wt.% Mo | 1.3 | 4.82 |
| 10 wt.% Mo | 4.2 | 4.74 |

Table A 4.2 Number of nearest neighbors and UV-Vis edge energy of several molybdenum oxide references.

| | No. of Mo–O–Mo bonds | Edge Energy [eV] |
|--|----------------------|------------------|
| Li₂MoO₄ | 0 | 4.34 |
| MgMoO₄ | 0 | 4.08 |
| Na₂MoO₄·2H₂O | 0 | 4.42 |
| Na₂Mo₂O₇ | 3.5 | 3.61 |
| AHM^a | 4 | 3.40 |
| MoO₃ | 5 | 3.15 |

^a AHM: ammonium heptamolybdate (NH₄)₆Mo₇O₂₄·4H₂O

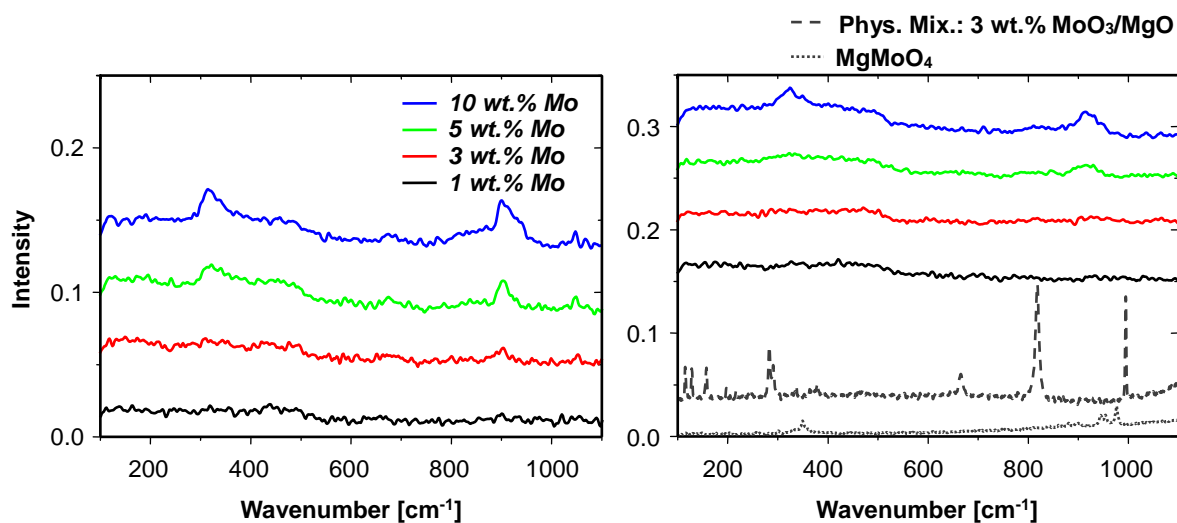


Fig. A 4.2 Raman spectra of uncalcined (left) and calcined (right) *Mo/MgO/SBA-15* with various catalyst loadings. For comparison the spectra of a physical mixture of molybdenum trioxide MoO₃ and magnesium molybdate MgMoO₄ are shown as well. Spectra were offset for clarity.

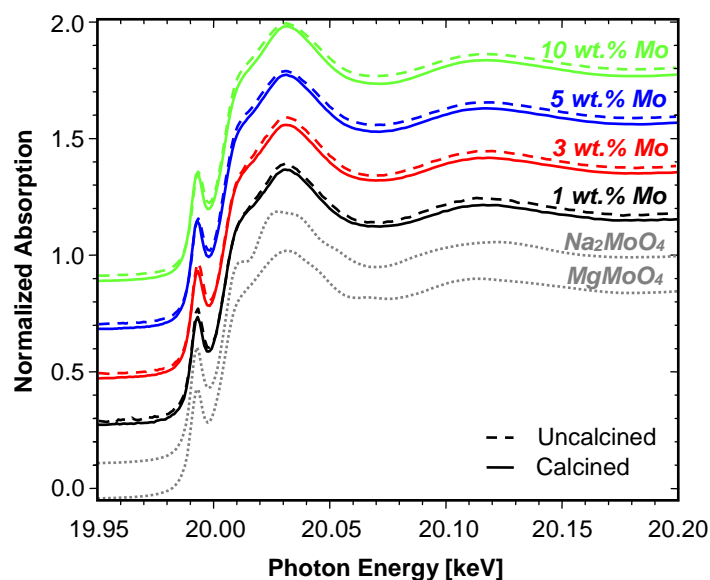


Fig. A 4.3 Normalized Mo K edge XANES spectra of supported molybdenum oxide catalysts together with those of molybdate references. The samples exhibited a similar near edge structure around the molybdenum atom compared to the structure of the depicted references.

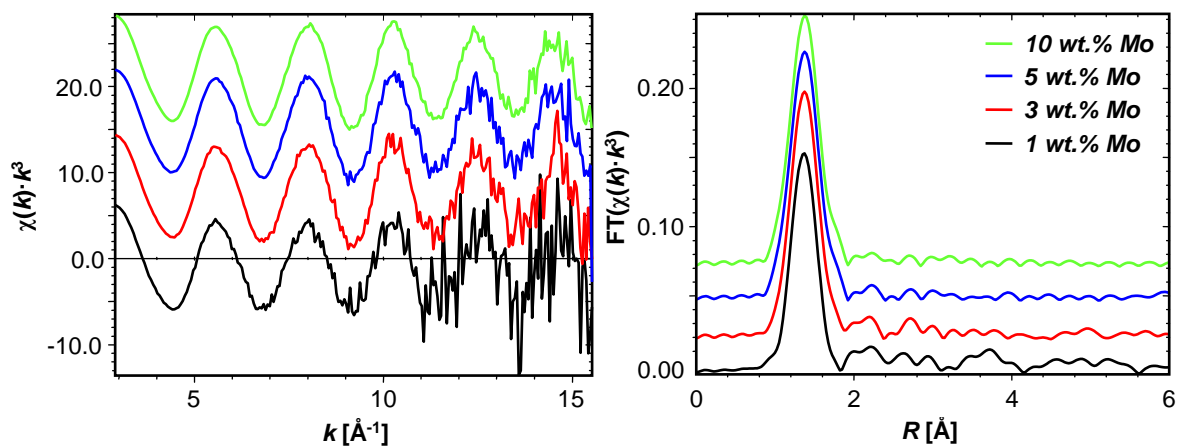


Fig. A 4.4 Mo K edge XAFS, $\chi(k) \cdot k^3$ (left), and pseudo-radial distribution functions, $\text{FT}(\chi(k) \cdot k^3)$ (right, not phase-shift corrected), of *Mo/MgO/SBA-15* catalysts at various molybdenum loadings.

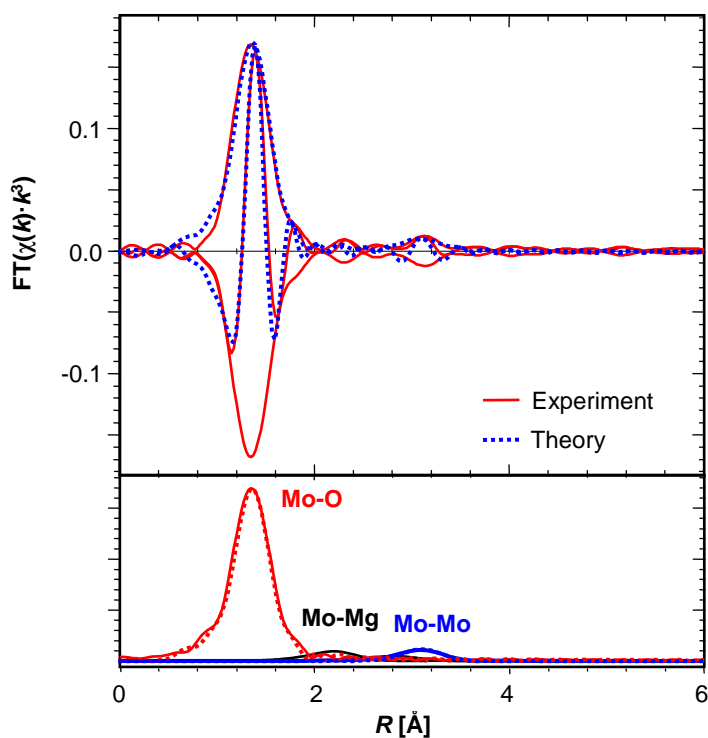


Fig. A 4.5 EXAFS refinement for the determination of the fraction of $[\text{MoO}_4]$ dimers in *Mo/MgO/SBA-15*. Shown are the experimental (solid line) Mo K edge $\text{FT}(\chi(k) \cdot k^3)$ of *Mo/MgO/SBA-15* together with a theoretical XAFS function (dotted). Corresponding fitting results are given in Table A 4.3. $\text{FT}(\chi(k) \cdot k^3)$ of the individual scattering paths are displayed below the fit.

Table A 4.3 Results of the EXAFS refinement for the determination of the ratio of [MoO₄] dimers in Mo/MgO/SBA-15. Given are number, N , of atoms at distance, R , from the absorbing molybdenum atom. Experimental distances, R , and XAFS disorder parameters, σ^2 , were obtained from the refinement of a MgMoO₄ model structure to the experimental Mo K edge XAFS FT($\chi(k) \cdot k^3$) of the samples (Fig. 5.16) (k range from 2.9–14.2 Å⁻¹, R range 0.9–4.1 Å, $N_{ind} = 24$, $N_{free} = 8$).

| Type | N | R [Å] | σ^2 [Å ²] |
|-----------------|-------|---------|------------------------------|
| Mo–O | 4_f | 1.78 | 0.0011 |
| Mo–Mo | 0.42 | 3.46 | 0.0035_f |
| <i>Residual</i> | | 9.5 | |

Note: Subscript f indicated parameters that were fixed in the refinement.

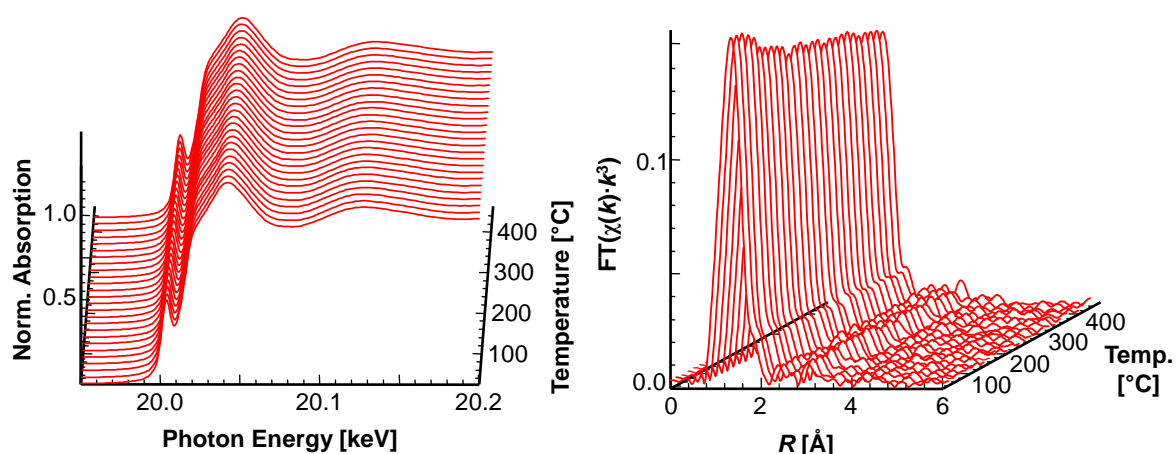


Fig. A 4.6 Evolution of Mo K edge XANES spectra (left) and of the Fourier transformed XAFS $\chi(k)$ (right, not phase-shift corrected) of Mo/MgO/SBA-15 during temperature programmed treatment in propene and oxygen (RT → 450 °C, 4 K/min, 5% propene, 5% O₂ in He).

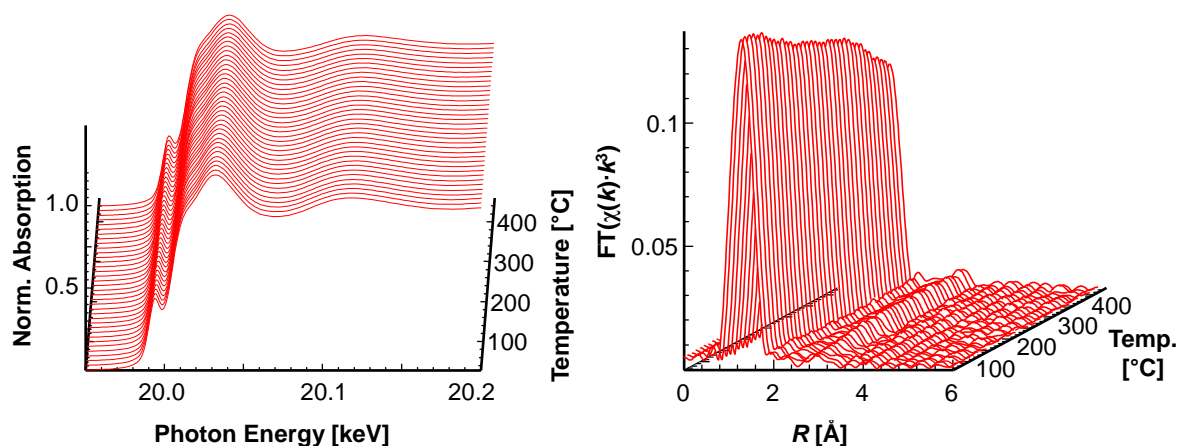


Fig. A 4.7 Evolution of Mo K edge XANES spectra (left) and of the Fourier transformed XAFS $\chi(k)$ (right, not phase-shift corrected) of *Mo/MgO/SBA-15* (5 wt.% Mo) during temperature programmed reduction in propene (RT \rightarrow 450 °C, 4 K/min, 5% propene in He).

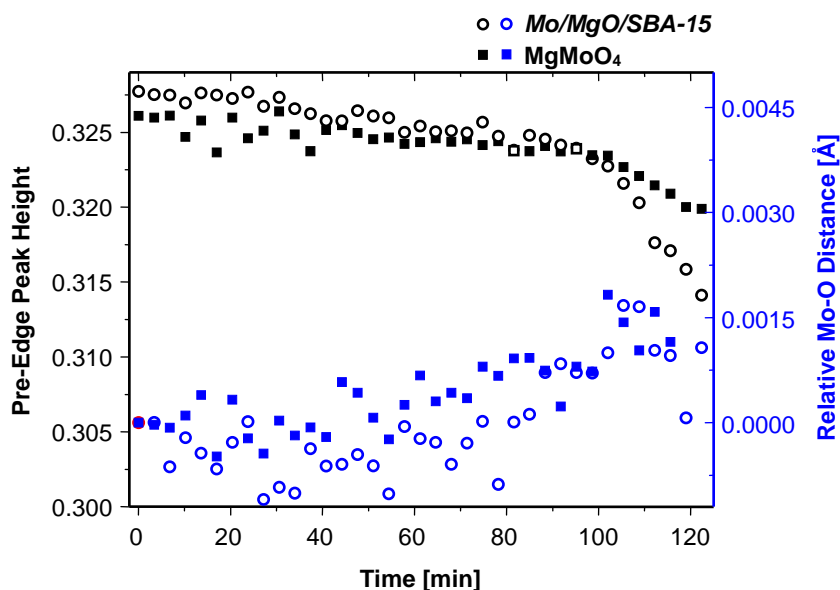


Fig. A 4.8 Evolution of the pre-edge peak height (left axis) derived from the *in situ* XANES spectra (Fig. A 4.7, left) and Mo-O distances (right axis) of *Mo/MgO/SBA-15* (5 wt.% Mo, open circles) and a magnesium molybdate reference *MgMoO₄* (filled squares) during temperature programmed reduction in propene. Mo-O distances were derived from a structure refinement to the first coordination shell of the experimental $\text{FT}(\chi(k) \cdot k^3)$ (Fig. A 4.7, right).

A5 Influence of Mass and Heat Transport Limitations

Calculation of the Weisz-Prater criterion:

The Knudsen diffusivity, D_{eff} , was calculated according to

$$D_{eff} = \frac{\tilde{v} d_{pore}}{3} = 1.21 \cdot 10^{-6} \text{ m}^2\text{s}^{-1} \quad (\text{A 5.1})$$

where \tilde{v} is the mean velocity of a propene molecule and d_{pore} is the pore diameter. The pore diameter, d_{pore} , was assumed to approximately 6 nm. The estimation of the mean velocity, \tilde{v} , of a propene molecule in the gas phase was derived from the Maxwell velocity distribution. Accordingly, the mean velocity is given as

$$\tilde{v} = \sqrt{\frac{8 R T}{\pi M_{propene}}} = 603.12 \text{ m s}^{-1} \quad (\text{A 5.2})$$

with the gas constant, R , the reaction temperature, T , and the molar mass of propene, $M_{propene}$. For calculation reaction temperature was assumed with $T = 450 \text{ }^\circ\text{C}$.

Assuming the maximum observed propene reaction rate of $r_{propene} = 0.25 \text{ mol g}^{-1}\text{s}^{-1}$ ($T = 450 \text{ }^\circ\text{C}$, 5% propene conversion), a catalyst density of $\rho_{cat} = 2 \text{ g cm}^{-3}$, a particle length, L_{cat} , of $50 \text{ }\mu\text{m}$, and a propene surface concentration of $C_{propene} = 1.36 \cdot 10^{-6} \text{ mol cm}^{-3}$ the Weisz-Prater criterion (eq.(6-5)) was calculated to

$$C_{WP} = \frac{r_{Propene} \rho_{cat} L_{cat}^2}{C_{propene} D_{eff}} = 0.0008$$

Since C_{WP} was well below one, influences of diffusional effects on the catalytic oxidation of propene were neglected.

A6 Influence of Support Material

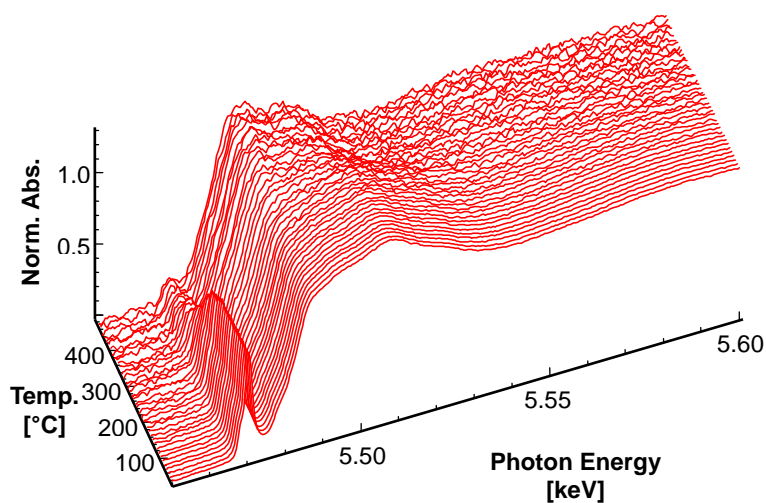


Fig. A 6.1 Evolution of V K edge XANES spectra of V/SBA-15 (7.7 wt.% V) during temperature programmed reduction in propene (RT \rightarrow 450 °C, 4 K/min, 5% propene in He).

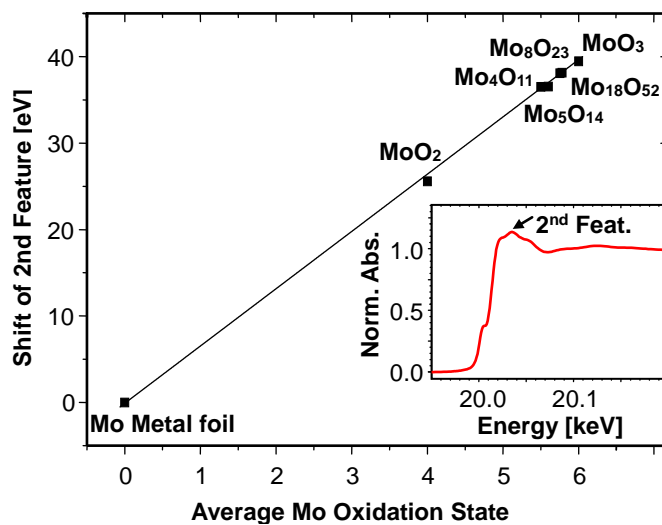


Fig. A 6.2 Shift of the "second XANES feature" derived from Mo K XANES spectra of various molybdenum oxide references as a function of the average Mo oxidation state. Inset: Mo K edge XANES spectra of Mo/SBA-15 (13 wt.% Mo). The arrow indicates the feature that was used to determine the average Mo oxidation state.

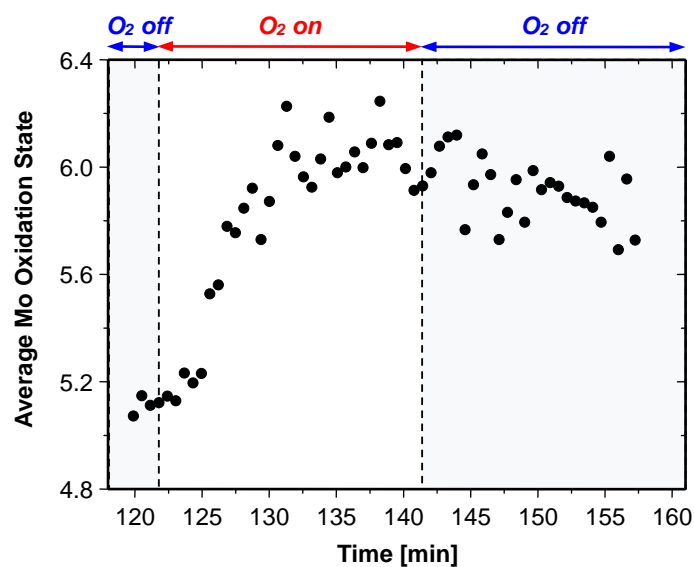


Fig. A 6.3 Evolution of the average Mo oxidation state of Mo/SBA-15 (13 wt.% Mo) evaluated from *in situ* XANES measurements at the Mo K edge during reduction/reoxidation cycle at 450 °C in 5% propene in He (O₂ off), and 5% propene, 5% O₂ in He (O₂ on). Before conduction of the redox experiments the sample underwent a temperature programmed reduction in 5% propene in He (not shown).

Epilogue

This study was performed between december 2009 and november 2013 at the Chemical Institute of the Technical University Berlin under the guidance of Prof. Dr. Thorsten Ressler. Parts of this work have previously been published or presented at scientific conferences.

Publications

J. Scholz, A. Walter, and T. Ressler, *Influence of MgO-modified SBA-15 on the structure and catalytic activity of supported vanadium oxide catalysts*, J. Catal. **2014**. 309(0): p. 105–114.

J. Scholz, A. Walter, A.H.P. Hahn, and T. Ressler, *Molybdenum oxide supported on nanostructured MgO: Influence of the alkaline support properties on MoO_x structure and catalytic behavior in selective oxidation*, Microporous Mesoporous Mater. **2013**. 180(0): p. 130–140.

J. Scholz, and T. Ressler, *Structure and Reactivity of Vanadium and Molybdenum Oxide-Based Catalysts Supported on MgO-Coated SBA-15*, Z. Anorg. Allg. Chem. **2012**. 638(10): p. 1630–1630.

R. Zubrzycki, A. Walter, J. Scholz, U. Dorn, and T. Ressler, *Structure and Properties of Heteropolyoxomolybdates Supported on Silica SBA-15*, Z. Anorg. Allg. Chem. **2010**. 636(11): p. 2085–2085.

J. Scholz, A. Walter, and T. Ressler, *Structural Investigations of Molybdenum Oxide Based Catalysts Supported on Nanostructured Magnesium Oxide*, Z. Anorg. Allg. Chem. **2010**. 636(11): p. 2079–2079.

T. Ressler, A. Walter, J. Scholz, J.P. Tessonnier, and D.S. Su, *Structure and properties of a Mo oxide catalyst supported on hollow carbon nanofibers in selective propene oxidation*, J. Catal. **2010**. 271(2): p. 305–314.

Talks

J. Scholz and T. Ressler, *Structure and reactivity of supported VO_x and MoO_x selective oxidation catalysts*, 46. Jahrestreffen Deutscher Katalytiker, March 13th–15th **2013**, Weimar, Germany.

Posters

J. Scholz and T. Ressler, *Structure and reactivity of supported VO_x and MoO_x selective oxidation catalysts* 46. Jahrestreffen Deutscher Katalytiker, March 13th–15th **2013**, Weimar, Germany.

J. Scholz and T. Ressler, *Structure and reactivity of supported VO_x and MoO_x selective oxidation catalysts*, 15. JCF-Frühjahrssymposium (GDCh), March 6th–9th **2013**, Berlin, Germany.

J. Scholz and T. Ressler, *Structure and reactivity of vanadium and molybdenum oxide based catalysts supported on MgO-coated SBA-15*, 15. Vortragstagung der Fachgruppe Festkörperchemie und Materialforschung (GDCh), September 17th–19th **2012**, Darmstadt, Germany.

J. Scholz, A. Walter, and T. Ressler, *Structure and property correlations of molybdenum and vanadium based oxide catalysts supported on nanostructured magnesium oxide*, 2. Berliner Chemie-Symposium (GDCh, JCF), April 3rd **2012**, Berlin, Germany.

J. Scholz, A. Walter, and T. Ressler, *Structure and property correlations of molybdenum and vanadium based oxide catalysts supported on nanostructured magnesium oxide*, 45. Jahrestreffen Deutscher Katalytiker, March 14th–16th **2012**, Weimar, Germany.

J. Scholz, A. Walter, and T. Ressler, *Structure and property correlations of molybdenum and vanadium oxides supported on mesoporous magnesium oxide*, EuropaCat X, August 28th – September 2nd **2011**, Glasgow, Scotland.

J. Scholz, A. Walter, and T. Ressler, *Molybdenum and vanadium based oxide catalysts supported on mesoporous magnesium oxide – structure and catalytic activity*, 44. Jahrestreffen Deutscher Katalytiker, March 16th–18th **2011**, Weimar, Germany.

J. Scholz, A. Walter, and T. Ressler, *Structural investigations of molybdenum oxide based catalysts supported on nanostructured magnesium oxide*, 15. Vortragstagung der Fachgruppe Festkörperchemie und Materialforschung (GDCh), September 20th–22nd **2010**, Berlin, Germany.

R. Zubrzycki, A. Walter, J. Scholz, U. Dorn, and T. Ressler, *Structure and Properties of Heteropolyoxomolybdates Supported on Silica SBA-15*, 15. Vortragstagung der Fachgruppe Festkörperchemie und Materialforschung (GDCh), September 20th–22nd **2010**, Berlin, Germany.

J. Scholz, A. Walter, and T. Ressler, *Structural investigations of molybdenum oxide based catalysts supported on nanostructured magnesium oxide*, 43. Jahrestreffen Deutscher Katalytiker, March 10th–12th **2010**, Weimar, Germany.

Danksagung

Ich bedanke mich bei Herrn Prof. Dr. Thorsten Ressler für die Überlassung dieser interessanten wissenschaftlichen Thematik. Insbesondere danke ich ihm auch für die exzellente fachliche Betreuung während der gesamten Zeit meiner Forschungstätigkeit in seinem Arbeitskreis. Ich danke außerdem Herrn Prof. Dr. Christian Hess für die Anfertigung des Zweitgutachtens.

Mein besonderer Dank gilt der gesamten Arbeitsgruppe Ressler für die angenehme und herzliche Arbeitsatmosphäre. Ich danke vor allem Gregor Koch, Alexander Müller und Rafael Zubrzycki für ihre stete Diskussionsbereitschaft. Bei Alexander Hahn und Dr. Thomas Christoph Rödel bedanke ich mich für die wissenschaftliche Unterstützung und Beratung bei der Durchführung zahlreicher Experimente. Ich danke auch Semiha Schwarz für die technische Hilfestellung bei der Durchführung der SBA-15-Synthesen und TG-Messungen. Dem gesamten Arbeitskreis Lerch sei für die Aufnahme der Weitwinkelbeugungsdaten gedankt. Dominik Weber danke ich außerdem für die Anfertigung und Bereitstellung der Vanadiumsuboxide als Referenzmaterialien. Zu Dank verpflichtet bin ich auch allen anderen Mitgliedern des Instituts für Chemie der TU Berlin, die mich bei meiner Arbeit unterstützt haben.

Meine Dissertation baute auf Vorarbeiten von Dr. Anke Walter auf, die mich insbesondere in den Anfängen der Arbeit mit Rat und Diskussionen vielfältig unterstützte, wofür ich ihr recht herzlich danke. Weiterer Dank gilt Dr. Ingo Piotrowski und Dr. Alper Ünal für die tatkräftige Unterstützung in allen Synthesefragen und dem Arbeitskreis Grohmann für die freundschaftliche Atmosphäre im Syntheselabor.

Dem DESY und dem HASYLAB in Hamburg sei für die Bereitstellung zahlreicher Messzeiten, sowie für die finanzielle Unterstützung gedankt. Auch der Deutschen Forschungsgemeinschaft (DFG) sei für die finanzielle Unterstützung gedankt.

Ich danke Dr. Andreas Garz und meiner Familie für den steten Rückhalt und ihre uneingeschränkte Unterstützung.

Eidesstattliche Versicherung

Hiermit versichere ich an Eides statt, dass ich die vorliegende Arbeit selbstständig verfasst und keine anderen als die in der Dissertation angegebenen Quellen und Hilfsmittel benutzt habe. Alle Ausführungen, die anderen veröffentlichten oder nicht veröffentlichten Schriften wörtlich oder sinngemäß entnommen wurden, habe ich kenntlich gemacht.

Die Arbeit hat in gleicher oder ähnlicher Fassung noch keiner anderen Prüfungsbehörde vorgelegen.

Ort, Datum

Unterschrift